Scanning Force Microscopy of Collagen and Biological Materials at Low Temperature

by

Mark B. Shattuck

DISSERTATION

Submitted in partial satisfaction of the requirements for the degree of

DOCTOR OF PHILOSOPHY

in

BIOENGINEERING

in the

GRADUATE DIVISION

of the

UNIVERSITY OF CALIFORNIA

San Francisco

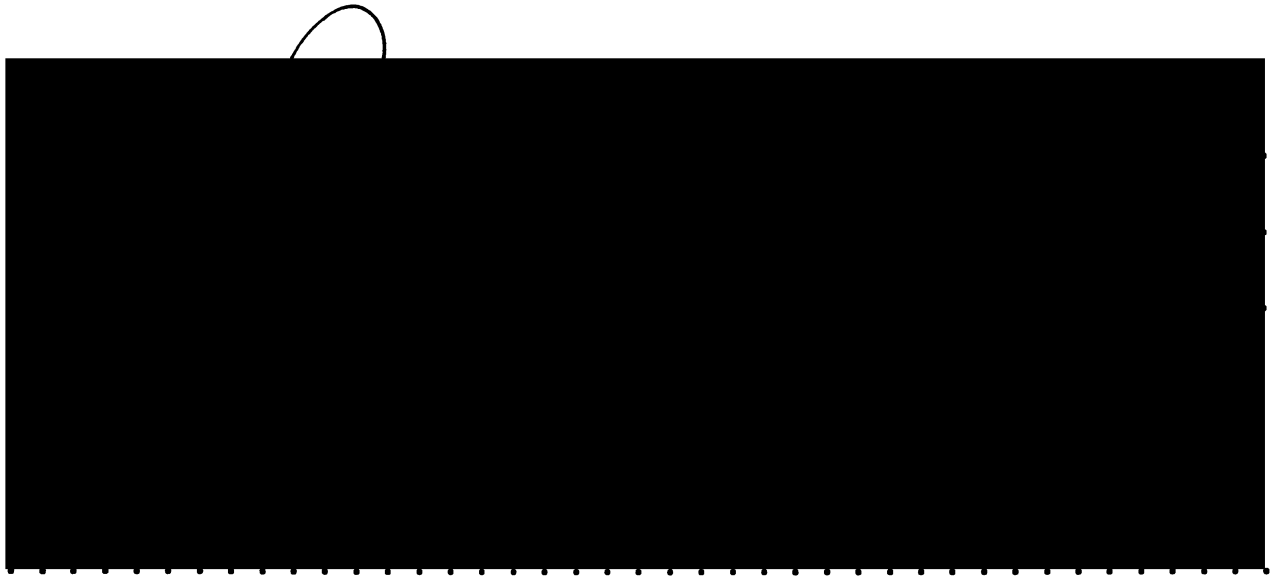

Date **University Librarian**

Degree Conferred: . . . . . .

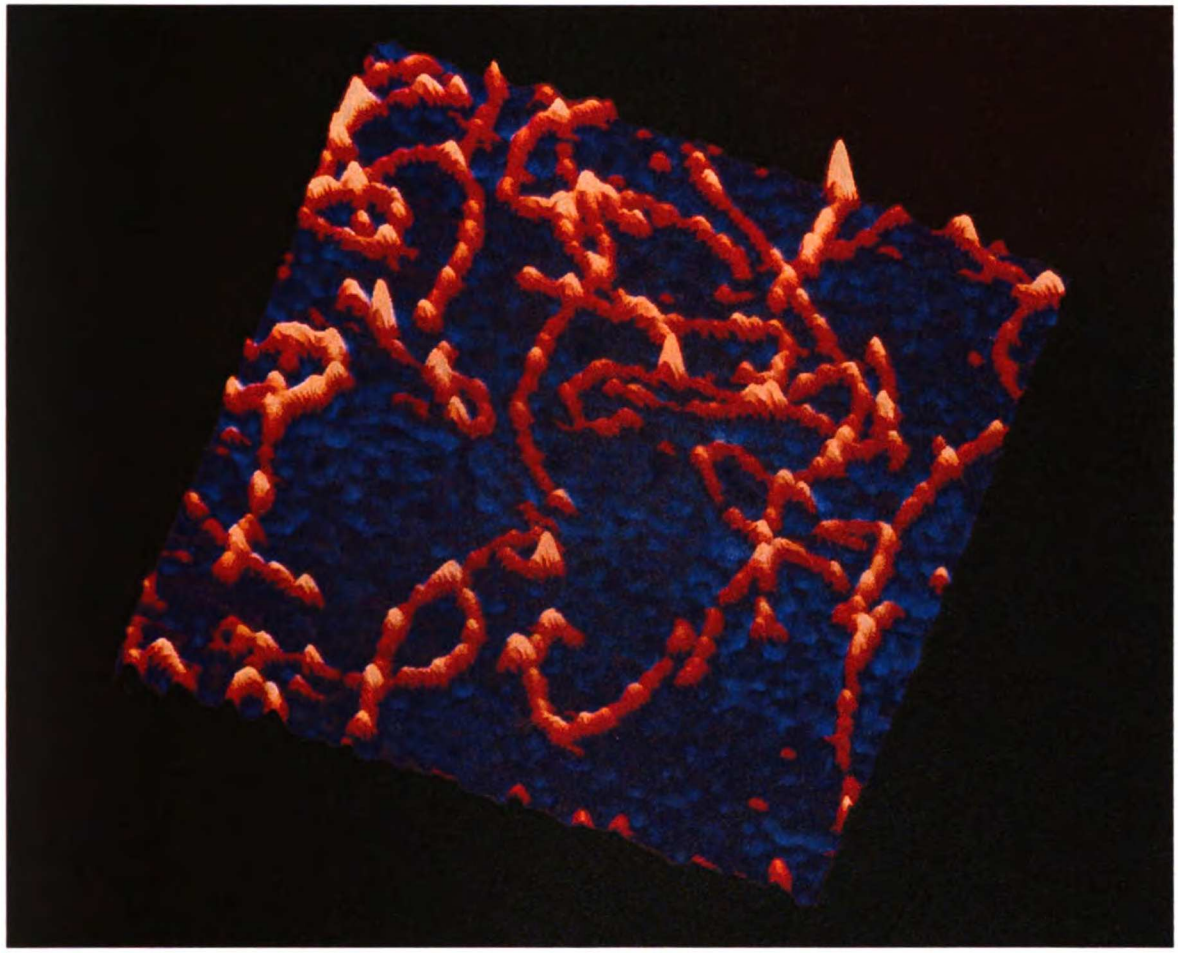

Single monomers of type I collagen imaged by Scanning Force Microscopy at 143 K. Molecules were deposited from solution onto a mica substrate. This is a three dimensional projection of the data of Figure III-28a C. Image size is about 500 nm by 500 nm.

Acknowledgments

As with any project, this work is a story that reflects the efforts of many at many different levels. I would like to thank them all.

Knute Fisher and Kathleen Yanagimoto, EM whizzes and scientists extraordinaire, instrumental in the conception of the project and much of the good work, whose devotion to careful experimental technique and unadulterated love of science made this project happen.

Mats Gustafsson and John Clarke, Mats remarkably built this machine, his talent evidenced in its extraordinary design and execution; my SFM partner in crime. John was the big boss of the Clarke lab in the Department of Physics, responsible for most of the resources of this project, and a place to transiently hang my hat.

Raj Bhatnagar, my research advisor, who got me into this gelatinous mess in the first place, and whose early support and guidance gave me the freedom and independence to pursue a project across the bay.

Art Veis at Northwestern, for his advice and all around collagen expertise. Additionally, Art provided all of the collagen for our SFM work, thankfully well characterized, and alleviating me of the daunting task of working with muti-cellular organisms.

Stan Glantz for help in the relm of biostatistics.

The rest of the Clarke lab for being willing teachers and good friends, especially:

Ruth Ellen Thomson, whose friendship and willingness to tackle life were highlights.

Sue Whitfield, my early STM collaborator in the pursuit of so many artifacts.

Steve Ross, really across the hall, a very good guy.

John Stewart and Marc Hertlein, unsung troops who did so much of the machine construction and computer programming.

Patti Wong, for taking on the thankless task of serving as the "unskilled operator" for data analysis, expert editing, encouragement and yummy cranberry/apple crisp.

Harald von Keszycki, a friend through so much of my life; and Lew Sachs, sage counselor and friend, both for wisdom, support, direction, and faith throughout my graduate school and other lives.

Paul J. Palatt, a wizard who fell off a mountain a long time ago.

Abstract

Scanning Force Microscopy of Collagen and Biological Materials at Low Temperature

Mark B. Shattuck

We have designed, constructed, and implemented an unusual Scanning Force Microscope (SFM), which we hope may address some of the difficulties encountered in the imaging of biological materials. The SFM (also known as the Atomic Force Microscope) is capable of extraordinary resolution, but has been limited in biological investigations by a lack of sample stability and reproducibility. Our SFM operates at temperatures as low as 143 K in a liquid pentane bath, which may increase both sample rigidity and stability, minimizing the problems encountered by other researchers, and opening the door for techniques such as freeze-fracture. We have successfully applied our low temperature SFM (LT-SFM) to a wide variety of biological materials including purple membrane, ferritin, and DNA. Our primary biological focus was on type I collagen, an important and ubiquitous protein. Collagen was selected given to its unusual and advantageous physical characteristics, previous experience including Scanning Tunneling Microscopy (STM), and its intrinsically interesting nature. Our efforts represent some of the highest resolution images currently available for native macromolecular structures, and our collagen monomer micrographs appear to be the first obtained with SFM (Shattuck *et al.*, 1992), both at room temperature and at 143 K. We are aware of several attempts at imaging collagen monomers with the SFM, most notably the work of Chernoff & Chernoff (1992), but apparently to date these studies have only resolved larger fibrillar

structures. Indeed, molecular biological SFM observations have been quite limited. Similarly, a previous LT-SFM, constructed by Prader (1991) in Hansma's group, was not successful in obtaining images of single molecules. Our collagen data is of sufficient quantity and quality that measurements of several intermolecular parameters and features are possible, with correlation to the known physical and biochemical properties of the molecule (Shattuck *et al.*, 1994), including charged molecular domains. We verified our collagen work with transmission electron microscopy and gel electrophoresis. Additionally we were able to extend our studies to direct physical manipulation at the molecular level, including machining of biological structures, measurements of molecular elasticity, and preliminary freeze-fracture studies.

Table of Contents

List of Tables

List of Figures

I. Introduction

Bioengineering has evolved as a discipline which combines the technological strengths of classical engineering techniques with the methodologies and problems of the biological sciences. It is fundamentally an interdisciplinary approach, integrating the resources and ideas of many diverse fields in a common pursuit of understanding that transcends each separate outlook. Bioengineering, not to be (but often) confused with genetic engineering, has found much success and application in the bio-medical sciences, often in the form of various imaging techniques and systems. Notable bioengineering developments have included computer aided tomography (CAT), magnetic resonance imaging (MRI) and positron emission tomography (PET). These new scanning techniques, in turn, have been applied to fundamental biological and biophysical problems. My interests in this project has been to develop and extend imaging technologies to the level of individual biological molecules, and most notably collagen, as explored with scanning probe microscopy (SPM). This study was undertaken with the hope of using these abilities to examine biological chemical, electrical and physical phenomena directly at the molecular level.

The recent introduction of scanned probe technologies, as exemplified by both the scanning tunneling microscope (STM) and the scanning force microscope (SFM), have made such direct molecular examination a reality. Both of these techniques have demonstrated atomic resolution imaging in the physical sciences, and are becoming capable of a wide range of much more interactive investigations, including the STM manipulation of single atoms on a surface (Eigler & Schweizer, 1990). In principle, the SFM is

capable of detecting a single electron on an insulating surface (Rugar & Hansma, 1990), and as few as three electrons have been resolved with certainty (Terris *et al.*, 1989).

Such potential has had a particular appeal in the study of biological materials, and most notably macromolecules. The immediate attraction is the possibility of studying biological samples at unprecedented resolution, in their "natural" environment. The possibility of examining molecules in their native state holds out the promise of examining molecular interactions and reactions directly at the level of a single molecule.

Despite much early optimism, based on the startling successes of STM examinations of solid state surfaces at atomic resolution, it quickly became apparent that STM of biological materials would not yield the same early advances with respect to resolution. SFM, introduced later (and not subject to the same experimental constraints as STM), similarly has yet to fully reach its potential for intramolecular resolution. This is due in large measure to the physical differences between a hard, solid state and typically crystalline surface; and a relatively soft biological compound loosely attached to an underlying substrate. Experience at room temperature has shown that tip/sample interactions perturb soft samples, resulting in reduced stability and reproducibility.

It was our hope that the development of cryogenic SFM for biological samples would alleviate some of the difficulties encountered in imaging, and might increase sample stability and reproducibility. Low temperatures would have the additional benefit of reducing the relatively large thermal fluctuations of a macromolecule, with a corresponding increase in the poten-

tial resolution of the image. This low temperature SFM (LT-SFM) could then be used to directly image biological materials, and particularly collagen.

Scanning Probe Microscopy

The recent development of the general class of scanned probe microscopes has been one of the most stunning analytical instrument advances of the last few decades (Balderschwieler *et al.*, 1991). Like its predecessor technique, transmission electron microscopy (TEM), SPM technologies, as typified primarily by scanning tunneling microscopy and scanning force microscopy, promise to revolutionize our view of the molecular and atomic world. This nano-technology revolution will be possible given the techniques' extremely high (atomic scale) resolution, potential for 3D imaging, and the ability to image most materials directly in a wide variety of environments. In addition, SPMs can be used to probe and manipulate samples directly at the atomic level, studying and rearranging matter atom by atom.

These advances in SPM technologies were all catalyzed with the development of the first STM by Binnig and Rohrer in 1982 (Binnig *et al.*, 1982; Binnig & Rohrer, 1985). The ability to "see" single atoms was a rather remarkable offshoot of their study of quantum mechanical tunneling behavior between a sharp metal tip and a conducting surface. The excitement that this development created in the physics community is evidenced by the awarding of the 1986 Noble prize to Binnig and Rohrer, in conjunction with Ernst Ruska for development of the TEM some 50 years earlier.

The relative simplicity of the operating principle of the STM is surpris-

ing. A sharp tunneling tip is attached to a ceramic piezoelectric actuator which is capable of 3-D motion, and is brought close to a sample surface where a tunneling current is induced by a bias voltage. A feedback circuit can then be used to regulate the tunneling current (and thus the height) between tip and sample. The piezoelectric material also allows one to scan the tip across an area in a raster pattern. Changes in the current as the tip is scanned can be interpreted as changes in height, generating a topographic representation of the sample surface. The result is an instrument capable of a vertical resolution of hundredths of an Ångstrom (due to the exponential dependence of the tunneling current with distance), and a horizontal resolution of about 1 Å (about an atomic diameter).

These tantalizing resolutions meant that the STM was quickly adopted for studies of surfaces and solid state physics. One of the first questions answered was the surface reconstruction of 7 x 7 silicon (Binnig *et al.*, 1983), indicative of the potential of this technique. STM studies are, however, all limited to conducting or semiconducting materials, due to the requirement of a tunneling current. Non-conducting samples became accessible to similar imaging with the emergence of the scanning force microscope (SFM), commonly (and somewhat erroneously) referred to as the atomic force microscope (AFM). Binnig and Gerber, in collaboration with Cal Quate at Stanford University, developed this technique in 1986 (Binnig *et al.*, 1986).

The SFM differs from the STM primarily in its method of detection, scanning the surface with a sharp tip mounted on a soft cantilever spring, much like a record player stylus. The vertical displacement of the cantilever is typically measured using a laser beam, otherwise the SFM works very

much like an STM with regard to scanning, feedback and electronics. This frees the SFM to image samples unconstrained by the material's conductivity.

The potential of both STM and SFM in the biological sciences was recognized immediately. The ability of STM to image simple organic molecules was particularly attractive, as demonstrated by images of benzene rings adsorbed to a rhodium surface at inter-molecular resolution (Ohtani *et al.*, 1988). Despite difficulties of sample stability, and the relative lack of conductivity of most biological materials (discussed below), a wide variety of samples have been successfully imaged, although at typically reduced resolution. SFM, available for a more limited time, is being increasingly applied to biomaterials. Work with both techniques have made it abundantly clear that sample preparation is a critical issue, especially for biology, given the interaction between the tip and the material to be imaged.

For studies of biological materials at unprecedented resolution, the potential of STM, and particularly SFM, is enormous. These techniques allow for imaging over a size scale from atoms to whole cells, with at least a theoretical resolution of about an atomic diameter, and thus the possibility of observing molecular substructure and intramolecular features. More intriguing from a biological perspective is the imaging of single molecules, such as proteins, in their native environment. This leads to the possibility of observing molecular interactions and dynamics in something close to real observational time. The ability to image all of these phenomena directly, without exposing samples to condensing metals and high vacuum (common in transmission electron microscopy preparations), has lead to a great deal of interest in developing STM and SFM techniques for application to biology.

The difficulties previous workers had encountered in STM and SFM biological studies led us to develop an unusual low temperature SFM approach to enhance sample stability and limit thermal motion. It was my hope to apply these techniques in the study of collagen, as well as more conventional studies on lipid membranes and DNA. Collagen had not been successfully imaged at the molecular level using STM or SFM. My previous experience with collagen suggested that it might be a particularly suitable biological material for SPM investigations, given its unique physical and electrical properties. In addition, STM and SFM might prove particularly useful in examining these properties at the molecular level.

Collagen

Importance

The physiological and biochemical importance of collagen is extraordinary. It is found in all metazoans (division of the animal kingdom "above" protozoa, including most humans) where it creates the extra-cellular framework, and is the most abundant protein found in the animal kingdom. Indeed, its ubiquitous nature, and its highly conserved molecular and genetic structure, is making collagen a very interesting study for evolutionary biologists (Mathews, 1988). In mammals, collagen comprises about 1/4 to 1/3 of the total protein (Stryer, 1988), most commonly forming fibrous elements in the body. It is found in virtually all organs, and is a primary component in tissues as diverse as the connective tissues (tendon, bone, and cartilage), teeth, and cornea.

Collagen actually comprises a family of related proteins and occurs in a

wide variety of types. The various forms of collagen are often associated with a specific tissue, and all types share common conformational characteristics. More than 20 types of genetically distinct collagen have been identified to date, and together determine the form, function, architecture, and biomechanical characteristics of all tissues. Of the 4 relatively common types of collagen (I – IV), type I collagen is by far the most abundant. As a structural element, fibrillar type I collagen provides the fundamental organizational scaffolding for cells in the body, and is responsible for much of the discrete compartmentalization present. Our physical form, shape, and texture; indeed much of what we perceive and associate with our humanness, is predominately related to the distribution and organization of collagen.

The importance of the structural role of collagen, with its emphasis on mechanical properties and stability, has overshadowed its physiologically active nature. However, collagen is now beginning to be appreciated for its much broader role beyond that of a simple structural element, with important and diverse biochemical functions. The collagens as a class occur in complexes with glycoproteins (Stryer, 1988), proteoglycans, and with laminin in basement membranes (type IV collagen). Collagen, furthermore, has a regulatory role, interacting with platelets during hemostasis, and in highly specific antigenic responses, much to the dismay of some individuals receiving cosmetic bovine collagen injections.

Collagen also actively binds to highly specific collagen receptors on the cell surface, and this interaction is important in determining cellular form and behavior. The collagen cell binding domain has been preliminarily identified as ^{766}GTPGPQGIAGQRGVV^{780} (Scaria *et al.*, 1990). Most stationary cells in the body contact the collagen matrix, and collagen is important

in mediating cell behavior, notably cell migration, proliferation and differentiation (Hay, 1990). In this capacity, one can view the extracellular matrix as a "conduit" for biomechanical signals, and thus information exchange, transmitted through specific receptors. These receptors are in turn connected to the intracellular cytoskeletal structure, which is subject to modification.

The polymer-like structure of the collagen monomer is responsible for the variety and scope of these characteristics, and can ultimately be related to the mechanical and electrical properties of individual molecules. Structural and topological studies at the molecular level are important in understanding collagen's wide physiological and biochemical role beyond that of a simple structural element. These roles are consistent with the unique triple helical conformational organization of collagen, in which the peptide sidechains, and thus the reactive areas of the molecule, project out from the molecular axis. Many collagens also have globular non-collagenous domains, potentially useful in identifying molecular ends and reactive sites.

Collagen is important at many other levels of human existence. Numerous human diseases involve collagen; including fatal collagen genetic defects, and the trashed knees, arthritis, and other connective tissue injuries common to most of us. Osteogenesis imperfecta can be caused by a single glycine mutation. Collagen is also an integral component in wound healing at several different levels, and is currently being explored as an oral drug for the treatment of rheumatoid arthritis (Trentham *et al.*, 1994). From a commercial perspective, the importance of collagenous materials is enormous, from leather goods to Jell-O Pudding. It is estimated that Kodak alone has made well over 500 billion dollars from the sale of collagen, in the form of gelatin in photographic films (S. C. Weber, Eastman Kodak Corporation).

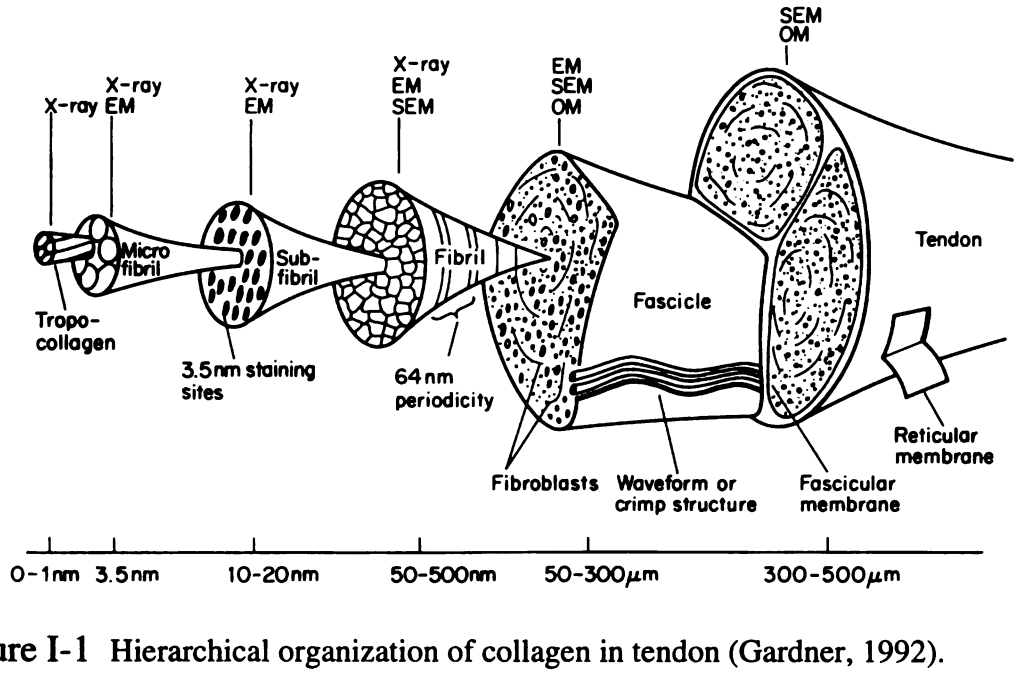

Figure I-1 Hierarchical organization of collagen in tendon (Gardner, 1992).

Organization

The physiological organization of type I collagen in the body, from the molecular to the macroscopic level, are depicted in Figure I-1. Molecules are axially aligned and organized into limiting micro-fibrils, which are about 10 nm in diameter and extremely long. These discrete fibrils can further form structural fibers, which can in turn be bundled together, much in the manner of a steel cable. Collagen in this form, which might be best exemplified by a tendon, exists effectively in a semi-crystalline state. This imparts remarkable mechanical and electrical properties, including a tensile strength by weight that is greater than that of steel, and semiconductive behavior. Mineralized collagen, such as bone, can support compressive loads as well. A different large scale organizational structure of collagen, where the fibers are not all parallel, is the basis for skin. Skin, the largest organ of the human body, is 70 % collagen (Arnold *et al.*, 1990). It has the

particularly difficult task of keeping the inside in and the hostile environment out, with both strength and flexibility.

Molecular Structure

The overall properties of collagen in the body are ultimately determined by the unique conformation and structural topography of the individual collagen molecules. The primary structure of type I collagen is well known, while the secondary and tertiary structures are fairly well understood. These structural topographic feature vary across the surface of the monomer, resulting in regions of varying hydrophobicity and net charge. These discrete surfaces, arising from the unique conformation of the collagen molecule, are important to the function and interaction of collagen in tissues.

The collagen monomer (type I) is composed of three individual subunits, or α chains (not to be confused with the α helix), two of which are identical, wound around each other to form a triple helix (Figure I-2). Each subunit is a long linear chain of amino acids, composed disproportionately of the imino acids and glycine. About 25 % of the total residues in type I collagen are proline and hydroxyproline, and are responsible for much of the stabilizing stereochemical interactions of individual chains. Glycine, the smallest amino acid, is found every third residue, forms the "interior" of the molecule, and is critical to the conformation of the monomer. Each chain is thus a polymer of glycine led triplets, which results to the triple helical form of the collagen molecule. Physically, each subunit is slightly coiled with a left hand helical twist, not unlike the polymer poly-L-proline. The helix is similar to the alpha helix, except that it is significantly more relaxed, with slightly more than 3 residues per turn as determined by x-ray diffraction.

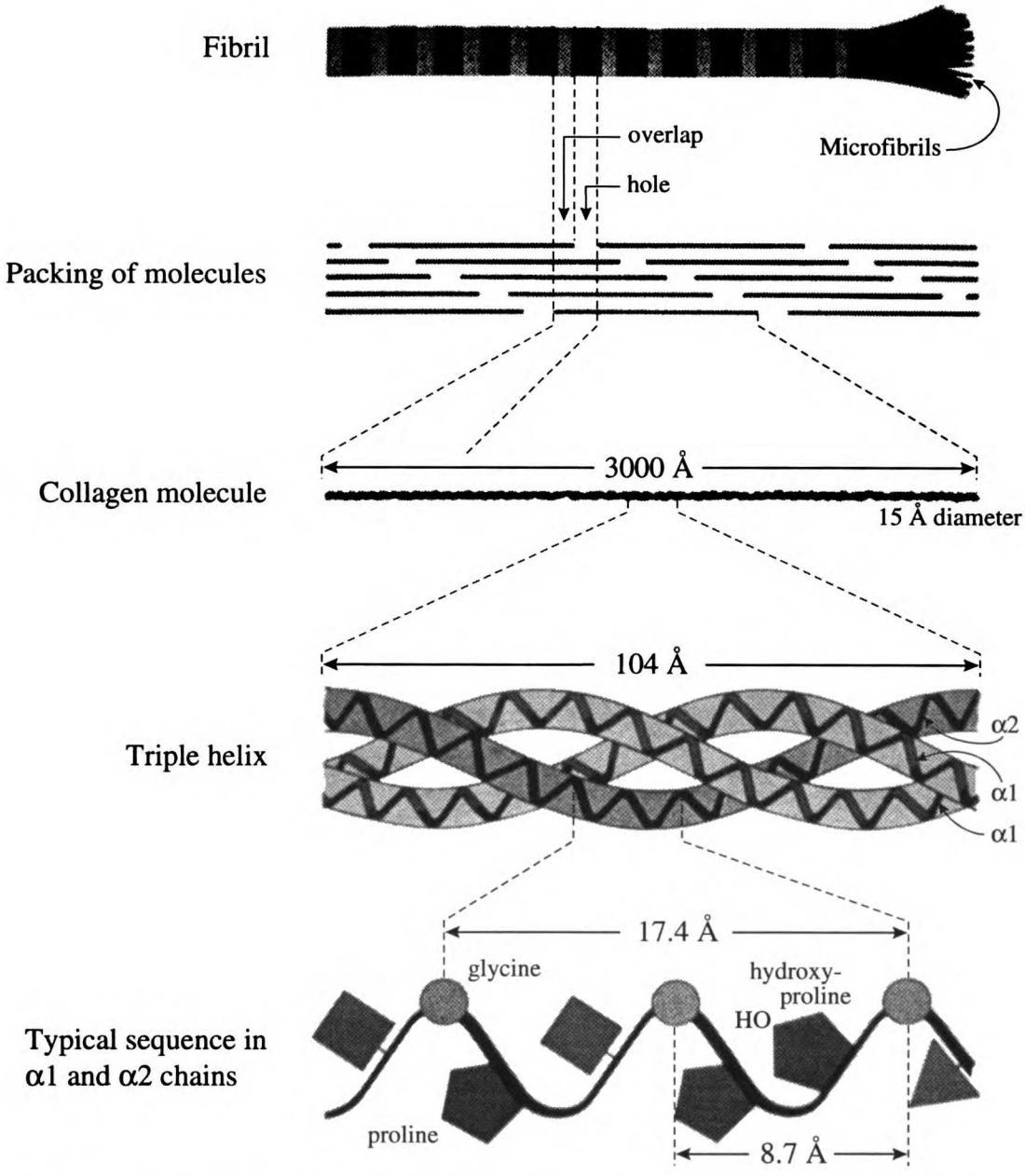

Figure I-2 The structure of collagen. Collagen fibrils are composed of individual molecules aligned in quarter stagger. Adapted from Uitto *et al.*, 1986.

X-ray diffraction has been critical in elucidating the molecular structure of the collagen triple helix. Ramachandran and Kartha determined the basic model of collagen in 1954 and 1955 (Ramachandran, 1967). Interestingly, this structure arose both from improvements in x-ray diffraction techniques, and from stereochemical considerations. They determined that the axial rise

of the subunit was 2.86 Å, with an azimuthal rotation of -108 °. The super-coil pitch length is generally accepted to be just under 9 Å.

X-ray models for the collagen molecule demonstrated that the three individual subunits are wound around each other to form a triple helix. This superhelix has a weight of about 285 kD (Stryer, 1988), an overall length of about 270 nm, a width of 1.5 nm, and a helical pitch of 2.9 nm. Glycine is particularly important sterically to this molecular conformation; it is small and can thus occupy the central core of the superhelix, allowing the three chains to pack together The proline and hydroxy-proline residues therefore make up much of the exterior surface of the molecule, and are important in stabilizing the molecule and imparting much of it's physical and biochemical properties. The molecule is stabilized by non-bonded cooperative interactions, primarily van der Waals contacts between adjacent rings (Bhatnagar *et al.*, 1988), and by interchain hydrogen bonds, as intrachain bonding does not occur.

Individual collagen molecules form larger structures such as tendon and bone. Single molecules associate together radially with an axial stagger of about one quarter of the molecular length, referred to as the "D" stagger or spacing, forming a microfibril. Microfibrils therefore have a 40 nm gap between the ends of individual molecules, providing nucleation sites for hydroxyapatite (calcium) deposition (Weiner & Traub, 1986). The addition of hard crystals of hydroxyapatite into the microfibril is what primarily distinguishes bone from tendon. This axial D stagger of the collagen molecules is repeated over and over (Figure I-2), resulting in very long structural elements. These microfibrils are in turn combined together to form macroscopic fibers, and larger physical structures. The exact cross section of the

microfibril is still a matter of some debate, with most models evoking 4, 5 or 6 molecules ordered in symmetrical arrays as the "unit cell."

The function of collagen is thus intimately related to several scales of structure. The packing of collagen into fibrils is driven by highly specific interactions between molecules and the entropy of excluding water. This is possible due to large nonpolar domains on the surface of the molecule, and is not unlike the processes that drive the folding of globular proteins. TEM studies have demonstrated the discrete distribution of large nonpolar domains interspaced with polar regions and charged residues. These domains have a role in the ordered self-assembly of collagen into fibrils, and in the biochemical function of collagen in the body.

Molecular Length

An understanding of collagen properties in the body begins with the determination of the structural characteristics of the collagen molecule. Even the most basic structural parameters, including molecular length, have only relatively recently become accessible, and are subject to some uncertainty. Due to the difficulty of extracting single collagen molecules from tissues, it was not until the 1950s that such work began in earnest, although it was previously known that the molecules were soluble in acetic acid (Zachariades, 1900; Nageotte, 1927). Solution studies allowed workers to begin to quantify physical structural parameters such as length and width.

Length estimates for the collagen molecule in solution have typically relied on a number of different techniques which yield varying results. Historically, the first reasonable estimates came from observations of collagen precipitates exhibiting "long spacing modification," as opposed to the native

fibril 64 nm D periodicity, and were in the range of 200 – 300 nm. Work with segment long spacing, in which molecules aggregate side by side, pointed to a length of about 250 nm. More exacting studies, including light scattering, viscosity, osmotic pressure, sedimentation and flow birefringence, yield a collagen model of a "rod-like structure" with a length of about 290 nm, a diameter of 1.4 nm and a molecular weight of 300,000 (Ramachandran, 1967). Early electron microscopic studies (Hall & Doty, 1958) confirmed these basic findings. Currently TEM provides the most direct measurement of molecular length. Presently, these dimensions are generally accepted with some minor variations, and are conventionally cited as 300 by 1.5 nm.

More recently, most workers defer to these earlier length measurements, or to the "contour length" inferred from the x-ray data cited above. The contour length is calculated by multiplying the total number of residues in the α-chain (1014) by the rise per residue (2.86 Å), which yields a length of 2900 Å (Parry & Craig, 1981). This assumes that the helical parameters determined by x-ray diffraction are constant, and maintained over the entire length of the subunit. X-ray diffraction has the disadvantage that it is an averaging technique requiring a large population of molecules, and that it is restricted dimensionally to about 10 x the width of a collagen molecule. As a result, it is very difficult to make any direct length measurements with this technique. Collagen does, however, occur naturally in a semi-crystalline state, a requirement for x-ray work. This means that x-ray data may be particularly well related to collagen in its native state. Collagen fibers are typically stretched about 10 % for x-ray diffraction in order to obtain clear diffraction patterns, and this may be an additional concern in applying x-ray

data to length estimates. STM and SFM, however, provide the ability to study the topography of collagen directly.

Molecular Flexibility

An interesting result of these studies of the length and conformation of the collagen molecule is the still common perception of collagen as a "rod-like" molecule, or as a "rigid rod." This may have arisen in part from early viscosity measurements, which can give some indication of the molecular stiffness as well as length. This perception may also arise from a difference in semantics; rod-like was certainly used to describe the unusually large length to width aspect ratio of the collagen molecule. I suspect that this characterization additionally implies the physical characteristic of stiffness as well, and many workers remain convinced that the molecule is in fact a rigid structure.

More recently, a picture of collagen as a more flexible structure has been developed. Viscoelastic measurements on dilute solutions of collagen, indicate a semi-flexible rod, with a persistence length of 170 nm (Nestler *et al.*, 1983). Persistence length is a measure of intrinsic flexibility, and was determined in this study using theories of intrinsic viscosity and rotational relaxation time. The authors additionally reconcile their observations for the Young's modulus of collagen molecules with that of bulk collagen as found in tendon. While collagen would appear to be more flexible than commonly thought, these data still indicate a structure that is about 40 times stiffer than DNA.

The model of collagen as a flexible molecule was reinforced by a study attempting to localize possible flexible regions of "thread-like" molecules,

including collagen (Hofmann *et al.*, 1984). The authors developed a computer program for measuring "kinks" and flexible site on molecules from digitized TEM images. They determined that at least one flexible site on the type I collagen molecule, at about 7 nm, corresponded with a region lacking proline residues at the N-terminal end. Generally, the molecule was found to have uniform flexibility, in that deviations could not be distinguished from error fluctuations, except at a site 12 nm from the C-terminal end.

These studies provide good evidence for the flexible nature of the collagen molecule. It should be noted that the collagen molecules studied were in solution, whereas in the body they essentially always occur as a bulk material, packed and constrained in a basically straight and linear configuration. The value of these studies was to present a picture of the collagen molecule as a dynamic entity rather than a fixed, uniform structural element. Flexible regions may in fact occur at more biochemically interesting sites on the molecule, and help understand the broad and highly interactive nature of collagen in the extracellular space. SPM as a technique might enable us to examine such structural, and by correlation biochemical, properties directly. STM and SFM provide methodologies for studying the electrical and mechanical behavior of collagen directly at the molecular level.

The physical properties of collagen at the macroscopic level, as exemplified by tendon and bone, are a reflection of these microscopic observations. Notably, collagen molecules interact as a self-assembling architecture that creates a "solid state" material with a nearly crystalline structure. This paracrystalline structure accounts for many of the remarkable physical characteristics of collagenous tissues as discussed. My interest in collagen, and as a result in the SPM technique, flowed from an interest in the interrelation-

ship of micro and macroscopic physical properties, particularly as reflected in collagen's unusual electrical characteristics.

Electrical Properties

One of the most unexpected aspects of collagen is its electrical properties, and their possible role in the physiology of collagen in the body. Collagen, usually thought of in terms of its structural capacity, has a wide range of electrical characteristics, arising from its relatively high conductivity. The molecule has a large electrical dipole moment (and net positive charge), associated with both the longitudinal distribution of charged amino acid groups (Appendix I) and the dipole contributions from individual peptide bonds. As a result, collagen will tend to align itself in the presence of an electric field. This distribution also imparts significant piezoelectric and pyroelectric qualities (Fukada *et al.*, 1976; Athenstaedt, 1970), with possible clinical relevance. Furthermore, collagen conducts anisotropically along the molecular axis, with a typical resistivity of about 1 x 10^8 Ω cm (Tomaselli & Shamos, 1974; Behari & Andrabi, 1978). Values as low as 1 x 10^6 Ω cm have been reported for fully hydrated collagen at 30 °C (Bardelmeyer, 1973). Conduction is influenced by hydration state, pH, temperature, frequency, and purity of the sample.

The conductivity of collagen is intimately associated with its state of hydration, which may indicate that the physical conduction mechanism is a mixture of both electronic and ionic (proton) transfer (Behari & Andrabi, 1978). Examination of the pronounced UV (and to some extent IR) photoelectric properties of collagen (Behari *et al.*, 1974; Fuller *et al.*, 1976; Andrabi & Behari, 1981), and the mobility of charge carriers with the Hall

effect (Behari & Andrabi, 1978), all point to a more complicated conduction mechanism. These suggest that a conventional band model is not sufficient, and that both excited electronic and protonic transport, and perhaps other ionic conduction mechanisms, are responsible. The complexity of this picture is illustrated by the ability to construct classic solid state P-N junction devices out of the appropriate collagenous biomaterial. Collagen and apatite, the two main constituents of bone, can be combined to form a P-N junction diode with the appropriate IV curve characteristics (Behari & Andrabi, 1980). These (and most) macroscopic measurements ultimately are examining the properties of the bulk material, which may not entirely reflect the electrical properties of a single molecule. SPM has the potential of allowing for the examination of electrical properties directly at the molecular level.

Some of these bioelectric properties may have clinical relevance. Athenstaedt's work (1970) found that the polarization vectors in long bones, centered on the epiphysis and diaphysis, reversed during the transition from juvenile to adult. Bone is piezoelectric, due to a combination of molecular characteristics and steaming potentials (motion of charged fluids), with a piezoelectric constant about 1/10 of that for quartz. Voltages of about 1 mV (Yasuda, 1977) develop in the human femur in a normal stride, and vary longitudinally but not around the transverse axis (Friedenberg *et al.*, 1973). Such electrical generation and structural information appear to be important in the healing and straightening of broken bones; a clinical effect known as Wolff's Law (Becker & Selden, 1985a). Currently, electric (E) fields are used clinically to mend bone non-unions, and the absence of bioelectric fields have been implicated in the osteoporosis experienced by astronauts in

a weightless environment (Marino *et al.*, 1979). Osteoblasts and bone growth can be stimulated in the lab using external electrical currents, and damaged bone and bone remodeling are both associated with changes in the structure of local E fields.

In wound healing, there has been interest in the possibility of triggering and directing limb regeneration using applied electric fields. This arises from the observation that amputated forelimbs in amphibian systems can be induced to regenerate the entire limb if the proper external E field geometry is applied to the wound (Smith, 1974). Mammalian systems, while less successful, show a similar effect (Neufeld, 1985; Becker & Seldon, 1985b). This is particularly interesting in light of recent observations of the ability of young children to regenerate partially amputated fingers, suggesting that humans have the capability for limb regeneration at some level. Such observations indicate that electromagnetic (EM) fields are in fact a central organizing tenet of any living organism.

Evidence for this central role of EM fields is emerging from studies in developmental biology, where relatively simple systems enable one to unambiguously measure the fields associated with growing structures. Early blast forms are accompanied by an E field structure which mirrors their physical shape. The blasts clearly develop their own field, and drive steady currents through themselves (Jaffee & Nuccitelli, 1977). Additionally, external physiological fields influence both the orientation and mobility of embryonic fibroblasts (Erickson & Nuccitelli, 1984). I find it particularly intriguing that some actively dividing cells emit natural RF electric fields (about 100 V/cm at cell surface; Pohl, 1981), and that the polarization pattern of these cells closely matches the pattern of collagen deposition by single fibroblasts

in culture (Stopak & Harris, 1982).

Electro-Magnetic Fields

It is reasonable to consider EM fields to be the fundamental organizing principle of biological systems at the molecular level from a physical perspective. All physical interactions at the molecular level, whether biological or biochemical, ionic or van der Waals bonding, tertiary structure or diffusional processes, are in essence simply electrostatic interactions. All of these processes result from organizing or moving atoms spatially, which can only result from the physical forces acting on atoms and molecules (Newton, 1686).

Of the four fundamental physical forces presently described and understood, electrostatic forces are the most important at the molecular level. Both the strong interaction and the weak interaction are nuclear forces, and thus really restricted to the scale of 10^{-13} cm (Feynman *et al.*, 1963). The magnitude of the gravitational force is actually extremely small at the atomic level (intuitively exaggerated by its most obvious effect of keeping us firmly attached to the surface of the earth). As an illustration, the electrostatic force between two electrons is about 10^{43} times larger than the gravitational force. The gravitational force of an electron to the mass of the earth is still about 10^{16} less than this electrostatic force. Clearly then electrostatic and electromagnetic forces are the largest, and are likely to be the fundamental, organizing "biological" forces at the molecular level. An interesting analogy is made by H. S. Burr (1973), who thinks of electromagnetic fields as a kind of matrix or mold for the body, responsible for the organization, direction and patterning of living, dynamic systems.

Connective tissues and collagen are a particularly interesting system to examine, given the importance of electric fields in the body and the electrical characteristics of the collagen molecule. Collagen assemblies provide the extracellular framework that physically organizes the body, and thus collagen represents an organizational structural bridge from the local molecular level, to the global organism level. The rather unusual electric properties of collagen and collagenous tissues, and the possible association of clinical and electrical phenomena, suggest this to be an engaging area of investigation.

SPM as Probe

My interest in SPM and particularly in STM evolved from the possibility of using STM as a direct molecular scale probe of the electrical characteristics of collagen. For example, STM might provide a means of examining the mechanism of conduction along a single collagen molecule. STM is, in effect, a fancy current meter (ultra-sensitive and highly localized ammeter), and capable of directly probing the electronic nature of a sample as well as generating a topographic image. More importantly, it is a technique usable in a "native" environment (in which macromolecules may retain their natural structure), and with a resolution comparable to the Debye shielding distance, which is typically less than 10 Å in physiological fluids (Plonsey, 1969).

STM Principles

The basic operating principles underling the STM (Figure I-3) are quite simple, and are generally applicable to all scanned probe microscopes. SPMs are all remarkably similar in nature, relying on largely identical elec-

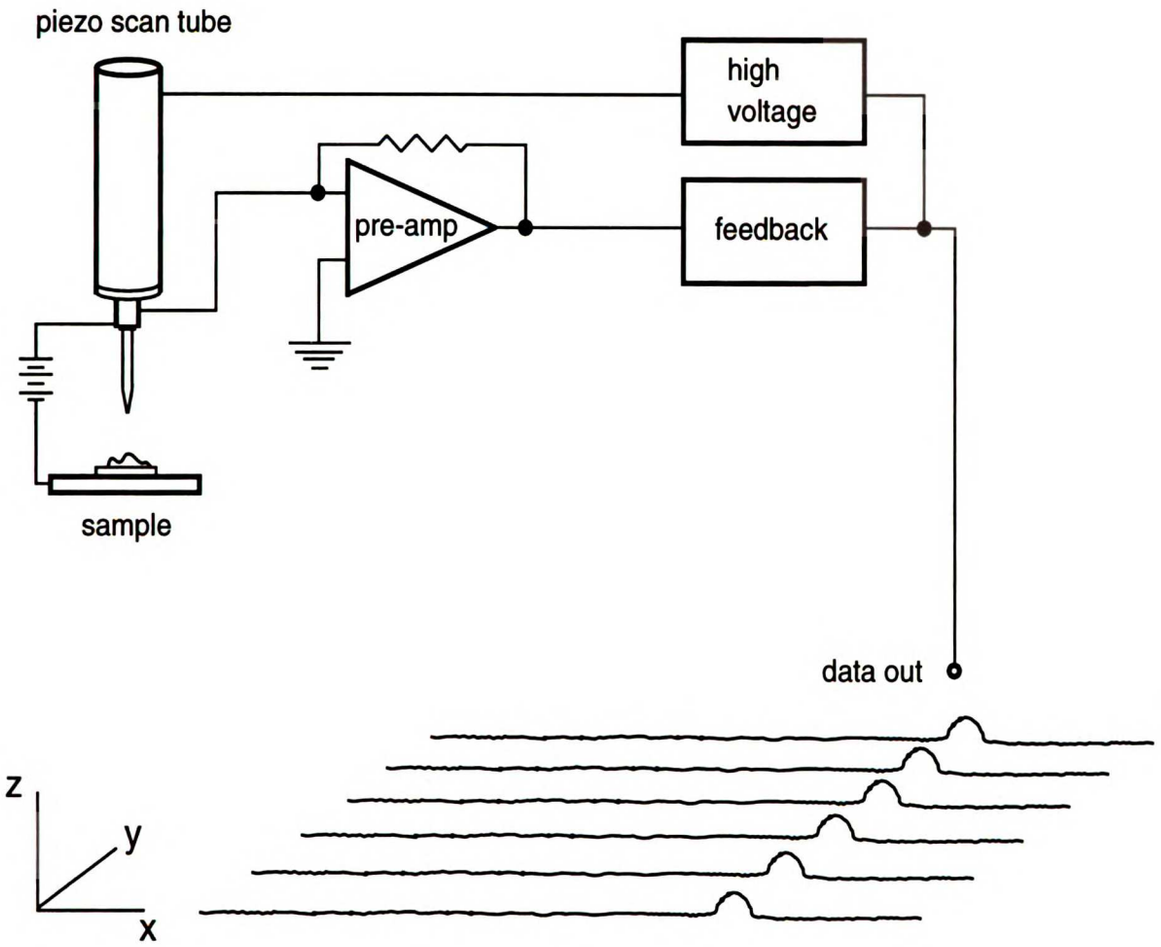

Figure I-3 Basic elements and operating principle of the STM (and most other SPMs). A quantum mechanical tunneling current is induced between the sample and tip by a bias voltage. Other SPMs vary in method of detection.

trical components and concepts including negative feedback. They vary fundamentally only in their method of detection of, or interaction with, the sample.

The heart of the STM is a very sharp metal scanning tip, often made of platinum, attached to a piezoelectric ceramic scanning tube. This tube is nickel plated, and electrically divided axially into four equal outer quadrants relative to a single continuous inner electrode (Binnig & Smith, 1986). By applying the appropriate voltages to the appropriate quadrant, the cylindrical

tube will "bend" in the desired lateral (X and Y) direction. Similarly, the voltage of all 4 outer quadrant surfaces can be varied together, relative to the inner surface, producing Z motions. Thus the tip can be electrically steered, or scanned, in three dimensions simultaneously, with sub-Ångstrom displacements. The overall scan range is typically limited to about 10 – 100 μm in X and Y, and a few μm vertically in Z, making most STMs (and indeed most SPMs) rather "short-sighted."

In practice, the tip, with the scanning tube at full extension, is carefully brought to within a few Å of a conducting sample surface using one of a variety of "coarse approach" schemes. At this short distance, a quantum mechanical tunneling current is induced between the sample surface and the tip by a small bias voltage. Theoretically, this gap is approximately 4 – 6 Å for a clean surface in vacuum, depending on the material. The tunneling current is exponentially dependent on the height Z of the tip above the surface, and is a function of the local electron density of states at the Fermi level in both the tip and the sample (Hansma & Tersoff, 1987). Roughly, a 1 Å decrease in the Z height of the tip results in an order of magnitude increase in the tunneling current. This exponential dependence makes the current a very sensitive indicator of the distance to the sample surface, with a vertical resolution of better than 0.1 Å. The tunneling current can be used to precisely control and maintain the tunneling gap using a negative feedback circuit. Thus the tip can be pulled back away from the sample surface as the coarse approach mechanism is turned off, maintaining a constant gap, and avoiding a "crash" of the tip into the sample surface. The use of feedback allows one to maintain a constant tunneling gap despite factors such as thermal drift, and movements of the tip relative to the sample.

The feedback circuit works by electronically monitoring the tunneling current, and any change in this current is used to reposition the tip so that the current, and therefore the gap, remains constant. A feedback signal is generated which is used to apply the appropriate high voltages on the scan tube in order to maintain a constant height of the tip above the sample surface.

To generate a topographic image of the sample surface, the tip is then scanned horizontally along the X and Y axis as illustrated (Figure I-3). The tunneling current flowing between sample and tip is converted to a voltage signal and amplified by a pre-amp circuit located near the tip (to minimize electrical noise). This amplified signal is then fed into the variable feedback circuit, which in turn controls the high-voltage op-amp circuits used to drive the piezoelectric scanner. As the tip moves laterally across the sample surface, the feedback maintains a constant gap between the sample and the tip. Any variation in the sample surface results in the feedback signal adjusting the Z position of the tip; the magnitude of this signal is proportional to the change in height. This feedback signal can be used to "trace out" a representation of the sample surface; and the "data out" signal can be used in conjunction with the X and Y scan ramp voltages, and the help of a computer, to generate a 3 dimensional topographic image. It is important to note that the images thus obtained are a combination of the topology of the sample surface, and the convolution of the electronic structure of the sample and the tip. In addition, other factors such as local deformation and surface contamination must be taken into account (Mamin *et al.,* 1986).

As a practical matter, STM has been found to be particularly useful for flat surfaces due to its short-sightedness. The technique's first early successes (Hansma & Tersoff, 1987) were concerned with problems in solid

state physics and materials sciences, typically involving crystal lattice structures such as graphite and silicon. Similarly, samples of a biological nature were usually deposited on highly ordered pyrolytic graphite (HOPG), which forms an atomically flat, easily cleaved (and thus clean) surfaces, and is a good electrical conductor. Other surfaces, such as gold, deposited by evaporation or epitaxially grown (Lindsay & Barris, 1988), are useful as substrates, but generally are not flat over such large areas, making studies on small molecules more difficult.

STM is further inherently limited to samples which electrically conduct at some level. Biological materials tend to be basically non-conducting and relatively mobile, and thus difficult to image (Hansma *et al.,* 1988; Baro *et al.,* 1985; Hameroff *et al.,* 1989). Both of these issues can be addressed by coating the sample with metals (Zasadzinski *et al.,* 1988; Guckenberger *et al.,* 1988), much as in transmission electron microscopy (TEM), but at the expense of no longer directly imaging the native sample, thus removing one of the most attractive advantages of SPM.

Lack of sample conduction, stability and reproducibility has made STM imaging of biology tedious at best. Generally, it is uncertain just what the conduction mechanisms are for successfully imaged biological structures. Additionally, some structures (including collagen) which have been "imaged" are undoubtedly artifacts associated with the HOPG substrate (to be discussed). Most of these difficulties seem to center on tip/sample interaction and perturbations, and lack of sample stability (Fisher *et al.,* 1990). However, STM has nevertheless been applied to a wide range of biological samples, as shown in Table I-1 from Fisher et al.

Table I-1 Examples of native and metal-coated organic and biological samples that have been examined by scanning tunneling microscopy. References are representative and not a complete list. From Fisher*et al.*, 1990. See Bibliography-Table I-1.

Category	Example	Reference
Molecular	Acetone	34
	Amino Acids	22
	Benzene-CO superlattice	14,48
	Organic conductors	6
	Phthalate	25
	Phthalocyanines	15,29,49
Macro	Cellulose	50
molecular	Cyclodextrin	47
	Nucleic Acids:	
	DNA in air	5,9,1,12,16,35,37
	DNA in water	8,38, 39,40,41,42,43,44
	RNA in air	4,37
	RNA in water	42
	Polypeptides	45,47
	Proteins:	
	Collagen fibrils	32,52,53,68,69
	Fibronectin	20
	Hemoglobin	57
	Phosphorylase	18,19
	Vicilin	70
	Wheat protein	47
	Synthetic Polymers	
Supra	Bacterial cell walls:	1,51
molecular	*D. radiodurans (HPI)*	30,31,46
	M. hungatei	13,17
	Conductive polymers	10,55,56
	Detergent monolayers	71
	Fatty acid bilayers	36,59
	Langmuir Blodgett films	27,36,50,59
	Liquid crystals	26,58,60
	Membranes:	
	Reconstituted	33,63
	Native:	
	Cancer cell	64
	Purple membrane	23,24,65,66
	Microtubules	32,54
	Phospholipid bilayers	32,36,64,67,68,72
	Protein crystals:	
	Catalase	62
	rec-DNA complexes	2,3,65
Viruses	Bacteriophages:	
	O 29	7
	T4 polyheads	21,28,61
	T7, fd	28
	Tobacco Mosaic virus	21,55

Initially, it was my hope to image and study the collagen molecule with STM, taking advantage of its unusual stability and electrical properties. STM might in fact allow for the direct exploration of these characteristics. Indeed, it might be possible to probe the mechanism of conduction along a single molecule of collagen. One could, for example, examine collagen on an etched substrate of conductive sub-micron lines of alternating polarity, allowing one to establish a potential difference between the ends of a single molecule. The STM could then be used to examine the axial electronic structure and current flow, a bit like a potentiometer. Not only would one obtain topographic information about the molecule, but possibly something of its electronic structure as well.

This is not an unreasonable expectation given the abilities of the STM. Successful imaging of similar polymers had been reported (Albrecht *et al.,* 1988; Dovek *et al.,* 1988), and more recently STM has been applied to point-probe conductivity measurements on conducting polymeric polyaniline (Jeon *et al.,* 1992). Semiconductor interfaces (GaAs P-N junction) can be studied directly using the STM in both topometric and potentionometric modes with nanometer resolution (Muralt, 1987). Similarly, the formation of a Schottky barrier between the metallic STM tip and polypyrrole, a semiconducting polymer, has been observed (Hoogenraad *et al.,* 1992). I was particularly encouraged by the successes in imaging organic conducting films capable of metallic conduction, composed of TTF-TCNQ (tetrathiafulvalene tetracyanoquinodimethane) or BEDT-TTF stacks (Sleator & Tycko, 1988; Troyanovskij *et al.,* 1990; Frainchtein *et al.,* 1992; Bar *et al.,* 1992). These compounds form a class of organic conductors and superconductors (Wudl, 1983; Cowan & Wlygul, 1986; Jerome, 1991; Will-

iams *et al.,* 1991) that have a passing conformational resemblance to collagen, with alternating stacks of ring structures that are characterized by anisotropic conduction. STM is uniquely suited to probing and modifying electronic structure at the molecular lever, with a demonstrated ability to control an electrical signal with a single molecule (in effect creating a molecular switch, Aviram *et al.,* 1988), and with the resolution to observe quantum sized electronic effects in metals (Avouris & Lyo, 1994). The potential for STM electrical investigations at the nanometer scale is remarkable.

Unfortunately, STM has been plagued by the difficulty in distinguishing biological structures from imaging artifacts. In spite of several recent papers (to be discussed) on the subject, a surprising number of artifact images continue to be published in the literature. Interestingly, these artifacts very much mimic anticipated biological structures, particularly in that they often have a linear periodic motif which is similar to biological structures such as collagen, DNA, and other helical forms. Furthermore, in microscopy it is inherently difficult to directly and independently confirm the nature of the material actually producing the image. This becomes particularly problematic in that the sample generally matches one's expected image of that sample, making these artifacts particularly seductive. Although such hallucinations on the part of the observer can be treated directly (Berghausen & Sachs, 1986), it is preferable to control for artifacts from the outset. Careful work, including several controls, and a particularly exhaustive investigation of the many forms these artifacts can take, are required before any definitive conclusions can be presented. These measures take an inordinate amount of time, and appear to routinely be curtailed or overlooked by some labs, especially in light of the convincing nature of the artifacts. In my experience, the

difficulty in distinguishing artifacts from possible images, and the difficulty in independently verifying the adsorbed sample, makes STM poorly suited for this study. Even for biological samples which can be imaged by STM, the very high local current densities created by the tunneling current represents a significant departure from a native environment. These high current densities are a large part of the interaction between the sample and tip, along with mechanical contact forces.

SFM Principles

Problems of stability, reproducibility, and STM artifacts have lead a large part of the biological STM research community to work with SFM, which is not constrained to conductive samples (Hansma & Hoh, 1994; Rugar & Hansma, 1990; Hansma *et al.,* 1988). Additionally, with SFM one is not faced with the complicating factor of deconvolving the effect of the electronic structure of the sample from the surface topology, although this in itself may be of interest. The major difficulty with SFM is that by nature it interacts with the sample through a force. This is particularly a problem for biological materials, which tend to be relatively soft, to adhere loosely to the substrate, and are not bound in a crystal lattice. One purpose of the present study was to examine these difficulties.

The SFM was invented by Binnig, Quate, and Gerber in 1985 (Binnig *et al.,* 1986). While very similar to STM in concept, it uses a very different imaging methodology. The basic operating theory is much as described above for the STM, utilizing most of the same electronics. However, the SFM detects a force between the sample and a scanning tip, rather than a

tunneling current. A typical SFM uses a piezoelectric scan tube to scan a sample laterally against a very sharp tip (Figure I-4). The tip is attached to a cantilever, which is deflected by the forces between the tip and the sample

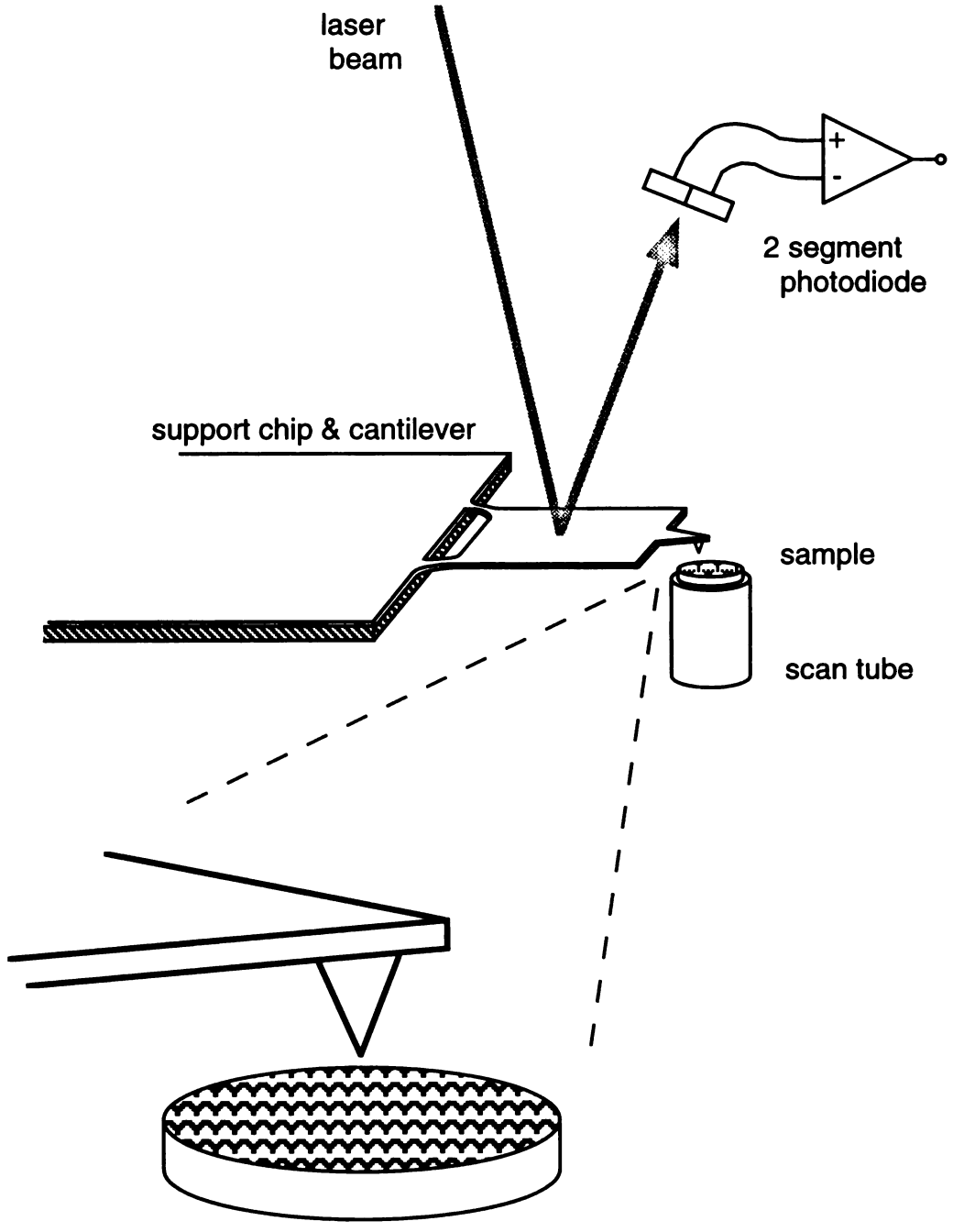

Figure I-4 Basic operating principle of our SFM, using a laser beam reflected off the back side of an imaging cantilever.

surface. This deflection can be detected by a number of different techniques, ranging originally from the changes in a tunneling current on the back of the cantilever (using a STM), to variable resistance or capacitance effects. Most detection systems are optically based, and rely on changes in a laser beam reflected off the cantilever. These optical detection schemes generally involve either interferometry (Rugar *et al.,* 1989) or beam deflection (Meyer & Amer, 1988; Alexander *et al.*, 1989). Our machine uses the latter, where a change in laser beam position, reflected off the cantilever, is measured using a split photo-diode, as shown in Figure I-4. Presently, most SFMs used in biological studies use silicon microfabricated tips; tip size and shape are critically important to the imaging process.

The resulting detector signal is used to construct a representation of the sample surface, either directly or through generation of a feedback signal. As with STM, the tip can be scanned across the sample in a fast, or "constant height" mode, where surface topology is determined by the change in force between sample and tip. Interactions between sample and tip can be minimized by scanning in a slow or "constant force" mode, in which a feedback signal can be used to keep the force constant between tip and sample. This feedback signal is additionally used to generate an image of the sample surface, as detailed above. A third mode of scanning is the "variable deflection" mode, where enough feedback is used to track the overall plane of the sample, but the local topology is still detected with changes in the force level. This mode effectively differentiates the topography signal, making quantitative determination of sample height very difficult. In contrast to STM, the SFM sample is generally scanned rather than the tip, simplifying the design of the optical path from laser to cantilever to photodiode.

Typically, the SFM is operated with the tip in physical contact with the sample in a "repulsive" force mode. In the repulsive mode, the tip tracks the surface of the sample at a force of about 1 nN (10^{-9} N), and with the appropriate samples is capable of atomic resolution. For comparison, the interatomic spring constant is on the order of 10 N/m (or 1 nN/Å) for a crystalline solid (Rugar & Hansma, 1990), and thus an applied force of 1 nN over the relatively large contact area of the tip will not remove the atoms from the lattice structure. For softer and more easily perturbed biological samples, one would expect it to be helpful to lower the contact force as much as possible, and to take steps to stabilize and strengthen the material of interest. The use of force for imaging can also be extended to electrostatic and magnetic forces, and SFM has proven quite successful at studying these interactions as well. It should be noted that all of these force measurements include the local sample (and tip) elasticity. It is also possible to operate in a non-contact mode to minimize interaction forces (Wigren *et al.*, 1991) where the imaging force is attractive due to van der Waals forces. However, non-contact imaging is at the cost of decreased lateral resolution (Yang *et al.*, 1993) and difficulties in tracking the sample surface, although atomic resolution images are possible on hard, well ordered surfaces (Ohnesorge & Binnig, 1993).

The use of a force to image biological samples, as opposed to crystal lattice structures, immediately raises the question of mechanical disruption. We can roughly estimate the maximum acceptable imaging forces for collagen from the observation that a "load" of 10 kg, or about 100 N, is needed to break a 1 mm diameter fiber of tendon (Stryer, 1988). A 1 mm fiber is composed of about 1×10^{11} molecules in cross section, subject to the uncer-

tainties in the 3-D structure in the collagen fibril. Therefore, each collagen molecule can sustain an axial force of at least 1 nN before breaking; although the fibril is most likely to break between molecules. If we make the assumption that this axial force is directly related to the perpendicular imaging forces due to the scanning tip, we can expect something on the order of at least 1 nN of imaging force will be required to break the molecule. This is a somewhat unfounded assumption, as the imaging force is really more like an elastic (and shear) deformation than a tensile force applied to the molecule. It also does not account for interactions between the adsorbed molecule and the substrate, or the differences between the strength of individual molecules and their behavior in bulk. It does, however, give us some indication of the lower bound for non-acceptable imaging forces. Lower interaction forces can still be expected to effect sample stability and resolution.

Sample Stabilization

It became apparent early on that sample stability and reproducibility were central issues in SFM of biological materials (Hansma *et al.,* 1988; Fisher, 1989a; Sarid, 1991; Amrein *et al.,* 1993; Apell *et al.,* 1993) as well as for STM. Early examinations of solid state materials were successful because the atoms were constrained in a crystal lattice. Biological samples, however, are routinely deposited onto a substrate surface. Moreover, biological materials tend to be relatively soft and elastic. Both of these conditions make biological samples particularly vulnerable to tip-sample interactions, and to displacement forces induced by the scanning process. Workers have concentrated on several approaches to stabilize samples and anchor them firmly to the substrate, in the hope of achieving higher lateral resolutions (Fisher, 1989a; Sarid, 1991; Blackford *et al.*, 1991).

Coating the samples with metals deposited in vacuo, (similar to TEM preparations) solves stability problems, and provides the electrical conductivity required for STM (Fisher *et al.*, 1990a). With this approach, however, the resolution is limited to the grain size of the evaporated metal. Furthermore, the sample is exposed to desiccating vacuum and to the latent heat of condensation. Unfortunately, this negates one of the most attractive features of SPM, the potential to examine native materials in a native environment. Conveniently, SFM does not require conductive samples.

Some biological samples are configured in a relatively self stabilizing pattern, and are thus more directly suitable for SPM imaging. Most biological samples have a relatively high aspect ratio, in which the sample is high compared to its contact area with the substrate, much like a sphere on a flat surface. As a result, the sample is prone to disturbance from forces induced by tip-sample interactions. Low and relatively flat samples, such as lipid membranes, Langmuir-Blodgett films, or molecules arranged as a liquid crystal lattice, tend to be more stable and result in relatively high resolution images. These larger and more stable structures can in turn be used to stabilize and immobilize single biological molecules. Molecules attached to lipid films (Weisenhorn *et al.*, 1986 & 1990; Egger *et al.*, 1990) or to liquid crystal arrays (Foster *et al.*, 1988; Spong *et al.*, 1989; Smith *et al.*, 1989 & 1990) have been imaged at high resolution.

Ideally, one would hope to examine samples, and particularly single molecules, directly on a planar substrate such as mica. Molecules can be directly adsorbed onto the mica surface (Weisenhorn *et al.*, 1986), although this usually requires treatment of the negatively charged mica surface to promote binding of biological molecules, which are typically negatively

Table I-2 Examples of organic and biological samples that have been examined by scanning force microscopy, based on Hansma & Hoh, 1994. References are representative and not a complete list. See Bibliography-Table I-2.

Category	Example	Reference
Molecular		
Macro	Nucleic Acids:	
molecular	DNA -first	38
	DNA -nucleotides	25,67,69
	DNA -plasmids	4,64
	DNA -singe & double stranded	21,39,63,75
	DNA in buffer	20,41
	DNA in propanol	22,24
	Proteins:	
	Actin	33,66
	Alpha-macroglobulin	2
	Collagen	61
	Ferritin	46
	Fibrinogen & fibrin	10,71
	Immunoglobulins	23,30,66
	Pertussis toxin	74
	Phosphorylase kinase	12
	RNA polymerase	32
Supra	DNA -protein complex:	
molecular	*E. coli* polymerase	20,57,78
	DNA polymerase	75
	Biotin -immunoglobulin	44,60
	T antigen (SV40 DNA)	43
	EcoR1 restriction enzyme	45
	DNA -gold labeled	60
	Chromosomes	1,49,50,56,60
	3D protein crystals:	
	Aspirin	42
	Ca - ATPase	35
	Collagen fibril	8
	Lysozyme growth process	11
	Membranes & 2D protein arrays:	
	Lipid bilayers	23,55,62,69
	Cadmium arachidate	59
	DMPG	13
	DMPE	77
	DPPC & DPPE	71
	Other Langmuir Blodgett films	15,23,53,59,73
	Purple membrane in air	72
	Purple membrane in water	5
	Bacterial S-layers	9
	Gap junctions	27,28
	Cholera toxin on DDPC	76
	HPI *D. radioduranss*non-contact	70
	HPI *D. radioduranss*contact	58
	Acetylcholine receptors	37
	Porin channels	36

Cellular	Surfaces:	
	Blood cells, plant & bacterial	3,6,16,17,18
	Actin filaments & cytoskeleton	7,26,31
	Lymphocytes -gold labeled	51
	Neurons & glial	47,48
	Processes:	
	Adhesion	48
	Platelet activation	14
	Platelet elasticity & viscosity	52,54
	Streptavidin binding	78
	Virus particle -emerging	19
	Virus:	
	Fd phage	40
	T4	29,34
	Tobacco mosaic	65

Table I-2 continued.

charged as well. Often the mica surface is washed with divalent cations, such as Mg or Ca, to promote binding.

A great deal of effort has been directed toward protocols for binding DNA directly to mica surface, I suspect in deference to the human genome project. These efforts have ranged from the techniques above, to covalent binding of mercurated DNA (Lyubchenko *et al.,* 1991) or silanated DNA (Lyubchenko *et al.,* 1992), to potentiostatic deposition (Lindsay *et al.,* 1992); all in an attempt to effectively tether the molecule to the substrate surface. Particularly nice results have been recently obtained of DNA imaged directly on mica in n-propanol (H. Hansma *et al.,* 1992). Rapid freezing of the sample, a successful TEM technique, has several inherent advantages, including minimal physical distortions and the avoidance of chemical modifications. It has been suggested that a similar approach in SFM might enhance sample stability, but has only been applied in a relatively limited manner. In general, however, SFM imaging of biological samples, as outlined in Table I-2, have been subject to limited reproducibility and stability,

and a lateral resolution typically on the order of tens of nanometers, far short of the demonstrated potential resolution of SFM. Good recent reviews of SFM in biological investigations are Marti and Amrein (1993), Yang et al. (1993), Lal and John (1994), and Hansma and Hoh (1994).

Thermal Motion

Part of the limits on the lateral resolution of biological samples examined by SFM is undoubtedly due to thermal motions. Atomic resolution images have been typically obtained on hard materials, where the thermal motions of single atoms are limited by the constraints of the crystal lattice structure. The situation for a single biological molecule, relatively unconstrained on a surface in air or in liquid, is very different. We can expect that a large, soft biological molecule at room temperature will be subject to a range of thermally induced motions, from those of single atoms to several modes of molecular vibration. Such motions will potentially reduce our imaging resolution. Furthermore, the molecule will be subject to the thermal fluctuations of the surrounding environment (Brownian motion). These thermal effects, along with the elasticity of the sample and the shape of the imaging tip, can be expected to be the major resolution constraints in SFM imaging.

An indication of the magnitude of these thermal vibrational effects can be inferred from studies of protein and nucleic acids dynamics. It is important to bear in mind that at room temperature, water itself is a very dynamic environment at the molecular level. Kinetic energy is high enough that hydrogen bonds between adjacent molecules will break and reform on a time scale of about 5 picoseconds. Similarly the dynamics of the conformational state of a biological molecule is driven by both instantaneous and highly

localized random forces, and by systematic forces (electrostatic and hydrophobic interactions).

Table I-3 Typical features of some internal motions of proteins and nucleic acids at room temperature. "Amplitude" characterizes the rapid local motions of the individual groups as indicated, while the slow collective distortions of large regions within the molecule are characterized by "spatial extent." From McCammon (1987).

Motion	Spatial extent (nm)	Amplitude (nm)	Log_{10} of time (s) [characteristic]
Relative vibration of bonded atoms	0.2 to 0.5	0.001 to 0.01	-14 to -13
Longitudinal motions of bases in double helices (nucleic acids)	0.5	0.01	-14 to -13
Lateral motions of bases in double helices (nucleic acids)	0.5	0.1	-13 to -12
Global stretching (nucleic acids)	1 to 30	0.03 to 0.3	-13 to -11
Global twisting (nucleic acids)	1 to 30	0.1 to 1.0	-13 to -11
Elastic vibration of globular region	1 to 2	0.005 to 0.05	-12 to -11
Sugar repuckering (nucleic acids)	0.5	0.2	-12 to -9
Rotation of sidechains at surface (protein)	0.5 to 1	0.5 to 1	-11 to -10
Torsional libration of buried groups	0.5 to 1	0.05	-11 to -9
Relative motion of different globular regions (hinge bending)	1 to 2	0.1 to 0.5	-11 to -7
Global binding (nucleic acids)	10 to 100	5 to 20	-10 to -7
Rotation of medium-sized sidechains in interior (protein)	0.5	0.5	-4 to 0
Allosteric transitions	0.5 to 4	0.1 to 0.5	-5 to 0
Local denaturation	0.5 to 1	0.5 to 1	-5 to +1

Proteins are capable of a large number of motions and vibrational modes, predominantly associated with the single covalent peptide bond between each amino acid residue. Within steric limits, and despite the high packing densities of proteins, this bond is particularly free to rotate, allowing for a large range of thermally induced motions. Some of these features of the internal motions of proteins and nucleic acids are shown in Table I-3 (McCammon, 1987). As indicated, the motions of side chains can be as large as 0.5 to 1.0 nm, and elastic vibrations of globular regions (such as

"breathing modes") can spatially range over 1 – 2 nm. The side chains in collagen, which are all essentially on the surface of the protein, can be expected to be sensitive to such thermal motions. Vibrational mode studies in our lab, based on neutron-scattering, has shown that there is an attenuation of intrachain motion at 110 K (Berney *et al.*, 1987).

Additionally, as McCammon points out, proteins undergo more complicated global transitions on longer time scales. These are due to the number of slightly different stable states that comprise the native conformation of a protein. These different states, and their transition, are often of biological importance. Several authors have compared these transitions with the structural rearrangements that occur in glassy materials (Goldanskii *et al.,* 1984; McCammon, 1984; Ansari *et al.,* 1985; Stein, 1985). Different states of stability, and thus conformation, can also be expected to impact the resolution, unless they can be identified as such.

Low Temperature SFM

One possibility which might both enhance sample stability and reduce the thermal motions of molecules is to image at cryogenic temperatures. Low temperatures can be expected to stiffen the molecule (discussed shortly), reducing the deformations induced by the tip imaging forces, and improve sample stability and image reproducibility. Imaging at low temperatures will also reduce the thermal motions of the molecules, which should further improve at least the potential resolution.

The possibility of using low temperatures to stabilize biological samples for SFM imaging was developed in the late 1980s, derived from similar discussions for STM imaging (Fisher *et al.,* 1989a). While low temperature

STMs were relatively common, the first really workable LT-SFM was described by Kirk et al., (1988), about three years after the first introduction of the SFM. This work, while restricted to solid state surfaces, did recognize the merits of low temperature SFM as "offering improved signal-to-noise ratio, elimination of thermal drift, increased sample stability, and the possibility of investigating low-temperature phenomena." The immediate design difficulties associated with a LT-SFM were recognized as well. While not directly addressing the applications of LT-SFM to biology, the authors did suggest the usefulness of LT-SFM as applied to molecules individually adsorbed onto a substrate. Low temperatures could be expected to enhance adhesion of molecules to the substrate, and lessen the distortion or destruction of the sample.

Our group had also been developing a similar low temperature SFM for the study of biological samples (Gustaffson *et al.,* 1990, Fisher *et al.,* 1991; Fisher *et al.,* 1990b; Gustaffson *et al.,* 1991). At the same time a similar LT-SFM effort for biological imaging was being undertaken by Paul Hansma's group at U.C. Santa Barbara. The results of this work, including one preliminary image of a patch of purple membrane imaged at 147 K, was published in 1991 (Prader *et al.,* 1991). This group similarly felt that low temperatures would enhance sample "anchoring" and stability, increase rigidity and decrease thermal motion. Proteins in particular were predicted to "freeze into a single conformational state and become much more rigid." This effort at low temperature imaging has not been followed up to a significant degree, due in part to the technical challenges associated with LT-SFM, and the subsequent development of chemical sample anchoring techniques, especially for DNA. The authors found major technical difficulties associ-

ated with vibrations from the boiling liquid N_2 cryogen, and with contamination and water freezing onto the sample surface. This freezing of contaminates, which in turn obscures the sample, was a particular problem, and indeed the sample presented was imaged in vacuum in an attempt to minimize this effect.

Recent attempts at developing biological LT-SFM techniques have been surprisingly limited. This may not be unreasonable given the difficulties described by Prater et al., and our own LT-SFM experiences. Two published efforts are of note, however, as they contain some interesting approaches for future work. Luo et al. (1993) have developed a relatively simple system, contained in a freezer compartment, which has successfully imaged lipids at -25 °C. Interestingly, the authors did not report an ice contamination imaging problem, and were able to image in a near physiological solution utilizing glycerol or DMSO as cryoprotectants.

A second LT-SFM effort from Zhiteng Shao's lab (Mou *et al.,* 1993) is particularly noteworthy given the unique design of the instrument. This LT-SFM relies on an SFM microscope which operates suspended directly over a pool of liquid N_2 in a small Dewar. As a result, the instrument operates in a cooled N_2 gas vapor environment, maintained by the liquid N_2 at the bottom of the Dewar. In this way, the microscope is not exposed directly to the boiling liquid N_2, and is shielded from the water and contaminates found in air by the N_2 vapor. The microscope, designed for biological work, operates within a few degrees of liquid N_2 temperatures (78 K), and is capable of atomic resolution. This approach does indeed have a great deal of appeal for biological investigations, but the application of this machine for biological samples has not yet been demonstrated.

It has been assumed that low temperatures will improve sample stability and rigidity as well as reduce thermal motions. However, evidence for such improvement is rather scarce. Indeed, direct investigation of such physical properties at the molecular level would require a LT-SFM. Presently, we are restricted to more indirect evidence for the idea of macromolecular stiffening at low temperatures.

Most of the arguments for low temperature stiffening center on the evidence that proteins undergo a transition into a glass-like state (Iben *et al.*, 1989). Protein conformational substrates can be modeled incorporating the concepts of frustration and disorder in analogy to glasses (Stein, 1985). Typically, proteins exist in a large number of conformational states, each representing a local conformational potential energy minima. Proteins can relax through a series of these equilibrium structures via "protein quakes" and related intermolecular equilibrium motions; these states and motions have a hierarchical glass-like structure (Ansari *et al.*, 1985).

At some low temperature, proteins can be expected to freeze into a single conformational state. Several lines of evidence, including Mossbauer spectroscopy (Parak *et al.*, 1981), x-ray structural analysis (Parak *et al.*, 1987), and quasi-static and kinetic studies (Iben *et al.*, 1989), indicate that this occurs at a transition temperature of about 200 K and in a manner analogous to a metastable glass state. Frozen into a single such conformational state, proteins will be strengthened by stabilizing hydrogen bonds, and hopefully exhibit a stiffened behavior.

Studies of protein dynamics similarly, and more directly, demonstrate a reduction in thermally mediated spatial and temporal motions in a manner

favoring a glass-like dynamic model. Experiments with electron spin resonance spectroscopy (Likhtenstein *et al.,* 1993), Mossbauer radiation (Parak, 1992), and spectroscopy (Knapp *et al.,* 1982), all favor such a model. This transition occurs in the neighborhood of 200 K, as indicated by electron transfer experiments (Peterson-Kennedy *et al.,* 1986), calorimetry and infrared absorption studies (Doster *et al.,* 1986) and x-ray crystallography (Tilton *et al.,* 1992). Inelastic neutron scattering studies in our own lab indicate that collagen molecules may be restricted to only low frequency vibrational modes at 110 K, and that attenuation of intrachain motion may result in a "relative stiffening" of the molecular chains (Berney *et al.,* 1987). The crystal structure of myoglobin, determined at 2 Å resolution, also indicates that the protein is stiffer at 80 K than at 300 K, and that "intramolecular motions can be frozen out to a surprisingly high degree" (Hartmann *et al.,* 1982).

The high resolution x-ray crystallographic studies of Tilton et al. (1992) demonstrate a biphasic characteristic for the Debye-Waller factor (indicative of atomic motions), with a transition temperature of 200 K to 220 K. Additionally, it has been shown that the same ribonuclease-A loses its function below this dynamical transition (Rasmussen *et al.*, 1992). Both of these studies suggest that this transition is directly related to a change in the mobility of the bound water incorporated into the protein, and may actually reflect a change in solvent dynamics. In essence, catalytic functionality is lost as the structure becomes "too rigid," a phenomena similarly observed in azidemethaemoglobin, and it is suggested that such "freezing" at 200 K to 220 K is a general property of protein structures (Perutz, 1992).

Clearly, there is good indirect evidence to anticipate in SFM an increase

in rigidity and stability of at least proteins at temperatures below 200 K. Proteins have been described as being "very rigid" at low temperature in conjunction with LT-SFM of biology (Prader *et al.*, 1991; Mou *et al.*, 1993), raising the additional issue of semantics. Rigidity can of course refer to the mechanical properties of a protein, but is also used to describe the conformational state of protein. "Rigid conformation" is sometimes used to indicate restriction to a single conformational state, and does not necessarily describe a mechanical property of a protein.

Direct evidence for the change in mechanical rigidity of biological molecules with decreasing temperature is a bit more scarce. Little work has been done in this area, although Prader and Mou state that "it is believed that the strength of biological molecules will improve by a factor of up to 10^4 in terms of Young's modulus" and cite Dorrington, 1979 (sic). I suspect that this increase mostly reflects the transition from liquid to solid water (Dorrington, 1980). We do know that the viscoelastic properties of biomaterials changes with temperature, at least in the range above freezing. Both the viscoelastic modulus and the relaxation time change with decreasing temperature (Dorrington, 1980), both acting to make a polymer appear more rigid. This work additionally indicates a series of glass transitions well below freezing, with corresponding increases in the isochronal relaxation modulus and the shear modulus at lower temperatures. Both of these moduli increase about 10^3 as the temperature falls below freezing (water), and increase by an additional factor of 5 or 10 from freezing to -200 °C. Interestingly, glass transitions of collagen and gelatin have been studied over a wide range of temperatures. Shear modulus vs. temp curves for 40/60 gelatin/ glycerol mixtures show an increase from about 1 x 10^7 dynes/cm^2 at warm

temperature to about 5 x 10^{10} dynes/cm^2 at -150 °C, where it levels off (Yannas, 1972). The majority of this change occurs below 0 °C. These changes are of course for bulk material, and the development of a LT-SFM will allow for the direct measurement of these physical properties at the molecular level.

Cooling the sample and system (particularly the cantilever) does have an intrinsic advantage in that it reduces the "thermal noise." This effect will be important at high levels of resolution, and may lower the background thermal noise, resulting in at least a qualitative improvement in imaging contrast. The approximate magnitude of this expected improvement can be estimated from the equipartition theory. If we make some simplifying assumptions, and restrict ourselves to a single (vertical) degree of freedom, the equipartition theory results in:

$$1/2\ C_0\ (\Delta z)^2 = 1/2\ kT$$

where C_0 is the "spring constant", Δz the vertical RMS amplitude, T the temperature and k the ubiquitous Boltzmann's constant (Rugar & Hansma, 1990). The difficulty is in estimating the spring constant for a system composed of a sample on a mica background with a layer of uncharacterized impurities.

Atoms in the substrate have an effective spring constant of about 10 N/m, which results in a Δz of 0.2 Å at room temperature. If we assume that the surface, including sample and impurities, has a spring constant of 1.0 N/m (similar to the cantilever), Δz = 0.64 Å at 300 K and is reduced to 0.44 Å at 143 K. In all likelihood, biological materials are somewhat softer, and a lower C_0 is more appropriate; for C_0 = 0.1 N/m, Δz is reduced from 2.0 Å to

1.4 Å at 143 K. These values serve as lower limits for the improvement in thermal background noise; we can expect about an Ångstrom or two of RMS amplitude with a 30 % reduction at 143 K. Despite the uncertainties of these approximations, the 30 % relative reduction in thermal noise (a function of kT) can be expected to be constant (assuming C_0 to be about constant over this temperature range).

The thermal background noise and the thermal vibrational modes of biological samples are significantly reduced at low temperature. Low temperature may further enhance the stability and reproducibility of biological materials imaged by SFM, a recurrent problem. Towards that end, we have developed a LT-SFM capable of imaging and manipulating biomaterials at the molecular level. We confirmed our observations with TEM and PAGE.

With our LT-SFM, we have obtained the first SFM images of collagen monomers, both at room temperature and 143 K. We are able to correlate some of our observed structural features with the known biophysical characteristics of the collagen molecule. Operation at low temperature results at the very least in a qualitative improvement in these data, subject to the resolution limitations of the scanning tip. Presently, our LT-SFM images of collagen are the highest quality scans of isolated protein molecules imaged by SFM.

We are able to use our LT-SFM to modify biological samples directly, using variable force application to disrupt and selectively remove membranes and molecules. This work opens the door for SFM freeze-fracture at the molecular level. Measurements of molecular physical properties, such as elasticity, as functions of temperature, are also possible with the LT-SFM.

Bibliography

1. Albrecht, T. R., M. M. Dovek, C. A. Lang, P. Grutter, C. F. Quate, S. W. J. Kuan, C. W. Frank, and R. F. W. Pease. 1 August 1988. Imaging and modification of polymers by scanning tunneling and atomic force microscopy. *J. Appl. Phys. (USA)* vol.64 (no.3): 1178-84.

2. Alexander, S., L. Hellemans, O. Marti, J. Schneir, V. Elings, P. K. Hansma, M. Longmire, and J. Gurley. 1 January 1989. An atomic-resolution atomic-force microscope implemented using an optical lever. *J. Appl. Phys. (USA)* vol.65 (no.1): 164-7.

3. Amrein, M., H. Gross, and R. Guckenberger. 1993. STM of proteins and membranes. *STM and SFM in Biology.* Marti, O., Amrein, M. 127-175. San Deigo: Academic Press.

4. Amrein, M., A. Stasiak, H. Gross, E. Stoll, and G. Travaglini. 22 April 1988. [Scanning tunnelling microscopy of recA-DNA complexes coated with a conducting film]. *Science (USA)* vol.240 (no.4851): 514-16.

5. Andrabi, W. H., and J. Behari. 1981. Bone photovoltaic cell in Hall geometry. *Calcif. Tissue Int.* 33: 239-242.

6. Arnold, H., H. Odom, and W. James. 1990. *Andrews' Diseases of the Skin.* 11. Philadelphia: W. B. Saunders.

7. Ansari, A., J. Berendzen, S. F. Bowne, H. Frauenfelder, I. E. T. Iben, T. B. Sauke, E. Shyamsunder, and R. D. Young. August 1985. Protein states and proteinquakes. *Proc. Natl. Acad. Sci. USA* 82: 5000-5004.

8. Apell, H., J. Colchero, A. Linder, and O. Marti. 1993. SFM in Biology: Investigation of the Na, K-ATPase by SFM. *STM and SFM in Biology.* Marti, O.//Amrein, M. 275-308. San Deigo: Academic Press.

9. Athenstaedt, H. 1970. Permanent logitudinal electric polarization and pyroelectric behaviour of collagenous structures and nervous tissue in man and other vertebrates. *Nature* 228: 830- 834.

10. Aviram, A., C. Joachim, and M. Pomerantz. 20 May 1988. [Evidence of switching and rectification by a single molecule effected with a scanning tunneling microscope]. *Chem. Phys. Lett. (Netherlands)* vol.146 (no.6): 490-5.

11. Avouris, P., and In-Whan Lyo. 13 May 1994. Observation of quantum-size effects at room temperature on metal surfaces with STM. *Science (USA)* vol.264 (no.5161): 942-5.

12. Baldeschwieler, J. D., J. M. Gill, and P. E. West. 1991. The scanning probe microscope: a powerful tool for visualizing the micro world. *American Laboratory* Feb: 34-39.

13. Bar, G., S. N. Magonov, H. J. Cantow, J. Gmeiner, and M. Schwoerer. July 1992. Atomic-scale imaging of anisotropic organic conductors by scanning probe techniques (STM/AFM). *Ultramicroscopy (Netherlands)* vol.42-44, pt.A: 644-52.

14. Bardelmeyer, G. H. 1973. Electrical conduction in collagen. II. Some aspects of hydration. *Biopolymers* 12: 2303-2307.

15. Baro, A. M., R. Miranda, J. Alaman, N. Garcia, G. Binnig, H. Rohrer, Ch. Gerber, and J. L. Carrascosa. 16 May 1985. Determination of surface topography of biological specimens at high resolution by scanning tunnelling microscopy. *Nature (UK)* vol.315 (no.6016): 253-4.

16. Becker, R. O., and G. Seldem. 1985A. *The Body Electric*. 122- 135. New York: Morrow.

17. —. 1985B. *The Body Electric*. 150-160. New York: Morrow.

18. Behari, J., and W. H. Andrabi. 1978. Generation of Hall voltage in bone. *Connective Tissue Research* 6: 181-184.

19. —. 1981. PN junction characteristics and photoelectromagnetic effect in bone. *Biomaterials* 2: 23.

20. Behari, J., S. K. Guha, and P. N. Agarwal. 1975. The effect of ultraviolet radiation on the electrical conductivity of human bone. *Calcif. Tiss Res.* 19: 223-227.

21. Berghausen, P. E., and L. B. Sachs. 1985. Hypnotic treatment of hallucinations and disordered impulse control. *Imagination, Cognition and Personality* 5 (4): 311-319.

22. Berney, C. V., V. Renugopalakrishnan, and R. S. Bhatnagar. 1987. An inelastic neutron-scattering study of low-frequency vibrational modes. *Biophys. J.* 52: 343-345.

23. Bhatnagar, R. S., N. Pattabiraman, K. R. Sorenson, R. Langridge, R. D. MacElroy, and V. Renugopalakrishnan. 1988. Inter-chain proline:proline contacts contribute to the stability of the triple helical conformation. *J. Biomolecular Structure and Dynamics* 6 (2): 223-233.

24. Binnig, G., C. F. Quate, and C. Gerber. 3 March 1986. [Atomic force microscope]. *Phys. Rev. Lett. (USA)* vol.56 (no.9): 930-3.

25. Binnig, G., H. Rohrer, Ch. Gerber, and E. Weibel. 1983. 7 x 7 Reconstruction on Si (111) resolved in real space. *Phys. Rev. Lett.* 50: 120-123.

26. —. 1982. *Phys. Rev. Lett.* 49: 57.

27. Binnig, G., and H. Rohrer. August 1985. [The scanning tunneling microscope]. *Sci. Am. (USA)* vol.253 (no.2): 40-6.

28. Binnig, G., and D. P. E. Smith. August 1986. [Single-tube three-dimensional scanner for scanning tunneling microscopy]. *Rev. Sci. Instrum. (USA)* vol.57 (no.8, pt.1): 1688-9.

29. Blackford, B. L., M. H. Jericho, and P. J. Mulhern. December 1991. A review of scanning tunneling microscope and atomic force microscope imaging of large biological structures: problems and prospects. *Scanning Microsc. (USA)* vol.5 (no.4): 907-18.

30. Burr, H. S. 1973. *The Fields of Life. Our Links to the Universe*. 1-7. New York: Ballantine Books.

31. Chernoff, E. A. G., and D. A. Chernoff. July 1992. Atomic force microscope images of collagen fibers. *J. Vac. Sci. Technol. A, Vac. Surf. Films (USA)* vol.10 (no.4, pt.1): 596-9.

32. Cowan, D. O., and F. M. Wiygul. 1986. The organic solid state. *Chem. & Eng. News* July 21: 28-45.

33. Dorrington, K. L. 1980. *Mechanical Properties of Biological Materials*. J. F. V. Vincent, and J. D. Currey, Cambridge, England: Cambridge University Press.

34. Doster, W., A. Bacheitner, R. Dunau, M. Hiebl, and E. Luscher. 1986. *Biophys. J.* 50: 213-219.

35. Dovek, M. M., T. R. Albrecht, S. W. J. Kuan, C. A. Lang, R. Emch, P. Grutter, C. W. Frank, R. F. W. Pease, and C. F. Quate. October 1988. Observation and manipulation of polymers by scanning tunnelling and atomic force microscopy. *J. Microsc. (UK)* vol.152, pt.1: 229-36.

36. Egger, M., F. Ohnesorge, A. L. Weisenhorn, B. Heyn, B. Drake, C. B. Prater, S. A. C. Gould, P. K. Hansma, and H. E. Gaub. 1990. *J. Struct. Biol.* 103: 89.

37. Eigler, D. M., C. P. Lutz, and W. E. Rudge. 15 August 1991. An atomic switch realized with the scanning tunnelling microscope. *Nature (UK)* vol.352 (no.6336): 600-3.

38. Eigler, D. M., and E. K. Schweizer. 5 April 1990. Positioning single atoms with a scanning tunnelling microscope. *Nature (UK)* vol.344 (no.6266): 524-6.

39. Erickson, C. A., and R. Nuccitelli. 1984. Embryonic fibroblast motility and orientation can be influenced by physiological electric fields. *J. Cell Bio.* 98: 296.

40. Fainchtein, R., S. T. D'Arcangelis, S. S. Yang, and D. O. Cowan. 15 May 1992. Order and low dimensionality in the organic superconductor (BEDT-TTF)/sub 2/Cu(NCS)/sub 2/ revealed by STM. *Science (USA)* vol.256 (no.5059): 1012-14.

41. Feynman, R. P., R. B. Leighton, and M. Sands. 1963. *The Feynman Lectures on Physics*, first ed. 12-12. Reading, Mass: Addison-Wesley.

42. Fisher, K. A. 1989. Monolayer freeze-fracture and scanning tunneling microscopy. *Journal of Electron Microscopy Technique* 13: 355-371.

43. Fisher, K. A., M. G. L. Gustafsson, R. E. Thomson, S. L. Whitfield, K. C. Yanagimoto, M. B. Shattuck, and J. Clarke. 1990b. Low temperature scanning probe microscopy. *Roy. Microsc. Soc., Proc.* 25: S3.

44. Fisher, K. A., M. G. L. Gustafsson, M. B. Shattuck, and J. Clarke. 1991. Proc. 49th Ann. Meet. Elect. Microsc. Soc. Amer., G. W. Bailey, 54-55. San Francisco, California: San Francisco Press.

45. Fisher, K. A., K. C. Yanagimoto, S. L. Whitfield, R. E. Thomson, M. G. L. Gustafsson, and J. Clarke. Aug. 1990a. Scanning tunneling microscopy of planar biomembranes. *Ultramicroscopy (Netherlands)* vol.33 (no.2): 117-26.

46. Foster, J. S., and J. E. Frommer. 9 June 1988. [Imaging of liquid crystals using a tunnelling microscope]. *Nature (UK)* vol.333 (no.6173): 542-5.

47. Friedenberg et al. 1973. The cellular origin of bioelectric potentials in bone. *Calcif. Tiss. Res.* 13: 53.

48. Fukada, E., H. Ueda, and R. Rinaldi. 1976. Piezoelectric and related properties of hydrated collagen. *Biophysical J.* 16: 911- 918.

49. Fuller, R. G., A. A. Marino, and R. O. Becker. 1976. Photoconductivity in bone and tendon. *Biophysical Journal* 16: 845-846.

50. Gardner, D. L. 1992. *Pathological Basis of the Connective Tissue Diseases*., 102. London: Lea and Febiger.

51. Goldanskii, V. I., Y. F. Krupyanskii, and V. N. Flerov. 1984. Tunneling between quasi-degenerate conformational states and low- temperature heat capacity of biopolymers. *Doklady Biophysics* 272: 209.

52. Guckenberger, R., W. Wiegrabe, and W. Baumeister. 1988. Scanning tunneling microscopy of biomolecules. *J. Microscopy* 152 (3): 795-802.

53. Gustafsson, M. G. L., K. A. Fisher, and J. Clarke. Pacific Conference Chem. Spectrosc., Palo Alto, California, 1990.

54. Gustafsson, M. G. L., K. A. Fisher, M. B. Shattuck, and J. Clarke. Sixth International Congress of STM, 28. Interlaken, Switzerland, 1991.

55. Hameroff, S., Y. Simic-Krstic, D. Koruga, M. Kelley, R. McCuskey, M. Krasovich, and C. Schneiker. 1989. Scanning tunneling microscopy of microtubules. Proceedings of the Annual Conference of the IEEE Engineering in Medicine and Biology Society. 1350-1 vol.4.

56. Hansma, H. G., and J. Hoh. 1994. Biomolecular imaging with the atomic force microscope. *Annual Review of Biophysics and Biomolecular Structure*. R. M. Stroud, C. R. Cantor, and T. D. Pollard,

115-139. Palo Alto: Annual Reviews Inc.

57. Hansma, H. G., J. Vesenka, C. Siegerist, G. Kelderman, H. Morrett, R. L. Sinsheimer, V. Elings, C. Bustamante, and P. K. Hansma. 22 May 1992. Reproducible imaging and dissection of plasmid DNA under liquid with the atomic force microscope. *Science (USA)* vol.256 (no.5060): 1180-4.

58. Hansma, P. K., J. P. Cleveland, M. Radmacher, D. A. Walters, P. E. Hillner, M. Bezanilla, M. Fritz, D. Vie, H. G. Hansma, C. B. Prater, J. Massie, L. Fukunaga, J. Gurley, and V. Elings. 28 March 1994. Tapping mode atomic force microscopy in liquids. *Appl. Phys. Lett. (USA)* vol.64 (no.13): 1738-40.

59. Hansma, P. K., V. B. Elings, O. Marti, and C. E. Bracker. 14 October 1988. Scanning tunneling microscopy and atomic force microscopy: application to biology and technology. *Science (USA)* vol.242 (no.4876): 209-16.

60. Hansma, P. K., and J. Tersoff. 15 January 1987. [Scanning tunnelling microscopy]. *J. Appl. Phys. (USA)* vol.61 (no.2): R1- 23.

61. Hartmann, H., F. Parak, W. Steigemann, G. A. Petsko, D. R. Ponzi, and H. Frauenfelder. August 1982. Conformational substates in a protein: structure and dynamics of metmyoglobin at 80K. *Proc. Natl. Acad. Sci. USA (USA)* vol.79 (no.16): 4967-71.

62. Hay, E. D. 1990. *Cell Biology of the Extracellular Matrix*. New York: Plenum Press.

63. Hofmann, H., T. Voss, and K. Kuhn. 1984. Localization of flexible sites in thread-like molecules from electron micrographs. *J. Mol. Biol.* 172: 325-343.

64. Hoogenraad, F. G. C., A. C. R. Hogervorst, P. M. L. O. Scholte, and F. Tuinstra. July 1992. Schottky-barrier formation in conducting polymers. *Ultramicroscopy (Netherlands)* vol.42-44, pt.B: 1004-8.

65. Iben, I. E. T., D. Braunstein, W. Doster, H. Frauenfelder, M. K. Hong, J. B. Johnson, S. Luck, P. Ormos, A. Schulte, P. J. Steinbach, A. H. Xie, and R. D. Young. 17 April 1989. Glassy behavior of a protein. *Phys. Rev. Lett. (USA)* vol.62 (no.16): 1916-19.

66. Jaffee, L. F., and R. Nuccitelli. 1977. Electrical controls of development. *Ann. Rev. Biophys. Bioeng.* 6: 445.

67. Jeon, D., J. Kim, M. C. Gallagher, and R. F. Willis. 19 June 1992. Scanning tunneling spectroscopic evidence for granular metallic conductivity in conducting polymeric polyaniline. *Science (USA)* vol.256 (no.5064): 1662-4.

68. Jerome, D. 1991. The physics of organic superconductors. *Science* 252: 1509-1514.

69. Kirk, M. D., T. R. Albrecht, and C. F. Quate. June 1988. [Low-temperature atomic force microscopy]. *Rev. Sci. Instrum. (USA)* vol.59 (no.6): 833-5.

70. Knapp, E. W., S. F. Fischer, and F. Parak. 23 December 1982. Protein dynamics from Mossbauer spectra. The temperature dependence. *J. Phys. Chem. (USA)* vol.86 (no.26): 5042-7.

71. Lal R, and John SA. January 1994. Biological applications of atomic force microscopy. *Am J Physiol* 266 (1 Pt 1): C1-21.

72. Likhtenstein, G. I., V. R. Bogatyrenko, and A. V. Kulikov. 1993. Low temperature protein dynamics studied by spin-labelling methods. *Appl. Magn. Reson. (Austria)* vol.4 (no.4): 513-21.

73. Lindsay, S. M., and B. Barris. March 1988. [Imaging deoxyribose nucleic acid molecules on a metal surface under water by scanning tunneling microscopy]. *J. Vac. Sci. Technol. A, Vac. Surf. Films (USA)* vol.6 (no.2): 544-7.

74. Lindsay, S. M., N. J. Tao, J. A. DeRose, P. I. Oden, Yu. L. Lyubchenko, R. E. Harrington, and L. Shlyakhtenko. June 1992. Potentiostatic deposition of DNA for scanning probe microscopy. *Biophys. J. (USA)* vol.61 (no.6): 1570-84.

75. Luo, K., M. Yorgancioglu, and D. Keller. 1993. Scanning force microscopy at -25 degC. *Ultramicroscopy* 50: 147-155.

76. Lyubchenko, Y. L., B. L. Jacobs, and S. M. Lindsay. 1992. Atomic force microscopy of reovirus dsRNA: a routine technique for length measurments. *Nucleic Acids Res.* 20 (15): 3983-3986.

77. Lyubchenko, Y. L., S. M. Lindsay, J. A. DeRose, and T. Thundat. March 1991. A technique for stable adhesion of DNA to a modified graphite surface for imaging by scanning tunneling microscopy. *J. Vac. Sci. Technol. B, Microelectron. Process. Phenom. (USA)* vol.9 (no.2, pt.2): 1288-90.

78. Mamin, H. J., E. Ganz, D. W. Abraham, R. E. Thomson, and J. Clarke. 15 December 1986. [Contamination-mediated deformation of graphite by the scanning tunneling microscope]. *Phys. Rev. B, Condens. Matter (USA)* vol.34 (no.12): 9015-18.

79. Marino, A. A. 1979. Space osteoporosis: an electromagnetic hypothesis. *Aviation Space Environ. Med.* 50: 409.

80. Marti, O., and M. Amrein. 1993. *STM and SFM in Biology.* San Diego: Academic Press.

81. Mathews, M. B. 1988. Evolution and collagen. *Biology of Invertebrate and Lower Vertebrate Collagen.* A. Bairati, and R. Garrone,New York: Plenum Press.

82. McCammon, J. A. 1984. Protein dynamics. *Reports on Progress in*

Physics 47: 1.

83. Meyer, G., and N. M. Amer. 19 September 1988. Novel optical approach to atomic force microscopy. *Appl. Phys. Lett. (USA)* vol.53 (no.12): 1045-7.

84. Miller, E. J., and R. K. Rhodes. 1982. Preparation and characterization of the different types of collagen. *Structural and Contractile Proteins.* L. W. Cunningham, and D. W. Frederiksen, 33-64. New York: Academic Press.

85. Mou, J., J. Yang, and Z. Shao. 1993. An optical detection low temperature atomic force microscope at ambient pressure for biological research. *Rev. Sci. Instrum.* 64 (6): 1483-1488.

86. Muralt, P. March 1987. [Semiconductor interfaces studied by scanning tunneling microscopy and potentiometry]. *Surf. Sci. (Netherlands)* vol.181 (no.1-2): 324-32.

87. Nageotte, J. 1927. *C. r. hebd. Soc. Biol.*, Paris vol.96: 172, 464, 559, 828, & 1268.

88. Nestler, F. H., S. Hvidt, J. D. Ferry, and A. Veis. 1983. Flexibility of collagen determined from dilute solution viscoelastic measurements. *Biopolymers* 22: 1747-1758.

89. Neufeld, D. A. 1985. Bone healing after amputation of mouse digits and newt limbs: Implications for induced regeneration in mammals. *Anat. Res.* 211: 156.

90. Newton, I. 1686. *Principia Mathematica Philosophiae Naturalis.*

91. M. E. Nimni, and R. D. Harkness. 1988. *Collagen.* M. E. Nimni, 113-137. Boca Raton, Florida: CRC Press.

92. Ohnesorge, F., and G. Binnig. 1993. True atomic resolution fy atomic force microscopy through repulsive and attractive forces. *Science* 260: 1451-1456.

93. Ohtani, H., R. J. Wilson, S. Chiang, and C. M. Mate. 6 June 1988. [Scanning tunneling microscopy observations of benzene molecules on the Rh(111)-(3*3)(C/sub 6/H/sub 6/+2CO) surface]. *Phys. Rev. Lett. (USA)* vol.60 (no.23): 2398-401.

94. Parak, F. 5 June 1992. Inter- and intramolecular motions in proteins. *Int. J. Quantum Chem. (USA)* vol.42 (no.5): 1491-8.

95. Parak, F., E. N. Frolou, R. L. Mössbauer, and V. J. Goldanskii. 1981. *J. Mol. Biol.* 145: 825-833.

96. Parak, F., H. Hartmann, K. D. Aumann, H. Reuscher, G. Rennekamp, H. Bartunik, and W. Steigemann. 1987. [Low temperature X-ray investigation of structural distributions in myoglobin]. *Eur. Biophys. J. (West Germany)* vol.15 (no.4): 237-49.

97. Parry, D. A. D., and A. S. Craig. 1981. The molecular structure of collagen. *The Chemistry and Biology of Mineralized Connective Tissues.* A. Veis, 63-77. New York: Elsevier/North- Holland.

98. Perutz MF. 13 August 1992. Protein function below 220 K [letter; comment]. *Nature* 358 (6387): 548.

99. Peterson-Kennedy, S. E., J. L. McGourty, J. A. Kalweit, and B. M. Hoffman. 1986. *J. Am. Chem. Soc.* 108: 1739-1746.

100. Plonsey, R. 1969. *Bioelelectric Phenomena.* 89. New York: McGraw-Hill.

101. Pohl, A. A. 1981. Natural electrical RF oscillation from cells. *J. Bioeng. Biomembr.* 13: 149.

102. Prater, C. B., M. R. Wilson, J. Garnaes, J. Massie, V. B. Elings, and P. K. Hansma. March 1991. Atomic force microscopy of biological samples at low temperature. *J. Vac. Sci. Technol. B, Microelectron. Process. Phenom. (USA)* vol.9 (no.2, pt.2): 989-91.

103. Ramachandran, G. N. 1967. Structure of collagen at the molecular level. *Treatise on Collagen.* G. N. Ramachandran, 103- 179. New York: Academic Press.

104. Ramachandran, G. N., and C. Ramakrishnan. 1976. *Biochemistry of Collagen.* G. N. Ramachandran, and A. H. Reddi, 45-84. New York: Plenum Press.

105. Rasmussen, B. F., A. M. Stock, D. Ringe, and G. A. Petsko. 4 June 1992. Crystalline ribonuclease A loses function below the dynamical transition at 220 K. *Nature* 357: 423-424.

106. Rugar, D., and P. Hansma. October 1990. Atomic force microscopy. *Phys. Today (USA)* vol.43 (no.10): 23-30.

107. Rugar, D., H. J. Mamin, R. Erlandsson, J. E. Stern, and B. D. Terris. November 1988. Force microscope using a fiber-optic displacement sensor. *Rev. Sci. Instrum. (USA)* vol.59 (no.11): 2337-40.

108. Sarid, D. 1991. *Scanning Force Microscopy.*Oxford: Oxford University Press.

109. Scaria, P. V., K. R. Sorensen, and R. S. Bhatnagar. 1990. *Am. Peptide Symp.* 11: 605-607.

110. Shattuck, M. B., M. G. L. Gustafsson, K. C. Yanagimoto, R. S. Bhatnagar, J. Clarke, and K. F. Fisher. 1992. Force microscopy of collagen at 143 K. *Molecular Biology of the Cell* 3: 227.

111. Shattuck, M. B., M. G. L. Gustafsson, K. A. Fisher, K. C. Yanagimoto, A. Veis, R. S. Bhatnagar, and J. Clarke. 1994. Monomeric collagen imaged by cryogenic force microscopy. *Journal of Microscopy* 174: RP1-RP2.

112. Sleator, T., and R. Tycko. 4 April 1988. [Observation of individual organic molecules at a crystal surface with use of a scanning tunneling microscope]. *Phys. Rev. Lett. (USA)* vol.60 (no.14): 1418-21.

113. Smith, D. P. E., J. K. H. Hober, G. Binnig, and H. Nejoh. 1990. Structure, registry and imaging mechanism of alkylcyanobiphenyl molecules by tunneling microscopy. *Nature* 344 (641-644):

114. Smith, D. P. E., H. Horber, C. Gerber, and G. Binnig. 7 July 1989. Smectic liquid crystal monolayers on graphite observed by scanning tunneling microscopy. *Science (USA)* vol.245 (no.4913): 43-5.

115. Smith, S. D. 1974. Effects of electrode placement on stimulation of adult frog limb regeneration. *Annals of the New York Acad. Sci.* 238: 500.

116. Spong, J. K., L. J. ,. J. LaComb, M. M. Dovek, J. E. Frommer, and J. S. Foster. 1 August 1989. Imaging of liquid crystals with tunneling microscopy. *J. Phys. (France)* vol.50 (no.15): 2139-46.

117. Stein, D. L. June 1985. A model of protein conformation substrates. *Proc .Natl. Acad. Sci. USA* 82: 3670-3672.

118. Stopak, D., and A. K. Harris. 1982. *Dev. Biol.* 90: 383-398.

119. Stryer, L. 1988. *Biochemistry*, third ed., New York: W. H. Freeman.

120. Terris, B. D., J. E. Stern, D. Rugar, and H. J. Mamin. 11 December 1989. Contact electrification using force microscopy. *Phys. Rev. Lett. (USA)* vol.63 (no.24): 2669-72.

121. Tilton, R. F., J. C. Dewan, and G. A. Petsko. 1992. Effects of temperature on protein structure and dynamics: X-ray crystallographic studies of the protein ribonuclease-A at nine different temperatures from 98 to 320 K. *Biochemistry* 31: 2469- 2481.

122. Tomaselli, V. P., and M. H. Shamos. 1974. Electrical properties of hydrated collagen. II. Semiconductor properties. *Biopolymers* 13: 2423-2434.

123. Trentham, D. E., R. A. Dynesius-Trentham, E. J. Orav, D. Combitchi, C. Lorenzo, K. L. Sewell, D. A. Hafler, and H. L. Weiner. 1993. Effects of oral administration of type II collagen on rheumatoid arthritis. *Science* 261: 1727-1729.

124. Troyanovskij, A. M., M. Hietschold, M. S. Khaikin, I. Androsch, W. Vollmann, and M. Starke. 15 July 1990. Scanning tunnelling microscopy investigations of organic thin film topography. *Thin Solid Films (Switzerland)* vol.188 (no.2): 329- 33.

125. Uitto, J. et al. 1986. Mechanical and physical functions of the skin. *Scientific Basis of Dermatology.* A. J. Thody, and P. S. Friedmann, 6. London: Churchill Livingstone.

126. Weiner, S., and W. Traub. 1986. Organization of hydroxyapatite crystals within collagen fibrils. *FEBS Lett* 206 (2): 262-266.

127. Weisenhorn, A. L., B. Drake, C. B. Prater, S. A. C. Gould, P. K. Hansma, F. Ohnesorge, M. Egger, S. P. Heyn, and H. E. Gaub. November 1990. Immobilized proteins in buffer imaged at molecular resolution by atomic force microscopy. *Biophys. J. (USA)* vol.58 (no.5): 1251-8.

128. Weisenhorn, A. L., H. E. Gaub, H. G. Hansma, R. L. Sinsheimer, G. L. Kelderman, and P. K. Hansma. September 1990. Imaging single-stranded DNA, antigen-antibody reaction and polymerized Langmuir-Blodgett films with an atomic force microscope. *Scanning Microsc. (USA)* vol.4 (no.3): 511-16.

129. Wigren R, Elwing H, Erlandsson R, Welin S, and Lundstrom I. 25 March 1991. Structure of adsorbed fibrinogen obtained by scanning force microscopy. *FEBS Lett* 280 (2): 225-8.

130. Williams, J., A. Schultz, U. Geiser, K. Carlson, M. Kini, H. Wang, W. Kwok, M. Whangbo, and J. Schirber. 1991. Organic superconductors-New benchmarks. *Science* 252: 1501-1508.

131. Wudl, F. 1984. From organic metals to superconductors: Managing conduction electrons in organic solids. *Acc. Chem. Res.* 17: 227-232.

132. Yang J, Tamm LK, Somlyo AP, and Shao Z. September 1993. Promises and problems of biological atomic force microscopy. *J Microsc* 171 (Pt 3): 183-98.

133. Yannas, I. V. 1972. Collagen and gelatin in the solid state. *J. Macromol. Sci* C7 (1): 49-104.

134. Yasuda, I. 1977. Electrical callus and callus formation by electret. *Clin. Orthop.* 124: 53.

135. Zachariades, P. A. 1900. *C. r. hebd. Soc. Biol.*, Paris vol.52: 182.

136. Zasadzinski, J. A., J. Schneir, J. Gurley, V. Elings, and P. K. Hansma. 1988. *Science* 239: 1013.

Bibliography- Table I-1

1. Albrecht, T. R., M. M. Dovek, C. A. Lang, P. Grutter, C. F. Quate, S. W. J. Kuan, C. W. Frank, and R. F. W. Pease. 1 August 1988. Imaging and modification of polymers by scanning tunneling and atomic force microscopy. *J. Appl. Phys. (USA)* vol.64 (no.3): 1178-84.

2. Amrein M, Durr R, Stasiak A, Gross H, and Travaglini G. 31 March 1989. Scanning tunneling microscopy of uncoated recA-DNA com-

plexes. *Science* 243 (4899): 1708-11.

3. Amrein M, Stasiak A, Gross H, Stoll E, and Travaglini G. 22 April 1988. Scanning tunneling microscopy of recA-DNA complexes coated with a conducting film. *Science* 240 (4851): 514-6.

4. Arscott PG, and Bloomfield VA. August 1990. Scanning tunnelling microscopy of nucleic acids and polynucleotides. *Ultramicroscopy* 33 (2): 127-31.

5. Arscott PG, Lee G, Bloomfield VA, and Evans DF. 8 June 1989. Scanning tunnelling microscopy of Z-DNA. *Nature* 339 (6224): 484- 6.

6. Aviram, A., C. Joachim, and M. Pomerantz. 20 May 1988. [Evidence of switching and rectification by a single molecule effected with a scanning tunneling microscope]. *Chem. Phys. Lett. (Netherlands)* vol.146 (no.6): 490-5.

7. Baro, A. M., R. Miranda, J. Alaman, N. Garcia, G. Binnig, H. Rohrer, Ch. Gerber, and J. L. Carrascosa. 16 May 1985. Determination of surface topography of biological specimens at high resolution by scanning tunnelling microscopy. *Nature (UK)* vol.315 (no.6016): 253-4.

8. Barris B, Knipping U, Lindsay SM, Nagahara L, and Thundat T. October 1988. Images of DNA fragments in an aqueous environment by scanning tunneling microscopy. *Biopolymers* 27 (10): 1691-6.

9. Beebe TP Jr, Wilson TE, Ogletree DF, Katz JE, Balhorn R, Salmeron MB, and Siekhaus WJ. 20 January 1989. Direct observation of native DNA structures with the scanning tunneling microscope. *Science* 243 (4889): 370-2.

10. Bilger, R. H., J. Cantow, J. Heinze, and S. Magonov. 1989. *Proceedings 47th Annual EMSA Meeting*. G. W. Bailey, 16. San Francisco: San Francisco Press.

11. Binnig, G., and H. Rohrer. December 1984. Scanning tunneling microscopy. *Physica B & C (Netherlands)* vol.127B+C (no.1-3): 37- 45.

12. —. August 1985. [The scanning tunneling microscope]. *Sci. Am. (USA)* vol.253 (no.2): 40-6.

13. Blackford, B. L., M. O. Watanabe, D. C. Dahn, M. H. Jericho, G. Southam, and T. J. Beveridge. May 1989. The imaging of a complete biological structure with the scanning tunnelling microscope. *Ultramicroscopy (Netherlands)* vol.27 (no.4): 427-32.

14. Chaing, S., R. J. Wilson, C. M. Mate, and H. Ohtani. 1988. *J. Microscopy* 152: 567.

15. Changhong Luo, Chuanfeng Zhu, Like Ruan, Guizhen Huang, Changchun Dai, Zhengbo Cheng, Chunli Bai, Yaxian Su, Sanduo Xu, Kechun Lin, and J. D. Baldeschwieler. January 1990. Scanning tunneling microscopy of the phosphatidycholine bilayers. *J. Vac. Sci.*

Technol. A, Vac. Surf. Films (USA) vol.8 (no.1): 684-6.

16. Cricenti A, Selci S, Felici AC, Generosi R, Gori E, Djaczenko W, and Chiarotti G. 15 September 1989. Molecular structure of DNA by scanning tunneling microscopy. *Science* 245 (4923): 1226-7.

17. Dahn, D. C., M. O. Watanabe, B. L. Blackford, M. H. Jericho, and T. J. Beveridge. March 1988. [Scanning tunneling microscopy imaging of biological structures]. *J. Vac. Sci. Technol. A, Vac. Surf. Films (USA)* vol.6 (no.2): 548-52.

18. Edstrom RD, Meinke MH, Yang X, Yang R, and Evans DF. 13 June 1989. Direct observation of phosphorylase kinase and phosphorylase b by scanning tunneling microscopy. *Biochemistry* 28 (12): 4939-42.

19. Edstrom RD, Meinke MH, Yang XR, Yang R, Elings V, and Evans DF. December 1990. Direct visualization of phosphorylase- phosphorylase kinase complexes by scanning tunneling and atomic force microscopy [see comments]. *Biophys J* 58 (6): 1437-48.

20. Emch, R., X. Clivaz, C. Taylor-Denes, P. Vaudaux, and P. Descouts. January 1990. Scanning tunneling microscopy for studying the biomaterial-biological tissue interface. *J. Vac. Sci. Technol. A, Vac. Surf. Films (USA)* vol.8 (no.1): 655-8.

21. Engel, A., A. Stemmer, and U. Aebi. 1989. *Proceedings 47th Annual EMSA Meeting*. G. W. Bailey, 12. San Francisco: San Francisco Press.

22. Feng, L., J. D. Andrade, and C. Z. Hu. June 1989. Scanning tunneling microscopy of proteins on graphite surfaces. *Scanning Microsc. (USA)* vol.3 (no.2): 399-410.

23. Fisher KA, Whitfield SL, Thomson RE, Yanagimoto KC, Gustafsson MG, and Clarke J. 30 April 1990. Measuring changes in membrane thickness by scanning tunneling microscopy. *Biochim Biophys Acta* 1023 (3): 325-34.

24. Fisher KA, Yanagimoto KC, Whitfield SL, Thomson RE, Gustafsson MG, and Clarke J. August 1990. Scanning tunneling microscopy of planar biomembranes. *Ultramicroscopy* 33 (2): 117- 26.

25. Foster, J. S., and J. E. Frommer. 9 June 1988. [Imaging of liquid crystals using a tunnelling microscope]. *Nature (UK)* vol.333 (no.6173): 542-5.

26. Foster, J. S., J. E. Frommer, and P. C. Arnett. 28 January 1988. [Molecular manipulation using a tunnelling microscope]. *Nature (UK)* vol.331 (no.6154): 324-6.

27. Fuchs, H., W. Schrepp, and H. Rohrer. March 1987. [STM investigation of Langmuir-Blodgett films]. *Surf. Sci. (Netherlands)* vol.181 (no.1-2): 391-3.

28. Garcia R, Keller D, Panitz J, Bear DG, and Bustamante C. 11 May 1989.

Imaging of metal-coated biological samples by scanning tunneling microscopy. *Ultramicroscopy* 27 (4): 367-73.

29. Gimzewski, J. K., E. Stoll, and R. R. Schlittler. March 1987. [Scanning tunneling microscopy of individual molecules of copper phthalocyanine adsorbed on polycrystalline silver surfaces]. *Surf. Sci. (Netherlands)* vol.181 (no.1-2): 267-77.

30. Guckenberger R, Kosslinger C, Gatz R, Breu H, Levai N, and Baumeister W. 1988. A scanning tunneling microscope (STM) for biological applications: design and performance. *Ultramicroscopy* 25 (2): 111-21.

31. Guckenberger, R., W. Wiegrabe, and W. Baumeister. 1988. *J. Microsc.* 152: 795.

32. Hameroff, S. R., J. Simic-Krstic, M. F. Kelley, M. A. Voelker, J. D. He, E. L. Dereniak, R. S. McCuskey, and C. W. Schneiker. July 1989. Scanning tunneling microscopy of biopolymers: conditions for microtubule stabilization. *J. Vac. Sci. Technol. A, Vac. Surf. Films (USA)* vol.7 (no.4): 2890-4.

33. Horber, J. K. H., C. A. Lang, T. W. Hansch, W. M. Heckl, and H. Mohwald. 25 March 1988. [Scanning tunneling microscopy of lipid films and embedded biomolecules]. *Chem. Phys. Lett. (Netherlands)* vol.145 (no.2): 151-8.

34. Hubacek, J. S., R. T. Brockenbrough, G. Gammie, S. L. Skala, J. W. Lyding, J. L. Latten, and J. R. Shapley. October 1988. Scanning tunnelling microscopy of graphite-adsorbed molecular species. *J. Microsc. (UK)* vol.152, pt.1: 221-7.

35. Keller D, Bustamante C, and Keller RW. July 1989. Imaging of single uncoated DNA molecules by scanning tunneling microscopy. *Proc Natl Acad Sci U S A* 86 (14): 5356-60.

36. Lang, C. A., J. K. H. Horber, T. W. Hansch, W. M. Heckl, and H. Mohwald. March 1988. [Scanning tunneling microscopy of Langmuir-Blodgett films on graphite]. *J. Vac. Sci. Technol. A, Vac. Surf. Films (USA)* vol.6 (no.2): 368-70.

37. Lee G, Arscott PG, Bloomfield VA, and Evans DF. 28 April 1989. Scanning tunneling microscopy of nucleic acids. *Science* 244 (4903): 475-7.

38. Lindsay SM, Nagahara LA, Thundat T, and Oden P. October 1989. Sequence, packing and nanometer scale structure in STM images of nucleic acids under water. *J Biomol Struct Dyn* 7 (2): 289-99.

39. Lindsay SM, Nagahara LA, Thundat T, Knipping U, Rill RL, Drake B, Prater CB, Weisenhorn AL, Gould SA, and Hansma PK. October 1989. STM and AFM images of nucleosome DNA under water. *J Biomol Struct Dyn* 7 (2): 279-87.

40. Lindsay SM, Thundat T, and Nagahara L. October 1988. Adsorbate deformation as a contrast mechanism in STM images of biopolymers in an aqueous environment: images of the unstained, hydrated DNA double helix. *J Microsc* 152 (Pt 1): 213-20.

41. Lindsay, S. M., and B. Barris. March 1988. [Imaging deoxyribose nucleic acid molecules on a metal surface under water by scanning tunneling microscopy]. *J. Vac. Sci. Technol. A, Vac. Surf. Films (USA)* vol.6 (no.2): 544-7.

42. Lindsay, S. M., L. Nagahara, and T. Thundat. 1989. *Proceedings 47th Annual EMSA Meeting*. G. W. Bailey, 36. San Francisco: San Francisco Press.

43. Lindsay, S. M., T. Thundat, and L. Nagahara. 1988. *Biological and Artificial Intelligence Systems*. E. Clementi, and S. Chin, 125. ESCOM Science Publications.

44. Lindsay, S. M., T. Thundat, L. Nagahara, U. Knipping, and R. L. Rill. 2 June 1989. Images of the DNA double helix in water. *Science (USA)* vol.244 (no.4908): 1063-4.

45. McMaster, T. J., H. Carr, M. J. Miles, P. Cairns, and V. J. Morris. January 1990. Adsorption of liquid crystals imaged using scanning tunneling microscopy. *J. Vac. Sci. Technol. A, Vac. Surf. Films (USA)* vol.8 (no.1): 672-4.

46. Michel, B., and G. Travaglini. 1988. *J. Microsc.* 152: 681.

47. Miles, M. J., T. McMaster, H. J. Carr, A. S. Tatham, P. R. Shewry, J. M. Field, P. S. Belton, D. Jeenes, B. Hanley, M. Whittam, P. Cairns, V. J. Morris, and N. Lambert. January 1990. Scanning tunneling microscopy of biomolecules. *J. Vac. Sci. Technol. A, Vac. Surf. Films (USA)* vol.8 (no.1): 698-702.

48. Ohtani, H., R. J. Wilson, S. Chiang, and C. M. Mate. 6 June 1988. [Scanning tunneling microscopy observations of benzene molecules on the Rh(111)-(3*3)(C/sub 6/H/sub 6/+2CO) surface]. *Phys. Rev. Lett. (USA)* vol.60 (no.23): 2398-401.

49. Okumura, A., K. Miyamura, and Y. Gohshi. January 1990. A scanning tunneling microscopy/current imaging tunneling spectroscopy investigation of an organic molecule: 4-cyano-4'-n- heptylbiphenyl. *J. Vac. Sci. Technol. A, Vac. Surf. Films (USA)* vol.8 (no.1): 625-7.

50. Rabe, J. P., S. Buchholz, and A. M. Ritcey. January 1990. Reactive graphite etch and the structure of an adsorbed organic monolayer-a scanning tunneling microscopy study. *J. Vac. Sci. Technol. A, Vac. Surf. Films (USA)* vol.8 (no.1): 679-83.

51. Rabe, J. P., M. Sano, D. Batchelder, and A. A. Kalatchev. 1988. *J. Microsc.* 152: 573.

52. Shattuck, M. B., S. L. Whitfield, R. E. Thomson, J. Clarke, and R. S.

Bhatnagar. 1990. Collagen molecules and aggregates imaged with scanning tunneling microscopy (STM). Fourth Annual Symposium of the Protein Society, San Diego, 1990.

53. Shattuck, M. B., S. L. Whitfield, R. E. Thomson, R. S. Bhatnagar, and J. Clarke. 1990. Scanning tunneling microscopy of native collagen. *Bull. Am. Phys. Soc.* 35: 500.

54. Simic-Krstic Y, Kelley M, Schneiker C, Krasovich M, McCuskey R, Koruga D, and Hameroff S. August 1989. Direct observation of microtubules with the scanning tunneling microscope. *FASEB J* 3 (10): 2184-8.

55. Sleator, T. 1988. *Bull. Amer. Phys. Soc.* 33: 257.

56. Sleator, T., and R. Tycko. 4 April 1988. [Observation of individual organic molecules at a crystal surface with use of a scanning tunneling microscope]. *Phys. Rev. Lett. (USA)* vol.60 (no.14): 1418-21.

57. Smith, D. P. E., H. Horber, C. Gerber, and J. L. Maddocks. 1989. Proceedings of the 4th International Conference on STM, 174. Ibaraki, Japan, 1989.

58. Smith, D. P. E., H. Horber, C. Gerber, and G. Binnig. 7 July 1989. Smectic liquid crystal monolayers on graphite observed by scanning tunneling microscopy. *Science (USA)* vol.245 (no.4913): 43-5.

59. Smith DP, Bryant A, Quate CF, Rabe JP, Gerber C, and Swalen JD. February 1987. Images of a lipid bilayer at molecular resolution by scanning tunneling microscopy. *Proc Natl Acad Sci U S A* 84 (4): 969-72.

60. Spong, J. K., H. A. Mizes, L. J. ,. J. LaComb, M. M. Dovek, J. E. Frommer, and J. S. Foster. 9 March 1989. Contrast mechanism for resolving organic molecules with tunnelling microscopy. *Nature (UK)* vol.338 (no.6211): 137-9.

61. Stemmer A, Hefti A, Aebi U, and Engel A. July 1989. Scanning tunneling and transmission electron microscopy on identical areas of biological specimens. *Ultramicroscopy* 30 (3): 263-80.

62. Stemmer, A., A. Engel, and R. Haring. 1988. *Proceedings 46th Annual EMSA Meeting*. G. W. Bailey, 444. San Francisco: San Francisco Press.

63. Stemmer, A., R. Reichelt, A. Engel, J. P. Rosenbusch, M. Ringger, H. R. Hidber, and H. J. Guntherodt. March 1987. [Scanning tunneling and scanning transmission electron microscopy of biological membranes]. *Surf. Sci. (Netherlands)* vol.181 (no.1- 2): 394-402.

64. Su Ya-Xian, Jiao Yue-Kan, Xu San-Duo, Yao Jun-En, and Lin Ke- Chun. January 1990. The surface structure of artificial and natural membranes as studied by scanning tunneling microscopy. *J. Vac. Sci. Technol. A, Vac. Surf. Films (USA)* vol.8 (no.1): 695-7.

65. Travaglini, G., H. Rohrer, M. Amrein, and H. Gross. March 1987. [Scanning tunneling microscopy on biological matter]. *Surf. Sci. (Netherlands)* vol.181 (no.1-2): 380-90.

66. Travaglini, G., E. Stoll, H. Roher, M. Amerin, J. Sogo, and H. Gross. 1987. Proceedings of the 2nd International Conference on STM, 97. Oxnard, California, 1987.

67. Vidic, B., and L. Nagahara. 1989. Proceedings of the 4th International Conference on STM, 179. Ibaraki, Japan, 1989.

68. Voelker MA, Hameroff SR, He JD, Dereniak EL, McCuskey RS, Schneiker CW, Chvapil TA, Bell LS, and Weiss LB. November 1988. STM imaging of molecular collagen and phospholipid membranes. *J Microsc* 152 (Pt 2): 557-66.

69. Voelker, M., D. He, E. Dereniak, R. McCuskey, C. Schneiker, and S. Hameroff. 1988. *Biophys. J.* 53: 396a.

70. Welland ME, Miles MJ, Lambert N, Morris VJ, Coombs JH, and Pethica JB. February 1989. Structure of the globular protein vicilin revealed by scanning tunnelling microscopy. *Int J Biol Macromol* 11 (1): 29-32.

71. Wu, W. L., and C. M. Lieger. 1988. *J. Phys. Chem.* 92: 5556.

72. Zasadzinski JA, Schneir J, Gurley J, Elings V, and Hansma PK. 26 February 1988. Scanning tunneling microscopy of freeze- fracture replicas of biomembranes. *Science* 239 (4843): 1013-5.

Bibliography- Table I-2

1. Allen MJ, Dong XF, O'Neill TE, Yau P, Kowalczykowski SC, Gatewood J, Balhorn R, and Bradbury EM. 24 August 1993. Atomic force microscope measurements of nucleosome cores assembled along defined DNA sequences. *Biochemistry* 32 (33): 8390-6.

2. Arakawa H, Umemura K, and Ikai A. 9 July 1992. Protein images obtained by STM, AFM and TEM. *Nature* 358 (6382): 171-3.

3. Blackford, B. L., M. H. Jericho, P. J. Mulhern, C. Frame, G. Southam, and T. J. Beveridge. March 1991. Scanning tunneling microscope imaging of hoops from the cell sheath of the bacteria methanospirillum hungatei and atomic force microscope imaging of complete sheathes. *J. Vac. Sci. Technol. B, Microelectron. Process. Phenom. (USA)* vol.9 (no.2, pt.2): 1242-7.

4. Bustamante C, Vesenka J, Tang CL, Rees W, Guthold M, and Keller R. 14 January 1992. Circular DNA molecules imaged in air by scanning force microscopy. *Biochemistry* 31 (1): 22-6.

5. Butt HJ, Downing KH, and Hansma PK. December 1990. Imaging the membrane protein bacteriorhodopsin with the atomic force microscope. *Biophys J* 58 (6): 1473-80.

6. Butt HJ, Wolff EK, Gould SA, Dixon Northern B, Peterson CM, and Hansma PK. October 1990. Imaging cells with the atomic force microscope. *J Struct Biol* 105 (1-3): 54-61.

7. Chang L, Kious T, Yorgancioglu M, Keller D, and Pfeiffer J. April 1993. Cytoskeleton of living, unstained cells imaged by scanning force microscopy. *Biophys J* 64 (4): 1282-6.

8. Chernoff, E. A. G., and D. A. Chernoff. July 1992. Atomic force microscope images of collagen fibers. *J. Vac. Sci. Technol. A, Vac. Surf. Films (USA)* vol.10 (no.4, pt.1): 596-9.

9. Devaud G, Furcinitti PS, Fleming JC, Lyon MK, and Douglas K. September 1992. Direct observation of defect structure in protein crystals by atomic force and transmission electron microscopy. *Biophys J* 63 (3): 630-8.

10. Drake B, Prater CB, Weisenhorn AL, Gould SA, Albrecht TR, Quate CF, Cannell DS, Hansma HG, and Hansma PK. 24 March 1989. Imaging crystals, polymers, and processes in water with the atomic force microscope. *Science* 243 (4898): 1586-9.

11. Durbin, S. D., and W. E. Carlson. August 1992. Lysozyme crystal growth studied by atomic force microscopy. *J. Cryst. Growth (Netherlands)* vol.122 (no.1-4): 71-9.

12. Edstrom RD, Meinke MH, Yang XR, Yang R, Elings V, and Evans DF. December 1990. Direct visualization of phosphorylase- phosphorylase kinase complexes by scanning tunneling and atomic force microscopy. *Biophys J* 58 (6): 1437-48.

13. Egger, M., F. Ohnesorge, A. L. Weisenhorn, S. P. Heyn, B. Drake, C. B. Prater, S. A. C. Gould, P. K. Hansma, and H. E. Gaub. 1990. Wet lipid-protein membranes imaged at submolecular resolution by atomic force microscopy. *J. Struct. Biol.* 103: 89- 94.

14. Fritz M, Radmacher M, and Gaub HE. March 1993. In vitro activation of human platelets triggered and probed by atomic force microscopy. *Exp Cell Res* 205 (1): 187-90.

15. Goettgens, B. M., R. W. Tillmann, M. Radmacher, and H. E. Gaub. 1992. Molecular order in polymerizable Langmuir-Blodgett films probed by microfluorescence and scanning force microscopy. *Langmuir* 8: 1768-1774.

16. Gould, S. A. C., B. Drake, C. B. Prater, A. L. Weisenhorn, S. Manne, G. L. Kelderman, H. J. Butt, H. Hansma, P. K. Hansma, S. Magonov, and H. J. Cantow. August 1990. The atomic force microscope: a tool for science and industry. *Ultramicroscopy (Netherlands)* vol.33 (no.2): 93-8.

17. Gould, S. A. C., B. Drake, C. B. Prater, A. L. Weisenhorn, S. Manne, H. G. Hansma, P. K. Hansma, J. Massie, M. Longmire, V. Elings, B. Dixon Northern, B. Mukergee, C. M. Peterson, W. Stoeckenius, T. R. Albrecht, and C. F. Quate. January 1990. From atoms to integrated circuit chips, blood cells, and bacteria with the atomic force microscope. *J. Vac. Sci. Technol. A, Vac. Surf. Films (USA)* vol.8 (no.1): 369-73.

18. Haeberle, W., J. K. H. Hoerber, and G. Binnig. 1991. Force microscopy on living cells. *J. Vac. Sci. Technol. B.* 9: 1210-1213.

19. Haeberle, W., J. K. Horber, F. Ohnesorge, D. P. Smith, and G. Binnig. 1992. In situ investigations of single living cells infected by viruses. *Ultramicroscopy* 42-44: 1161-1167.

20. Hansma HG, Bezanilla M, Zenhausern F, Adrian M, and Sinsheimer RL. 11 February 1993. Atomic force microscopy of DNA in aqueous solutions. *Nucleic Acids Res* 21 (3): 505-12.

21. Hansma HG, Sinsheimer RL, Li MQ, and Hansma PK. 25 July 1992. Atomic force microscopy of single- and double-stranded DNA. *Nucleic Acids Res* 20 (14): 3585-90.

22. Hansma HG, Vesenka J, Siegerist C, Kelderman G, Morrett H, Sinsheimer RL, Elings V, Bustamante C, and Hansma PK. 22 May 1992. Reproducible imaging and dissection of plasmid DNA under liquid with the atomic force microscope. *Science* 256 (5060): 1180-4.

23. Hansma HG, Weisenhorn AL, Edmundson AB, Gaub HE, and Hansma PK. September 1991. Atomic force microscopy: seeing molecules of lipid and immunoglobulin. *Clin Chem* 37 (9): 1497-501.

24. Hansma, H. G., and P. K. Hansma. 1993. Potential applications of atomic force microscopy of DNA to the human genome project. *SPIC* 1891: 66-70.

25. Hansma, H. G., A. L. Weisenhorn, S. A. C. Gould, R. L. Sinsheimer, H. E. Gaub, G. D. Stucky, C. M. Zaremba, and P. K. Hansma. March 1991. Progress in sequencing deoxyribonucleic acid with an atomic force microscope. *J. Vac. Sci. Technol. B, Microelectron. Process. Phenom. (USA)* vol.9 (no.2, pt.2): 1282-4.

26. Henderson E, Haydon PG, and Sakaguchi DS. 25 September 1992. Actin filament dynamics in living glial cells imaged by atomic force microscopy. *Science* 257 (5078): 1944-6.

27. Hoh JH, Lal R, John SA, Revel JP, and Arnsdorf MF. 20 September 1991. Atomic force microscopy and dissection of gap junctions. *Science* 253 (5026): 1405-8.

28. Hoh JH, Sosinsky GE, Revel JP, and Hansma PK. July 1993. Structure of the extracellular surface of the gap junction by atomic force microscopy. *Biophys J* 65 (1): 149-63.

29. Ikai A, Yoshimura K, Arisaka F, Ritani A, and Imai K. 12 July 1993. Atomic force microscopy of bacteriophage T4 and its tube- baseplate complex. *FEBS Lett* 326 (1-3): 39-41.

30. Ill CR, Keivens VM, Hale JE, Nakamura KK, Jue RA, Cheng S, Melcher ED, Drake B, and Smith MC. March 1993. A COOH-terminal peptide confers regiospecific orientation and facilitates atomic force microscopy of an IgG1. *Biophys J* 64 (3): 919-24.

31. Kasas S, Gotzos V, and Celio MR. February 1993. Observation of living cells using the atomic force microscope. *Biophys J* 64 (2): 539-44.

32. Keller RW, Keller DJ, Bear D, Vasenka J, and Bustamante C. July 1992. Electrodeposition procedure of E. coli RNA polymerase onto gold and deposition of E. coli RNA polymerase onto mica for observation with scanning force microscopy. *Ultramicroscopy* 42-44 (Pt B): 1173-80.

33. Keller, D., J. Hoh, E. Delaine, S. P. Marchese-Ragona, and T. Boland. 1992. Actin Reports. Workshop on STM-AFM and Standard Biological Objects, 38-46. Guilbert, France, 1992. Foundation Fourmentin.

34. Kolbe WF, Ogletree DF, and Salmeron MB. July 1992. Atomic force microscopy imaging of T4 bacteriophages on silicon substrates. *Ultramicroscopy* 42-44 (Pt B): 1113-7.

35. Lacapere JJ, Stokes DL, and Chatenay D. August 1992. Atomic force microscopy of three-dimensional membrane protein crystals. Ca-ATPase of sarcoplasmic reticulum. *Biophys J* 63 (2): 303-8.

36. Lal R, Kim H, Garavito RM, and Arnsdorf MF. September 1993. Imaging of reconstituted biological channels at molecular resolution by atomic force microscopy. *Am J Physiol* 265 (3 Pt 1): C851-6.

37. Lal R, and Yu L. 1 August 1993. Atomic force microscopy of cloned nicotinic acetylcholine receptor expressed in Xenopus oocytes. *Proc Natl Acad Sci U S A* 90 (15): 7280-4.

38. Lindsay SM, Nagahara LA, Thundat T, Knipping U, Rill RL, Drake B, Prater CB, Weisenhorn AL, Gould SA, and Hansma PK. October 1989. STM and AFM images of nucleosome DNA under water. *J Biomol Struct Dyn* 7 (2): 279-87.

39. Lyubchenko YL, Gall AA, Shlyakhtenko LS, Harrington RE, Jacobs BL, Oden PI, and Lindsay SM. December 1992. Atomic force microscopy imaging of double stranded DNA and RNA. *J Biomol Struct Dyn* 10 (3): 589-606.

40. Lyubchenko YL, Oden PI, Lampner D, Lindsay SM, and Dunker KA. 11 March 1993. Atomic force microscopy of DNA and bacteriophage in air, water and propanol: the role of adhesion forces. *Nucleic Acids Res* 21 (5): 1117-23.

41. Lyubchenko Y, Shlyakhtenko L, Harrington R, Oden P, and Lindsay S. 15 March 1993. Atomic force microscopy of long DNA: imaging in

air and under water. *Proc Natl Acad Sci U S A* 90 (6): 2137-40.

42. Masaki N, Machida K, Kado H, Yokoyama K, and Tohda T. July 1992. Molecular-resolution images of aspirin crystals with atomic force microscopy. *Ultramicroscopy* 42-44 (Pt B): 1148-54.

43. Mastrangelo, I. A., M. Bezanilla, P. K. Hansma, P. V. Hough, and H. G. Hansma. February 1994. Structures of large T antigen at the origin of SV40 DNA replication by atomic force microscopy. *Biophys J* 66 (2 Pt 1): 293-8.

44. Murray MN, Hansma HG, Bezanilla M, Sano T, Ogletree DF, Kolbe W, Smith CL, Cantor CR, Spengler S, Hansma PK, and et al. 1 May 1993. Atomic force microscopy of biochemically tagged DNA. *Proc Natl Acad Sci U S A* 90 (9): 3811-4.

45. Niu, L., W. L. Shaiu, J. Vesenka, D. D. Larson, and E. Henderson. 1993. Atomic force microscopy of DNA-colloidal gold and DNA-protein interactions. *SPIC* 1891: 71-77.

46. Ohnishi, S., M. Hara, T. Furuno, and H. Sasabe. November 1992. Imaging the ordered arrays of water-soluble protein ferritin with the atomic force microscope. *Biophys. J. (USA)* vol.63 (no.5): 1425-31.

47. Parpura V, Haydon PG, and Henderson E. February 1993. Three- dimensional imaging of living neurons and glia with the atomic force microscope. *J Cell Sci* 104 (Pt 2): 427-32.

48. Parpura, V., P. G. Haydon, D. S. Sakaguchi, and E. Henderson. July 1993. Atomic force microscopy and manipulation of living glial cells. *J. Vac. Sci. Technol. A, Vac. Surf. Films (USA)* vol.11 (no.4, pt.1): 773-5.

49. Puppels, G. J., C. A. J. Putman, B. G. Grooth, and J. Greve. 1992. Raman microspectroscopy and atomic force microscopy of chromosomal banding patterns. *Proc. LALS* in press:

50. Putman CA, De Grooth BG, Wiegant J, Raap AK, Van der Werf KO, Van Hulst NF, and Greve J. 1993. Detection of in situ hybridization to human chromosomes with the atomic force microscope. *Cytometry* 14 (4): 356-61.

51. Putman, C. A. J., B. G. de Grooth, P. K. Hansma, N. F. van Hulst, and J. Greve. January 1993. Immunogold labels: cell- surface markers in atomic force microscopy. *Ultramicroscopy (Netherlands)* vol.48 (no.1-2): 177-82.

52. Radmacher M, Tillamnn RW, Fritz M, and Gaub HE. 25 September 1992. From molecules to cells: imaging soft samples with the atomic force microscope. *Science* 257 (5078): 1900-5.

53. Radmacher, M., B. M. Goettgens, R. W. Tillmann, H. G. Hansma, P. K. Hansma, and H. E. Gaub. 1991. Morphology of polymerized membranes on an amorphous substrate at molecular resolution by AFM.

AIP Conf. Proc. (USA) (no.241): 144-53.

54. Radmacher, M., R. W. Tillmann, and H. E. Gaub. March 1993. Imaging viscoelasticity by force modulation with the atomic force microscope. *Biophys. J. (USA)* vol.64 (no.3): 735-42.

55. Radmacher, M., R. M. Zimmerman, and H. E. Gaub. 1992. Does the scanning force microscope resolve individual lipid molecules? *The Structure and Conformation of Amphiphilic Membranes*. R. Zipowsky, D. Richter, and K. Kremer, Berlin: Springer.

56. Rasch P, Wiedemann U, Wienberg J, and Heckl WM. 15 March 1993. Analysis of banded human chromosomes and in situ hybridization patterns by scanning force microscopy. *Proc Natl Acad Sci U S A* 90 (6): 2509-11.

57. Rees, W. A., R. W. Keller, J. P. Vesenka, G. Yang, and C. Bustamante. 11 June 1993. Evidence of DNA bending in transcription complexes imaged by scanning force microscopy. *Science (USA)* vol.260 (no.5114): 1646-9.

58. Schabert, F., A. Hefti, K. Goldie, A. Stemmer, A. Engel, E. Meyer, R. Overney, and H. J. Guntherodt. July 1992. Ambient- pressure scanning probe microscopy of 2D regular protein arrays. *Ultramicroscopy (Netherlands)* vol.42-44, pt.B: 1118-24.

59. Schwartz, D. K., J. Garnaes, R. Viswanathan, and J. A. N. Zasadzinski. 24 July 1992. Surface order and stability of Langmuir-Blodgett films. *Science (USA)* vol.257 (no.5069): 508-11.

60. Shaiu WL, Larson DD, Vesenka J, and Henderson E. 11 January 1993. Atomic force microscopy of oriented linear DNA molecules labeled with 5nm gold spheres. *Nucleic Acids Res* 21 (1): 99-103.

61. Shattuck, M. B., M. G. L. Gustafsson, K. A. Fisher, K. C. Yanagimoto, A. Veis, R. S. Bhatnagar, and J. Clarke. 1994. Monomeric collagen imaged by cryogenic force microscopy. *Journal of Microscopy* 174: RP1-RP2.

62. Singh S, and Keller DJ. December 1991. Atomic force microscopy of supported planar membrane bilayers. *Biophys J* 60 (6): 1401-10.

63. Thundat, T., D. P. Allison, R. J. Warmack, M. J. Doktycz, K. B. Jacobsen, and G. M. Brown. July 1993. Atomic force microscopy of single- and double-stranded deoxyribonucleic acid. *J. Vac. Sci. Technol. A, Vac. Surf. Films (USA)* vol.11 (no.4, pt.1): 824-8.

64. Vesenka J, Guthold M, Tang CL, Keller D, Delaine E, and Bustamante C. July 1992. Substrate preparation for reliable imaging of DNA molecules with the scanning force microscope. *Ultramicroscopy* 42-44 (Pt B): 1243-9.

65. Vesenka J, Manne S, Giberson R, Marsh T, and Henderson E. September 1993. Colloidal gold particles as an incompressible atomic force

microscope imaging standard for assessing the compressibility of biomolecules. *Biophys J* 65 (3): 992-7.

66. Weisenhorn AL, Drake B, Prater CB, Gould SA, Hansma PK, Ohnesorge F, Egger M, Heyn SP, and Gaub HE. November 1990. Immobilized proteins in buffer imaged at molecular resolution by atomic force microscopy. *Biophys J* 58 (5): 1251-8.

67. Weisenhorn AL, Gaub HE, Hansma HG, Sinsheimer RL, Kelderman GL, and Hansma PK. September 1990. Imaging single-stranded DNA, antigen-antibody reaction and polymerized Langmuir-Blodgett films with an atomic force microscope. *Scanning Microsc* 4 (3): 511-6.

68. Weisenhorn AL, Schmitt FJ, Knoll W, and Hansma PK. July 1992. Streptavidin binding observed with an atomic force microscope. *Ultramicroscopy* 42-44 (Pt B): 1125-32.

69. Weisenhorn, A. L., M. Egger, F. Ohnesorge, S. A. C. Gould, S. P. Heyn, H. G. Hansma, R. L. Sinsheimer, H. E. Gaub, and P. K. Hansma. 1991. Molecular resolution images of Langmuir-Blodgett films and DNA by atomic force microscopy. *Langmuir* 7: 8-12.

70. Wiegrabe W, Nonnenmacher M, Guckenberger R, and Wolter O. July 1991. Atomic force microscopy of a hydrated bacterial surface protein. *J Microsc* 163 (Pt 1): 79-84.

71. Wigren R, Elwing H, Erlandsson R, Welin S, and Lundstrom I. 25 March 1991. Structure of adsorbed fibrinogen obtained by scanning force microscopy. *FEBS Lett* 280 (2): 225-8.

72. Worcester, D. L., H. S. Kim, R. G. Miller, and P. J. Bryant. January 1990. Imaging bacteriorhodopsin lattices in purple membranes with atomic force microscopy. *J. Vac. Sci. Technol. A, Vac. Surf. Films (USA)* vol.8 (no.1): 403-5.

73. Yamada, H., S. Akamine, and C. F. Quate. July 1992. Imaging of organic molecular films with the atomic force microscope. *Ultramicroscopy (Netherlands)* vol.42-44, pt.B: 1044-8.

74. Yang J, Mou J, and Shao Z. 24 January 1994. Structure and stability of pertussis toxin studied by in situ atomic force microscopy. *FEBS Lett* 338 (1): 89-92.

75. Yang J, Takeyasu K, and Shao Z. 20 April 1992. Atomic force microscopy of DNA molecules. *FEBS Lett* 301 (2): 173-6.

76. Yang J, Tamm LK, Tillack TW, and Shao Z. 20 January 1993. New approach for atomic force microscopy of membrane proteins. The imaging of cholera toxin. *J Mol Biol* 229 (2): 286-90.

77. Zasadzinski JA, Helm CA, Longo ML, Weisenhorn AL, Gould SA, and Hansma PK. March 1991. Atomic force microscopy of hydrated phosphatidylethanolamine bilayers. *Biophys J* 59 (3): 755-60.

78. Zenhausern, F., M. Adrian, B. Ten Heggeler-Bordier, L. M. Eng, and P. Descouts. July 1992. DNA and RNA polymerase/DNA complex imaged by scanning force microscopy: influence of molecular-scale friction. *Scanning (USA)* vol.14 (no.4): 212-17.

II. Materials and Methods

Scanning Tunneling Microscope

The STM used in this study was built primarily by Ruth Ellen Thomson, and basically operates as described in the Introduction. The machine is based on designs by Kaiser and Jacklevic (1987), and Drake et al., (1987), and is fully described in Thomson's dissertation (Thomson, 1991; some of the electronics appear in Ganz, 1988). It was unusual in that it allowed for variable temperature work, operating in a Dewar, and was constructed of invar to minimize thermal drift. The microscope plate was small and rigid, and the Dewar/microscope assembly was mounted in a bell jar on a small laser table, to minimize the effects of building and acoustical vibrations. It used a 12.7 mm (0.5 inch) piezoelectric scan tube after Binnig and Smith (1986), with a diameter of 6.35 mm and a wall thickness of 0.75 mm (PZT 5A). The scan tube had a room temperature response of approximately 120 Å/V laterally (X and Y), as calibrated by resolving the atomic lattice of graphite, and of about 30 Å/V in Z (height). The scanning tip was made from Pt 20 % Rh wire (1 mm diameter), formed by cutting diagonally with a pair of wire cutters. Tunneling bias voltages were supplied by an alkaline battery, and were typically -200 to -400 mV. The electronics were relatively straight forward, using a variable feedback circuit, high voltage op-amp circuits to drive the scanner, analog X and Y ramp generators, electric motor coarse approach, signal amplifier, A to D converter, and an endearing and historical Digital Equipment PDP-11/73 computer for control and data acquisition.

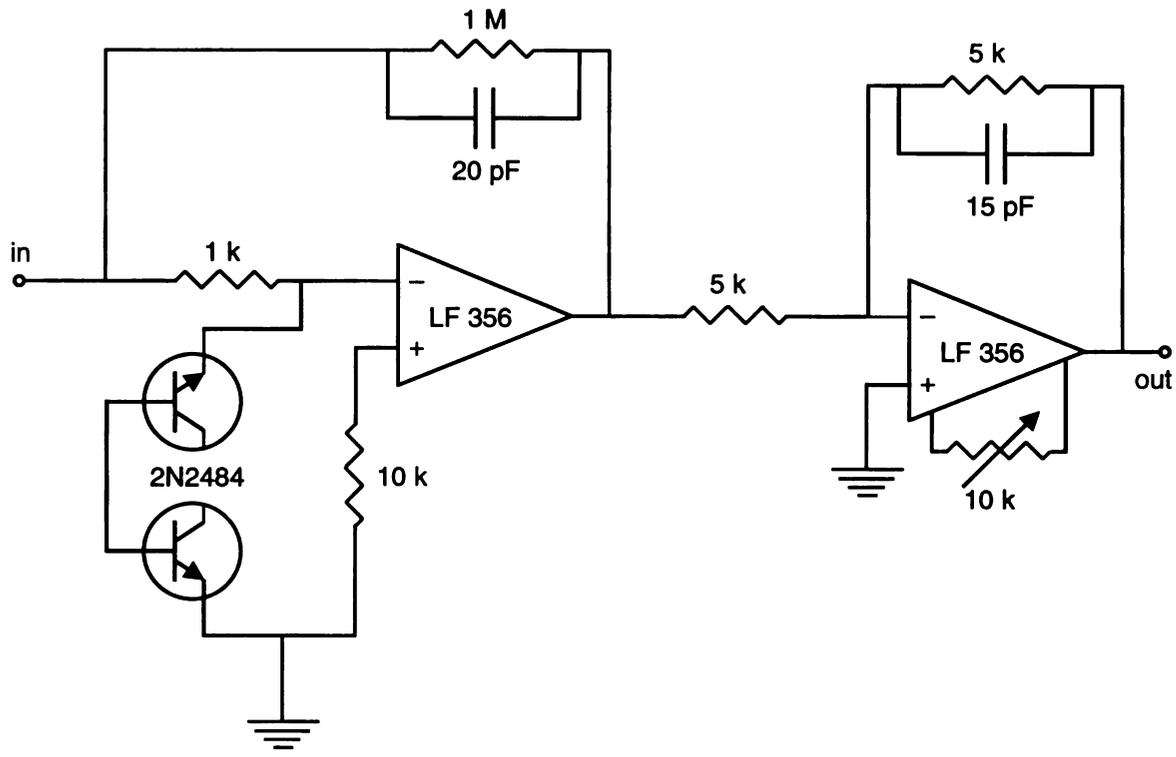

Figure II-1 Redesigned pre-amp circut for STM of biological materials.

For biological work, it is important to work at relatively low tunneling currents, to minimize tip/sample interactions and maximize the signal to noise ratio. Therefore, I improved the original pre-amp circuit as shown in Figure II-1, utilizing a simple current to voltage converter followed by a second gain stage. Additionally, I redesigned and constructed a new tube scanner assembly, incorporating a ground plane between the tip and the high voltage scan tube to minimize noise "pick-up." These modifications resulted in about an order of magnitude increase in the signal to noise ratio. Due to the relatively long lead length between the tip and the pre-amp, the final noise level of this circuit was about 10 mV, which corresponded to an input current of 0.1 nA (or a height of about 0.3 Å). These modifications allowed us to operate at lower currents (about 0.2 nA) and thus larger tunneling gaps, important in minimizing tip disturbances of the sample.

In general, samples for imaging were placed on freshly cleaved highly ordered pyrolytic graphite (HOPG). Cleaving was accomplished by simply applying and removing a piece of cellophane tape, which leaves behind a clean and very flat graphite surface. The material of interest was applied to this conducting surface, and could be imaged in one of two modes. Most commonly, I used the topographic, or "slow mode," in which the tip tracks the sample surface at a constant current. The data signal was thus the feedback signal required to maintain a constant tunneling gap, and the imaging time was limited by the response time of the feedback circuit and the resonant frequency of the scanner assembly. Additionally, some control and surface data were obtained in constant height, or "fast," mode, in which the tip was scanned back and forth at a fixed distance above the sample. In fast mode, variations in the sample surface are now monitored as a change in the tunneling current. While not limited in speed by the time constant of the feedback circuit, fast mode results in greater interaction between the sample and the tip, which can damage the sample surface. This is especially a concern for samples such as collagen which are physically larger than the tunneling gap.

Scanning Force Microscope

Our SFM was originally envisioned by Mats Gustafsson, Knute Fisher, and John Clarke to specifically address the particular difficulties in the scanning of biological materials (see Introduction), which tend to be physically soft and rather loosely bound to the underlying substrate. It was decided to incorporate some rather unusual features not found in commercial machines that might be expected to enhance the quality of our images. It was clear

from previous work that the SFM would operate in a liquid environment to reduce the imaging forces and surface tension effects encountered in working in a room air environment. Similarly, it was hoped that operating the SFM at cryogenic temperatures would increase sample stability and reproducibility, possibly through the mechanism of "freezing" the sample or increasing sample stiffness. Low temperatures would also reduce thermal vibrational modes, and might additionally allow for freeze-fracture studies, which have been particularly successful in producing new information about biological structures in conventional electron microscopic work. These requirements, however, made the design, implementation, actual construction, and use of our SFM quite challenging.

The final configuration of our low temperature SFM (LT-SFM) is depicted in Figure II-2 (Gustafsson, 1993). At the center of the figure is the microscope plate containing the optical detection components, coarse approach walker, scan tube, cantilever, and sample. This SFM stage (shown separately in Figure II-3) is connected by a single mode optical fiber to an external laser diode, operating at 780 nm. Additionally, a wiring harness for signal output, walker pulses, and high voltage scan tube connections is required. The entire plate operates submerged in liquid isopentane surrounded by an n-pentane ice bath. The n-pentane ice bath is contained in a sealed chamber with a "well" in the center, and can thus be cooled with liquid N_2 from outside the apparatus to maintain low temperature. The ice point of n-pentane is 143 K, which is 30 °C above the freezing point of isopentane, minimizing the possibility of freezing the microscope plate. Additionally, isopentane is a hydrophobic nonconductive hydrocarbon, which will not "short out" the high voltage connections and scan tube. The n-pentane ice

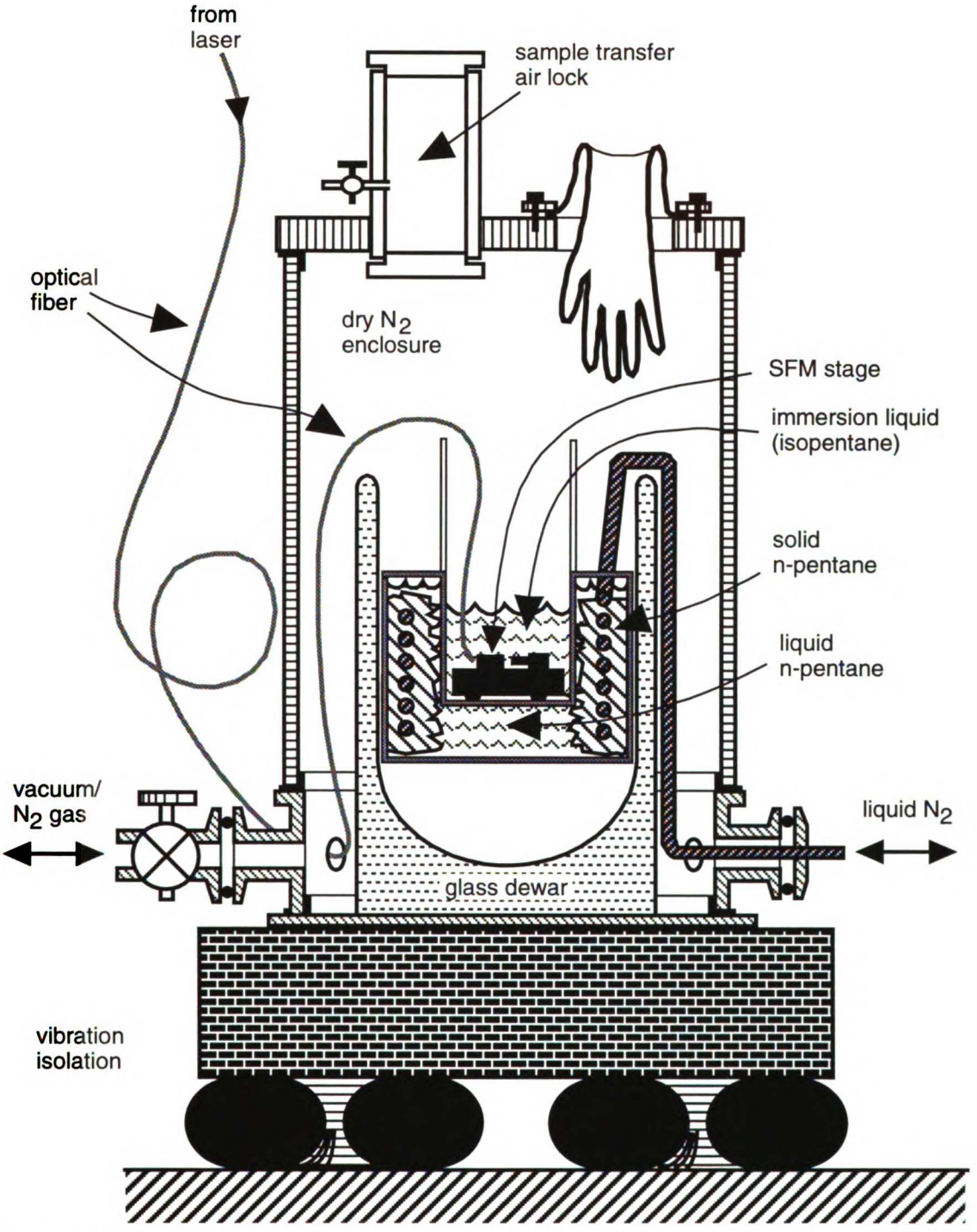

Figure II-2 Cross section of low temperature SFM. Microscope is at center immersed in liquid isopentane. See text for excruciating details. After Gustaffson, 1993.

bath is in turn placed in a covered glass Dewar to minimize heat flow and warming from the environment. The cover consists of a Teflon lid with a

removable port for sample exchange, both covered on the cold side with reflective aluminized mylar. Once equilibrated at 143 K, with a partially solidified n-pentane cooler, the temperature drift of the microscope is less

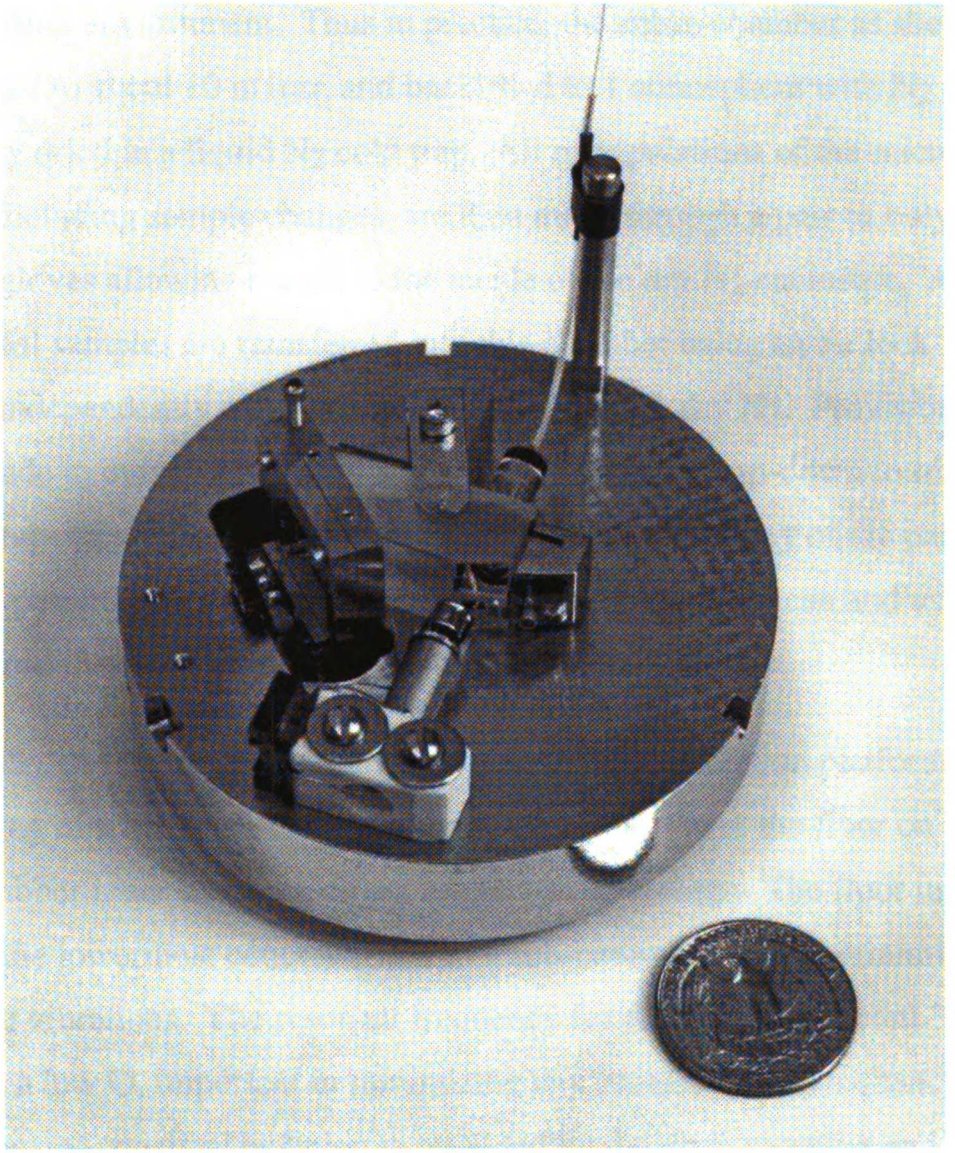

Figure II-3 SFM microscope stage with sample carrier mounted on scan tube.

than 10 mK/minute over a period of about 4 hours. The microscope can be subsequently re-cooled and maintained at 143 K for long periods of time by reintroducing external liquid N_2 to re-freeze the n-pentane bath.

The entire apparatus described operates in a dry N_2 enclosure to minimize the formation of frozen contaminates around the microscope. Any particulates with might interfere with the laser beam are particularly detrimental, and it is paramount to remove as much water as possible from the surrounding environment. Thus in practice, the entire chamber as shown is evacuated to about 10 mTorr, and backfilled to 1 atmosphere with N_2 gas carefully dried in a liquid N_2 cold trap. All manipulations of the microscope, including sample changes, are then made through a pair of butyl rubber gloves allowing access to the inside of the dry N_2 enclosure. Any additional samples are transferred into this chamber using an air lock which can be independently evacuated and backfilled with dry N_2. Provision has been made to outgas both sides of the gloves during pump-down to remove water and contaminates. It is imperative to remove as many of the particulates as possible, as any disturbance in the laser beam light can and usually does cause the cantilever to crash into the sample surface.

Finally, the entire cold system sits on a vibration isolation platform, consisting of a heavy cast concrete base supported above the floor on three small rubber inner tubes which act as pneumatic springs. The floor in this case is the lowermost concrete floor in a sub-basement, which minimizes building vibrations. The resonant frequency for this system is about 3 Hz, and has a low Q, important in minimizing any sustained low frequency vibrations. Acoustical isolation is provided by the glass chamber and by minimizing external noise. During imaging, the chamber is disconnected mechanically from the pumping system and external N_2 tanks.

The heart of the system is the microscope plate, which is depicted schematically in Figure II-4 in a similar orientation as the photograph of Figure

II-3. The base plate itself is a machined 81 mm by 17 mm disk of invar, characterized by it's very low thermal coefficient of expansion. The scan tube assembly, optical prism and photo detector translation stage are mounted with screws or clips as shown.

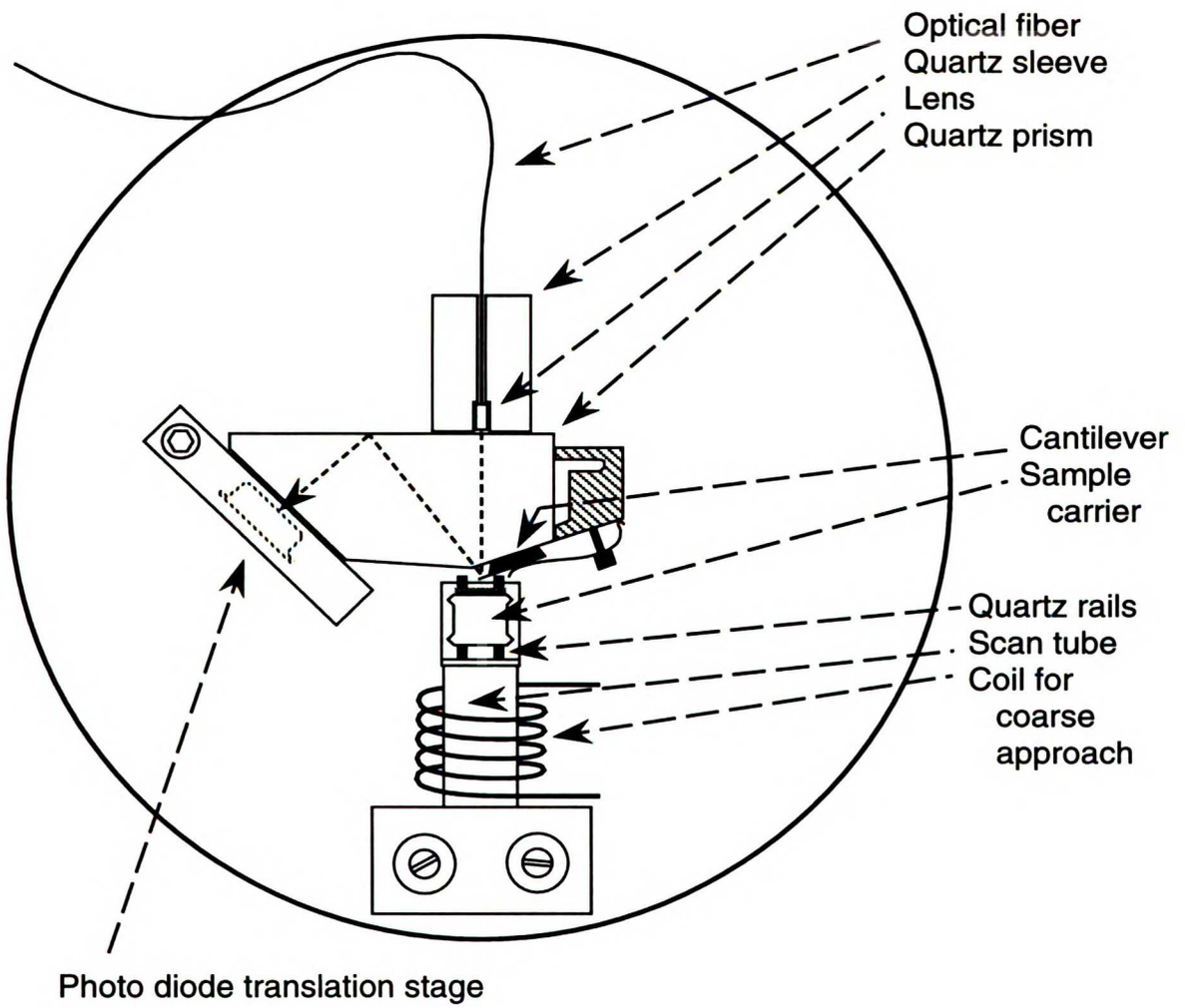

Figure II-4 Schematic of microscope plate shown in previous figure.

For imaging, the sample is mounted on a sample carrier, comprised of a stainless steel thimble containing a rare earth cobalt magnet. This assembly is then loaded from above onto the two quartz rails which are mounted at the end of the scan tube assembly, as depicted in Figure II-5. These rails allow

the sample carrier to be moved axially for coarse approach, and then be scanned laterally by the scan tube during imaging. Coarse approach is made by pulsing the concentric "kicker" coil as shown, much like a solenoid. The pulse duration and amplitude can be varied, and controlled forward and backward steps can be achieved. This coarse walkup is terminated automatically when the cantilever is deflected by a controlled scan tube extension testing cycle. The rails are evaporatively coated with Cr, so that the sample carrier can be grounded to eliminate electrostatic effects between the sample and the tip.

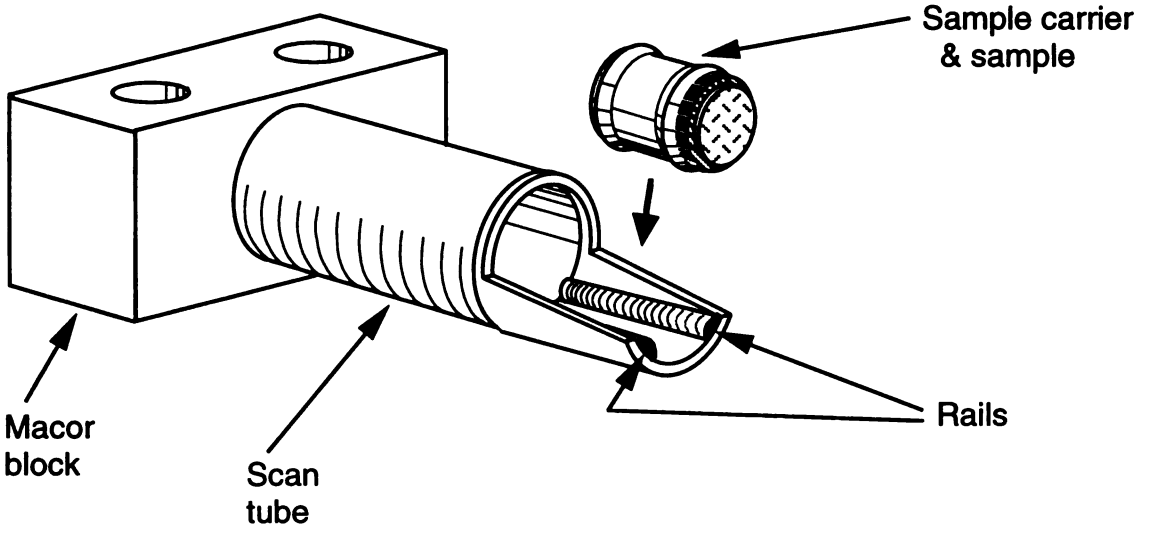

Figure II-5 Scan tube assembly with sample carrier.

The beam from the laser diode enters the microscope through an optical fiber supported by a quartz sleeve (Figure II-4). The fiber terminates in a graded index lens, which focuses the beam on the mirror of the cantilever. From the lens, the light beam (dotted line) passes through the quartz prism, emerges, and is reflected off the cantilever back into the prism. The beam traverses back through the prism, and is reflected off the aluminized rear

surface into the photodetector. It should be noted that this path confines all but about 2 mm of the beam's path to solid materials, which minimizes the light's disturbance due to contaminates or density gradients in the surrounding liquid. This path forms an "optical lever," as deflection of the cantilever results in a relatively large position change at the split photodiode detector. The difference signal from the two sides of this split photodiode is thus related to the force between cantilever and sample. The photodiode is mounted in a translation stage allowing for centering of the laser beam. The cantilever is held against one face of the prism as shown with a beryllium copper spring clip. It is installed and aligned relative to the laser beam at the beginning of each run, and cannot be exchanged when the machine is cold.

The laser beam is supplied by a Sharp LTO23MF0 780 nm laser diode powered by a Sharp IR3CO1 regulator. This is a multi-mode laser, characterized by white noise of a very stable, and therefore desirable, nature. Additionally, the laser has an internal photo-diode which monitors, corrects (via the regulator) and thus keeps constant the beam power. The optical fiber is single mode and transmits 210 uW of power to the graded index focusing lens supplied by NSG America (SELFOC SLW-1.0-25). The photo-diode from Hamamatsu Photonics is a S994-13 quadrant diode, used with two segments connected in parallel, and with a sensitivity of 0.45 A/W at 780 nm. This diode could theoretically be configured as a quadrant detector, allowing for simultaneous measurement of lateral forces (available in several commercial machines).

The cantilevers used in SFM are very important, as they determine the force/deflection characteristics of the system, and their shape typically determines the limit of resolution. An image is a convolution of the structure of

the sample and tip, and if the object of interest becomes smaller than the local structure of the tip, one can be imaging the tip instead of the sample! We used three different cantilevers in our experimental procedures. The majority of my work was done using cantilevers designed and fabricated by Mats Gustafsson (Gustafsson, 1993), which incorporate several unique features.

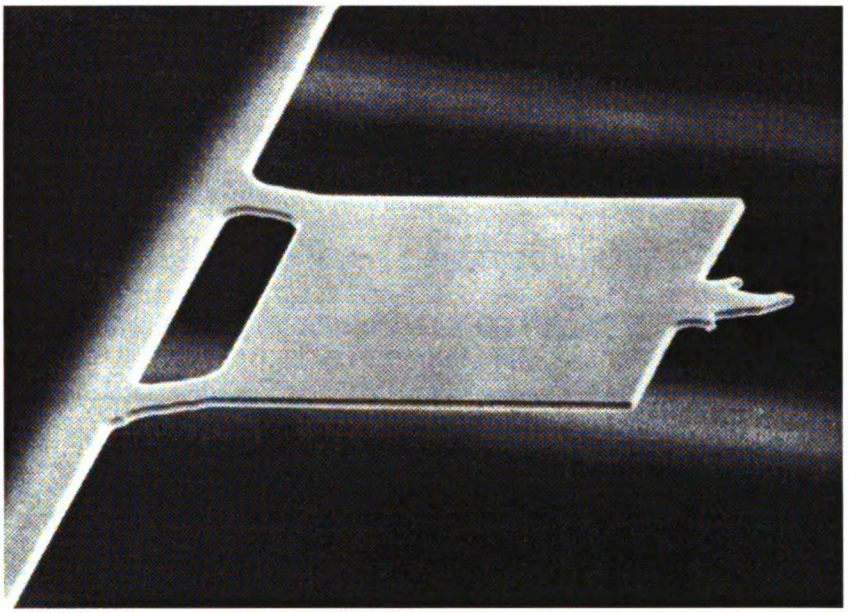

Figure II-6a Cantilever spring (50 μm in length) of Gustafsson's design as typically used in our SFM studies. Note square mirror plate and fractured tip.

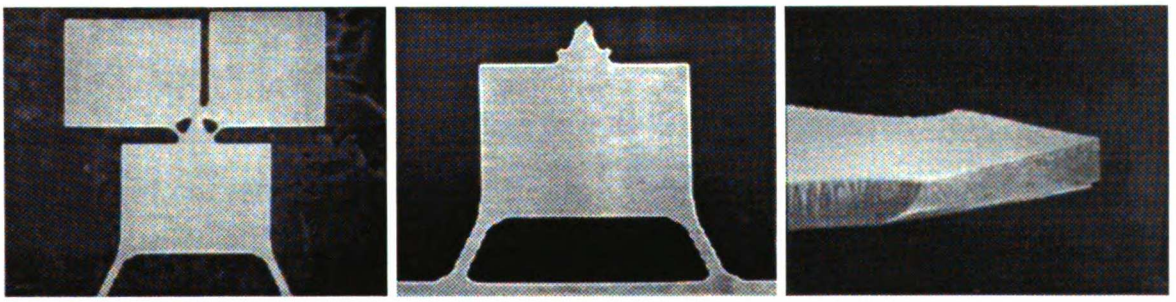

Figure II-6b Cantilever spring is fracture sharpened by removing "break-plates" in left image. Imaging tip is formed by intersection of two lines, shown from side at right.

These cantilevers were made using standard microfabrication techniques, and a large number of tips could be manufactured from a single wafer. The tips were constructed from a 700 nm thick layer of amorphous silicon nitride deposited on a silicon substrate using low pressure chemical vapor deposition. After etching the wafers appropriately, a reflective layer of aluminum was evaporated onto the back side of the tip to form a reflective surface.

Several of the unique features found in these cantilever springs can be seen in Figure II-6. The tip incorporates a large "mirror plate" which reflects the laser beam, and has the advantage of a large reflected signal and improved noise characteristics (Gustafsson & Clarke, 1994; Gustafsson & Clarke, 1990). The legs at the base of the cantilever thus become the "spring." Also unusual is the actual imaging tip itself at the end of the cantilever. This tip is formed by the controlled fracture of two intersecting planes made as the final step in manufacture. This results in a tip formed by the bottom flat surface of the spring, and by the two fracture surfaces, much like the corner of a cube. Although this tip does not protrude from the plane of the cantilever, and therefore is scanned at a 20 degree angle from the sample surface, it is locally quite sharp.

We also used tips modified so that they had a more conventional protruding tip. Using an electron beam process (Ximen & Russell, 1992), GaN tips were grown at the end of the lever by Dr. Phil Russel. These modified tips typically had a shank about 1.0 μm in length with a diameter of 0.1 μm, and a radius of curvature as sharp as 25 nm. This overall tip structure was expected to be advantageous in imaging large scale structures. We also used a commercially available tip, "ultralevers," obtained from Park Scientific (Sunnyvale, California), for a few of our studies.

Our tips were designed by Mats Gustafsson to minimize noise by using a large reflective mirror, as compared to the small triangular mirrors commonly found in the "V" design of most commercial tips. Meyer and Amer (1988) pointed out that the dominant noise source in optical beam deflection designs is due to the photon shot noise of the laser beam. This shot noise is proportional to the length of the cantilever, or spring, divided by the length of the mirror, and thus can be minimized by maximizing the length of the mirror relative to the effective length of the spring. In fact, it is possible for the length of the mirror to exceed the length of the spring by using a torsional design (Gustafsson 1993), and we have demonstrated the feasibility of using such torsional tips on biological samples. However, all of the images reported here were obtained with the three tips previously described. We typically used the fractured tip design described, with a length of 100 μm, a force constant of 0.6 N/m, and a resonant frequency of about 200 kHz. The tip radius is conservatively estimated to be no greater than 10 nm based on scanning electron microscopic examination.

The scanner assembly itself was constructed from a PZT 5A piezoelectric scan tube with a 0.03 inch wall thickness. The overall tube dimensions were 0.5 inches long with a 0.25 inch outer diameter, yielding a lateral scan range of about 3.6 mm and a Z range of 300 nm at room temperature. These ranges were reduced to less than 2.0 μm and 200 nm at 143 K, due to the temperature dependence of the tube material. The scan tube was mounted in a Macor block at one end, and had an aluminum cradle with quartz rails at the other on which we loaded the sample carrier. The scanner assembly imposed a mechanical restriction on scan speed, with a resonant frequency of about 4 kHz. This low frequency was primarily due to the mass of the

sample carrier, which was "cantilevered" off the end of the tube.

An illustration detailing the components of the electrical system is de-

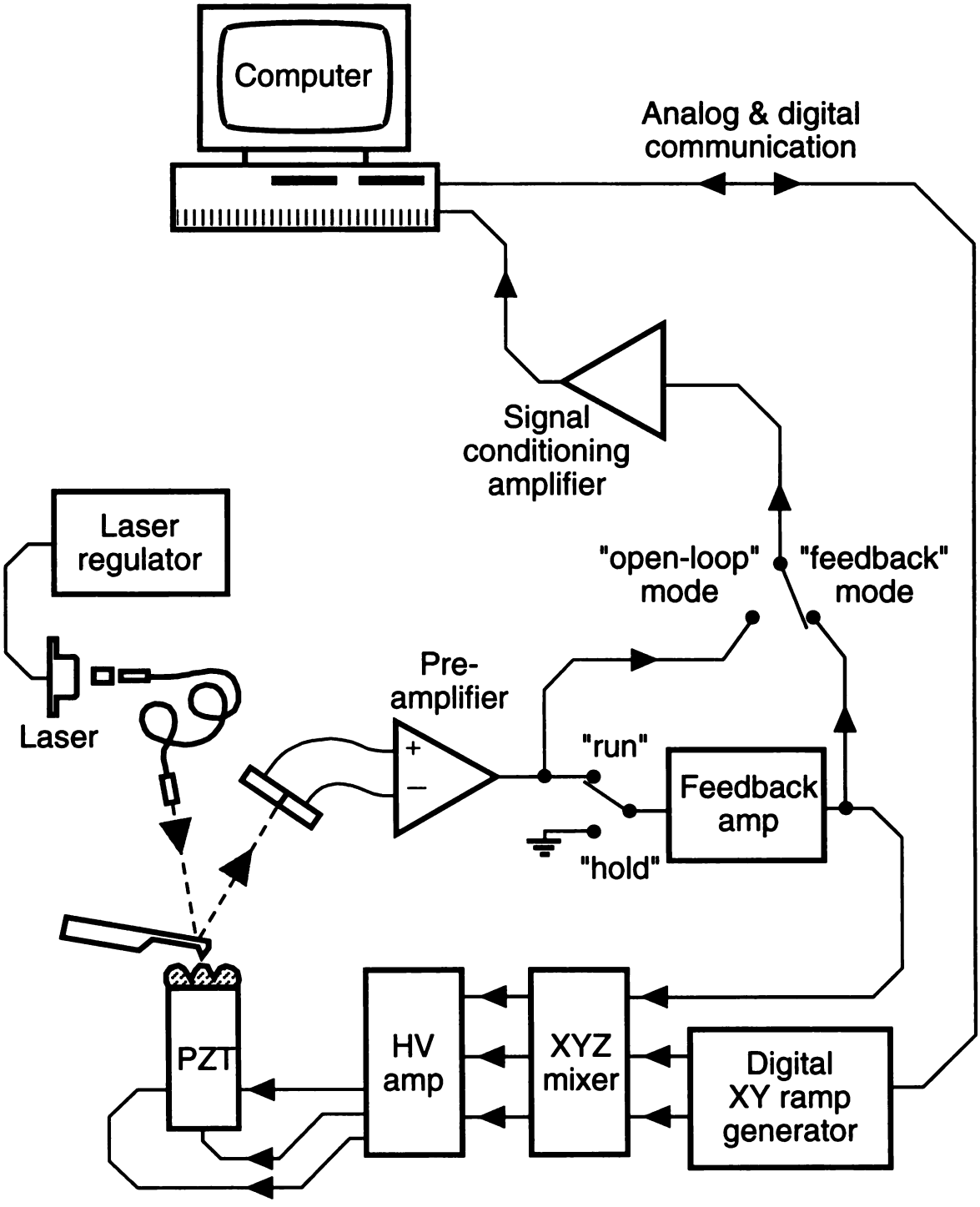

Figure II-7 Schematic of electronics and data acquisition system.

picted in Figure II-7. Several of these components, including the amplifiers, XYZ mixing box (for matching sample and scan planes), and the magnetic walker circuitry (not shown) are fully described in Thomson (1991). Other circuits, including the digital XY ramp generator with XY rotator, low noise FET differential pre-amp, and an interrupt circuit to protect against tip crashes due to particulate interference (not shown), were designed and built specifically for this project (Gustafsson, 1993).

The whole system was controlled by a Mac II computer system and data acquisition hardware (National Instruments Corporation), with eight A/D input channels for monitoring the image signal, ramp size and rotation angle from the ramp generator, and the original preamp signal during initial walkup. Two D/A converters, eight digital I/O channels, and several timers were used to control and communicate with the ramp generator, initiating and resetting data acquisition, and control the magnetic walker box. A maximum data rate, allowing for the capture of a 256 x 256 pixel image in 1.7 seconds, was achieved with the aid of a second plug-in board for direct data to RAM memory access

These functions were all controlled by the custom MacAcquire computer program, which was additionally capable of a wide range of data analysis. The program was particularly useful in that most of the SFM control and data taking functions were mouse controlled. MacAcquire, comprising about 20,000 lines of code, was written by Mats Gustafsson and Marc Hertlein, and was quite remarkable in its elegance and utility. The Mac thus controlled the initial coarse sample walkup, the actual taking of data, data storage, and data manipulation and display.

Other elements not shown consist of the required experimental support elements and the isopentane storage bottle. The entire chamber as shown in Figure II-2 was pumped down by a diffusion pump through a liquid N_2 cold trap. Similarly, dry N_2 for tasks such as backfilling the chamber was supplied from a compressed N_2 gas cylinder through a cold trap. Liquid N_2 for cold traps and for freezing the microscope pentane cooler were supplied from a large liquid N_2 Dewar. Since the entire chamber was evacuated prior to use (in order to outgas as much water as possible), the isopentane was stored inside the chamber in a sealed metal can with a valve and spigot. The isopentane was distilled directly into this storage can, which was chilled in a bath of liquid N_2, from a glass 4 liter bottle of bulk isopentane containing 4 Å molecular sieves. These precautions were all necessary to remove as much water from the imaging fluid as possible, which could form "snow" at cryogenic temperatures. Such water and contamination snow was quite harmful and disruptive to the imaging process. Care had to be taken not to transfer minute particles of the sieves themselves during distillation. After distillation, the pentane bottle was lightly pressurized with dried N_2 gas.

SFM Experimental Protocol

The actual experimental procedure begins with the preparation of the samples, as outlined below, and with the readying of the SFM. The SFM can be used either at low temperature or at room temperature, and for a few experiments we cycled between the two in a single run. Similarly, although designed primarily to image in a liquid, the machine is capable of working in air. Our cryo-SFM is not well suited for working in water (and thus most physiological solutions), due to problems with immersing the high voltage

piezo tube elements.

All procedures began with the installation and alignment of the cantilever. The cantilever's support chip is held against the face of the quartz prism passively with a beryllium copper spring clip tensioned with a small hex screw. The SFM microscope plate is placed in a holding fixture under a dissecting microscope with the scan tube removed. Positioning the chip under the spring clip allows for the alignment of the cantilever relative to the laser beam (set on low power!). For operation in fluids, the laser beam must be appropriately offset relative to the mirror plate of the tip to account for the index of refraction of the liquid. The microscope plate is then removed from it's holding fixture, the scan tube is reinstalled, and the entire plate lowered into the copper well in the pentane cooling chamber, depicted centrally in Figure II-2.

Once the microscope is in position, the pentane storage bottle is placed inside the enclosure along with a few tools. Sample carriers with dry samples, stored in a covered transporter, are generally placed in the enclosure at this point. However, samples stored under fluids, such as required for freeze-fracture, must be transferred into the chamber later. The glove lid is installed, and the entire chamber is pumped down to less than 10 mTorr, usually overnight. The chamber is fitted with external circular plates which are placed on the external side of the gloves, allowing both sides of the gloves to be outgassed simultaneously in a relaxed state. Once the desired vacuum has been achieved, the chamber is valved off and backfilled slowly with dried N_2 gas to atmospheric pressure. This allows the operator to use the gloves to work inside the microscope chamber while maintaining the dry environment inside. The isopentane is transferred from the bottle into the

microscope well, and the well is cooled by introducing external liquid N_2 through the cooling coils in the surrounding n-pentane ice bath chamber. Freezing of the n-pentane in this sealed chamber is monitored with a series of strategically located thermocouples, allowing us to stop the freezing when the can contains a mixture of solid and liquid n-pentane. The temperature of the can and the microscope stage, both located inside the glass Dewar, is allowed to stabilize.

Once the temperature has stabilized, the desired sample carrier is plunged into the isopentane surrounding the microscope stage, and placed on the scanner rails. The position of the photo-diode is optimized by adjusting the translator stage, and the cover is placed on the glass Dewar to minimize heat absorption. The sample carrier is then walked up using the magnetic walker, controlled by the Mac; initial contact is occasionally monitored with a digital storage oscilloscope. An inertial walking mode is available, but has proven less reliable in use. The sample is then scanned. A new area of the same sample can usually be scanned simply by walking back, rotating the sample, and walking forward again (as the tip rarely contacts the exact center of the sample). Samples can be changed while the system is cold, allowing about 20 min for the temperature to re-stabilize.

The temperature is quite stable for several hours, and the machine can be re-cooled indefinitely to extend the experiment. For re-cooling, we back the sample away from the cantilever, as vibrations associated with the reintroduction of liquid N_2 into the cooling coils can crash the tip. We have found, however, that there is a practical limit of a day or two on the length of an experiment, due to the slow accumulation of condensed contaminates in the microscope well. There is also typically a limit due to the finite lifetime of

the tip, which seems to inevitably crash into the sample surface, usually resulting in degradation of the image quality. These crashes are due mostly to "operator error," but are occasionally due to machine glitches. Sample changing involves a reasonable risk of tip damage, aggravated by interaction between the magnetic sample carrier and the invar baseplate. Unfortunately, the cantilever is not replaceable during an experimental run.

Biological samples, which are relatively soft, are typically scanned at as low a force as possible, which for our machine is generally about 0.1 to 0.5 nN. Generally, "constant force" mode is desirable as it produces the most immediately accurate height information, but in our machine typically takes about 5 or 10 minutes per scan. In the interests of time we often use variable deflection mode, with an imaging time of 10 to 20 seconds, although the sample may be exposed to momentarily higher forces. These shorter times further have the advantage that a given image has less chance of being disrupted by particulate interference or by thermal drift effects. While height information is harder to obtain, lateral dimensions are uncompromised.

At the conclusion of the experimental run, the microscope is removed from the well and the isopentane is transferred into an evacuated canister. The residual pentane, which is highly inflammable, is removed by evacuating the chamber through a cold trap. Warming of the microscope well helps evaporate the remaining pentane. The chamber can then be backfilled, and is ready to be set up for another experiment.

A few of our elasticity experiments required imaging the same sample at both 143 K and at room temperature. Following low temperature imaging, the chamber was brought to room temperature over several hours using a

small externally powered resistance heater located at the bottom of the glass Dewar. The sample is walked back prior to heating to minimize the risk of a tip crash due to thermal changes, and can then be re-imaged at room temperature. Such walking usually, but not always, results in imaging a new area of the sample surface. In principle, a sample could be imaged at a whole series of temperature steps. However, thermal drift effects at intermediate temperatures limit the imaging time to a few minutes, after which the sample invariably either drifts out of the scanner's range or the tip crashes into the surface.

Our SFM can be used at room temperature in air or liquid. As previously discussed, we are basically limited to non-conductive liquids without further modification. The room temperature liquid work reported here were either run in pentane, or in hexadecane, which has the advantage of a high boiling point. Hexadecane, with the consistency of a light oil, is messier and requires that the microscope be cleaned before the system can again be used at low temperature. Pentane can be dangerous to work with, since it is inflammable and has potential health effects, and appropriate care must be exercised. It is, however, one of a few liquids which meets the stringent requirements of this application at low temperature.

SFM Calibration

Calibration of our SFM was a critical step in the interpretation of our SFM images. Calibration was complicated by a 50 % reduction in sensitivity of our scan tube material at 143 K, and by a permanent change in tube characteristics due to thermal cycling. The basic lateral XY calibration was

determined by several methods, depending on size range and temperature. Very high magnification scans can be calibrated with images of the known atomic lattices of mica or graphite. For larger scan ranges, we used a cross-ruled "waffle grating" replica (Ted Pella Incorporated), with 21,000 lines per cm. Such gratings are commonly used to calibrate TEMs, and we used them for our TEM work as well. Cross ruled replicas were particularly important for cold calibration, as we were not able to obtain satisfactory images of the mica lattice in pentane at 143 K. This may have been due to a thin layer of contamination or impurities condensing on the mica surface under these conditions, obscuring the atomic lattice.

It was also necessary to correct the scanned images for the inherent non-linearities in the piezoelectric scan tube. These distortions result primarily from slight manufacturing asymmetries in the tube and its nickel contacts, and from hysteretic effects in the scan tube itself. The result is a dimensional variation across the scanned image of up to ± 20 % in X and Y. Furthermore, there are second order effects that distort the scan by "twisting" and "pulling" the apparent image. We determined these various coefficients from scans of the calibration replica grating, and applied them to correct the images with computer sub-routines. We estimate the remaining uncertainty in the lateral dimensions to be generally about ± 5 %. Despite this uncertainty in the absolute calibration, we expect that the uncertainty in the relative dimensions of objects within a given image or groups of images is substantially lower. This of course assumes that the properties of the scan tube do not change on a time scale similar to the imaging time.

We do know, however, that the calibration of the scan tube does change with each thermal cycling. The Å/V sensitivity of the tube is reduced each

time the tube is cooled, possibly due to fatigue of the piezoelectric ceramic. We have found this change to be about 0.25 % per cooldown, and have corrected our data to reflect this. We were not able to include a calibration sample with every experimental run, so we interpolated this correction based on the history of the tube, and our cold calibration data.

Calibration on Mica

The three dimensional calibration of our SFM, along with tip shape, are perhaps the most important factors in interpreting the results of our SFM images. I will consider this problem at two levels of understanding for clarity, in deference to the importance of the calibration problem. First, we will look at the idealized case, where calibration is simply a linear measurement of a known standard. Then we will consider the more complicated actual calibration, incorporating the non-linear behavior of the piezoelectric scan tube. Finally, we will attempt to understand and, at some level, model the problem.

Ideally, of course, we would hope that the calibration of our SFM might be direct, and simply require measuring a known structure to determine the actual sizes of our images, and thus of the dimensions of the sample. One approach is shown in Figure II-8, which are images of the crystal structure of the mica substrate scanned both in air and in hexadecane. The hard, solid state nature of mica, coupled with it's mono-atomic flatness, makes it an ideal calibration standard, even at the relatively high imaging forces typical of work in air. The atomic lattice of mica is visible in these images, particularly in scan B, which is less than 10 nm on a side. These images demonstrate the atomic level capability of our SFM, and raise the possibility of

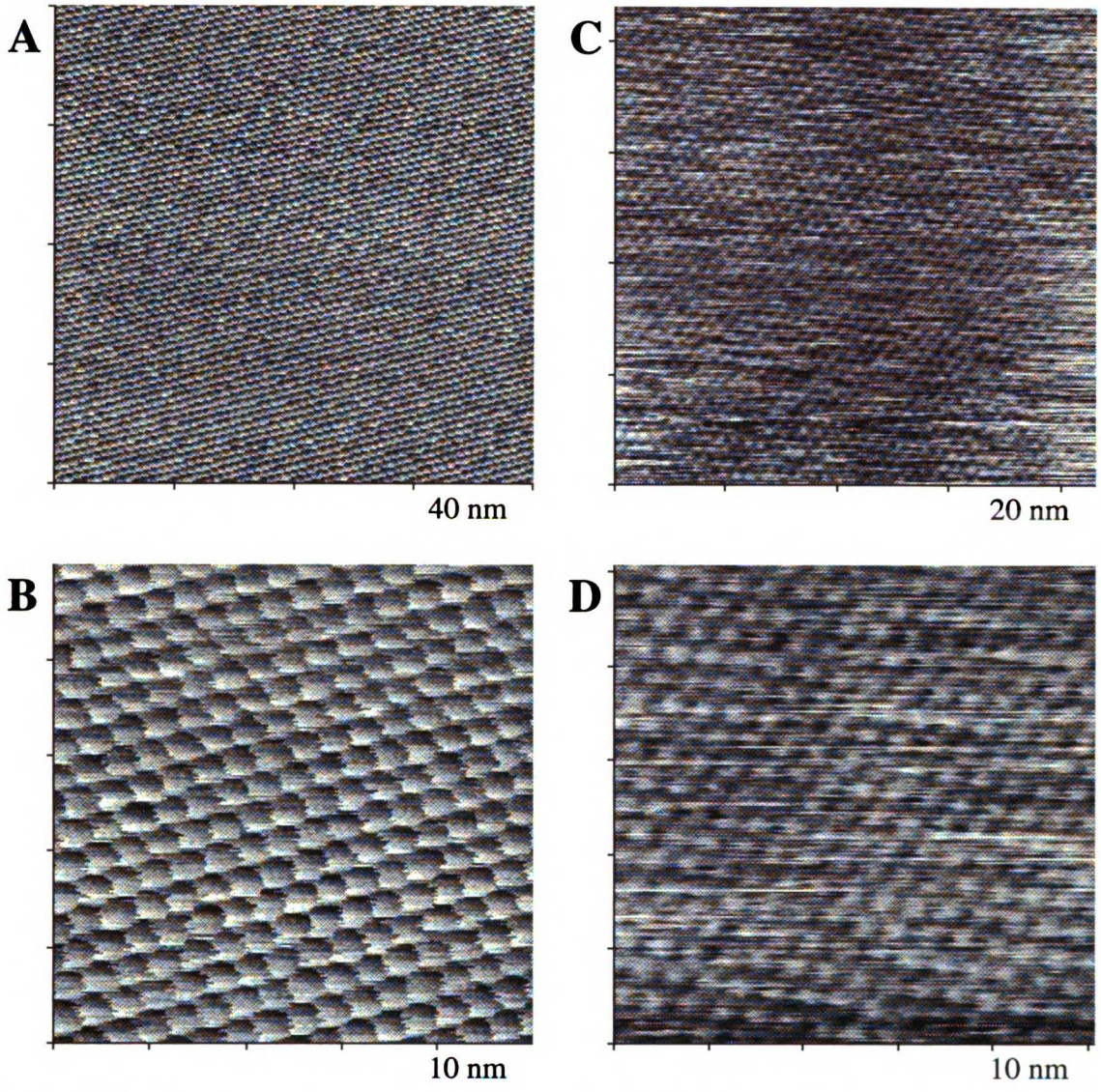

Figure II-8 Mica imaged at room temperature in air (A & B) and in hexadecane (C & D). Total scan size as shown.

using the mica lattice to calibrate the lateral X and Y motion of our scanner. Physically, we are scanning our SFM by applying high voltage ramps to the PZT scan tube. These images of mica, with a lattice spacing of 5.2 Å, gives us the means of calibrating the fixed scan voltages. Calibration becomes simply a problem of measuring the imaged lattice constant in Angstroms for a given scan voltage to arrive at some Å/V calibration coefficient. One would expect this to be useful over small scan sizes where the lattice struc-

ture is clearly resolvable, and not limited by the pixelization of the image, or about 40 – 50 nm, as seen in image A.

Calibration on Cross-Ruled Replica

However, calibration is not so simple, as becomes apparent when we address larger scan sizes. In order to calibrate our SFM at scan sizes of several μm, we used thin film replicas (on copper grids) of a cross-ruled grating, with 21,600 lines per cm, that are routinely used to calibrate TEM magnification. When imaged, they appear as a "waffle" (our own term for the replica grating), with lines 463 nm apart, which is useful for calibrating our largest scan sizes. In order to image these waffles in our SFM, we needed to remount the replicas on the mica sample carriers. Replicas were floated nitric acid, to etch away the underlying copper grid; then cleaned and transfixed to a freshly cleaved mica surface for SFM imaging.

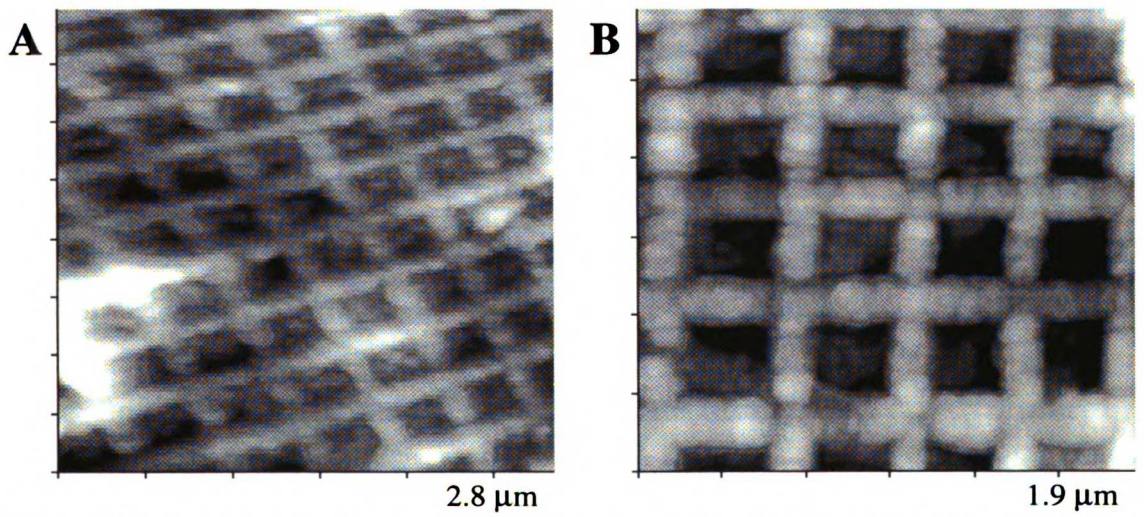

Figure II-9a Scan calibration replicas imaged at room temperature. Line spacing = 463 nm. A is a 10 V scan, B is a 8 V scan.

Examples of SFM images of calibration waffles are shown in Figure II-

9a. A and B are respectively 10 V and 8 V images (actual scan tube voltage 10V x 25 and 8V x 25) at room temperature. These waffles made good calibration standards at this size range and temperature, with a reasonable number of points across the image, and fairly distinct "lattice points." However, close inspection of images A and B reveal a number of image distortions, which make it clear that our simple idealized calibration approach is not very accurate. Image A shows that the lines of the waffle, which in reality are straight, appear to curve in both X and Y. Equally disconcerting is the observation that the uniform "squares" of the waffle in image B appear as different sized objects across the face of the image. Clearly, a simple linear calibration model is insufficient.

These deviations from linearity can be understood from the properties of the PZT scan tube. Our SFM, and indeed most SPMs, use a piezoelectric ceramic (a lead zirconate titanate composite), designated as PZT-5A. Scan tubes constructed of this material have particularly good sensitivity, but have complicated and not completely understood voltage response characteristics. These non-linear characteristics are further compounded by the physical design of the tube in which lateral displacements are created by a "bending" of the tube. The tip therefore actually moves laterally in a slight arc, and not exactly in the plane of the sample (Carr, 1988).

The voltage response characteristics are thus primarily comprised of a number of effects. PZT scan tubes have an intrinsic non-linearity which can range from 2 % to 10 % (Howland, 1994), and are subject to hysteresis effects of up to 15 %. Errors due to hysteresis can be minimized by taking data in only one scan direction for X and Y, although this approach is difficult for Z measurements. More troublesome are time dependent behaviors,

most notably "creep." In response to a scan ramp voltage, or offset voltage, the tube initially responds in milliseconds, but continues creep over a period of 10 – 100 seconds. This is a time comparable with our imaging times, and can introduce errors of about 5 %, particularly in the Y (slower) scan direction. Errors due to creep are sensitive to the "short-term" history of the tube, and can be minimized by allowing the scan tube to equilibrate for a few minutes, particularly after introducing a voltage offset to move to a new area.

There are a number of effects associated with the "long-term" history of the scan tube as well. A scan tube ages with time, and ages differently for different levels of use. We also have observed that the sensitivity of the tube decreases with each cryogenic temperature cycle. These effects seem to mostly depend on changes in the polarization structure of the tube itself, and are very difficult, if not impossible, to predict.

Both the linear and nonlinear calibration parameters are generally dependent on the scan conditions as well as the tube history. They vary in response to scan speed (period), direction, size, and location relative to the overall scan range of the tube. Ideally, one needs to control these factors as closely as possible. Practically, these effects will always introduce some uncertainty in most SFM measurements. Our low temperature SFM has an additional temperature dependence, as seen in Figure II-9b. Images A and B were taken at the same scan voltage as image II-9a B, but at 143 K. There is a substantial reduction in scan size associated with low temperature work, making temperature stability and cold calibration very important.

The net result of these linear and nonlinear effects is substantial, and

must be measured using internal calibration standards. While it is possible to correct for tube non-linearities by independently measuring tube motions in real time (Barrett & Quate, 1991), most systems rely on application software corrections determined from scans of calibration gratings, like the waffle images above.

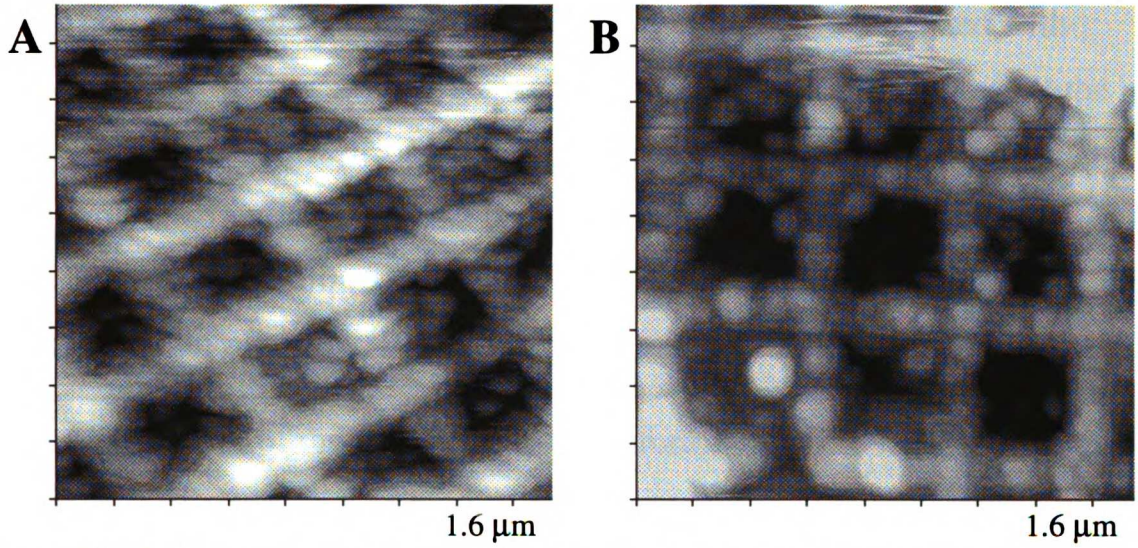

Figure II-9b Calibration waffle imaged at 143 K. Note reduced scan range of tube.

Commercial machines typically correct for non-linear responses by using a simple look-up table. A calibration grid is scanned, and used to create a table of calibration errors that can often be applied to correct the data in real time. Our calibration method relies on a similar technique based on imaging a cross-ruled replica grating, calibrated by diffraction and verified by electron microscopy.

Our method is based on fitting the known lattice points of the waffle grid to a relatively simple second order model of X and Y tube motion and dynamics. We scan the calibration waffle, which represents known points in "real space," to obtain an image of the waffle in "image space." Points in

image space (typically waffle lattice points) are then fit to our model, giving us a transform of these points across the image face back to points in real space. The result of this calibration procedure is a set of calibration parameters applicable to those specific scan conditions including size and period. These calibration parameters are in turn used to correct experimental images obtained under the same conditions. While effective, this procedure is not able to correct for all scan tube effects, particularly those associated with short-term tube history. The largest uncontrolled effect is undoubtedly tube creep, due to recent offsets or to large excursions of the scanner, which can distort an image something like 5 %, particularly in the Y scan direction. This effect can be minimized by allowing the tube to equilibrate for a few minutes after an offset and before taking data, or by taking full-sized scans.

The basic form of the model for the transformation from real space coordinates to the corresponding point in image space is

$$X_r = A_x x + A_{xx} x^2 + A_y y$$

$$Y_r = B_y y + B_{yy} y^2$$

where X_r and Y_r are a physical point in real space, and x and y are the coordinates in image space (Gustafsson, 1993). A_x and B_y are the linear calibration coefficients for X and Y scans respectively, and are all that is required for an ideal linear calibration. The tube non-linearities previously discussed are reflected in the second order x and y terms, A_{xx} and B_{yy}. The final term, A_y, accounts for any "coupling" between y and x scans, which would "skew" the image.

This model is actually a simplification of a fuller, more general transform

including all possible second order terms in X and Y reflected in both X and Y. Several of these terms can be simplified or dropped, or effectively combined, resulting in the transform given above.

The five coefficients for this transform are determined by the operator from images of the calibration waffle using a least squares fit. The MacAcquire program contains several such calibration routines, and the dialog window for this primary calibration is shown in Figure II-10. A previously obtained waffle image (in this example Figure II-9a), with a known lattice spacing, is read into the routine as shown. This image should optimally be controlled for scan period, size, temperature; and to the extent possible, history. The operator then successively picks each lattice point (or any prominent lattice feature) corresponding to the "next lattice point" matrix at the bottom of the screen. Finally, the program returns the best least squares fit of these points to the 5 parameter model discussed. Additionally, the routine produces an angle for the lattice, derived from an angular iteration of the 5 coefficients (and two transitional terms, which are not shown), and a "mean error" of the fit of each lattice point to the resulting transform. This error, and the line overlay of the best fit transform, allows one to evaluate the success of the calibration fit.

The resulting calibration coefficients are then used to transform an object in image space into its appropriate coordinates in real space. This allows for corrected measurement of physical characteristics, such as molecular length, in images obtained under the same conditions. A corrected image of our calibration waffle is seen in Figure II-10, "straightened" by application of the calibration parameters as determined in the dialog box. Notice that the resulting grid image has straight, normal lattice lines, and that the size of

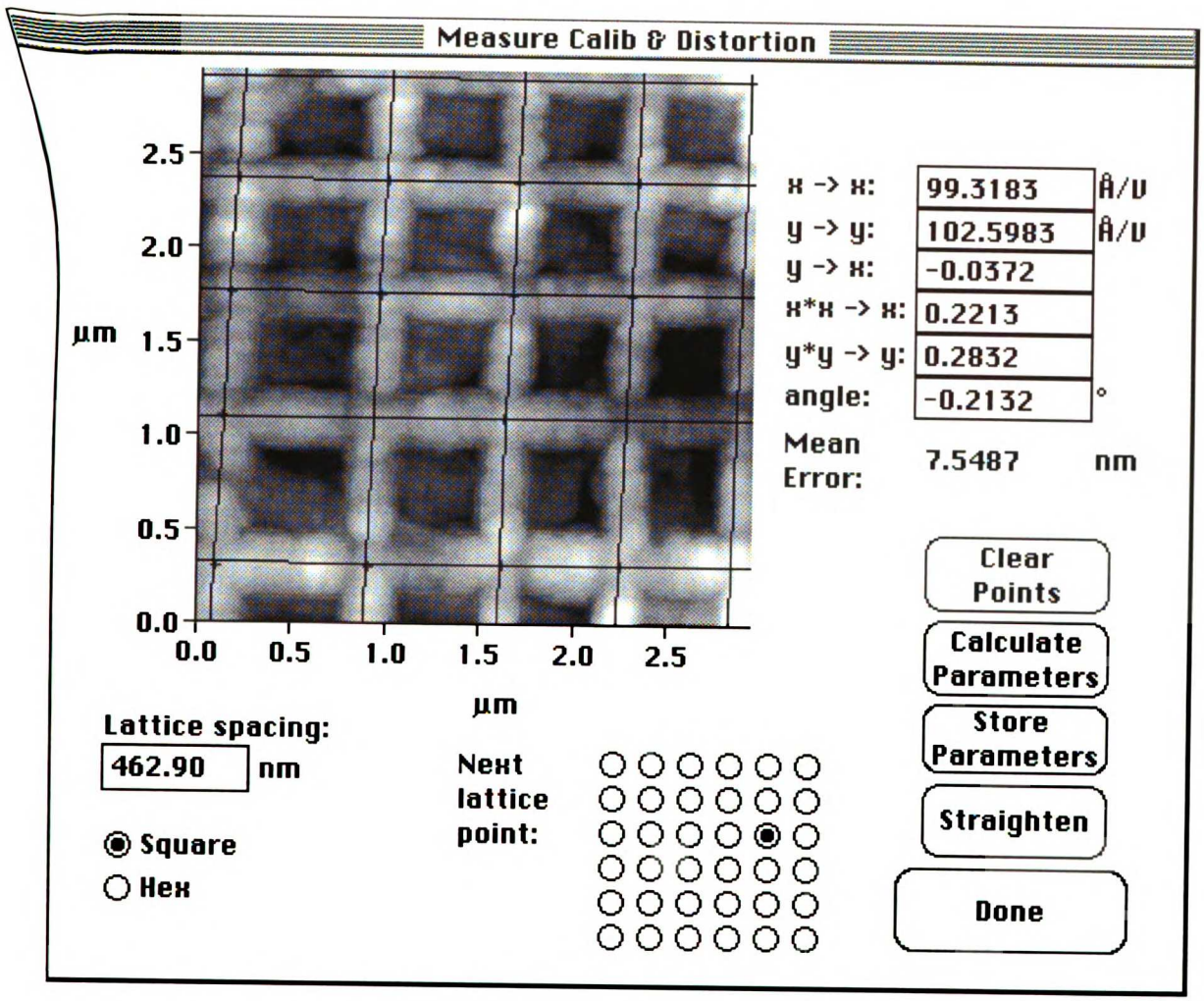

Figure II-10 Dialog box for measuring scan distortions and generating calibration parameters. Corrected image (of Figure II-9a B) is at right.

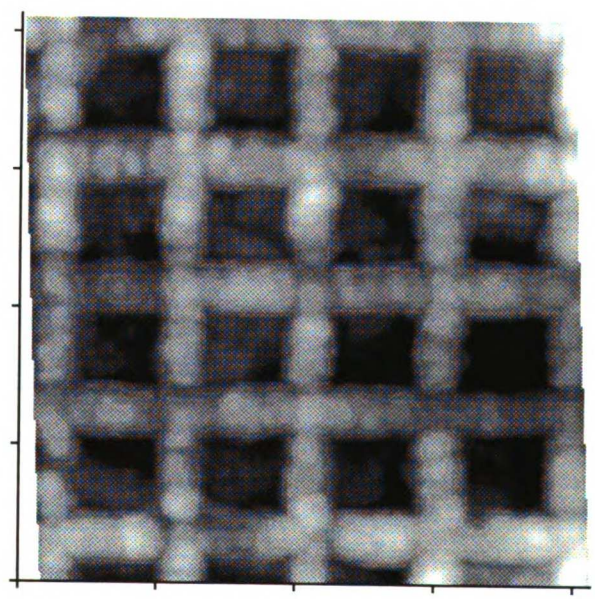

each lattice square is constant over the face of the image.

There are several difficulties to this approach which add uncertainties to the calibration measurement. First is the problem of accurately determining the intersecting lattice points on the rather broad waffle calibration structure. Additionally, the fixed (and large) lattice spacing limits this portion of the calibration to full-size scans (particularly at low temperature) in order to include a reasonable number of lattice points. Repetitive measurements, and the mean error calculation, help in arriving at reasonable calibration coefficients, and some confidence in the fit of the second order model. The distribution of these measurements will be helpful in determining the variability in image dimensions determined with these parameters. More difficult to control is the issue of the short-term use history, primarily reflected as creep. Images can be made after a settling time of several minutes, or several different images (with different histories) can be calibrated to determine the variability introduced by creep. While letting the image stabilize should increase the accuracy of the parameters, repeated images may more accurately reflect real experimental variability. As expected, creep is particularly a problem in the slower Y scan direction.

Calibration coefficients obtained with this procedure are only applicable under similar conditions of temperature, scan speed (period) and scan size. These calibration gratings were not suitable for scan sizes less than full size, and we needed a calibration procedure for smaller scans of 500 nm and 1000 nm in width, encompassing more molecular (collagen) sized dimensions. Mica calibrations were not useful much above 40 nm, and attempts to image some intermediate lattice structure, such as catalase, did not work. As a result, we used a second MacAcquire calibration routine which calculated

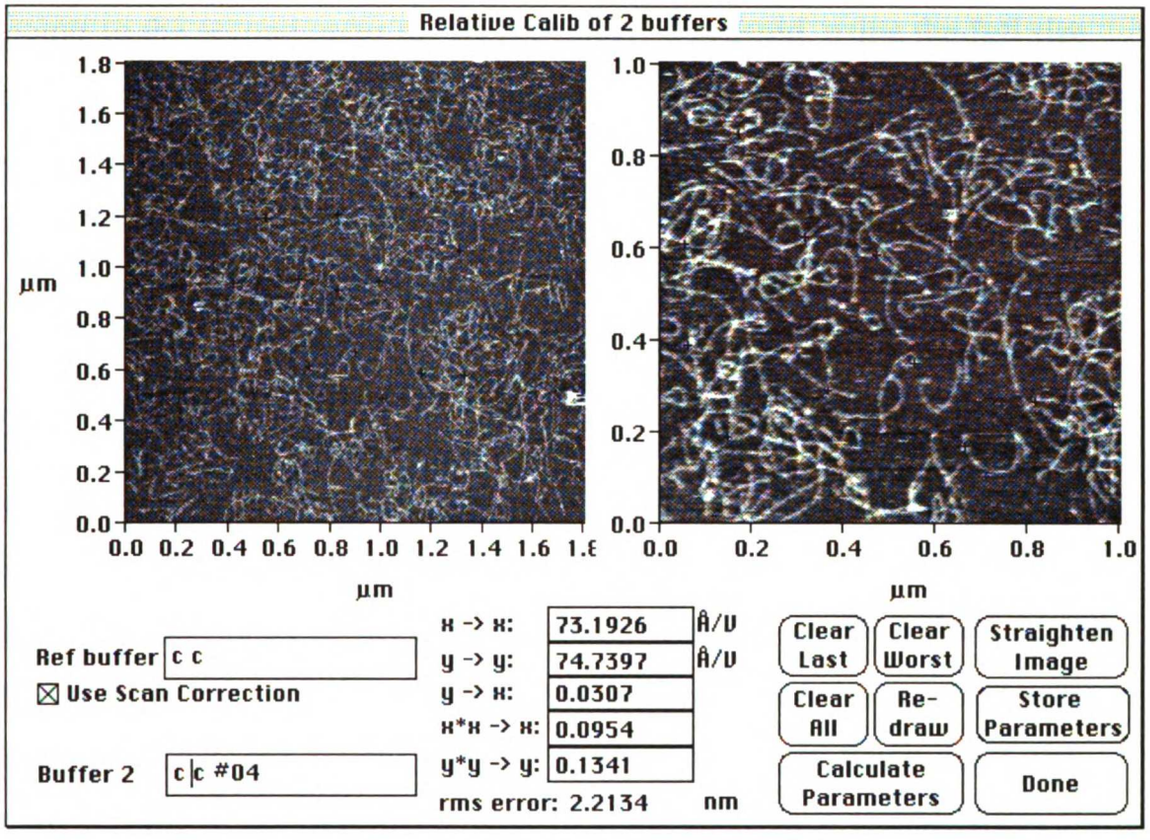

Figure II-11 Relative calibration of two scans, allowing for the determination of the calibration parameters of a small scan based on the coefficients of a full size scan, as in Figure II-10. Individual corresponding points are picked by operator as shown (+).

the relative calibration of two images of different size.

The relative calibration routine allowed us to determine the calibration coefficients for a smaller experimental image based on a full size image taken with known calibration parameters. The full size image, with calibration coefficients determined as above using a calibration waffle, is loaded as a reference buffer. This buffer is the left hand image shown in the MacAcquire dialog box of Figure II-11. A second, smaller experimental image, a subset of the reference image, is loaded on the right side (buffer 2), Using the mouse, the operator then picks corresponding points in both images (shown in the images as black "+" marks). The program refits these

points to the second order model previously discussed, using the full size scan calibration parameters as manually entered. This produces a new set of corrected scan parameters applicable to the smaller scan size of the experimental image. The new calibration parameters can then be further used for other similarly sized experimental scans taken under the same conditions.

The variability in these relative calibration parameters are again indicative of the variability due to the short-term history of the tube, and operator point selection errors. Repeated measurements of a large number of images provide a distribution for each calibration parameter, useful for determining the final uncertainty in any experimental measurement. The relative calibration routine also includes an RMS error statistic (averaged for all fit points) to help evaluate the goodness of fit. The relative calibration routine typically has low RMS fit errors compared to the calibration waffle, primarily due to the increased relative precision of individual point selection. We are able to rely on much smaller and well defined points, such as the intersection of two molecules, compared to the broad and rather ill-defined waffle grating.

Z Calibration

Vertical, or Z, height was more difficult to calibrate due to the difficulty in obtaining precise vertical dimensional changes. An initial calibration was derived simply from the known geometry and properties of the laser/prism/cantilever/photodiode optical system, with surprising accuracy. This was supported with our experience in Z calibration of the STM, which we conducted with a KAMAN magnetic measuring system (Thomsom, 1991). However, the Z behavior of the piezoelectric scan tube was subject to the

same constraints and non-linearities as the lateral calibration parameters. Similarly, we must be as concerned with the resulting variation in Z calibration parameters, or limit our interpretation of height measurements appropriately.

As with our lateral calibration, our Z calibration was based on a well characterized standard. We experimented with several height calibration possibilities, including catalase crystals, before turning to a microfabricated (photolithography) SiO_2 grating. The micro-integrated circuit facility at UC Berkeley provided independent step height measurements of this calibration standard based on profilometry, interferometry and ellipsometry (Gustafsson, 1993).

A single line scan from an SFM image of the SiO_2 grating is shown in Figure II-12a. The steps are 1.2 nm apart, and the previously measured height of each step is 56 nm, allowing us to vertically calibrate the SFM under these scan conditions. Additionally, this single slow scan, with a period of 4.0 sec, demonstrates the vertical piezotube creep and feedback effects analogous to those discussed earlier. The apparent height is seen to change with time after a large vertical deflection, as the feedback circuit compensates for the creep of the scan tube.

This creep can be eliminated by scanning the image in the "hold" or "open loop mode." In this mode, the feedback signal is not applied to the scanner, which now scans laterally at a constant height. However, the imaging force between sample and tip is not constant in this mode, and increases with increasing sample height. The signal is supplied directly by the vertical defection of the cantilever, resulting in the undistorted image of Figure II-

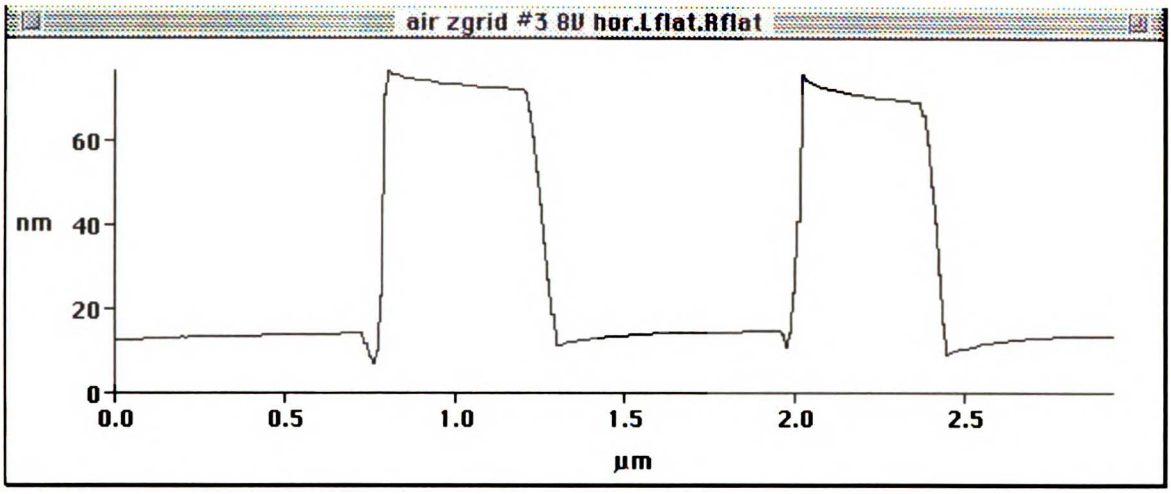

Figure II-12a Single scan through SiO_2 vertical calibration standard. Note non-linear and feedback effects in slow mode.

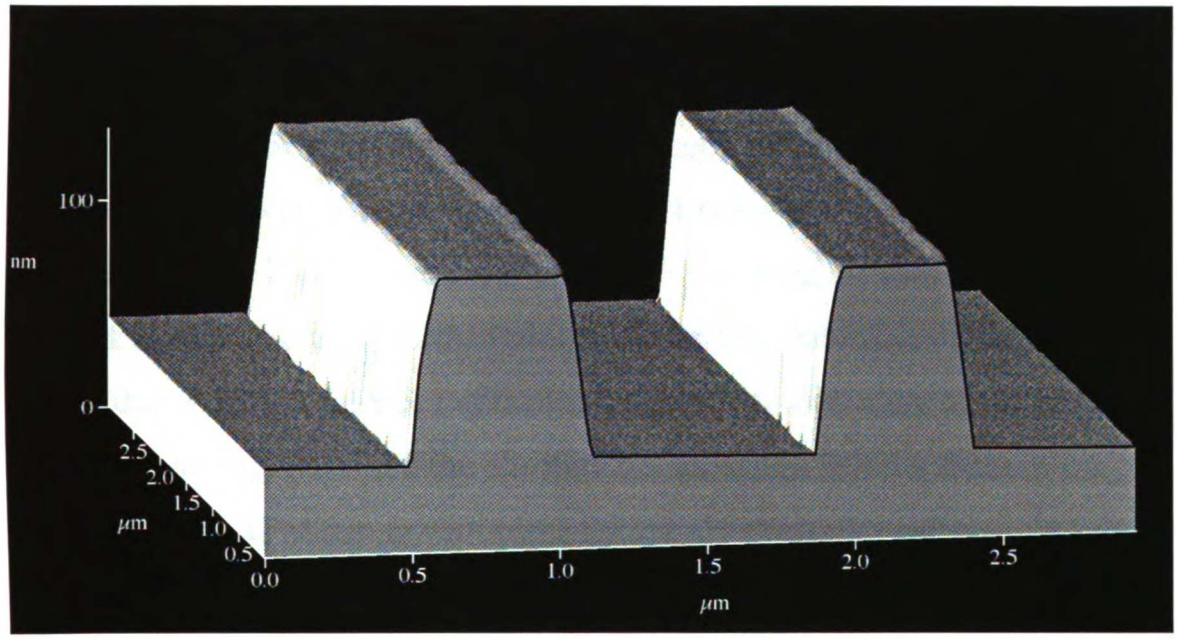

Figure II-12b 3-D view of same standard taken in hold mode. Single line scan (outlined in black at front) is free of the distortions of II-12a above.

12b. This figure is a 3-D projection of a SiO_2 grating image, and the initial X scan, outlined in black, is analogous to the single line scan of Figure II-12a. Images like B can then be used to determine an average Z calibration

over the image surface under the appropriate experimental conditions.

We made no attempt to correct our Z deflections for non-linearities; as a result, we must be careful in interpreting any height information. Absolute heights are therefore subject to significant uncertainties, on the order of 20 %. Relative height comparisons made in a given experiment were more accurate than absolute height determinations. For relative comparisons, these uncorrected parameters were likely to be reasonably constant under the same conditions of temperature, scan speed and scan size. This was true for most of our height difference measurements as they were derived from the same image or series of images. This is not such a stringent limitation, as height uncertainties are inherently a significant and systematic problem in the imaging of relatively soft materials, such as biological materials, where there is sample compression due to finite imaging forces. We will thus refrain from drawing strenuous conclusions from absolute height data. Our low temperature Z calibration was about 19 Å/V, with an uncertainty of about ± 20 %. There are further concerns with the distortion of the sample height due to imaging force interactions, so conclusions must be conservatively drawn. Again, while the absolute uncertainties in Z calibration may be rather high, SFM can nevertheless accurately determine very slight relative differences in height.

STM Sample Preparation

Collagen

Collagen solutions used for all STM investigations were prepared prior to this study. Rat tail tendons were removed from the animal and the type I

collagen was purified using an acetic acid soluble extraction in the presence of protease inhibitors. The resulting collagen solution was characterized using sodium dodecyl sulfate polyacrylamide gel electrophoresis (SDS-PAGE), lyophilized, and stored frozen. Stored collagen was reconstituted in 0.5 N acetic acid at a concentration of 1 mg/ml. This solution was filtered through a 0.22 μm Millipore filter to remove debris, and stored at 4 °C. No further characterization or verification was made of these solutions.

For STM, collagen samples were typically applied to a rectangular piece of HOPG as a conductive substrate. As HOPG is hydrophobic by nature, 20 to 40 % glycerol was added to the final collagen concentration to act as a wetting agent. Alternatively, HOPG surfaces were etched by plasma glow discharge (300 V at 200 mTorr for 5 min) to generate a hydrophilic surface. Collagen STM stock solutions were diluted if necessary with 0.05 N acetic acid. HOPG was freshly cleaved just before each use using cellophane tape, and the desired concentration applied with a disposable pipette tip. The sample was then allowed to air dry at room temperature and then placed in the STM.

SFM Sample Preparation

Monolayers

The central SFM and TEM sample preparation technique involved producing single "monolayers" on flat mica surfaces (Fisher, 1982). Monolayers were used, with some variation, for virtually all of the samples examined, and their preparation was a critical element in the successful imaging of collagen. For SFM, it was particularly important to achieve homogenous,

consistent, and repeatable monolayers over relatively large areas. Green mica sheets (Ted Pella) were punched into 3 mm disks and glued to the stainless steel sample carrier disks using 5 minute epoxy or Stycast. These disks would later be magnetically mounted onto the SFM sample carriers for examination.

Immediately prior to use, the mica surface of the disk was cleaved with cellophane tape to ensure a clean sample surface. The sample of interest was micropipetted (5 µl) onto this freshly cleaved surface, usually for 5 min. During this period, samples were placed in a covered petri dish with a piece of wet filter paper to keep the samples from drying out. This hydration chamber may further be important to control relative humidity during monolayer preparation. After 5 min, the sample was removed using non-magnetic stainless steel tweezers, and washed for 10 sec with glass double distilled water (dd H_2O) from a washbottle. The sample was then gently dried with a stream of N_2 gas, and stored in a sealed petri dish until imaging. Samples were satisfactorily imaged up to a week later, although the best results were obtained when they were examined in a day or two.

As most biological samples other than collagen are negatively charged, they require an additional polylysine step to convert the positive mica surface to anionic substrate (Fisher, 1982). After cleaving the mica surface, it was flooded with 5 µl of a polylysine solution for 30 sec, followed by a 10 sec dd H_2O wash and drying with a burst of N_2 gas. The samples were then applied to this modified surface as described.

Polylysine

Cationic poly-L-lysine was used to promote the binding of negatively

charged samples, such as ferritin, to the negative mica surface (Fisher, 1982). Crystalline polylysine of low molecular weight (short chain length) was obtained from ICN. Working 5 mM solutions were prepared using dd H_2O, and stored at 4 °C.

Ferritin

Ferritin stock solutions were made from 6x crystallized equine spleen ferritin obtained from IC Biochemicals. Typically, a 0.5 ml aliquot was added to 10 ml dd H_2O and sonicated at room temperature for 2 min. This solution was centrifuged at 40,000 x g for 90 minutes at 4 °C, and the central 8 ml of rust colored supernatant (between upper clear, and lower dark regions) was decanted. The supernatant was diluted to an optical density (OD) of 1.34, measured at 270 nm, and stored at 4 °C. Further dilution in dd H_2O was made at the time of sample preparation.

Ferritin monolayer samples were prepared on polylysine-mica. Freshly cleaved mica was first flooded with the polylysine solution for 30 sec. This was followed by a 10 sec dd H_2O wash and N_2 gun dry. 5 µl of the ferritin concentration of interest was immediately applied and allowed to bind for 30 sec. This binding step was ended with a 10 sec dd H_2O wash and N_2 gun dry. Occasionally, ferritin was prepared on mica treated with 1 % alcian blue in dd H_2O, rinsed in dd H_2O, and N_2 gun dried.

Purple membrane

Purple membrane samples were prepared from cultured *Halobacterium halobium* R1 stocks by Kathleen Yanagimoto (Oesterhelt & Stoeckenius, 1974; Fisher, 1982). Single colony isolates, selected for proper color and

morphology, were used to inoculate a 10 ml starter culture. This in turn was used to inoculate 250 ml of complex culture media in 1 L flasks, and incubated at 37 °C under fluorescent illumination for 4 days on a rotary shaker. Each 250 ml culture was then transferred to a 500 ml flask and sealed with Parafilm to reduce oxygen levels and stimulate purple membrane production. Cultures were incubated for an additional 6 days, and harvested.

Purple membrane was harvested from lysed *H. halobium* using sucrose density gradients. Briefly, this technique involved centrifugation of the cultured cells at 6,000 x g for 20 min, followed by resuspension in basal salts containing DNAase I (Sigma Scientific), and dialyzation against 0.1 N NaCl at 4 °C. The lysate was then centrifuged and resuspended several times in 0.1 N NaCl at 28,000 x g. During washing the color of the supernatant changed from pink to light purple. The pellet was spun twice more in distilled water at 40,000 x g, and finally resuspended in a small amount of distilled water and loaded on top of the stepwise sucrose density gradient (30 %, 35 %, 40 % and 50 %). This density gradient was centrifuged at 106,000 x g for 2 hrs. The purple membrane was subsequently recovered from the 40 % band, and dialyzed twice against dd H_2O at 4 °C for 24 hrs. This final purple membrane preparation was characterized by measuring its optical density at 570 nm, and stored at 4 °C.

Purple membrane was adjusted to an optical density of 1.0 (about 3 mg/ml) for SFM sample preparation. 1 µl per mm^2 (5 µl per SFM disk) was micropipetted onto the cleaved mica surface immediately after treatment with polylysine. We allowed the purple membrane to bind to the polylysine surface for 30 sec, removed the excess by washing with dd H_2O for 10 sec, and dried the sample with a burst of N_2 gas. This resulted in a monolayer of

the membrane with a surface coverage of about 50 %.

Several experiments were conducted on purple membrane in which the monolayer surface was never allowed to dry. Samples were transferred and scanned at room temperature in hexadecane. The samples were prepared, transferred and imaged entirely under liquid to diminish possible air drying and surface tension artifacts, and loss of detail. These samples were transferred through an intermediate series of ethanol and/or acetone washes before being stored in hexadecane for transport and imaging.

DNA and RNA

Double stranded DNA and RNA samples prepared on mica surfaces were generously supplied by Dr. Yuri Lyubchenko of Arizona State University. These samples were examples of direct chemical binding of biological materials to an imaging substrate. Mica strips were exposed to 3-diaminopropyl triethoxysilane (APTES), which covalently binds to mica, and effectively "silanates" the anionic surface. These strips were placed in a 0.1 μg/ml solution of reovirus RNA in diluted buffer for 2 hours, washed in deionized H_2O, and dried under vacuum (Lyubchenko *et al.*, 1992). The samples were then sent to us in a dry nitrogen atmosphere, mounted on our sample carriers, and imaged.

Collagen

Type I collagen solutions for use in all SFM and TEM studies were prepared by Dr. Art Veis at Northwestern University. These preparations were particularly pure and well characterized, and alleviated us of many of the difficulties associated with animal work. Importantly, these collagen solu-

tions were obtained from lathyritic rats, resulting in non-crosslinked (and thus highly soluble) intact molecules. The importance of such well characterized samples cannot be overstated, particularly when artifacts are a major concern.

The basic procedure involved extracting type I collagen from the skin of lathyritic rats as reported by Payne and Veis (1988), and outlined here. Weanling rats were fed a normal diet with 0.2 % ß-aminoproprionitrile fumarate in their water as a lathyritic agent. The skins were collected after 6 to 8 weeks, the hair and fat removed, and finally frozen in liquid N_2 and pulverized. This material was extracted for 12 h at 4 °C in a neutral salt solution of 0.3M NaCl and 0.05 M Tris buffer at pH 7.4. A mixture of protease inhibitors was included to minimize any alterations to the collagen molecule, particularly the cleaving of the telopeptides (Miller & Rhodes, 1982).

Collagen was purified from this preparation with a series of salt precipitations. Two initial precipitations were made in 3.5 M NaCl in a neutral phosphate buffer, followed by a third in 0.6 M NaCl in 0.5 M acetic acid. The resulting precipitate was resuspended in 0.1 M acetic acid, dialyzed several times to remove any remaining salt, and centrifuged for an hour at 40,000 x g to remove particulates. The supernatant was removed and stored at -70 °C for future use.

Prior to use, the collagen solution was thawed, dialyzed into a pH 7.4 buffer of 0.062 M Na_2HPO_4 and 0.014 M KH_2PO_4, and again centrifuged as above. The sample concentration was then adjusted to 1 mg/ml using a differential refractometer (Brice & Halwer, 1951). These solutions were shipped to our labs via overnight air packaged on dry ice, where they were

used over a period of about 6 months. If required, this last centrifugation step was repeated to remove any debris or aggregates. All solutions were made, handled and stored at 4 °C. Further dilutions for examination were subsequently made in 0.22 μm filtered 0.05 M acetic acid in HPLC grade water to minimize particulate contamination.

It is important to note that these collagen preparations were well characterized by Dr. Veis. Gel electrophoresis was used to verify that the lathyritic collagen was non-crosslinked type I collagen, with less than 5 % cross-linked α-chains, and a "trace" of type V collagen. Dr. Veis further verified that there were no noncollagenous contaminates using animo acid analysis. I am indebted to Dr. Veis for his generous contribution of these samples.

Collagen samples for SFM experiments were prepared on freshly cleaved mica sample disks as described above for monolayers. 5 μl of the desired solution was applied directly to the anionic mica surface for 5 min, followed by a dd H_2O wash and N_2 gun dry.

Vitrogen (Collagen Corporation) was obtained for use in the collagen GEL studies as a control, and is basically bovine type I collagen. Vitrogen is typically characterized by colorimetric assay for hydroxyproline.

Techniques

Transmission Electron Microscopy

Transmission electron microscopy was used to develop sample preparation methodologies, and to compare and contrast our SFM results. All TEM work was done using a Zeiss EM-10 electron microscope. The EM-10 was

well suited to my requirements due to it's ease of use and consistent micrographs. Micrographs were shot on Kodak film, and all processing and printing was done in our labs.

Samples were prepared for TEM from monolayers as described. Collagen solutions (1 $\mu l/mm^2$) were applied to 2 x 5 mm freshly cleaved mica strips, washed and N_2 dried. These collagen coated mica strips were then rotary shadowed (Schotten *et al.*, 1979) in a vacuum evaporator (Varian VE-61) at 2 x 10^{-6} Torr and a rotational speed of about 100 rpm. Platinum/carbon was evaporated for about 8 sec at an angle of 10 ° to the surface, followed by about 8 sec of carbon shadowing at 90 ° to the sample surface. A few samples, notably purple membrane, were shadowed unidirectionally.

The metal replicas were then separated from the mica surface by floating them off in hydrofluoric acid (HF), typically diluted 1:1 with dd H_2O, and subsequently processed through four separate cleaning and washing steps. First, the replicas were transferred using a platinum loop to a well in a porcelain staining dish that was half-filled with dd H_2O. The remainder of this well was then filled with household bleach using a Pasteur pipette, after which the replica was transferred to a second well, half filled with bleach, for 15 min. The bleach is a cleaning agent, and the initial transfer acted to minimize disruption of the delicate replicas by surface tension effects. Similarly, the cleaning was finished by pipetting dd H_2O into this second well. Finally, the replicas were transferred through two additional washes of dd H_2O for at least 5 min each.

Replicas were picked up from the surface of the last wash step directly onto formvar coated 200 – 400 mesh TEM grids. A Static-Master polonium

strip was used to neutralize the surface charges between the replica surface and the grid, and was helpful in minimizing disruption during this transfer. Grids were stored for TEM imaging in petri dishes. For negative staining, a 5 µl aliquot of the appropriate concentration of the desired sample was micro-pipetted directly onto the surface of a formvar coated grid and imaged immediately after drying.

Polyacrylamide Gel Electrophoresis

Polyacrylamide Gel Electrophoresis (PAGE) in SDS was also used to characterize our collagen solutions, and evaluate our monolayer preparations. Collagen monolayers were prepared on 6 pieces of freshly cleaved mica each measuring 11 x 22 mm. The mica strips were cleaved on both sides to ensure a clean sample for the gel. Each mica strip was flooded with 25 µl of a 10^{-1} mg/ml solution of collagen, roughly calculated to yield a total of about 10 µg of surface bound collagen for all 6 strips. Thus about 2 µg of collagen was applied to the gel. Samples were kept in petri dishes sealed with Parafilm for a short period of time prior to PAGE.

Other control samples were prepared for SDS-PAGE along with the collagen monolayers. The collagen stock solution was applied directly at loads of 1, 2, and 5 µg to compare band migration and density. The same concentrations of Vitrogen were simultaneously elecrophoresed as well. High molecular weight standards from Bio-Rad were diluted to run at 100 ng per band, and 160 ng of ferritin was included as an additional control.

Collagen was extracted from the mica strips by placing the strips in 500 µl of diluted (50 %) gel sample buffer, heating at 70 °C for 3 min, and vigorous vortexing. The final collagen solution was calculated at about 2 µg per

gel lane. The other samples were also heated for 3 min in 70 °C sample buffer prior to being applied to the gels.

A Hoefer (Bio Rad) electrophoresis system was used, with 1.5 mm thick poured gels, and a Kepco power supply. The 5 % separating gels were poured from a solution of 8 ml of lower sample buffer, 5.3 ml polyacrylamide, 18.7 ml distilled water, 160 µl 10 % AP , and 16 µl tetramethylethylenediamine (TEMED). The 4 % stacking gels were made from 4 ml of lower sample buffer, 2.12 ml polyacrylamide, 9.88 ml distilled water, 80 µl 10 % ammonium persulfate (AP), and 8 µl TEMED.

The gel lanes were loaded with the appropriate samples, and electrophoresis initiated at a current of 16 mA. We increased the current to 32 mA after one hour, once the bands had run through the stacker gel. The total gel run-times were about 3.5 hr, and the gels were subsequently fixed in 10 % glutaraldehyde for 30 min. The gels were then silver stained (Poehling & Neuhoff, 1988), typically for about 15 min, during which time the gel was monitored for development of the collagen bands.

SFM Freeze-Fracture

We additionally attempted to examine red blood cell (RBC) membrane monolayers with a modified freeze-fracture technique. Fresh whole blood was washed, centrifuged, and then lysed in 20 miOsM pH 7.4 phosphate buffer (Fisher, 1982a & 1989). RBC vesicles were used to prepare monolayers on both mica strips and glass coverslips. Both monolayers were subsequently characterized using light and transmission electron microscopy to verify vesicle condition and surface coverage. Ultimately, mica proved unsuitable for our freeze-fracture attempt due to it's tendency to cleave

before fracture of the monolayer/ice interface. Our SFM freeze-fracture work was therefor done on glass disks epoxied directly to magnetic sample carriers.

Samples for freeze-fracture were prepared directly on these glass disks. First, we cleaned the glass disk and sample carrier using Isoclean detergent (2 %, 100 °C, 10 min) in a porcelain dish. All implements were cleaned as well. We then applied 4 µl of polylysine to the glass surface for 30 sec, followed by a 30 sec dd H_2O rinse and a N_2 gun dry. 4 µl of RBC vesicles was then applied for 30 sec, followed by a 20 sec rinse in 20 miOsM pH 7.4 phosphate buffer, and then a 10 sec rinse in dd H_2O. The excess liquid was blotted away from the sample carrier, and the glass disk then immediately sandwiched against a cleaned copper hat. The sample-carrier/copper-hat assembly was frozen in a pool of liquid n-pentane cooled by a bath of liquid N_2. Freezing rate is a concern, so we placed the sample into the n-pentane copper hat first. The frozen sample carrier was then transferred onto a holder in a liquid N_2 Dewar for transport to the SFM.

Transfer and fracturing of the sample in the SFM was tricky but actually worked quite well. Experimental setup was as described above, with a few modifications. We prepared the SFM for a cold run, and transferred the freeze-fracture sample into the chamber after it had been backfilled with dry N_2 gas as follows. The sample carrier was transferred (in a pool of liquid N_2) into a small machined copper box, and then into a small Dewar containing an aluminum block to act as a "cold sink," with a small quantity of liquid N_2. The external walls and lip of the Dewar were preheated with a heat gun, to reduce water condensation and minimize the introduction of water into the dry glove chamber. We then placed this Dewar into the sample transfer air

lock, and evacuated the lock through a separate port. This not only removed the air, and moisture, from the air lock, it also helped boil (in combination with a resistive heater) the liquid N_2 in the Dewar, further flushing out the air lock and cooling the sample. The air lock was backfilled with dry N_2 gas, opened, and the Dewar placed into the main chamber. The copper box was placed into the microscope well where it was covered by the 143 K pentane. The cover from the box was removed, allowing us to detach the copper hat from the glass sample disk/carrier using a razor blade on a long handle. This freshly freeze-fractured sample could then be placed on the scan tube for imaging, having remained completely submerged in the isopentane.

Initially we had difficulty with the static charge separation generated during sample cleaving. High attractive forces were then produced between the sample and the tip. This made imaging impossible, and we even resorted to attempting to neutralize the charge using ionizing radiation. The solution ultimately was to simply distill n-propanol with the isopentane to render it very slightly conductive. This allowed the charge to dissipate into the microscope well. We found that about a 10 % propanol mixture worked well, and that the conductivity was low enough that we had no problems with the high voltages associated with the tube scanner. Additionally, we found that the propanol had the added benefit of allowing the isopentane mixture to absorb some of the contaminating moisture, lessening imaging problems associated with "snow."

Image Processing

Image processing is currently widely used in SPM investigations, prima-

rily to improve the visual quality of the images to the viewer. Such processing techniques are also important in the characterization of image features. The range of processing techniques extends from simple high and low pass filtering (which occurs to some extent during scanning due to hardware limitations), to techniques in the frequency domain, such as Fourier transforms. I have elected to keep all such image processing to a minimum for a number of reasons.

The foremost reason to limit image processing is to limit the enhancement or introduction of misleading elements in the scanned images (Howland, 1994). The Fourier transform, for example, can be inadvertently used to "enhance" periodic structures that in fact do not exist, by selecting the appropriate random noise contributions in the frequency domain. A problem with image processing, like artifacts, is that the operator may, consciously or unconsciously, attempt to bias the process to match an expected result. An easy way to avoid unforeseen errors due to the over processing of images is to avoid it without a clear reason for its use.

Our data are generally of sufficiently high quality that image processing really is not needed. This is particularly true for the collagen scans, which so far have no consistent visible periodic component. Interestingly, the human eye (and brain) seems to automatically apply its own "image processing," and it appears to be quite effective in maximizing the image quality to the viewer. As a result, I have basically made only a few changes to the images reported here, in an effort to maximize the gray scale available for the features of interest.

Our images were initially experimentally taken with about 100 shades of

gray to represent the "height" (or force for SFM) of each pixel across a 256 x 256 pixel image. This image is often flattened to maximize the gray scale values of the feature of interest relative to the flat mica background. This mica background often appears tilted due to drift and creep effects in the piezoelectric scan tube, or due to an actual tilt of the sample relative to the plane of the scan. Occasionally, the height of the background will suddenly change from one X scan to the next, probably due to a change in the tip or transient interference in the laser beam as it passes through the liquid to the cantilever. The MacAcquire computer program contains a number of least squares routines to flatten the overall background and maximize the gray scale variation of the sample features.

Similarly, the gray scale can be linearly transformed to enhance the sample structures. This involves simply compressing the gray scale over a limited range encompassing the features. Larger "features" or "holes," due to the presence of contaminates and sticking between the cantilever and the surface, are saturated at the ends of the gray scale. Such "histogram equalizations" dramatically improve the local visibility of structural details, but does alter the relationship between image brightness and sample height (Russ, 1992, an excellent image processing handbook). Individual X scan glitches can additionally be removed from the scanned image. In effect, these image modifications act to redistribute the available gray scale over the object of interest in a linear fashion, allowing us to control the image contrast and brightness.

Bibliography

1. Barrett, R. C., and C. F. Quate. June 1991. Optical scan- correction system applied to atomic force microscopy. *Rev. Sci. Instrum. (USA)* vol.62 (no.6): 1393-9.

2. Binnig, G., C. F. Quate, and C. Gerber. 3 March 1986. [Atomic force microscope]. *Phys. Rev. Lett. (USA)* vol.56 (no.9): 930-3.

3. Binnig, G., and H. Rohrer. August 1985. [The scanning tunneling microscope]. *Sci. Am. (USA)* vol.253 (no.2): 40-6.

4. Binnig, G., and D. P. E. Smith. August 1986. [Single-tube three-dimensional scanner for scanning tunneling microscopy]. *Rev. Sci. Instrum. (USA)* vol.57 (no.8, pt.1): 1688-9.

5. Brice, B. A., and M. Halwer. 1951. *J. Opt. Soc. Am.* 41: 1033-1037.

6. Carr, R. G. 1988. Finite element analysis of PZT tube scanner motion for scanning tunneling microscopy. *J. of Microscopy* 152 (2): 379-385.

7. Drake, B., R. Sonnenfeld, J. Schneir, and P. K. Hansma. March 1987. [Scanning tunneling microscopy of processes at liquid-solid interfaces]. *Surf. Sci. (Netherlands)* vol.181 (no.1-2): 92-7.

8. Fisher, K. A. 1989. Monolayer freeze-fracture and scanning tunneling microscopy. *Journal of Electron Microscopy Technique* 13: 355-371.

9. —. 1982. Preparation of planer membrane monolayers for spectroscopy and elecrton microscopy. *Methods in Enzymology* 88: 230-235.

10. Fisher, K. A., and K. C. Yanagimoto. 1986. Effect of membrane splitting on transmembrane polypeptides. *J. Cell Biology* 102: 551-559.

11. Ganz, E. D. 1988. Ph.D. diss., University of California, Berkeley, Berkeley, California.

12. Gustafsson, M. G. L. 1993. A Low Temperature Scanning Force Microscope for Biological Samples. Ph.D. diss., University of California, Berkeley, Berkeley, California.

13. Gustafsson, M. G. L., and J. Clarke. 1990. Bull. Am. Phys. Soc., 760.

14. —. 1994. SFM springs optimized for optical beamdiflection and with tips made by controlled fracture. *J. App. Phys.* 76 (1): 172-181.

15. Howland, R. S. 1994. *How to Buy a Scanning Probe Microscope*. Sunnyvale, California: Park Scientific Instruments.

16. Kaiser, W. J., and R. C. Jaklevic. April 1987. [Direct observation of an ordered step surface reconstruction on Au(111) by scanning tunneling microscopy]. *Surf. Sci. (Netherlands)* vol.182 (no.3): L227-33.

17. Lyubchenko YL, Jacobs BL, and Lindsay SM. 11 August 1992. Atomic force microscopy of reovirus dsRNA: a routine technique for length measurements. *Nucleic Acids Res* 20 (15): 3983-6.

18. Meyer, G., and N. M. Amer. 1988. Novel optical approach to atomic force microscopy. *Appl. Phys. Lett.* 53 (12): 1045-1047.

19. Miller, E. J., and R. K. Rhodes. 1982. *Methods in Enzymology* 82 (A): 33-64.

20. Oesterhelt, D., and W. Stoeckenius. 1974. Isolation of the cell membrane of *Halobacterium halobium* and its fractionation into red and purple membrane. *Methods in Enzymology* 31: 667-678.

21. Payne, K. J., and A. Veis. 1988. Fourier transform IR spectroscopy of collagen and gelatin solutions: deconvolution of the amide I band for conformational studies. *Biopolymers* 27: 1749-1760.

22. Poehling, H. M., and V. Neuhoff. 1981. Visualization of proteins with a silver "stain": a criticle analysis. *Electrophoresis* 2: 141-147.

23. Russ, J. C. 1992. *The Image Processing Handbook*, 101-113. Boca Raton, Florida: CRC Press.

24. Shotton, D. M., B. E. Burke, and D. Branton. 1979. The molecular structure of human erythrocyte spectrin. *J. Mol. Biol.* 131: 303-329.

25. Thomson, R. E. 1991. Scanning Tunneling Microscopy of Charge Density Wave Structure in 1T-TaS2. Ph.D. diss., University of California, Berkeley, Berkeley, California.

26. Ximen, H., and P. E. Russell. 1992. Microfabrication of AFM tips using focused ion and electron beam techniques. *Ultramicroscopy* 42: 1526-1532.

III. Results and Observations

Scanning Tunneling Microscopy

Results

My initial SPM attempts at imaging biological samples were made using STM. While the STM was built in the Department of Physics for solid state studies, it was easily adaptable to my work with collagen. This allowed me the opportunity to develop initial sample preparation techniques, and to gain a practical knowledge of the fundamentals of SPM, acquired while modifying the STM for biological work. Most importantly, my experience with the STM gave me a basis for evaluating the subtleties of SPM. I found that many images, in my own work and appearing in the literature, were in actuality artifacts. My experience with artifacts in STM ultimately led me to pursue SFM for the imaging and examination of biological materials.

Several examples of my STM images are shown in Figure III-1. This panel shows what appear to be single molecules of collagen at high magnification. Figure III-1 A was one of the first images that I obtained, and was particularly heartening in that it appears to have a helical twist. In this image one can also see a very light parallel ghost image, rather common in STM images on HOPG. The second micrograph (Figure III-1 B) shows a clearly defined periodic structure running at about a 60 degree angle over a mono-atomic step in the graphite surface. In my experience, such steps are not uncommon on HOPG, and in fact can be useful in calibrating the Z (height) of the instrument. It is commonly assumed that the orientation of such a structure across a step makes it unlikely that the structure is an arti-

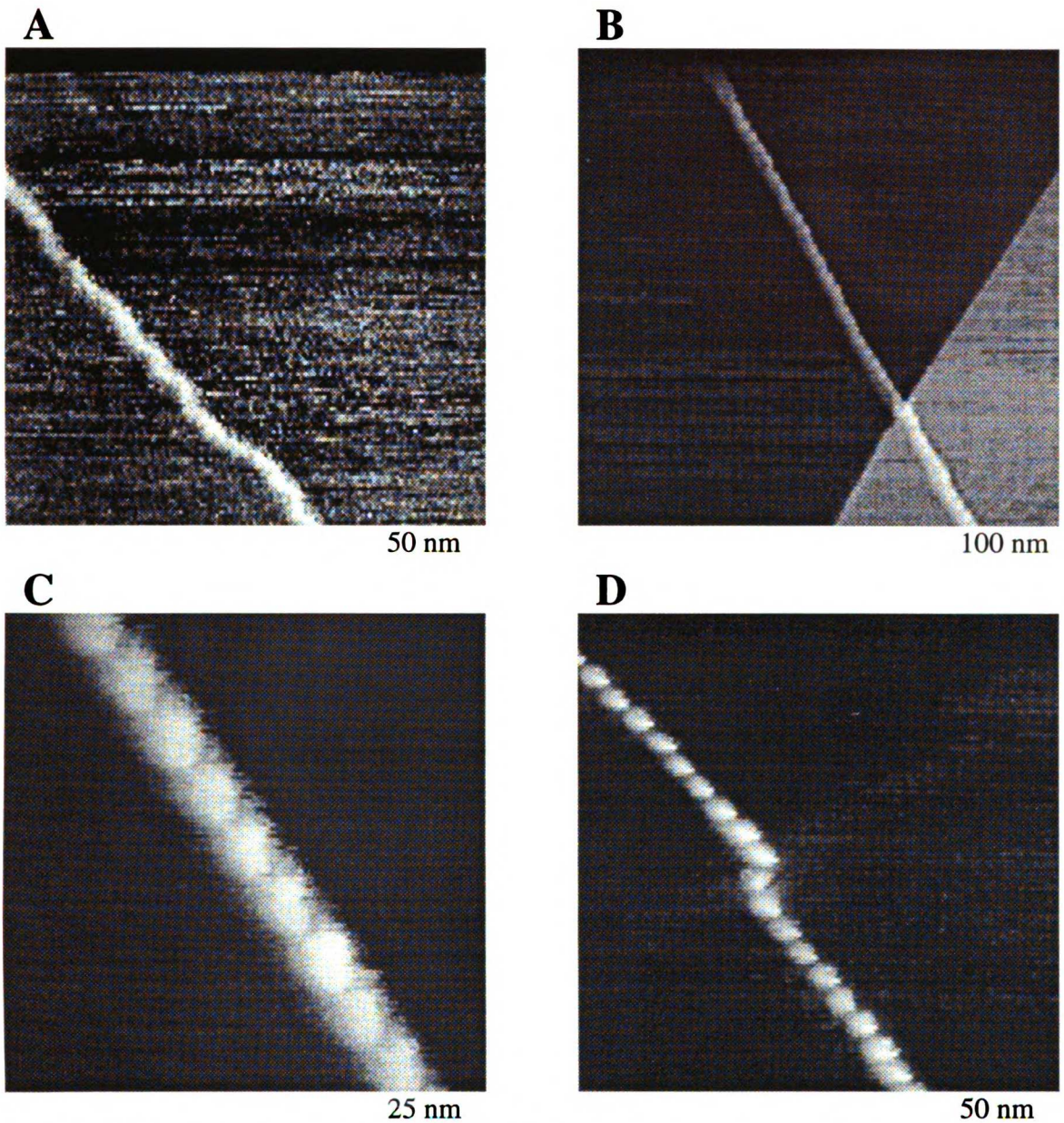

Figure III-1 STM images of single periodic structures. Images B–D acquired with improved pre-amp circuit.

fact associated with the graphite surface. Artifacts are a difficult problem in most SPM technologies, and particularly in STM of or on graphite, as it is very difficult to independently confirm that the imaged object is indeed the sample of interest. Typically, one examines a sample until one sees an object matching one's expectations. Experience, and controls (also difficult as

one is typically looking to "not see" something), are what one relies on to assess the validity of the image. Both are often in short supply, which is particularly a problem for a technique that is by and large at the early "what you see is what you get" phase of development.

Figure III-1 C shows a higher magnification scan of the structure in B, showing a very distinct periodic nature. The periodicity is found to be 3.3 nm, remarkably close to the expected 3.0 nm periodicity for the collagen molecule. This number is within the estimated ± 10 % uncertainty for this experiment. More accurate lateral calibration was possible by analyzing the atomic lattice structure of the underlying graphite surface. The apparent width of the structure is about 3.0 nm (compared to 1.5 nm from x-ray data), an expected result. Such a topographic image is a convolution of both the sample surface topography and the shape of the imaging tip, leading to a broadening of the apparent width of the structure (due to the width of the tip). The apparent height of the structure is also typically distorted, given the interaction of the tip and sample, and the compliance of the sample and of the HOPG substrate. Interactions between the sample and tip can be expected due to both mechanical forces, and effects from the large local current densities (about 0.5 nA over 5 square angstroms, or 10^6 A/cm^2 !). These interactions can be a particular problem for samples whose conductivity varies across the sample surface.

A similar periodic structure is shown at slightly lower magnification in Figure III-1 D. This image is from a different experiment and shows similar physical textures, including a periodicity of 3.2 nm. In addition, this image shows a pronounced "kink" in the structure, which was a common motif.

These kinks were found to be remarkably consistent, where the structure seems to jog over about one width, then continue in the original direction. Certain other common characteristics emerged, most notably that the structures are usually very straight (collagen is described as rod like), and very long (many μm). Such unexpected lengths would require invoking some unknown mechanism for collagen molecules to associate end-to-end.

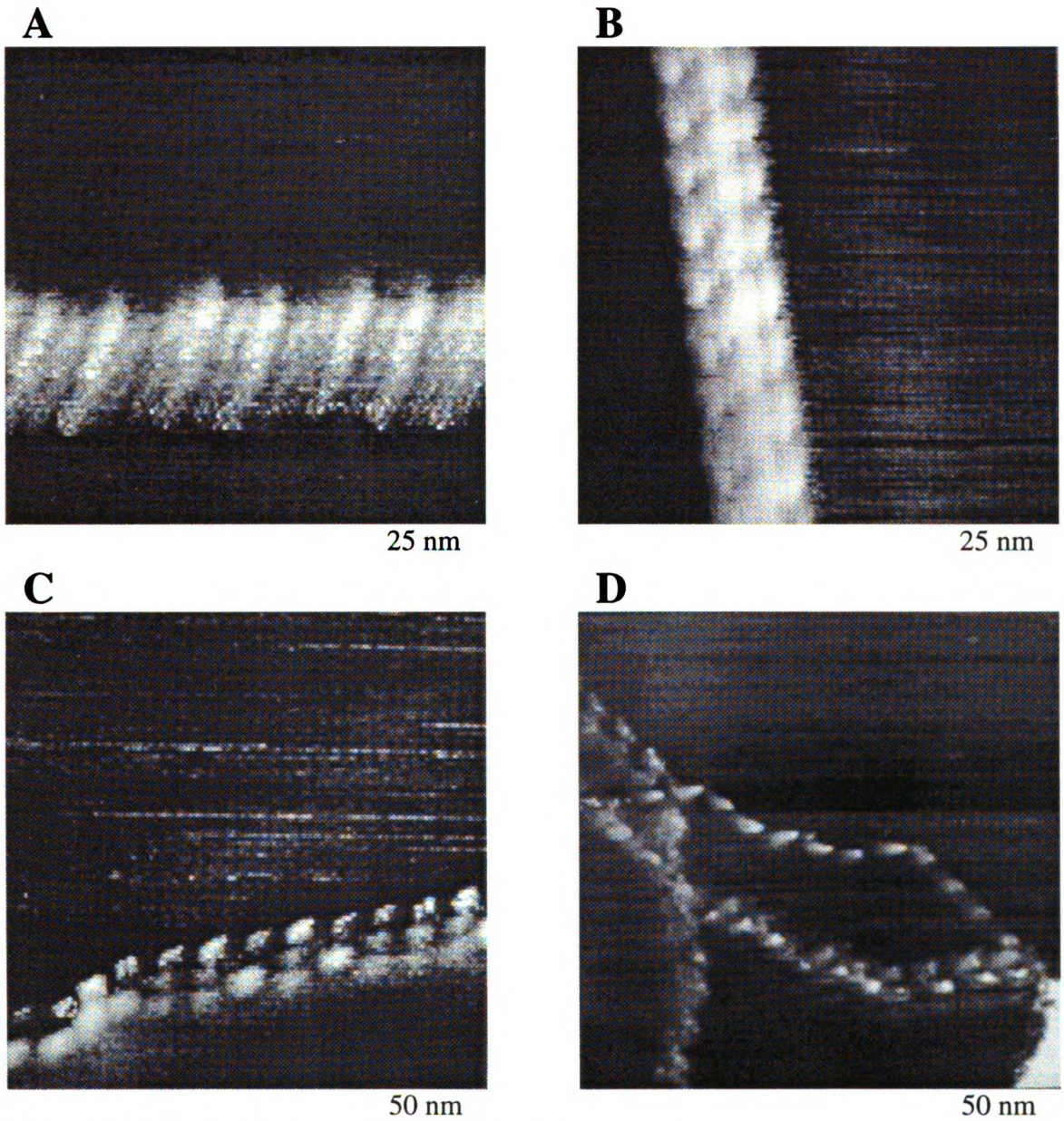

Figure III-2 STM images of triple and helical structures.

The variability and surprising nature of the STM images are shown in Figure III-2. Figure III-2 A and B are larger structures of about 5.0 – 7.5 nm widths which show more pronounced and complicated patterns. In image A there is a decided helical, or twisted, appearance; in B a pattern resembling three of the earlier periodic structures associated together (molecular associations ?). These two scans also have perpendicular orientations, suggesting that they are not induced by some phenomena associated with the scanning direction. Figure III-2 C shows a section of a structure similar to III-2 B, where the periodic elements appear to diverge. Figure III-2 D is an image of one of the few experiments where the structures were rather nonlinear, with bends and twists. These structures are located in the image just below an atomic step in the graphite substrate, visible in the lower right corner.

Despite my fondest hope that these structures might be collagen, their true nature started to emerge with the data depicted in Figure III-3 A and B. This figure shows two examples of a Moiré pattern observed during my

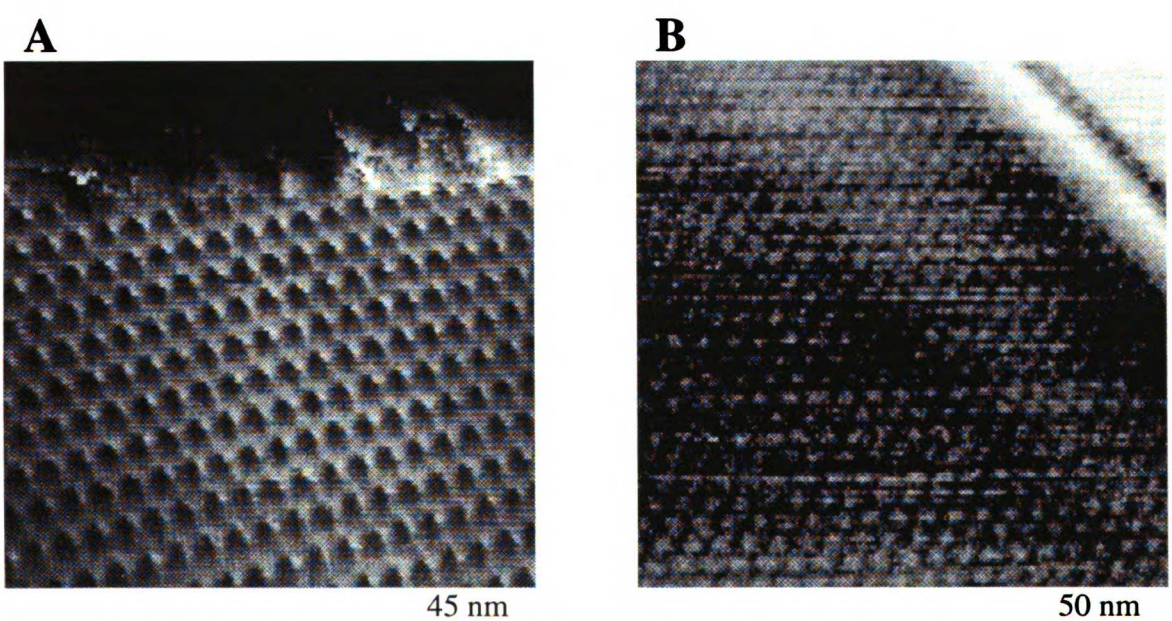

Figure III-3 STM images of Moiré patterns on mica surface.

STM studies, and encountered occasionally in STM studies on graphite. A Moiré pattern occurs on HOPG when an open layer of carbon atoms becomes distorted, or displaced, relative to the underlying bulk material (Kuwabara *et al.*, 1990; Xhie *et al.*, 1993). This results in a "phasing" of the upper and lower layers of the two dimensional atomic lattices (and their electronic states), and produces a third apparent lattice structure with a larger periodicity. Figure III-3 A is a high magnification image of the edge of a graphite flake, taken at low temperature (liquid N_2). The flake shows a distinct 2.5 nm periodicity, much larger than the underlying atomic lattice. The upper area of the photo shows a series of several flake edges receding down to the solid bulk material, generating some rather complicated and ill-defined structures.

A similarly defined Moiré pattern is seen in Figure III-3 B, with a few notable differences. In this image, the pattern occurs just below a step in the HOPG, seen in the upper right corner. One or two graphite layers may have pulled away from the step, generating a Moiré pattern with a periodicity of about 2.6 nm. What is particularly interesting is the presence of a linear structure on top of the Moiré pattern running parallel to the step edge, and exhibiting a periodic structure in phase with the underlying pattern. This structure by itself is rather reminiscent of the single structures seen in Figure III-1.

A more direct link between the periodic structures of Figure III-1 and a Moiré pattern is seen in Figure III-4. All four micrographs in this figure show a distinct Moiré pattern similar to the previous image. The periodicity of this Moiré pattern is 4.8 nm, about twice as large as the pattern observed in Figure III-3, and this is not uncommon. Similarly, patterns of single

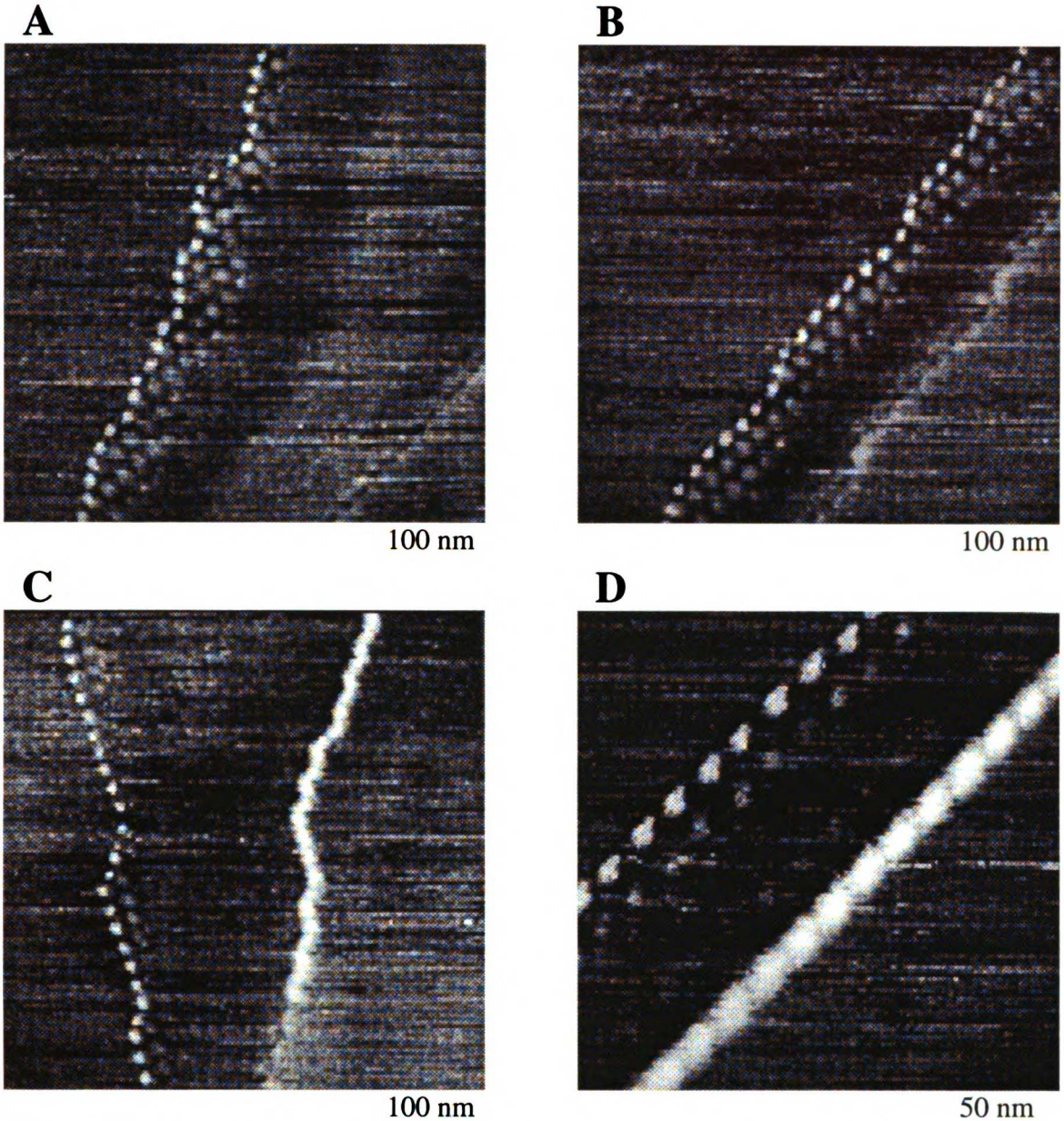

Figure III-4 STM images of linear periodic structures associated with Moiré patterns.

structures are occasionally found with a 2 x periodicity. The Moiré pattern is also less distinct. What is quite unusual, however, is the presence of a much more distinct periodic structure superimposed on the Moiré pattern. These patterns, taken without the underlying Moiré pattern, would be virtually indistinguishable from the structures of Figure III-1. These data were obtained during only one experiment, but may represent a direct link between

the long periodic structures often described as biological samples, and Moiré patterns formed on the graphite surface. It is particularly interesting to note that the kink seen in the image of Figure III-1 D can be easily explained as a "jumping" of the image to another row of the Moiré pattern, as seen in Figure III-4 B. Although this sample had been treated with our collagen solution, these structures are clearly not collagen, as verified by later controls. In retrospect, only Figure III-2D may represent successful imaging of collagen by STM.

Discussion

My studies of collagen using the STM were severely curtailed by the technical difficulties associated with the technique, and by the presence of artifacts. The artifacts were particularly troubling, due to their similarity to anticipated biological structures, and the difficulty in independently confirming the origin of a structure observed with this imaging technique. Unfortunately, this is a problem that extends well past this work into the general published literature, with images virtually identical to the ones presented in Figure III-1 appearing regularly.

Such artifacts are clearly associated with the use of HOPG as a substrate, which has been pointed out to by at least several groups (Tiedje *et al.*, 1987; Albrecht *et al.*, 1988; Rong & Kuiper, 1993). Unfortunately, attempts at molecular level biological imaging with STM generally require use of HOPG as a substrate. STM, which relies on the measurement of a tunneling current, requires both a conducting sample and substrate. Additionally, as the STM is extremely "short-sighted" with a limited vertical range, one requires a substrate that is quite flat, at least relative to the sample of inter-

est. Optimally, for molecules such as collagen, one needs a substrate surface that is flat to within a few atoms over regions of a square micron or larger. HOPG meets these requirements, with its ability to cleave on mono-atomic planes. Other substrates, such as epitaxially grown gold, gold films, or silicon surfaces, do not have the combination of conductivity, flatness, and ease of preparation (by simply cleaving) as HOPG.

It is rather surprising how convincing these artifacts can be for molecules of a helical nature such as DNA or collagen. Recently, a few published papers (Salmeron *et al.*, 1990; Clemmer & Beebe, 1991) have confirmed our findings as to the physical appearance of such structures, which are typically long, straight, and often periodic. These studies similarly note that such artifacts can "meander" over graphite steps, an argument once generally used to affirm that an image was indeed not an artifact. The general consensus of these papers is that the artifacts are due to step edges, often associated with flakes, and Moiré patterns that might be confused with two-dimensional arrays of proteins. No attempt is made, however, to reconcile the lack in an apparent change in height that one would expect for an artifact associated with a step edge.

My data indicates that the physical basis of these artifacts may be a bit more complicated, and may actually arise out of a combination of several factors. The data in Figure III-4 are unusual in that they show a linear, one dimensional, periodic artifact associated with a two dimensional Moiré pattern, suggesting that the two may be intimately connected. This might explain why more steps do not exhibit periodic artifacts. It appears that such periodic structures associated with the Moiré pattern are quite common, although the two dimensional Moiré pattern is not visible (Figure III-1). The

data in Figure III-4 may be a rare glimpse of the relationship between a Moiré pattern and the more common one dimensional periodic artifact. The origin of these biological artifacts may thus result from a combination of a step edge effect and the periodicity of an underlying Moiré pattern. A similar pattern at a graphite step boundary has been observed by Buckley et al. (1990).

A possible mechanism which might explain how these artifacts are generated therefore could involve the interaction of the tip with the HOPG surface, and the compliance of the sample and the HOPG substrate. It is important to remember that the imaging process is dynamic, with the tip exerting not only an electrical force on the sample surface, but a mechanical force as well. It is often overlooked that the graphite is subject to a substantial contamination-mediated deformation during the scanning process, particularly in air. Mamin et al. (1986) observed surface compressions of up to 100 Å, while maintaining atomic resolution. An STM, operating in a feedback mode, could thus image a step, and due to a slight difference in compressibility, see little or no change in the apparent height of the sample surface on either side of the step. In fact, hysteretic effects between the imaging current and the tip displacement could account easily for the apparent flattening of an HOPG step. Lateral hysteretic effects may be important as well, and it might be appropriate to consider a shear model of behavior when imaging on HOPG (Todd & Pethica, 1989).

An additional factor in producing the artifacts might be associated with a possible change in the local conductivity of the HOPG surface. A flake, or surface layer, which is loose enough to allow for some rotation (and thus generate a Moiré pattern) may be displaced enough to lower its electrical

contact with the bulk material, thereby lowering its conductivity. Such a reduction in conductivity would displace the tip downward, as the feedback acts to maintain a constant current. I do not know of any attempts to measure or model such a change in conductivity for graphite, and they can be expected to be difficult.

A possible mechanism for generation of these biological artifacts might involve the compliance of the surface, and possibly a change in the conductivity of a flake or step. As the scanning tip approaches a step in the graphite surface, the tip would experience an increase in tunneling current due to an additional horizontal tunneling gap to the step edge. This increase might be further enhanced due to the presence of broken carbon bonds which will "dangle" at the step edge. The increased current will, during feedback regulation, cause the tip to retract away from the surface. Once on top of the graphite edge, the current will attempt to drop back to its single vertical tunneling gap value, and the feedback circuit will in turn extend the tip to keep the current constant. Under certain conditions, a change in the compliance, a local reduction in graphite conductivity, or even hysteretic effects, may result in the tip returning to about the same relative height as at the beginning of the scan. This would result in a topographic representation of the graphite step edge as a one dimensional, linear structure. The periodicity of this structure could easily be contributed by the underlying Moiré pattern, as seen in Figure III-4.

I have attempted to verify experimentally some aspects of this hypothesis with limited results. Using the STM, I measured the compliance above and below a graphite step, by measuring the change in tip tunneling current for a given change in displacement. This was accomplished using a signal gen-

erator to oscillate the scan tube vertically a known distance. I did not reproducibly find any difference in compliance, although deformations similar to those reported by Maimen et al. were observed. This may not be surprising, since a change in compliance of only a few percent could account for the effect. I do believe it might be possible to conduct a similar experiment, using an UHV environment, to determine if this effect is real.

Whatever their exact nature, these artifacts, or "carbon flakes" as Lew Sachs likes to call them, are a real limitation on the use of STM in biology. The physics of these flakes, however, is interesting in its own right, and in fact are artifacts only from our point of view of using HOPG as a biological substrate. These carbon flakes will hopefully continue to be explored, or at least catalogued, since HOPG is still very useful for some biological investigations. I believe the unique properties of HOPG, and of STM in general, will ultimately prove useful in looking at the electrical properties of some biological materials. For studies of biological samples, and particularly collagen, I found it advantageous to turn to SFM.

Transmission Electron Microscopy

Ferritin

TEM was used to characterize our SFM samples, thus serving as a control for artifacts. Furthermore, TEM was instrumental in developing sample preparation techniques for our SFM studies. Representative TEM images are shown in Figures III-5 through III-9. All of these images were prepared and shadowed as described in the methods section. Figure III-5 is an example of rotary-shadowed ferritin, a globular protein with a diameter of 12

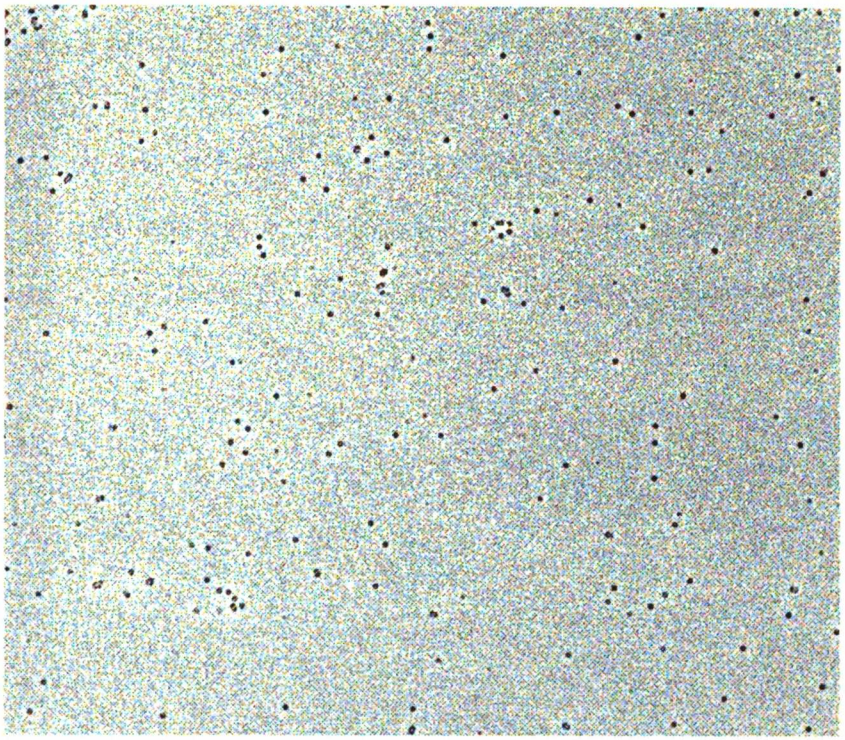

Figure III-5 TEM micrograph of rotary shadowed ferritin applied at $OD_{270} = 0.1$, mag = 40k.

nm. Individual molecules are distinctly visible. The finer grain structure in the background is the platinum metal coating, which typically has an optimal grain size of about 0.2 – 0.4 nm. This image shows how nicely TEM can resolve individual molecules. Rotary shadowed images can also be used to measure molecular "height" from the length of the lighter platinum "shadow" that surrounds the molecule, and the angle of deposition. TEM requires electron scattering for imaging contrast, and what we are actually imaging is the evaporated metal replica covering the mica surface and the ferritin molecules.

Purple Membrane

TEM has also been instrumental in studies of larger structures such as lipid membranes, and of purple membrane from the bacteria *Halobacterium*

halobium (Fisher & Stoeckenius, 1977; Fisher *et al.*, 1978). This membrane is particularly interesting in that it contains a large fraction (75 % by weight) of a single membrane spanning protein bacteriorhodopsin (26 kD), which functions as a light driven proton pump. Patches of purple membrane are shown in Figure III-6; note the characteristic grain of the metal coating.

Figure III-6 TEM of purple membrane, unidirectional shadow, mag = 56k.

A higher magnification TEM image of purple membrane (Figure III-7), shows some interesting membrane modifications. This figure, from the previous study of Fisher et al. (1978), shows a lot of "holes," or pits, in the membrane surface. These pits were introduced into the cytoplasmic side of the membrane during slow air drying of the membrane on a polylysine-coated glass surface. Adsorption could be controlled by altering the membrane surface charge by manipulating pH and light intensity. Although the

origin of the pits was not entirely clear, their 120 ° angular structure (corresponding to the paracrystalline lattice) suggested that they may be discrete patches of membrane removed by surface tension effects (Fisher, 1994 personal communication).

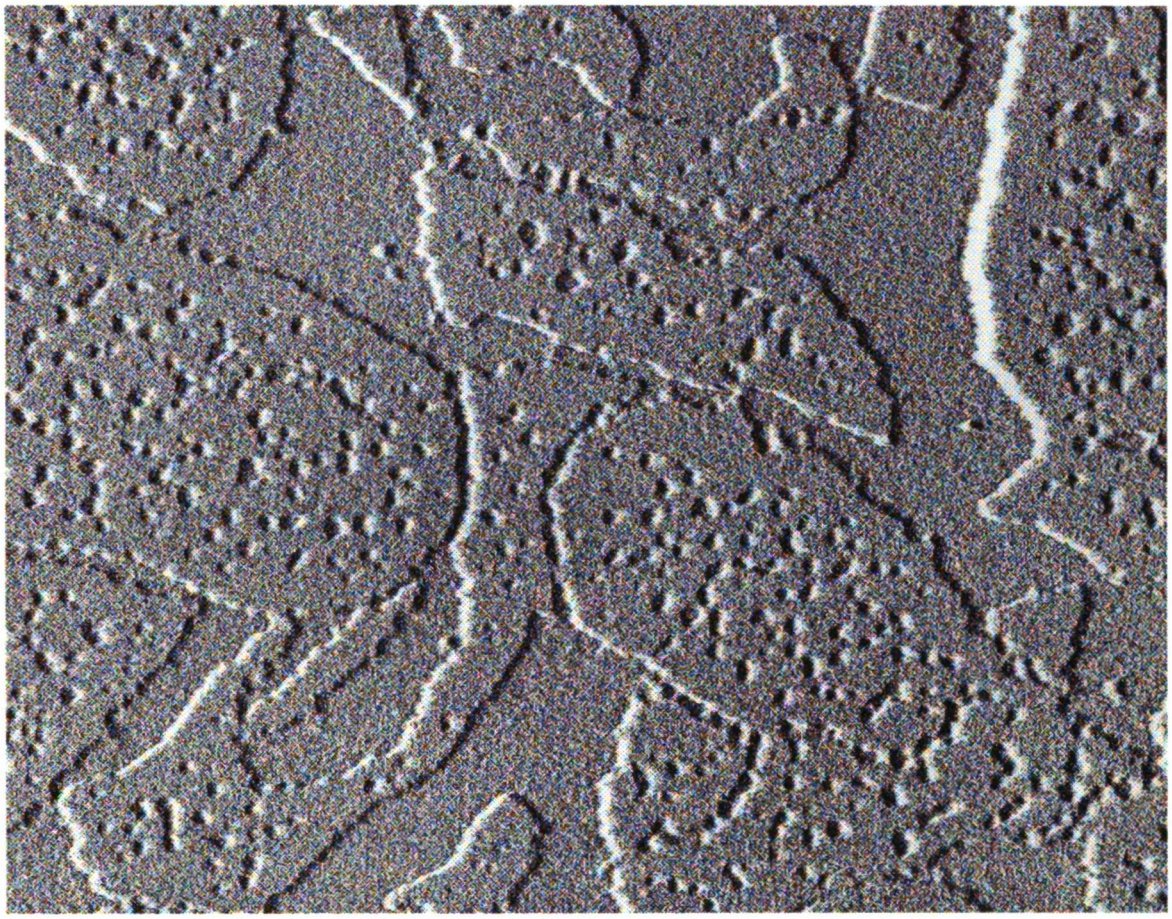

Figure III-7 TEM of purple membrane, with pits in cytoplasmic surface, as discussed in text. Unidirectional shadow, mag = 88k.

Collagen

Representative rotary-shadowed TEM micrographs of lathyritic rat skin type I collagen are presented in Figures III-8 and III-9. Figure III-8 is a micrograph (magnification = 60k, or about 5 μm^2) of a collagen monolayer on mica, prepared from a 1 ng/µl solution as previously describe. Individual

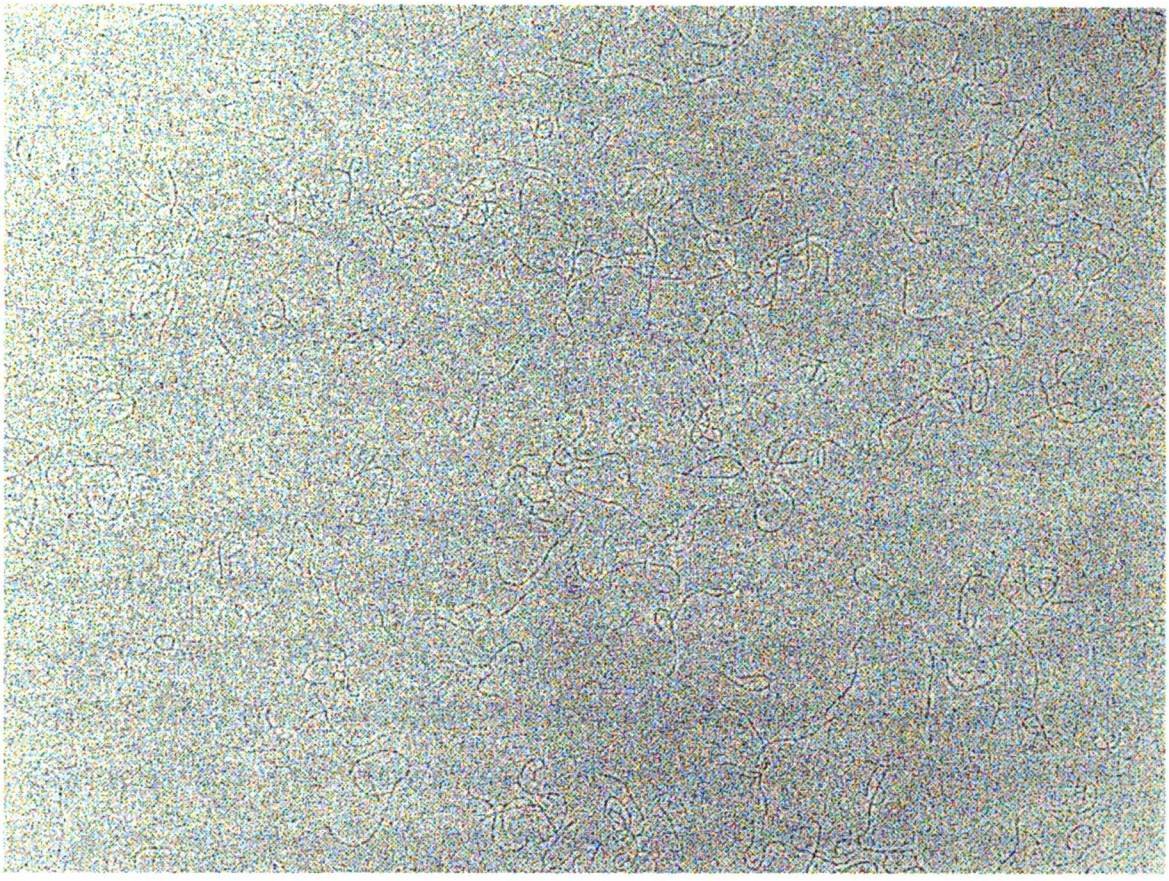

Figure III-8 TEM of collagen preparation as used for SFM studies, rotary shadowed, mag = 59k (1 cm = 0.17μm).

molecules are readily apparent, and are quite flexible, as suggested by Nestler et al. (1983). The lengths of single molecules can be estimated from similar lower concentration micrographs, where the molecular ends are more distinct. The molecular shape can be "traced" with a piece of flexible ruled wire in order to determine a length distribution for collagen molecules. The distribution for 35 such molecules has a mean $x = 247$ nm and a standard deviation $\sigma = 28$ nm, which compares reasonably well with the results from a previous study of $x = 250$ nm and $\sigma = 47.5$ nm (sample size $n = 80$) (Veis, 1992 personal communication). TEM lengths range from 179 nm to 303 nm, as compared to a range of 161 nm to 480 nm for Dr. Veis' data. The

value of 480 nm may in fact represent a molecular dimer, and might help account for the greater standard deviation in these data. Both of these data sets have a greater variability in molecular length than might otherwise be expected, as reflected in their standard deviations.

Our SFM scanner in particular was quite limited in lateral range, making the sample quality very important. Thus the physical distribution of collagen molecules on the mica surface is important. For a given sample and a single coarse approach, we were restricted to imaging an area of about 10 μm^2 at room temperature, or about 4 μm^2 at 143 K. To image a new area required at least walking the sample back, followed by a new coarse approach. More typically we manually rotated the sample carrier positioned on the scan tube. Each walkup involved a reasonable risk (something like 10 – 20 %) of a tip crash. It was important that our sample preparation technique resulted in uniform surface coverage, evenly distributed over large areas of the mica surface. These TEM studies were instrumental in verifying sample homogeneity.

A high magnification (200k) TEM micrograph of type I collagen molecules, at a higher concentration (8 ng/µl), is shown in Figure III-9. The overall physical characteristics of the molecules are much like Figure III-8, with a corresponding increase in the surface coverage. At this magnification, some of the limits of TEM are becoming more noticeable. The image quality, in terms of contrast and resolution, is limited by the characteristics of the platinum/carbon replica, most notably by graininess under our metal deposition conditions. As the metal accumulates on the sample surface during deposition, it forms discrete "clumps" or grains about 0.5 nm in diameter. The "image" of the collagen molecule is formed by the selective

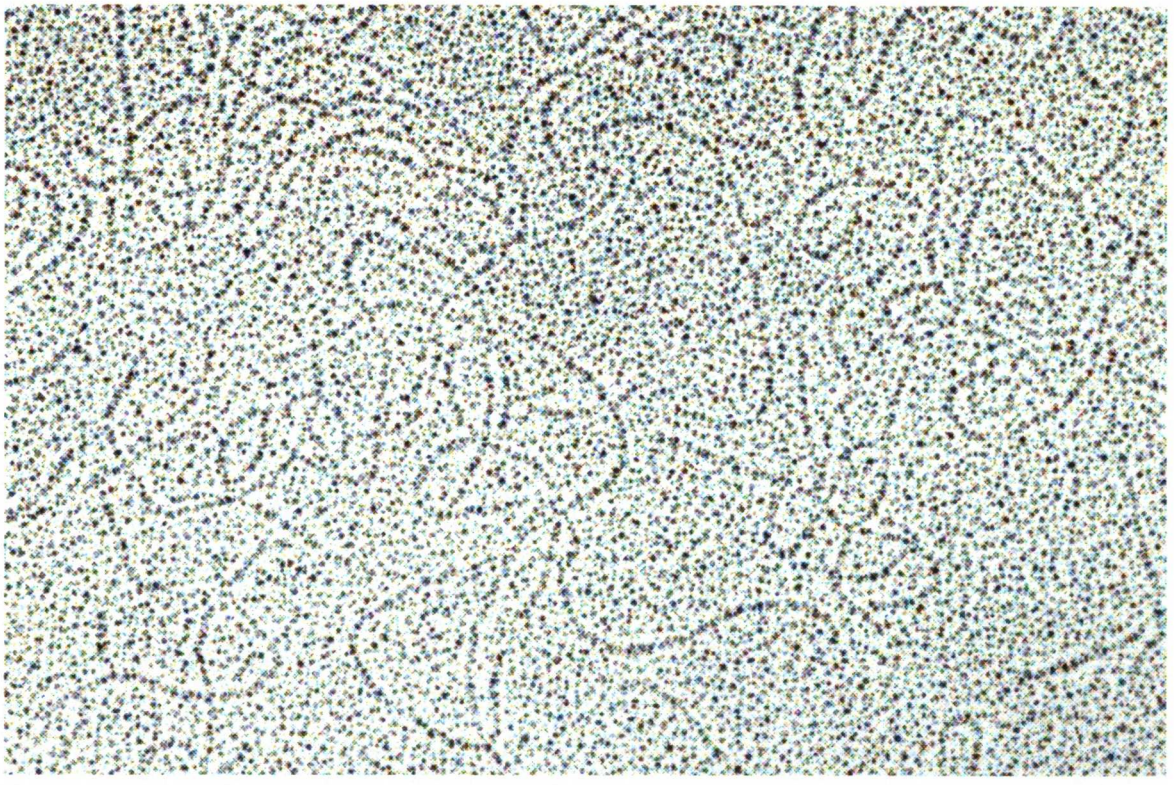

Figure III-9 High magnification (mag = 202k) TEM of collagen showing distinct individual molecules and the grain of the Pt-C shadow.

alignment and accumulation of these grains around the molecule during shadowing. At this magnification, the resolution and contrast of the image has become dominated by the structural grain of the metal film, making determination of the molecular ends difficult.

Gel Electrophoresis

SDS gel electrophoresis was run on our type I collagen samples, both in solution and as extracted from mica sheets. After my experience with artifacts during the STM studies, it seemed prudent to independently verify the samples as prepared for SFM. The gel data plus the TEM work characterized the samples bound to the mica surface, allowed some estimate of the

amount present, and gave some indication that the bound molecules were biochemically representative of the collagen in solution.

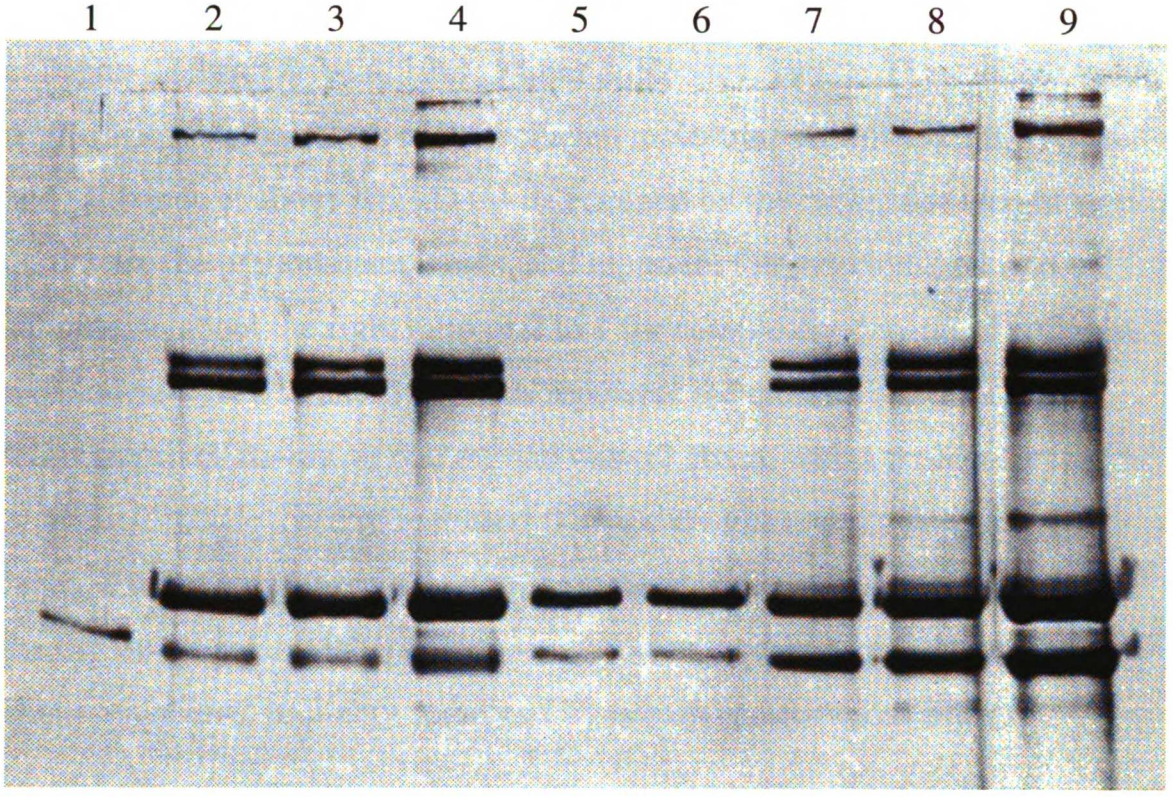

Figure III-10 SDS-PAGE of collagen both in solution (7, 8 & 9) and as recovered from monolayer on mica (5 & 6) as indicated. Molecular weight standards (1) and Vitrogen (2, 3 & 4) included as well. Bands explained in text.

A typical gel of collagen is shown in Figure III-10. We prepared collagen monolayers in the same manner as we would for SFM, using larger mica sheets in order to obtain a reasonable amount of collagen. We roughly calculated the area of mica required to yield about 2 ng of collagen for a single lane of the gel, based on the observed TEM surface coverage. Duplicates of these stripped collagen solutions are seen in lanes 5 and 6. Lanes 7, 8 and 9 are increasing amounts of the type I collagen in solution (1 ng, 2 ng, & 5 ng). As an additional control, we included 1 ng, 2 ng, and 5 ng loads of

Vitrogen, a commercially available collagen preparation, in lanes 2, 3 and 4. Molecular weight standards are in lane 1.

The collagen and Vitrogen solution bands show the expected patterns for collagen (Helseth & Veis, 1981; Miller & Rhodes, 1982). These bands result from various associations of the collagen molecular subunit chains. The α1 and α2 bands at about 100 kD (as determined by the molecular weight standards) are the predominant bands, and represent the individual α1 and α2 submits, in about the right ratio of 2 to 1 for completely denatured collagen molecules. The β11 and β12 bands represent the crosslinked dimers containing two α1 chains, or one α1 and one α2 chain, with a molecular weight of about 200 kD: these pronounced β bands are unusual for lathyritic collagen, and may result from an aged sample or silver stain saturation. Near the top of the gel are the γ components, corresponding to complete, triple chain molecules, probably stabilized by intramolecular cross links.

Collagen bands 5 and 6, extracted from the mica surface, compare very well to the collagen and Vitrogen solution bands. The α1 and α2 bands are particularly distinct, and this banding pattern confirms that collagen is in fact bound to the mica surface in a monolayer. The overall α1 and α2 band density indicates that the recovered collagen is lower than the anticipated 2 ng, and the β11 and β12 are only very faintly visible in this particular gel. Other gels, using lower concentration control solutions, indicate that the recovered collagen has a load of between 0.1 – 0.5 ng per lane. The β11 and β12 bands at these lower concentrations also match reasonably closely, although they may indicate that a greater portion of the recovered collagen exists as free α1 and α2 chains after treatment with SDS.

Ferritin

One of our first biological samples for SFM was ferritin. Ferritin is an iron storage protein composed of 24 subunits. The globular molecule is about 12 nm in diameter, making it relatively large and easily distinguished. The structure of ferritin has been extensively studied and characterized by TEM; its 5.5 nm iron core can be directly imaged. The ferritin molecule (and indeed most proteins) is negatively charged, but binds to negatively

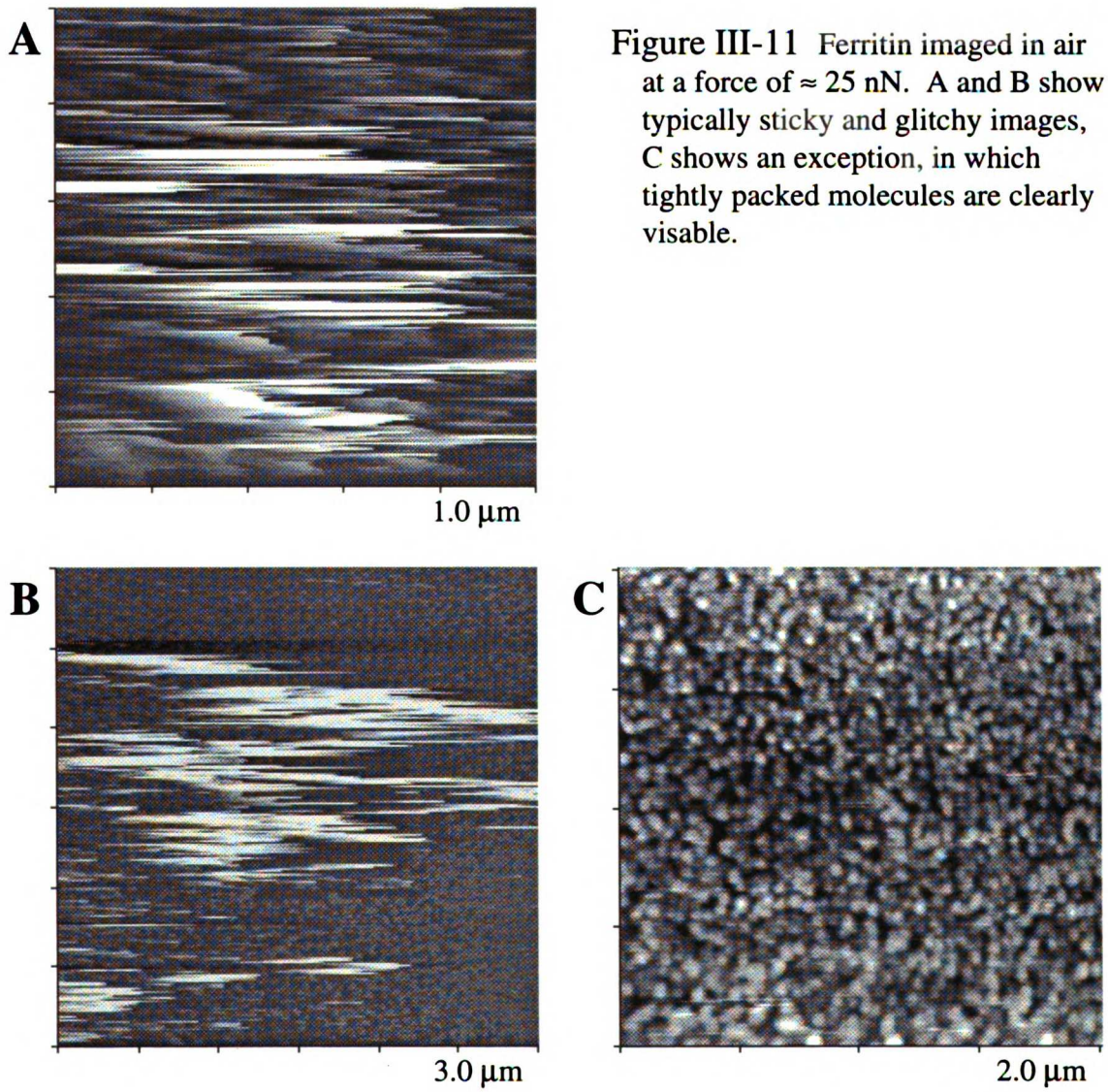

Figure III-11 Ferritin imaged in air at a force of ≈ 25 nN. A and B show typically sticky and glitchy images, C shows an exception, in which tightly packed molecules are clearly visable.

charged mica surfaces treated with polylysine.

Our attempts to image ferritin at room temperature in air met with very limited success. Figure III-11 is a series of images of ferritin from two experiments, and a typical 1.0 μm scan is shown in image A. Nothing readily discernible as a round (or spherical) object is obvious. What is apparent is a "smearing" of the image in the scan (X) direction, as well as some very light or white "glitches." Glitches result from torsional bending of the cantilever due to stick-slip effects between the tip and the surface, and appear "higher" as the SFM attempts to track the deflected laser beam. This effect is more fully discussed in the section on force series measurements. Sticking of the tip may be expected, due to the large imaging forces required when operating in air. Surface tension effects at the sample surface result in large, and difficult to control, attractive forces between the sample and the tip. These large imaging forces, while not detrimental to hard surfaces (such as mica), are a problem for relatively soft and mobile biological samples. The imaging force for Figure III-11 A was 25 nN.

A subsequent 3 μm scan is shown in image Figure III-11 B. The 1 μm area scanned to produce image A is seen at the center of B, and has been "scraped" clean by the scanning cantilever tip. It appears that some of the ferritin removed by the tip has been deposited along the left hand edge of the 1 μm scan area. Image B also has a sticky appearance, particularly in the previously scanned area. Interestingly, closely-packed ferritin molecules are visible in image B, but are somewhat obscured by the large apparent height of the glitches associated with tip/sample sticking. This was the only image in this experiment where individual ferritin molecules were visible, and all other images had the appearance of image A.

Numerous experiments and many repeated attempts to image ferritin in air yielded similar results, with one notable exception. We obtained several unanticipated images of ferritin in air (during a checkout of the machine electronics), one of which is shown in Figure III-11 C. In our experience, this was a highly unusual occurrence, possibly due to an unusually low imaging force. Unfortunately, the imaging force for this image is not known. The very close packing of the ferritin molecules may have acted to stabilize the sample, and resist movement or removal of individual molecules by the scanning tip. Such an effect has been noted for 2 dimensional arrays of liquid crystals (Smith & Frommer, 1993). Our ferritin sample may have been similarly stabilized. In any event, work with ferritin in air has convinced us that it is not a suitable system for reproducible study of biological samples.

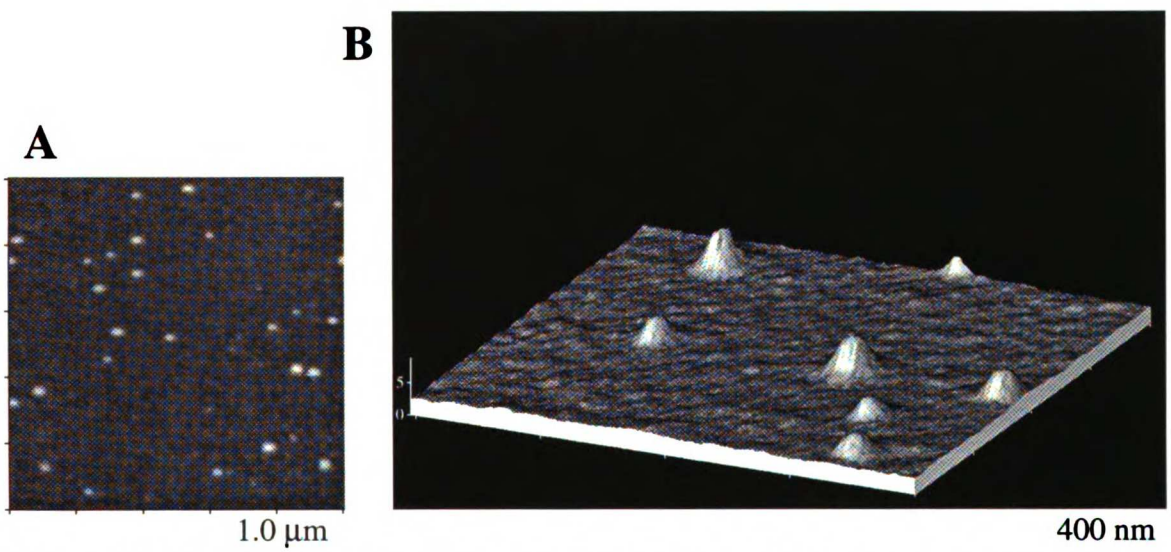

Figure III-12 Ferritin molecules shadowed with 2 nm of chromium imaged in air.

One technique to overcome the difficulties of imaging in air is to coat the sample with a metal shadow or replica, as is common in TEM preparations. While this nullifies the SFM advantage of studying the molecule directly, it

produces a stable and reproducible sample surface. We rotary-shadowed ferritin molecules with 2 nm of chromium and imaged this sample in air (Figure III-12). Image A is a 1 μm scan showing distinct shadowed molecules, and image B is a 400 nm scan in 3-D. These scans show individual molecules that vary in relative height, an observation that holds true for all of our ferritin studies including TEM. This may be a result of different binding configurations of the protein to the sample surface, or possibly due to a distribution in the ferritin size fraction used to make the sample. Chromium shadowing did give us highly reproducible images of ferritin in air.

Another technique in use is to scan samples immersed in a liquid. This lowers the imaging forces at least one to two orders of magnitude, and can be expected to enhance the image quality by reducing the interactions between the imaging tip and the sample. Scanning hydrated samples has the further advantage of direct examination of native molecules in a more native environment. Imaging in physiological solutions may allow for observations of selected biological interactions and processes in "real (video) time" (Drake *et al.*, 1989). Our machine, designed for low temperature work, is also capable of imaging in liquids at room temperature. However, it is limited to non-conducting fluids, as the tube scanner is immersed and carries high voltage. We typically used hexadecane, and occasionally pentane, for imaging in a liquid at room temperature.

The results of imaging ferritin under these conditions is shown in Figure III-13. Images A and B are mid and high-magnification scans showing individual and distinct ferritin molecules. Both images are taken in slow scan mode, as were those in Figure III-11. Note the absence of the smeared and glitchy appearance seen in the air images. The imaging force for Figure

III-13 is about 1 nN, 25 times lower than the force for ferritin samples imaged in air. Imaging in liquid, with its reduction in force between sample and tip, is clearly advantageous for biological samples such as ferritin.

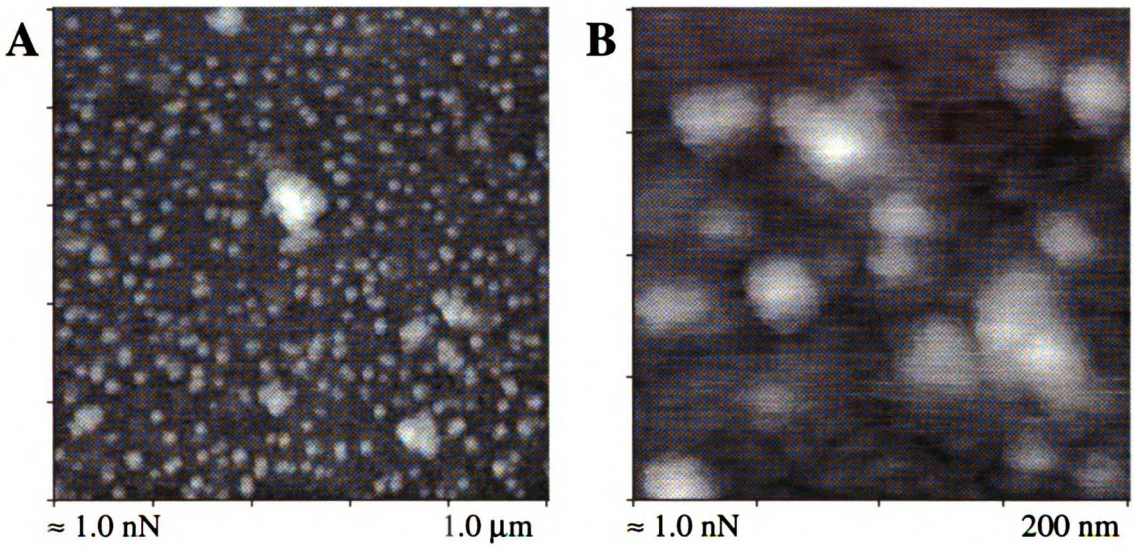

Figure III-13 Scan images of ferritin in hexadecane at room temperature. Force ≈ 1 nN.

To ultimately extend the SFM technique to low temperatures required choosing a suitable liquid, such as liquid pentane (Materials & Methods). We initially tested our SFM in liquid pentane at room temperature; one such image is shown in Figure III-14. This image is a 3 µm scan, which was the largest area our SFM could scan. The image is unusual in that mica substrate contains a diagonal step. Numerous individual ferritin molecules, small at this relatively low magnification, can be seen on both sides of the step, and the step height is clearly larger than the adjacent molecules. Furthermore, the step demonstrates one aspect of the importance of tip shape in SFM imaging.

All SFM images involve a convolution of the shape of the sample with the shape of the tip. When these shapes are similar in size, images are generated which are really due to both sample and tip. In fact, under the right

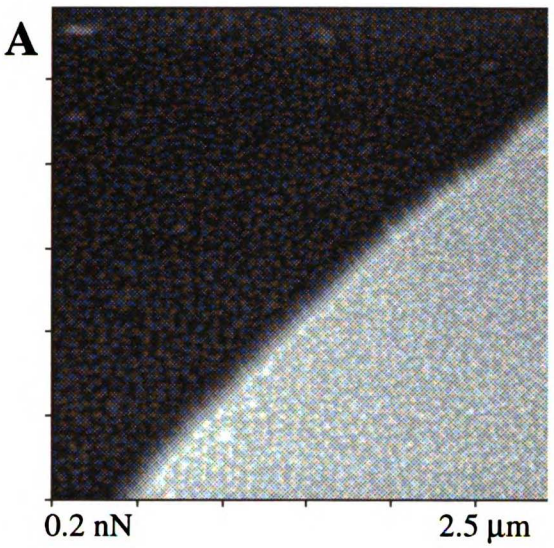

Figure III-14 Room temperature (in pentane) scan of ferritin on an atomic step in the mica substrate. Diagram B demonstrates distortion in topography of step due to tip shape.

B

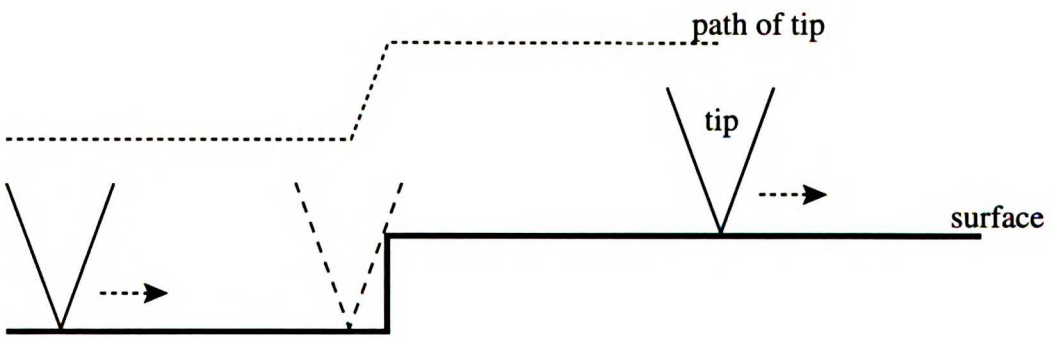

conditions, one can actually be imaging the tip with the sample! This is what we see in image A when our tip attempts to image a large vertical step. The tip is unable to track into the vertical corner, as the upper shoulder of the tip contacts the upper step edge as it scans the sample (Figure III-14 B).

What we get instead is a "ramp" rather than a vertical step, really representing the shape of the tip at that size scale. This ramp appears smeared, and is devoid of information about the sample corner. The result is that the apparent width of the object is exaggerated by and dependent on tip shape.

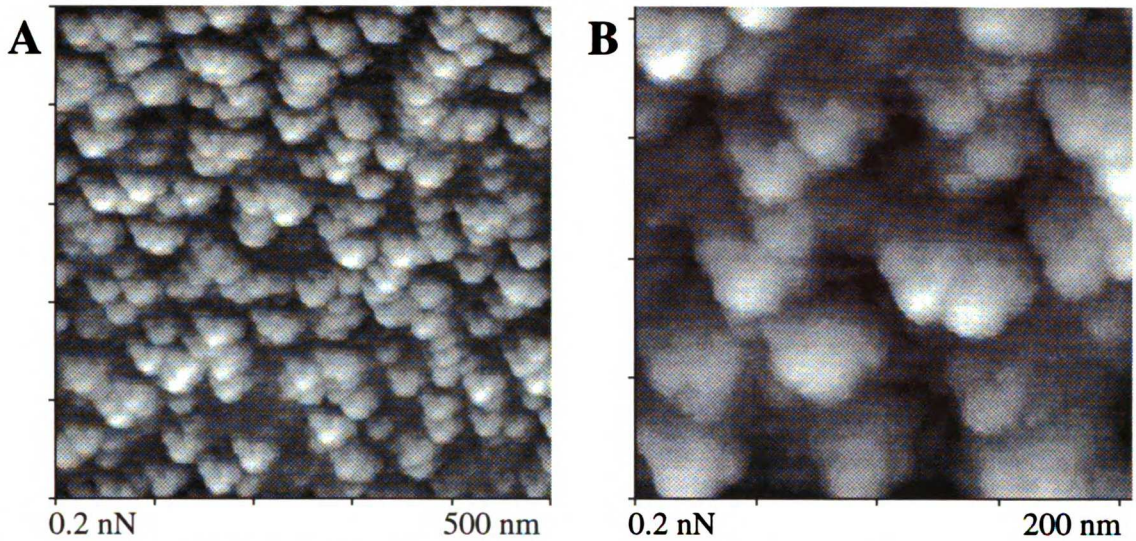

Figure III-15 High magnification ferritin images from same experiment as previous figure. "Vee" distortion of molecules due to local structure of fractured tip.

Figure III-15 A and B show this tip width broadening effect at the molecular level. Both of these images show ferritin molecules at high magnification. The apparent width of the molecules is much larger than expected. A molecule in image B (a 200 nm scan) appears to be about 20 – 30 nm, compared to the known value of about 12 nm. Some of the increased apparent width in the molecule may be due to elastic compression and deflection of the molecules by imaging forces.

Furthermore, the local tip shape is reflected in the molecules seen in image B. The fractured tip is imaged by the molecules as a flat plane, shaped in a vee, and angled at 20 ° relative to the sample surface (see Materials and Methods). This can result in a slightly vee shaped appearance of the sample, and varies from tip to tip. The fractured tips were designed to be sharp on a scale smaller than ferritin molecules, and this distortion results from the overall large scale structure of the tip. These images do, however, demonstrate the feasibility of imaging biological molecules in pentane, at least at room temperature. Microscopic and macroscopic tip effects on

image formation, and the minimization of artifacts, has been reviewed (Schwarz *et al.*, 1994).

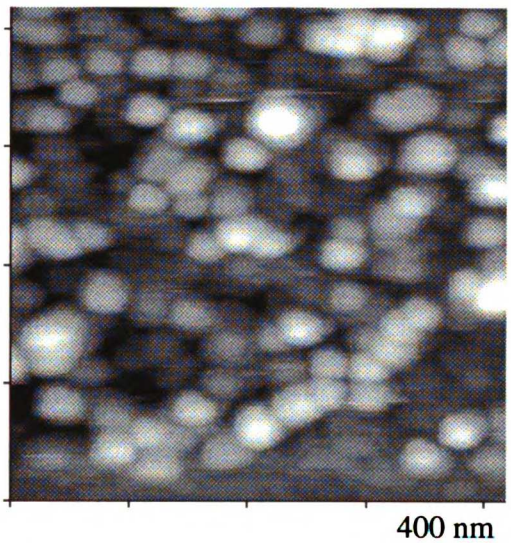

Figure III-16 Ferritin imaged at 143 K, showing several layers of molecules.

The first real success at imaging biological molecules at low temperature is shown in Figure III-16. This is an image of ferritin in pentane at 143 K. The image shows a large amount of ferritin, at least two layers deep, on the mica surface. Nevertheless, individual ferritin molecules are quite distinct, and notably images were quite reproducible. Many scans of the same area were made with little or no visible change in the image, although individual molecules could be selectively removed from the sample surface by the controlled application of locally high scanning forces. Images of ferritin at 143 K additionally had improved "image quality" compared to the room temperature scans. Some of this improvement in quality may have been due to scanning at low temperature (as predicted in the Introduction). However, the quality of the image was also directly dependent on the individual tip, sample preparation, and experimental conditions.

Purple Membrane

We next studied the photosynthetic membrane from *Halobacterium halobium*, commonly known as purple membrane. Purple membrane (PM) contains a hexagonal semi-crystalline arrangement of a single transmembrane protein bacteriorhodopsin. We anticipated that LT-SFM might limit the fluidity of the lipid membrane, further stabilize the arrangement of the bacteriorhodopsin molecules, and thus produce high resolution structural information. Membrane patches and Langmuir-Blodgett films were useful samples for early SPM studies, due to their relatively large size and stability. Metal-coated PM has been imaged by STM (Fisher, 1989a; Fisher *et al.*, 1990), and native PM by AFM (Worcester *et al.*, 1988 & 1990; Butt *et al.*, 1990). The small "aspect ratio" (height ÷ width) of membranes minimized tip/sample interactions. Our interest in purple membranes grew out of the research experience and interest of Dr. Fisher, whose sample preparation development experience was critical to the success of this entire project.

Figure III-17 A and B are low and medium magnification images of

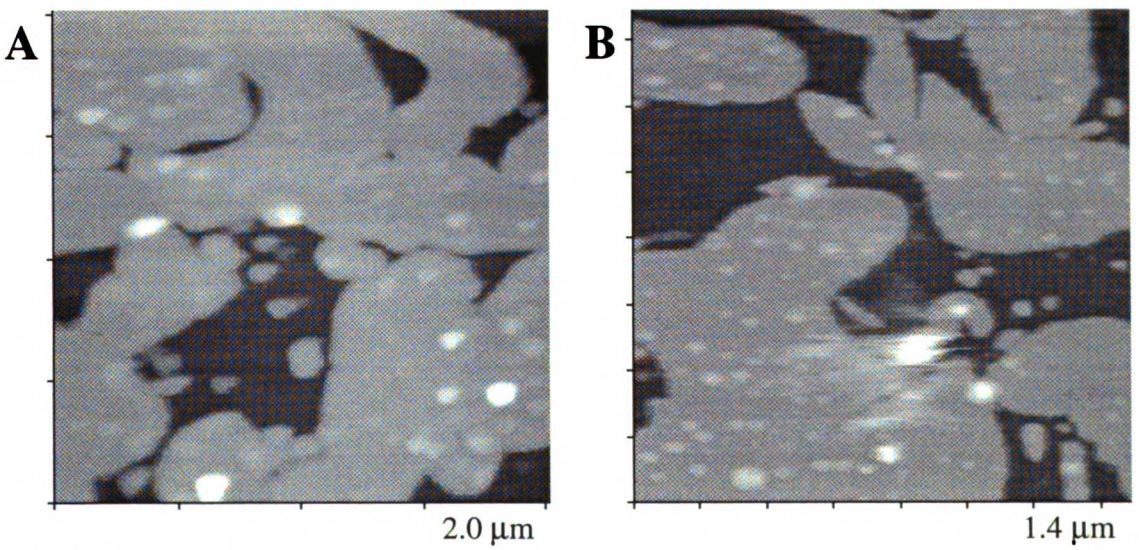

Figure III-17 Coated purple membrane imaged in air.

purple membrane attached to poly-lysine treated mica scanned in air at room temperature. The sample was prepared as described, and was additionally carbon-coated to stabilize the membrane against the high imaging forces (10^{-7} N) encountered in air. This stabilization technique was used during earlier STM studies of purple membrane (Fisher *et al.*, 1990). This STM study determined the thickness of purple membrane to be 4.6 nm to 4.8 nm, depending on sample preparation technique. Our SFM height measurements for Figure III-17 B indicated a membrane thickness of about 4.5 nm, although the Z calibration for this experiment was not well characterized.

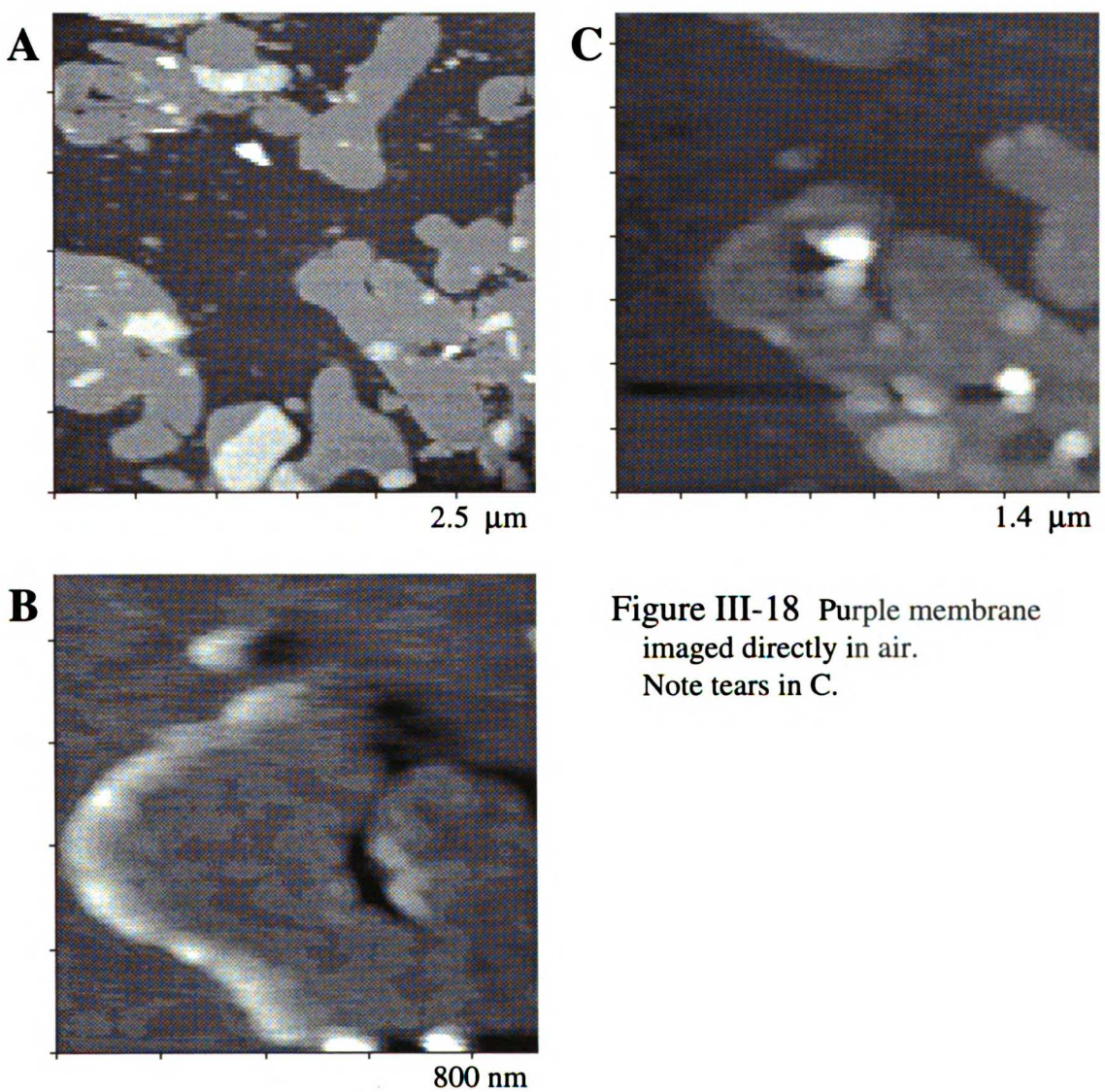

Figure III-18 Purple membrane imaged directly in air. Note tears in C.

Carbon coating the membrane sample reduces the resolution of its surface features. Ideally one would hope to image uncoated samples. Figure III-18 shows the results of our efforts to image uncoated purple membrane directly in air. Image A shows a similar pattern of layered membrane as seen in Figure III-17, again with a height of about 4.5 nm. The central features of this image are shown at higher magnification in image B. At this magnification, it is clear that little or no surface structure is visible on the membrane patch. The membrane appears rather ill-defined and displaced in the scan (X) direction. These observations were expected, given the relatively high imaging forces encountered in air, on the order of 10^{-7} N. Such high forces routinely result in sample damage as shown in image C, a lower magnification rescan of the area of B. Several repeated scans over the same patch of membrane produced a number of "tears" in the membrane surface.

As previously discussed, the imaging force can be reduced by two orders of magnitude if the sample is scanned in a liquid. A low magnification image of purple membrane scanned in hexadecane (Figure III-19 A), looks very similar to the images produced in air. Higher magnification images are noticeably improved (Figure III-19 B and C). In comparing Figure III-19 C to Figure III-18 B, one sees a large improvement in the resolution of surface structure on similarly sized membrane patches. Moreover, there is an improvement in the imaged quality of the background substrate (TaS_2 in this case), which is typically covered with some amount of contamination or impurities. This same or similar contamination can be expected to contribute to the structure observed on the membrane surface. The single line scan indicated in Figure III-19 B is shown in Figure III-20, and shows the size of surface structure features relative to the overall height of the membrane.

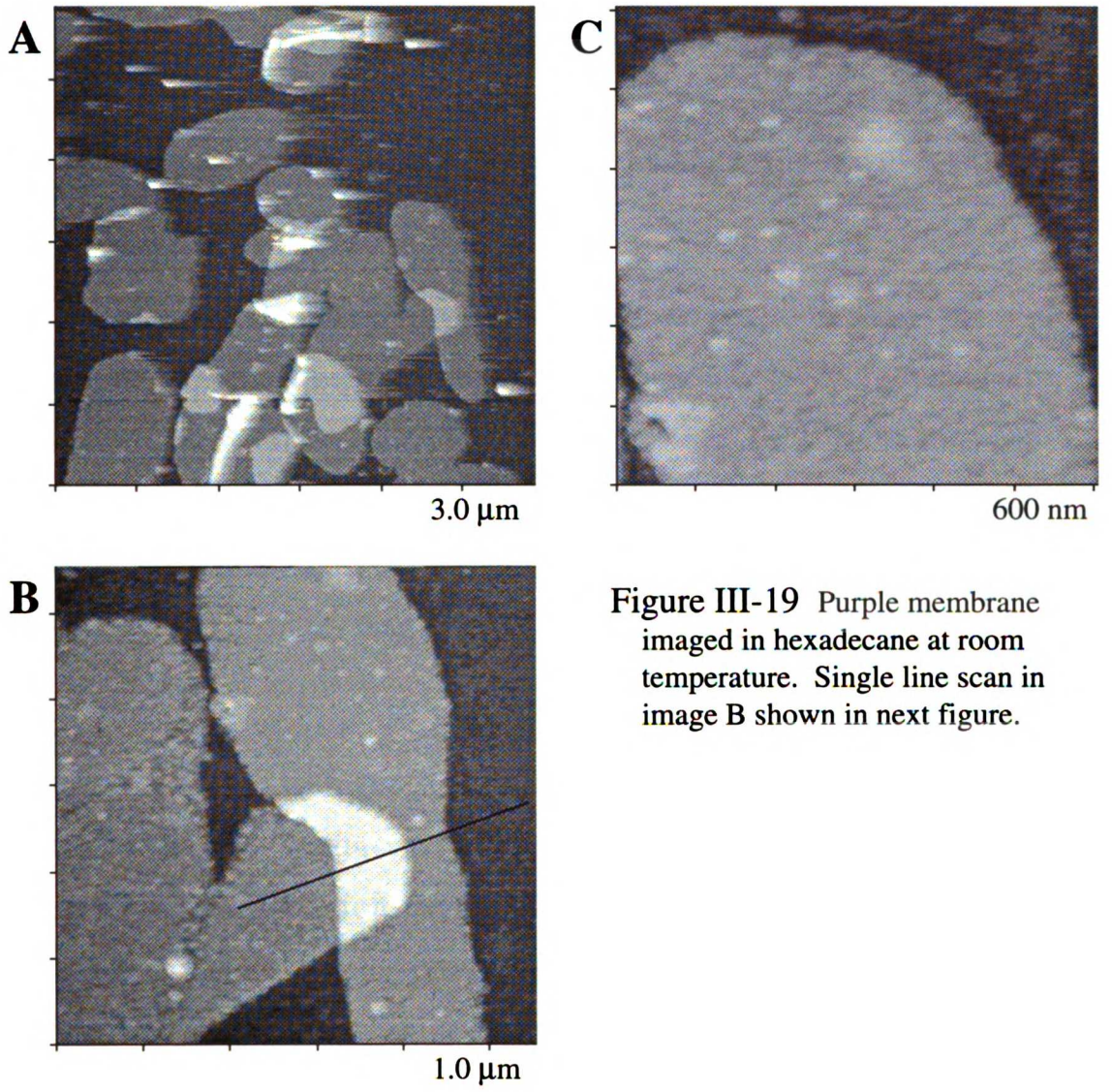

Figure III-19 Purple membrane imaged in hexadecane at room temperature. Single line scan in image B shown in next figure.

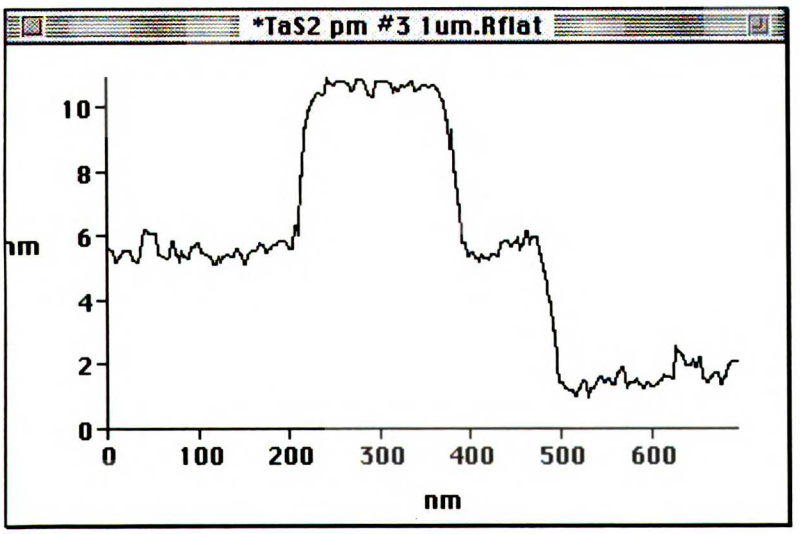

Figure III-20 Single line scan as indicated in previous figure. Note height of double layer of membrane.

This was a slow scan, and thus represents our best height data, given the uncertainty of our Z calibration. Clearly, lower imaging forces resulting from scanning samples in liquids improved the image quality of relatively elastic biological samples.

Scanning samples in liquids potentially allows one to examine the sample in something approaching their native state. This has several advantages, including the possibility of perturbing the sample and observing the results, in real time. Although the design of our machine precluded making any biochemical sample modifications while scanning, we were able to observe some interesting changes made during the sample preparation/imaging process.

During our work with purple membrane, we became interested in preparing and imaging our samples without exposure to air. This was in the hope of minimizing the distortions and possible artifacts that can be expected to occur to the lipid surface and protein lattice due to drying in N_2 or air. We modified our sample preparation procedure so that the sample surface was not dried. Purple membrane monolayers were made as before, except that the sample remained in a buffered aqueous solution. Sample carriers were then washed and transferred through a series of increasing concentrations of ethanol, or more typically acetone. The acetone, soluble in both water and non-polar hexadecane, allowed us to transfer the samples into hexadecane for scanning.

An intriguing purple membrane sample, treated with acetone, is shown in Figure III-21. In these images, the membrane surface is seen to exhibit a large number of holes, typically with regular sides. These holes (image III-

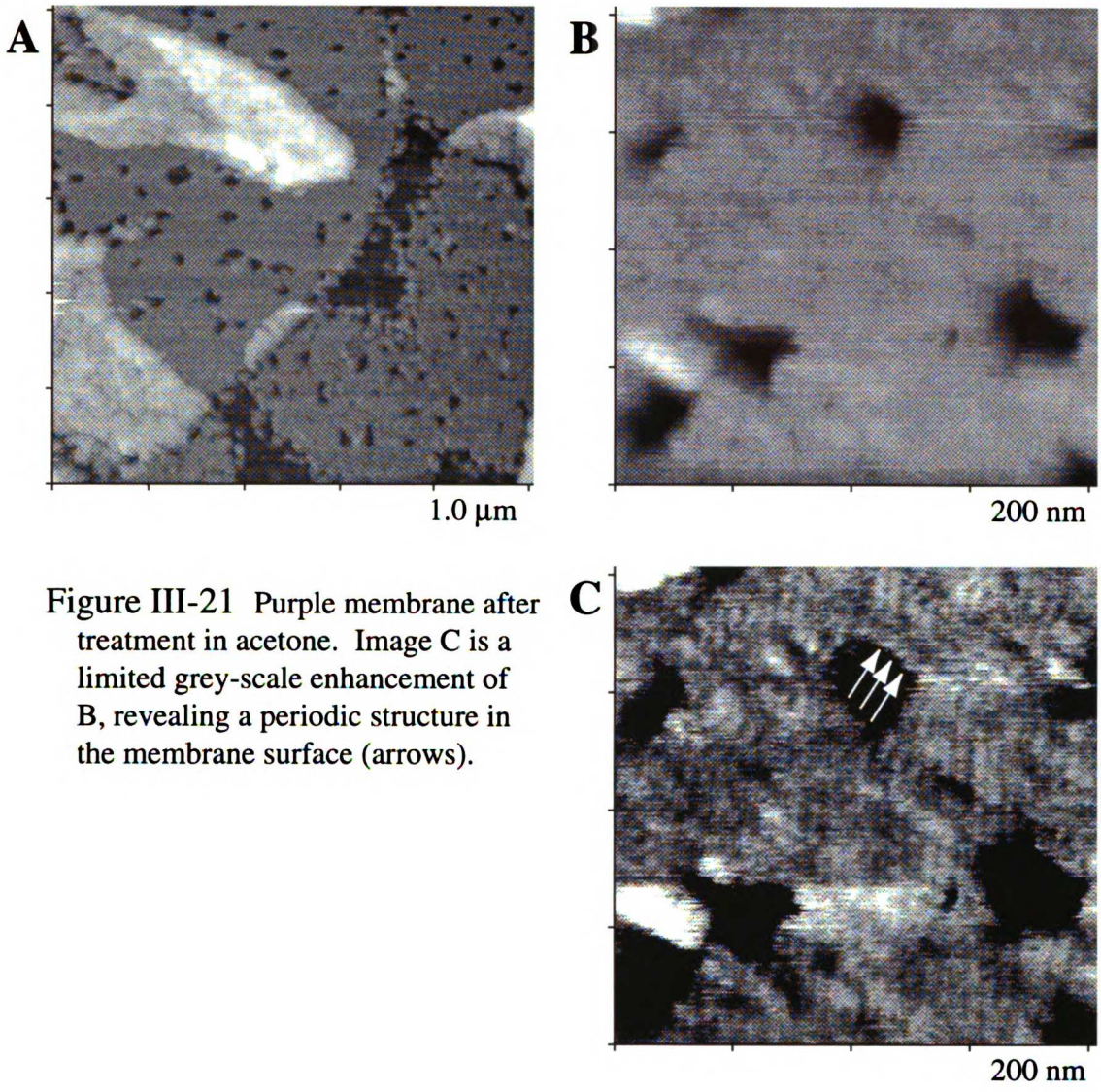

Figure III-21 Purple membrane after treatment in acetone. Image C is a limited grey-scale enhancement of B, revealing a periodic structure in the membrane surface (arrows).

21 B) are similar to the pits observed in one of our purple membrane TEM images (Figure III-7), and may be due to localized removal of membrane protein by the acetone wash. Closer examination of these images reveals subtler surface features as well; the membrane surface (Figure III-21 C) has a smaller scale surface structure not apparent in our earlier micrographs. Image III-21 C is identical to image III-21 B except that the gray scale has been compressed to maximize image contrast of the membrane surface. As a result, elevated and depressed image details appear "saturated" as white or black. In image III-21 C, we see a number of periodic components, at differ-

ent angles, as indicated by the arrows. These patterns appear to have a periodicity of about 7 nm, measured directly on the image. The strongest periodic components are in the scan direction, which raises the possibility of a scan associated artifact. The visual observation of several other angular orientations, however, make this rather unlikely. Interestingly, this 7 nm pattern is quite close to the expected lattice size of 6.2 nm for the bacteriorhodopsin molecules. It is possible that we are beginning to resolve the lattice structure in these images.

We imaged purple membrane at low temperature in liquid n-pentane and isopentane. Figure III-22 is a series of images of PM in isopentane at 143 K from mid to high magnification. Figure III-22 A shows membrane patches similar to those seen at room temperature; note sections of overlap. Image III-22 B is a higher magnification scan of a single patch of membrane, and image III-22 D a 300 nm scan of the membrane surface. Figure III-22 C and E are the corresponding expanded gray scale images, chosen to enhance any surface structure or features. The height of these membrane layers is about 4.2 nm, which compares reasonably well to room temperature values, and is subject to an uncertainty of about ± 20 %.

The surface of the membrane (Figure III-22 C & E) has a characteristic roughness. This apparent surface structure was quite stable and reproducible during the experiment, but the features are clearly too large to be the lattice structure of the membrane. These features are also too rough to be the membrane surface directly, and in all likelihood are due to a layer of surface contamination. A difficulty of working in liquids, or indeed any conditions other than ultra high vacuum (UHV), is that the surface adsorbs a thin layer of contamination. Interestingly, working in air can actually be advantageous

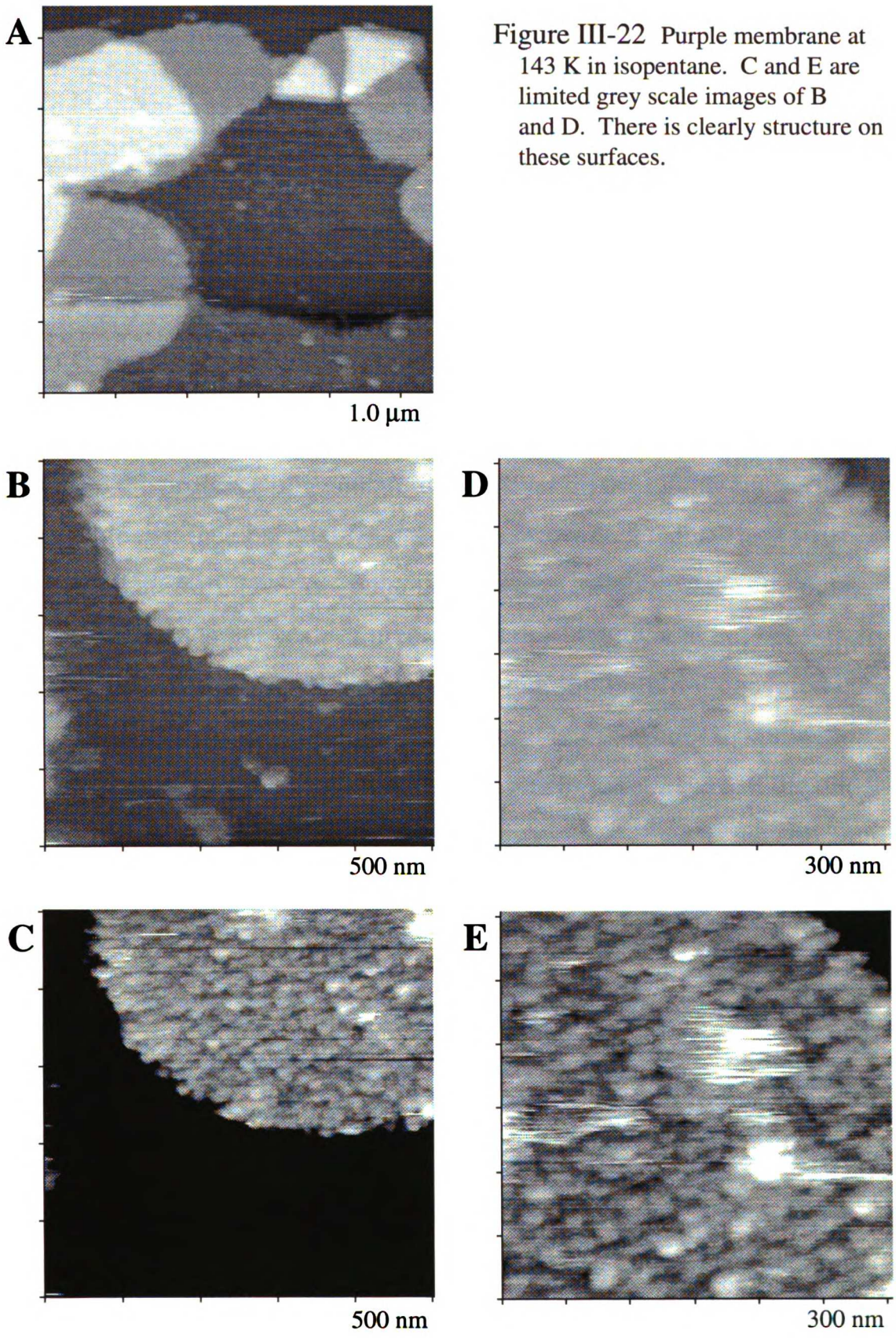

Figure III-22 Purple membrane at 143 K in isopentane. C and E are limited grey scale images of B and D. There is clearly structure on these surfaces.

in that the higher imaging forces can sweep the sample clean.

The idea that the surface texture of these images is associated with a contamination layer is supported by the presence of a similar roughness on the mica substrate. Freshly-cleaved mica often exhibits a roughness when imaged in liquids; adsorbed contamination might explain why it has so far been virtually impossible to image mica atoms at 143 K. The roughness pattern on the membrane does usually exhibit a larger amplitude than the mica background, possibly due to the added elasticity of the membrane.

Despite the presence of a contamination layer on the membrane surface, it is possible that the observed features do in fact reflect real surface structure. A thin, uniform layer of contamination may follow surface contours, and even enhance larger scale structures. Such a layer would not necessarily result in an overestimation of the surface height, if it uniformly covered both sample and substrate. A discontinuous, or localized, surface contamination may be influenced by the topographical and biochemical nature of the underlying sample surface. An interesting possibility is that some of the contaminating species may preferentially adsorb to specific reactive areas on the membrane surface.

Such a mechanism might help explain why some of the surface structure, if it is surface contamination, appears to be oriented in rows over certain localized areas of the membrane surface. A 250 nm subset of Figure III-22 E, and its 2-D Fourier transform, both unfiltered, are shown in Figure III-23. The subtle periodic pattern is reflected as diagonal points in the transform, although rather faintly, and is unlikely to be due to scanning artifacts. It is possible that such surface "decoration" (analogous to metal decoration in

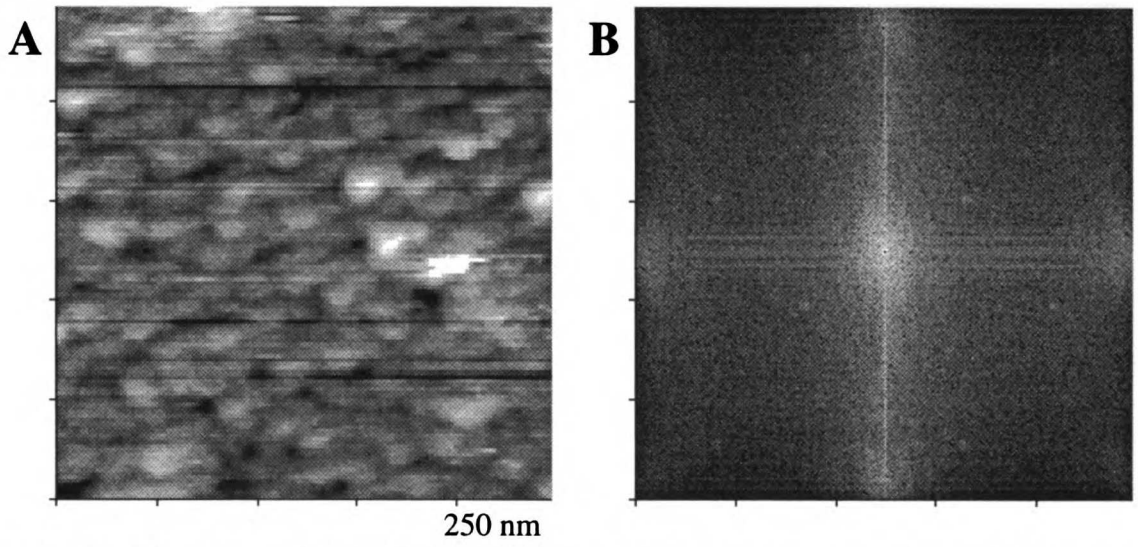

Figure III-23 A is a subset of figure III-22 B; and B is the corresponding 2-D Fourier transform, indicating some periodic structure.

TEM), intentional or otherwise, may yield structural or biochemical information about a sample.

RNA

Our SFM examination of biological materials will now proceed from large membrane samples to relatively large single molecules and molecular fragments of double-stranded RNA (ds-RNA). RNA is a good candidate for SFM due to its large size, and structure topographically similar to collagen. Our images of reovirus ds-RNA were obtained from samples prepared and provided by Dr. Yuri Lyubchenko (Arizona State University). The ds-RNA was chemically attached to the mica surface by treating the mica with 3-diaminopropyl triethoxysilane, to create a silanated substrate (Lyubchenko *et al.*, 1992; Henderson *et al.*, 1992). The treated mica surface is placed in a 0.1 μg/ml solution for several hours, removed, rinsed in dd H_2O and vacuum dried. These samples were additionally characterized by TEM, gel and SFM at room temperature by Dr. Lyubchenko.

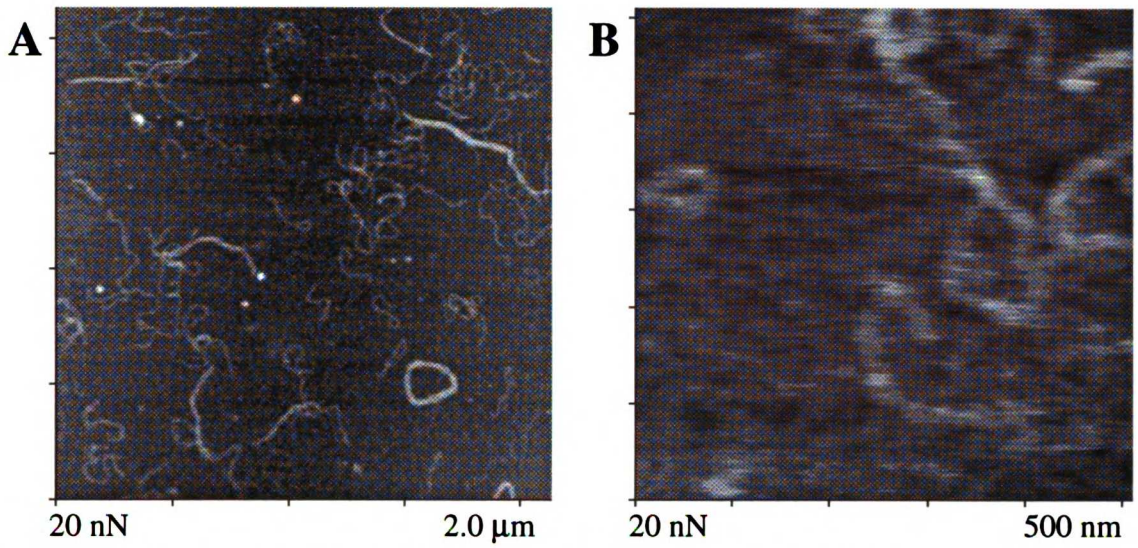

Figure III-24 Double stranded RNA images in air. Note high forces.

Our SFM scans of ds-RNA at room temperature are shown in Figure III-24. Figure III-24 A, a 2.0 µm low magnification scan, shows distinct ds-RNA fragments from a few tenths to about 1 µm in length. In the lower right corner is a coil of ds-RNA, a pattern we saw repeatedly, which appears to be made up of multiple strands. As we have seen previously, however, at high magnification (image III-24 B) the image becomes smeared and sticky due to high imaging forces. Both of these images were acquired at a relatively low force (for air) of about 20 nN. These data do show the utility of this preparation technique, given the difficulty other workers have had in imaging DNA and RNA in air.

Two similar ds-RNA samples, scanned at 143 K, comprise Figure III-25. Figure III-25 A and C are 1.6 µm scans from separate experiments; images B and D are their higher magnification counterparts. Images III-25 A and B show coils of ds-RNA which are more distinct than those imaged in air. The coils are clearly comprised of multiple loops of ds-RNA. A second common ds-RNA motif that we observed is shown in Figure III-25 C, in which a

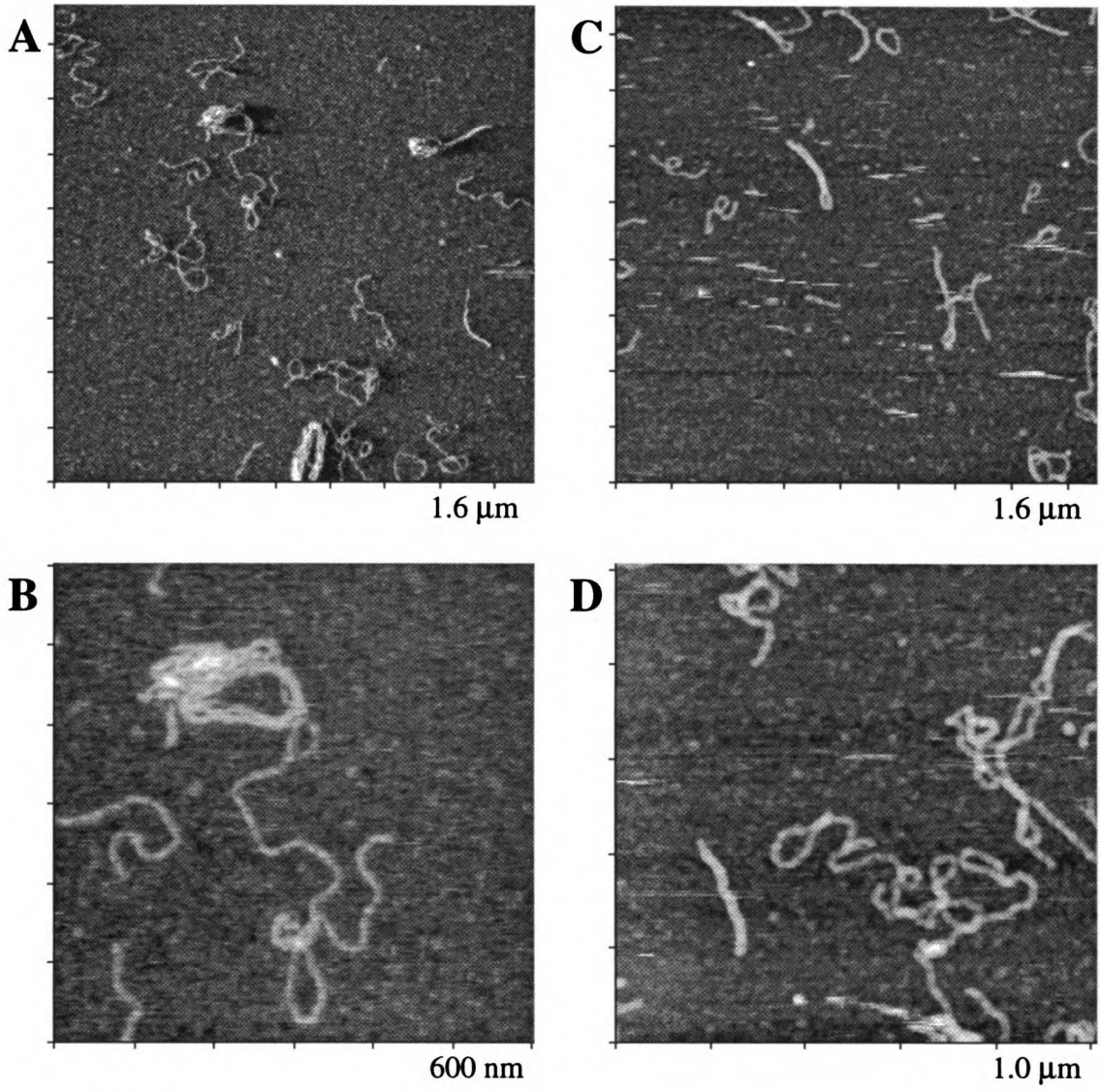

Figure III-25 Double stranded RNA at 143 K, force ≤ 1 nN.

strand of ds-RNA appears to double back on itself and twist together (arrow). These images all show a quantitative improvement in image quality when compared to the room temperature air images. This is due in large measure to the lower (≈ 1 nN) scanning forces used for the 143 K images. Additionally, there appears to be a qualitative improvement in the images that may be attributable to scanning at low temperature, reinforcing our earlier observations of ferritin at 143 K. However, we have no comparable room temperature data for ds-RNA in liquid, so the improvement seen here

may be due solely to the reduction in imaging forces.

We can use selective application of imaging force to modify a single piece of ds-RNA. Figure III-26 A is a 500 nm scan of the single twisted ds-RNA fragment depicted in Figure III-25 C. After image 26 A was taken, the tip was scanned at a fixed Y position at a force of about 100 nN. A subsequent scan (Figure III-26 B) shows that this localized high force scan cut the ds-RNA molecule.

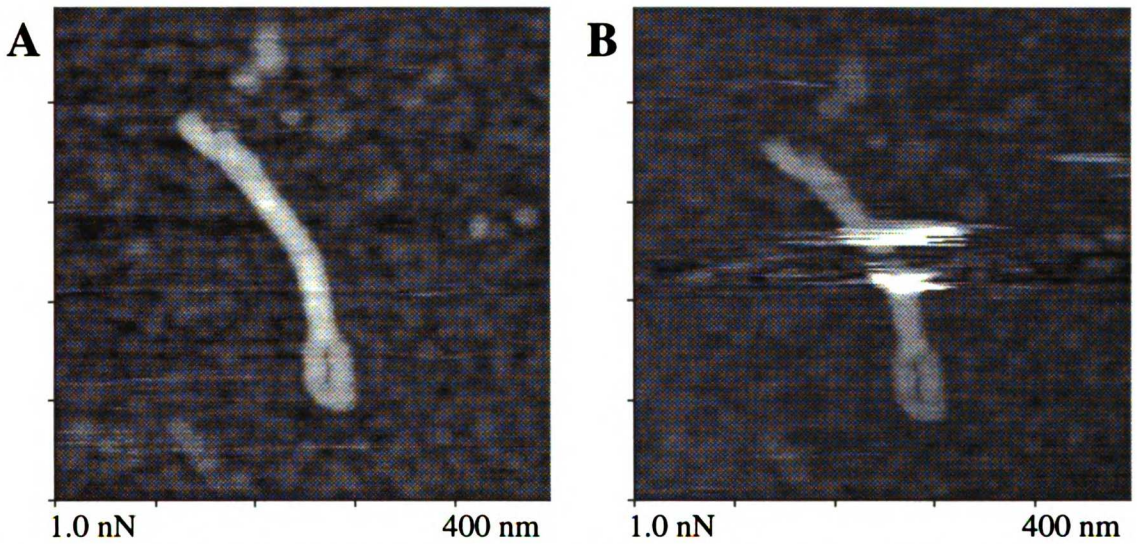

Figure III-26 RNA strand from III-25 C, machined with a localized 100 nN X scan.

Room Temperature Collagen

The first SFM collagen images presented here (Figure III-27) were obtained in isopentane at room temperature. This type I lathyritic collagen sample was applied at 2 ng/µl, diluted from the same solution used for all collagen SFM preps, TEM, and gel work. This particular experiment represents our best room temperature images, and will serve as a comparison for our low temperature images. Individual molecules are distinct, although not

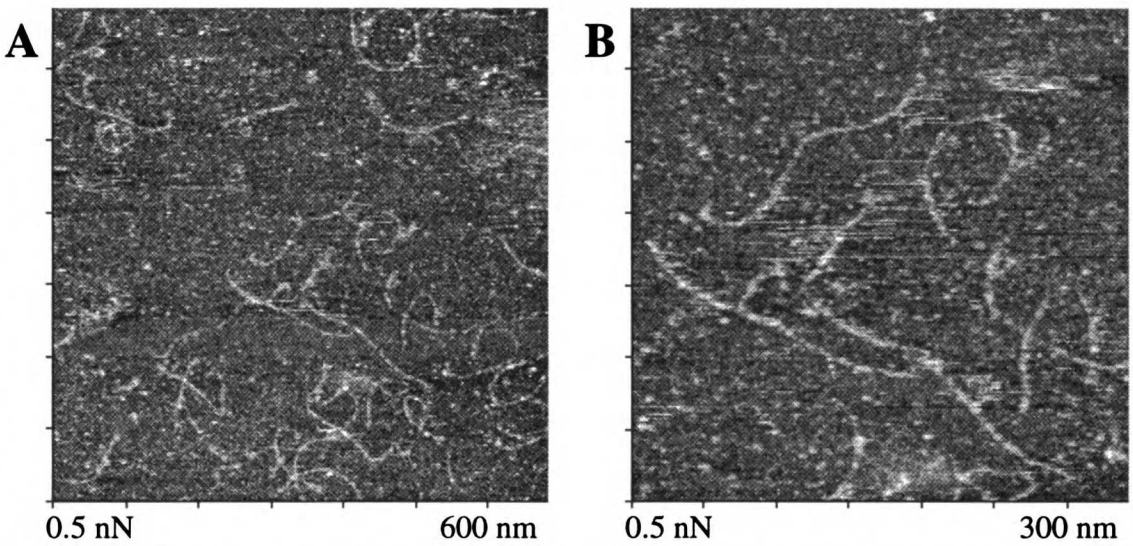

Figure III-27 Collagen monomers imaged at room temperature in isopentane.

very clear. Despite an imaging force of only 0.25 nN, the images are sticky.

The length of the molecules is similar to that determined by our TEM studies (Figure III-9). However, the ends of the molecules are not very distinct in either case, creating measurement uncertainties. Part of the problem is that the background is quite rough, at least in the SFM images, most likely due to contamination. Some of the background is comparable in height to the collagen molecules, and forms a sort of noise. A similar background would be difficult to image in shadowed TEM preparations. We are able to characterize the surface "roughness" of a sample as part of the MacAcquire program, by measuring the RMS deviation of a surface region relative to a plane fitted to the same region. The background of Figure III-27 B has a RMS roughness value of 0.24 nm, which is a quantitative estimate of the background surface noise. This value is typical for our room temperature data, although we did obtain one image during another experiment with a RMS roughness of 0.15 nm.

The apparent height of these collagen molecules is about 0.6 nm, com-

pared to an expected value of 1.5 nm. This reduction in molecular height is generally about what we measure for all of our collagen images, and the discrepancy is probably due to a number of factors. The elasticity of the collagen molecule will allow for compression by the imaging forces, which locally have high tip contact pressures. Additionally, the collagen is bound to a mica surface which is covered with an uncharacterized layer of contamination. Thus the collagen may be embedded in contamination or impurities, which appears to raise the background surface relative to the molecule.

Measurements of the width similarly are not in agreement with the known dimensions of the collagen molecule. The width in these images appears to be about 10 nm, compared to an expected value of 1.5 nm. This result is a function of the convolution of the shapes of the tip and sample. Our tips typically have a radius of 5 – 10 nm, which exaggerates the apparent width of smaller structures. The widening effect is a consideration in length measurements. However, due to the long length as compared to the width of the collagen molecule, it is a small percentage error. This error also has the benefit of being basically systematic, and thus potentially correctable, and does not influence height measurements, which are determined by vertical displacements.

The room temperature collagen images of Figure III-27 represent a control for our low temperature work. These are the best collagen images we obtained at room temperature out of 3 or 4 successful experiments, and give us some images to which we can qualitatively compare our collagen images at 143 K. Images of collagen fibrils in air have been published by Chernoff and Chernoff (1991) and by Baselt et al. (1993), and demonstrated the feasibility of imaging fibrillar sub-structure, but were unable to resolve collagen

monomers. We also attempted to obtain images of collagen in water using a Topometrix SFM, as an additional control. While this was a somewhat limited attempt, we did see a fleeting indication of molecules in a "lateral force" (frictional) mode. However, we were unable to obtain actual images. Recently, it appears that Chernoff and Chernoff have obtained images of single molecules in water using "tapping mode," although these images have not yet appeared in the literature.

Cold Collagen General

Collagen was my primary interest and the focus of the imaging phase of the LT-SFM project, and the area where we spent the greatest part of our effort. Each experiment with our cold SFM invariably had its own "character" in terms of image quality, sample appearance, and dynamic changes during the imaging process and from image to image. This was due to the large number of variables in a given experiment, some of which were not easily controllable or quantifiable. Probably the greatest variability centered on the individual tip shape, which was convoluted with the sample shape, and thus important to the resolution and topology of an image. Moreover, tip shape can change during an experiment, or become contaminated. Additional factors that influenced the quality of the images included the force/deflection characteristics of the cantilever, the resonant frequency of the entire imaging/scanning mechanical system, and alignment of the laser system.

The characteristics of the electrical portion of the experimental setup was important to each experiment, and to the quality of the imaging process. Noise was a constant consideration, and affected each experiment directly.

The response of the system to the feedback circuit could vary substantially, limiting the tracking of the tip and the scan speed.

Sample preparation was critical. A great deal of effort went into developing the collagen procedures outlined in the materials and methods. These represent a refinement of TEM preparation techniques adopted for our SFM. However, the requirements for SFM samples are exacting, including low contamination, uniform surface coverage over large areas, and proper concentration. Each collagen sample preparation proved to be somewhat variable, and quite unique. I suspect that pH, sample preparation technique, and possibly room humidity, were all important. Part of the difficulty was that a full successful cryogenic SFM experimental run was required to evaluate the quality of a SFM sample preparation. An experiment took two days to run at best, often without any usable data, making well defined and consistent sample evaluation difficult.

Perhaps the largest experimental variable was that each set-up and operation of the LT-SFM was a highly dynamic process, subject to the ability and behavior of two human operators (Shattuck & Gustafsson). Our low temperature SFM, by its nature, was designed to be a careful compromise of many different and demanding experimental factors. Although the machine performed remarkably well, it required the balancing of many experimental parameters to achieve a successful result, and could be charitably described as technically challenging. We would navigate through each experiment, which more often than not would end without any immediately useful data. Probably our biggest technical difficulty, aside from sample preparation, were problems that resulted in crashing the tip into the sample surface. Tip crashes were unfortunately periodically induced by the operators as well as

the machine hard and software. A reasonable analogy might be the "landing" of the tip on a remote planet surface, although in SFM it is a surface remote at the nanometer scale.

These dynamic experimental elements made it quite difficult to systematically investigate most experimental parameters. Each experiment would have distinct characteristics and nuances, and it was quite difficult to repeat and control each exactly. Ideally, enough data would have been collected that one would have increased confidence in our results, and a better understanding of the many interrelated experimental variables. However, it was difficult to collect a large quantity of data with our LT-SFM, as it often took months to get a single experimental result. Care must therefore be taken not to generalize our results too broadly, at least until other low temperature work is done in the SFM community.

Cold Collagen I

Images of collagen molecules at 143 K are shown in Figure III-28a. This particular experiment (January 15th, or 1/15, 1992) used our fractured tip as modified by Dr. Phil Russell (Materials & Methods). The images have particularly good contrast compared to the room temperature data of Figure III-27. The tip quality may have been related to the low initial contact force of about 1.5 nN during walk-up. Collagen was applied at 1.0 ng/μl and coverage was quite uniform, as seen in the large scale (1.4 μm) scan of Figure III-28a image A.

This series of images (Figure III-28a) is a set of sequential scans of the same area, at differing magnifications. A number of observations are immediately remarkable: the stability of the sample and the reproducibility of the

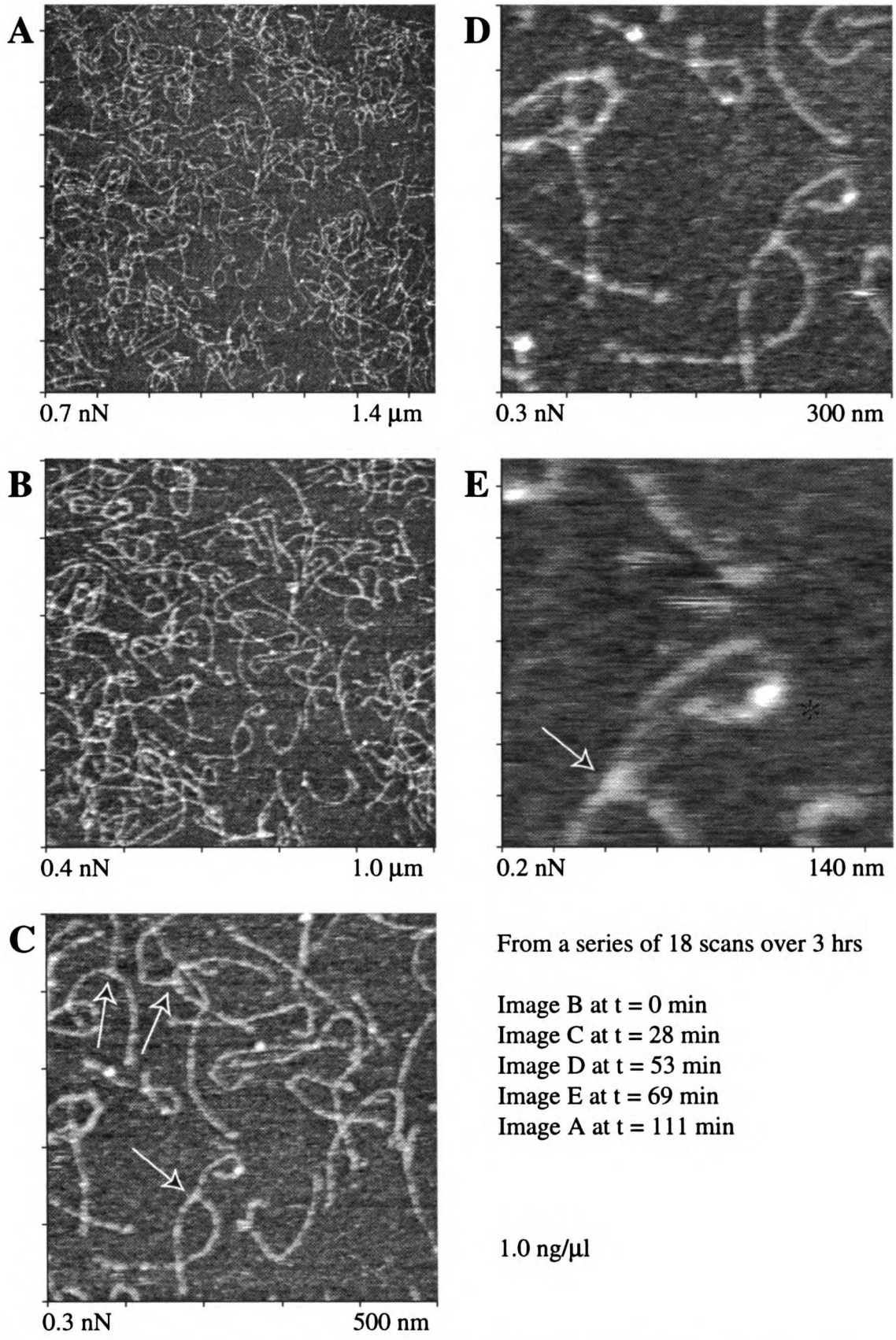

Figure III-28a Collagen molecules at 143 K (1/15 exp.) at increasing magnification.

images. Images A through E were obtained over a period of about 2 hours; in all we took 18 scans over a period of 3 hours. None of the images shows any noticeable changes, except, of course, for the size of the area imaged. As an example, image E is a high magnification view of the intersection of two molecules, which appear to be associated in the form of a "tee" (lower left corner, arrow). These two molecules can be observed back through the entire magnification series, and are still visible in the lower center of image A. There is no discernible change in the appearance of the two molecules. Subtler features, including variations along the molecular axis, such as the "bump" in the upper curving arm of the tee, are re-imaged with a high degree of consistency.

The images shown in Figure III-28a are qualitatively improved compared to room temperature images. This was true for the majority of our cold work. A large part of the qualitative difference may simply be due to a less sticky image, or reduction in the roughness of the background. At this point, it may be premature to directly associate this improvement with operation at low temperature, due in part to the difficulty in obtaining data controlled for other experimental variables, such as the imaging tip. The cold images are, however, of consistently higher quality.

One clear improvement is a significant and quantitative reduction in background surface roughness. The RMS roughness for the central background area of image D is 0.09 nm, which compares favorably to the value of about 0.2 nm obtained for the room temperature images of Figure III-27. This reduction certainly makes the molecular images more distinct, effectively improving the signal to noise ratio of the image. Such improvements have the advantage of making it easier to determine some structural features,

such as the ends of the molecule.

Dimensions of the collagen molecules, while easier to see, are not significantly improved at low temperature. The apparent width and height of the molecules are about that of room temperature images. This is not surprising, given that tip size is temperature independent and resolution limiting. The smooth background does, however, make features more readily visible, as shown in Figure III-28b. This figure is a single line scan taken from a subset of Figure III-28a E. The plot is a vertical slice taken through the image, so that the x axis is the lateral position along the line scan, and the y axis is the vertical height of the image at that point. The line scan passes through both the molecular axis and the larger bump at about 90 degrees. The molecule has an apparent width of about 10 nm and a height of about 0.5 nm; the bump is 15 nm wide, with a height of about 1.0 nm.

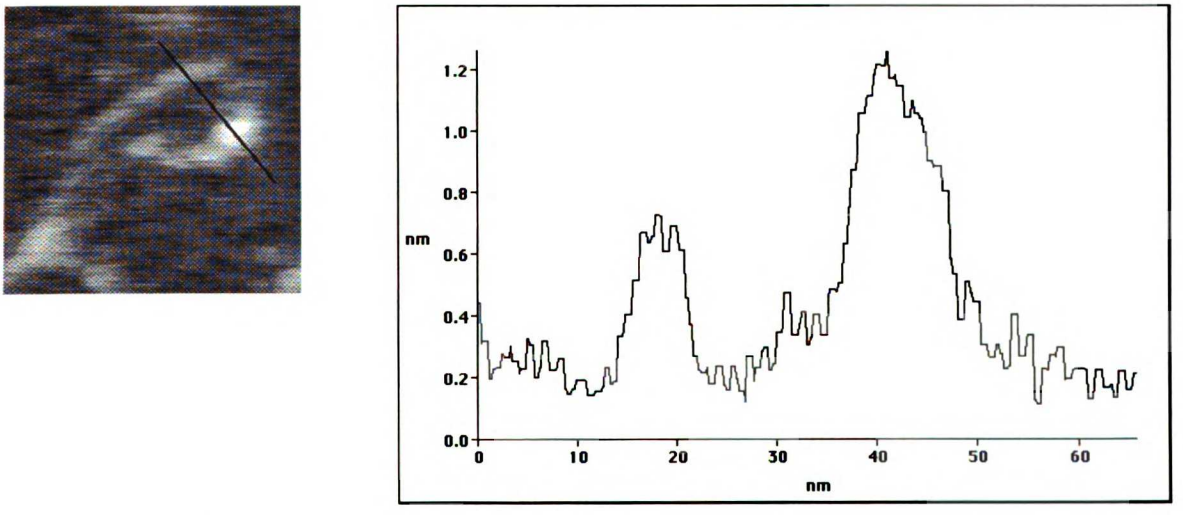

Figure III-28b Subset and corresponding line scan from image III-28a E showing apparent height of features.

"Bumps" are interesting features of unknown origin. Our collagen images are unable to resolve molecular substructure directly, at least with any

certainty (such as helical periodicity or α chains). The bump shown in Figure III-28b, which is a relatively large structure, was thus unlikely to be due to any direct imaging of a molecular feature. Similar bumps were, however, quite common, at least in this experiment. In image B and C (Figure III-28a), one sees a relatively large number of these bumps located along collagen molecules, while there are few such bumps in the background.

Although it is possible that these bumps may be due to some change in or local denaturation of the triple helical structure, it is likely that the bumps are some form of uncharacterized sample impurity "decorating" the collagen molecule. Small amounts of impurities in the system could be acquired during preparation of the collagen, or during the generation of samples for SFM. In fact, sample preparation may have served to concentrate impurities in solution; a large volume of sample in contact with a surface for a long time could contaminate the surface by continuous adsorption. Nevertheless, bumps may still reflect the underlying structure of the molecule, since these impurities may be preferentially adsorbed, or attached, to reactive regions of the molecule. This is not unlike procedures used in TEM in which a sample is deliberately decorated with another compound.

Another feature of these images is inter-molecular associations of collagen molecules which resemble a "tee." Images D and E (Figure III-28a) show such a tee, where the end of one molecule associates with the middle of another. There are three clear examples of these tees in image C (arrows), as well as several other possible candidates. While it is certainly possible that tees could be due to random alignment of the molecules, I believe that they are due to some direct, although unknown, interaction of the molecules. This could possibly involve the telopeptides of one molecule with a reactive

site on the other. It is unlikely that tees are purely random, since we do not see them in all experiments, and in the same high proportion, as in these images. Furthermore, the images imply some active interaction; the presence of one molecule appears to directly effect another. Note how the middle of the upper tee molecule in image D appears to be deflected, or "tugged" in the axial direction of the lower molecule.

The overall physical appearance of the molecules reaffirms that collagen molecules are indeed flexible. These molecules, as adsorbed to the mica surface, demonstrate a great deal of curvature, in contrast to the popular and continuing misconception of collagen molecules as "rigid rods". It may be that some parts of the molecule are more flexible than others as well. Curvatures are often seen to vary abruptly, resulting in distinctive "kinks" in the molecule. This is consistent with the notion of intramolecular flexible regions.

In its natural state, most collagen occurs in a largely straight, linear conformation, bound into a semi-crystalline state of fibrils and fibers. One must therefore consider the argument that individual collagen molecules do not really represent the native state. We have taken molecules in a 3 dimensional solution and bound them onto a surface, no doubt with some locally high forces due to drying and surface tension effects. So the argument that we are not examining molecules in a native state is reasonable; and in fact a similar argument can be made for a variety of biophysical investigations. Nevertheless, we are interested in examining the physical characteristics of single molecules, changes in these physical characteristics due to external forces, and possibly the relationship between individual monomers and properties of the bulk material. For such investigations, our approach is

reasonable. Additionally, we ultimately may be able to relate physical characteristics to biochemical ones; for example flexibility to biochemically reactive regions of the molecule. This is one of the potential strengths of SFM investigations, allowing one to conduct dynamic investigations at the sub-molecular level. We will, however, have to be cautious about generalizing to the native state.

A second duplicate sample scanned during the 1/15 experiment is shown in Figure III-29. Sample changing involved a delicate procedure where the sample, mounted on a magnetic carrier, was removed from the cold SFM. A new sample was plunged into the cold isopentane, and mounted on the scanner rails (Materials & Methods), with some chance of crashing the tip (and occasionally completely breaking it off!). This sample change was followed by re-cooling the n-pentane ice bath with liquid N_2.

The images in Figure III-29 are a series of scans at increasing magnification that focus on an extended collagen molecule with two distinctive bumps. The images are a bit confusing due to the double image of each feature, slightly displaced in the X direction. This is the result of imaging with a "double tip," a relatively common artifact in both STM and SFM. Compare this figure with the previous figure. Both images were made during the same experiment and with the same tip (albeit different samples). A modification of the tip, possibly due to a tip crash during sample changing or approach, has altered the image significantly. Interestingly, the double tip has resulted in two images of a given feature, with apparently higher resolution than seen in Figure III-28a. This could be a candidate for the "if you can't fix it, feature it" axiom prevalent among professional auto racing teams. As pointed out by Helen Hansma (1992), the presence of two images

of the identical molecule, effectively made by two separate tips, could be an advantage in determining unique information about both the sample of interest and the structure of the tip. This does demonstrate the importance of the tip on image formation in any SFM interpretation.

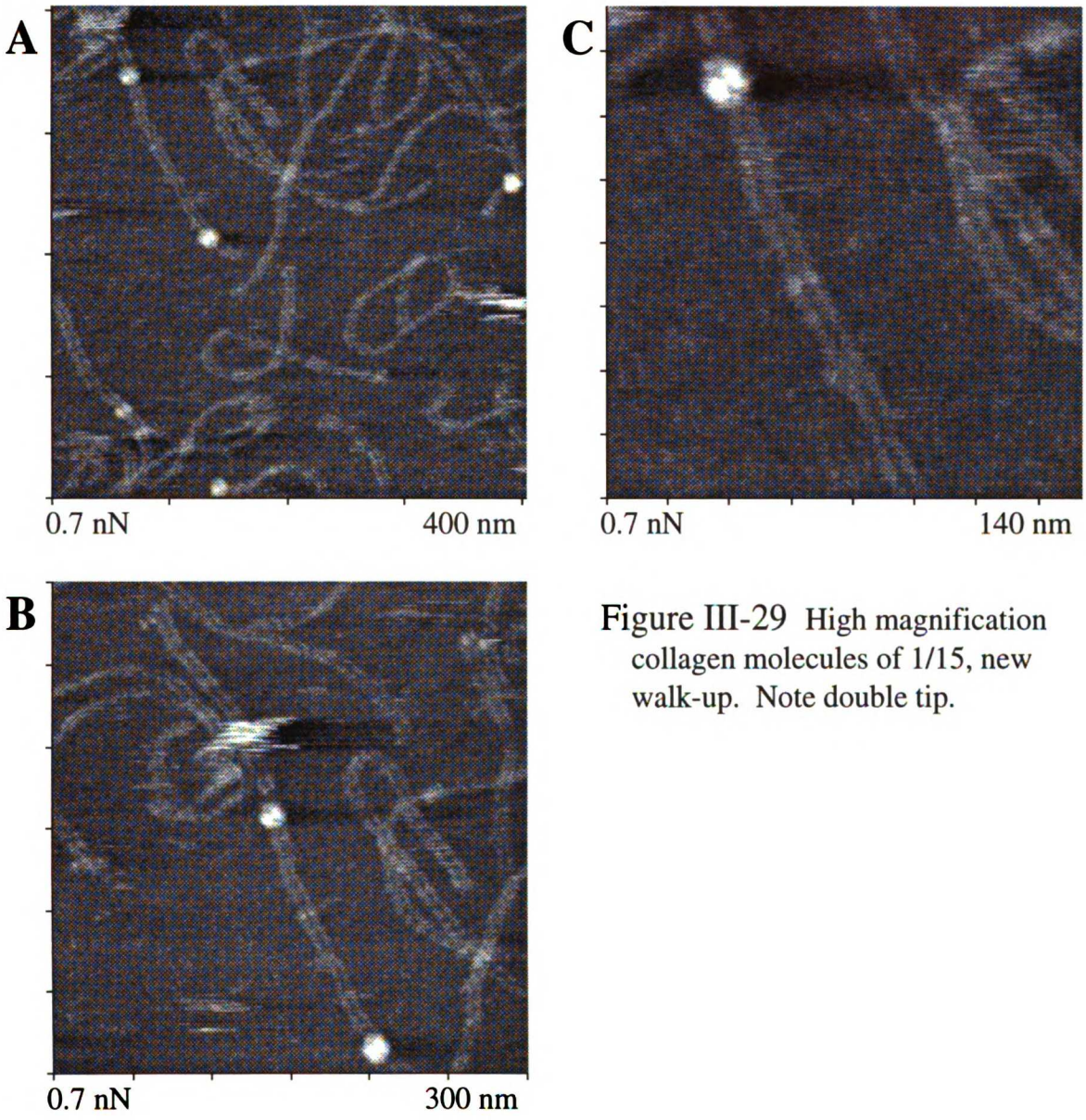

Figure III-29 High magnification collagen molecules of 1/15, new walk-up. Note double tip.

The tip of Figure III-29 has produced apparent molecular widths that were narrower than those of Figure III-29a. Image III-29 C has widths of 4

to 5 nm, a significant improvement. The background roughness is also slightly improved, to about 0.08 nm. The bumps in these images are also clearly associated with the collagen molecule.

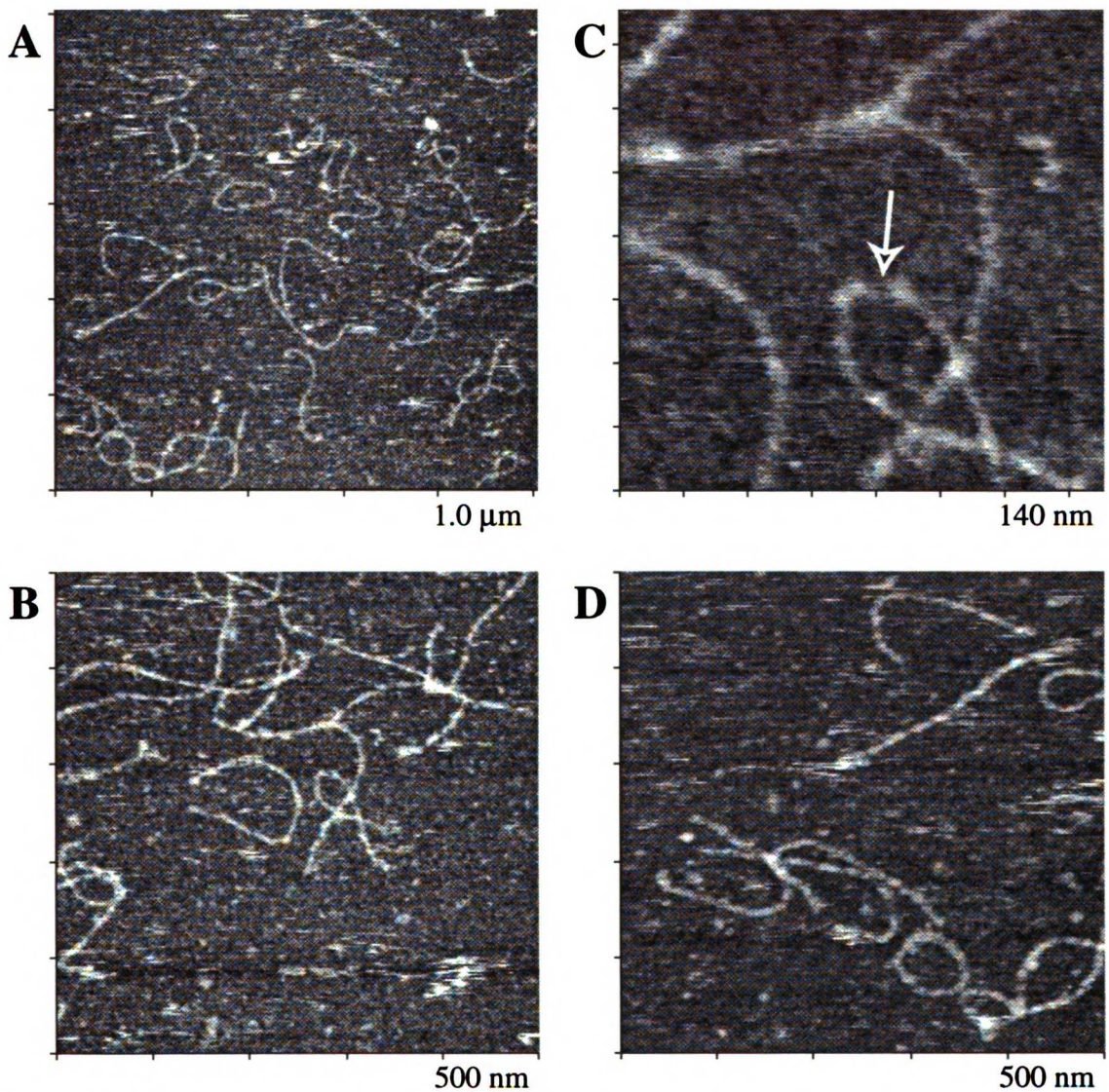

Figure III-30 Collagen images from 1/17 experiment (0.4 ng/µl). Note apparent break in C (arrow).

Cold Collagen II

The images from a second low temperature collagen experiment from January 17, 1992 (1/17) are shown in Figure III-30. Image A is a 1.0 nm

scan showing individual molecules similar in appearance to 1/15. The coverage is lower; a collagen concentration of 0.4 ng/μl was used to prepare the samples. Lower coverage has the advantage that it is easier to locate isolated, individual molecules; making it simpler to measure molecular features. We see fewer associated molecules in this experiment, possibly a result of the lower concentration, or variability in some other experimental conditions.

Image quality of 1/17, and the apparent width of the molecules (about 10 nm), is comparable to the initial 1/15 data. Since the tip used for the 1/17 images was an unmodified fractured tip, these data indicate that our tip has an imaging resolution at this size scale comparable to the e-beam grown tip used on 1/15. The background roughness is also comparable, with a RMS value of 0.12 for image B (Figure III-30). Image B, and a subsequent scan at higher magnification (image C), show flexible molecules, and possibly a tee. Additionally, one of the molecules appears to have sustained a break, most likely induced by the scanning tip, as indicated by the arrow in image C.

Image D shows an interesting set of three molecules (lower left). All the molecules overlap at about the same distance from one end of the molecule. This suggests a reactive area of the molecule. This area of these molecules, 62 to 68 nm from one end, may correspond to the P-15 region known for its functional reactivity (Scaria *et al.*, 1990). Future work could possibly establish and test this relationship.

The clarity of these LT-SFM collagen images, compared to TEM micrographs, raises the hope of accurately and directly measuring molecular fea-

tures, such as length. I would hesitate to claim a great resolution advantage of SFM over TEM, as SFM dimensions are convoluted with and limited by tip shape. This limitation is comparable to the resolution limits imposed by the metal grain size of TEM images. SFM, however, measures molecular dimensions directly, and relatively small dimensional changes can be expected to be resolved with high precision. Tip errors can, in principle, be corrected, if the tip shape is accurately known (Griffith *et al.*, 1991); a difficult proposition, as the tip/sample interaction is not linear. There is a fundamental advantage in that tip errors are systematic, whereas the TEM grain-size distributions are relatively random. Systematic errors directly bias the absolute value of a parameter (such as the mean length), but do not necessarily affect the variability in that parameter. Moreover, SFM images appear "clearer" than corresponding TEM images, since the background is smoother and less "noisy." This facilitates accurate determination of molecular lengths by SFM.

Measuring molecular lengths from our SFM data is a relatively straightforward process, ignoring (for the moment) the issue of scanner calibration. The MacAcquire program has a curve length measurement routine (Figure III-31). Using the mouse, the operator traces a series of points along the molecule, which in turn are converted into a corresponding set of line segments. The program applies the appropriate scan corrections, and calculates the total length of these segments. In this way, the measurement is corrected for X and Y scan non-linearities inherent in the scan tube. Estimates of total length, as well as the position of interesting features, can be readily determined.

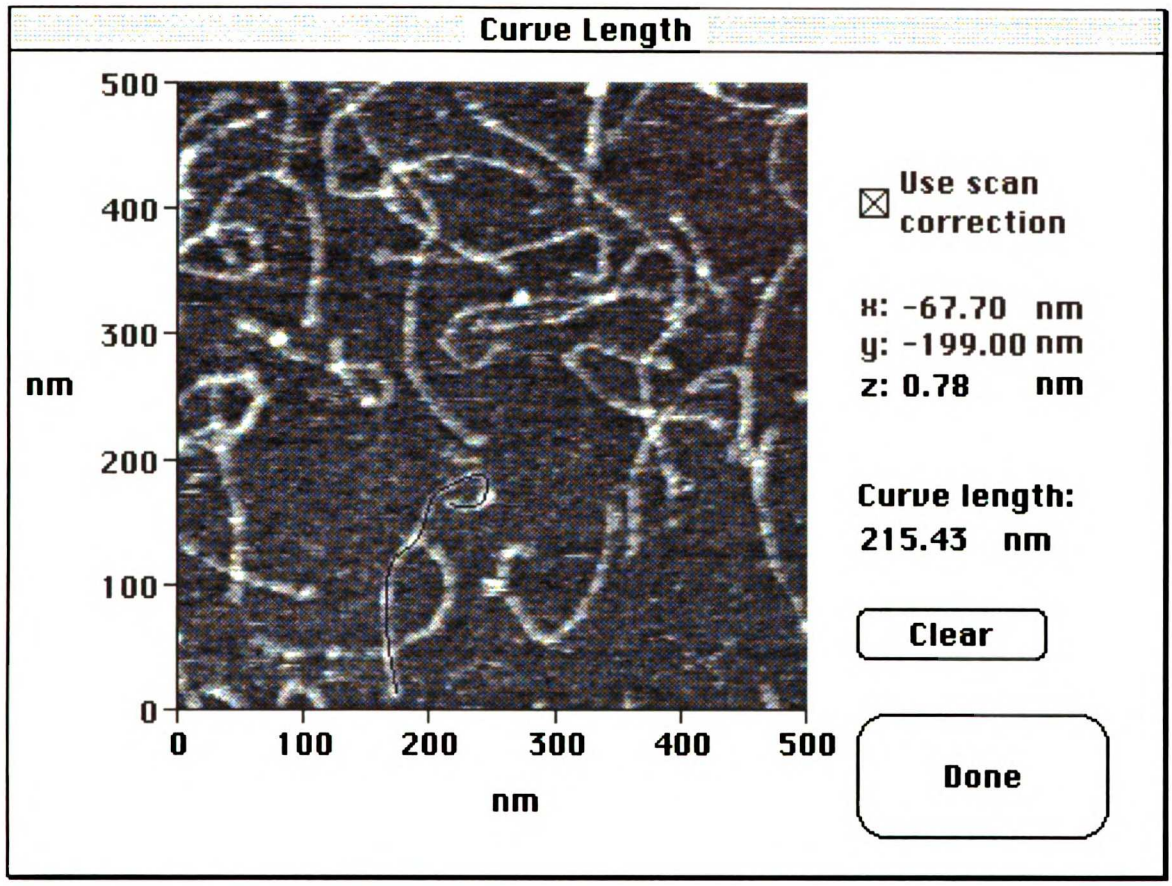

Figure III-31 MacAquire curve length dialog box and length of single molecule.

Cold Collagen Early Lengths

Estimates of total molecular length for both the 1/15 and the 1/17 experiments are shown in a histogram (Figure III-32). I combined both data sets due to the individually small sample sizes, and the proximity of data collection. The resulting length distribution has a mean (x) of 221 nm with a standard deviation (σ) of 17 nm. The total of n = 44 molecules ranged in length from 179 to 255 nm. This is substantially lower than the expected value of about 270 – 280 nm.

This mean length is close to values measured from our TEM images of identically prepared collagen. The lengths for individual molecules were

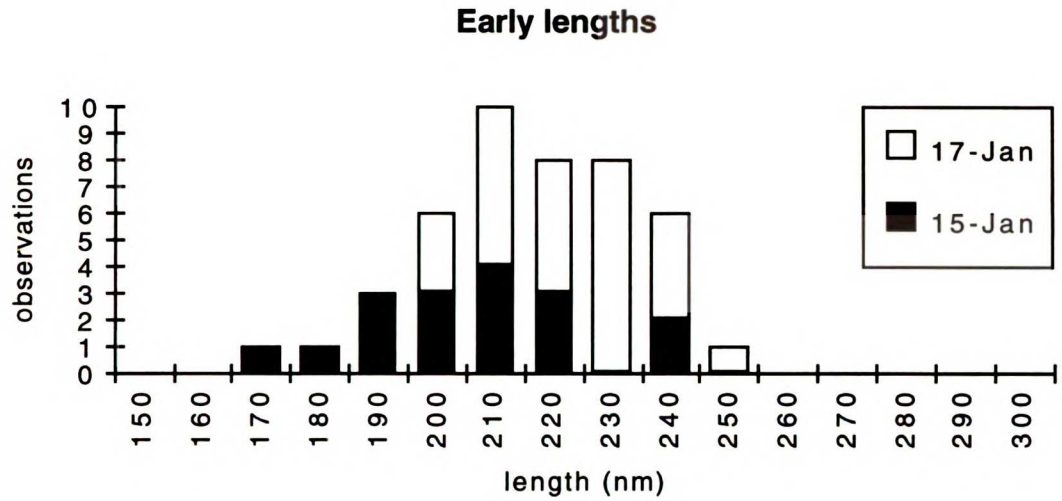

Figure III-32 Histogram of collagen length measurements of early data from 1/15 & 1/17 experiments.

determined by tracing the contours in the TEM micrograph (Figure III-8), and are subject to an uncertainty of about 5 %. The uncertainty of precisely determining the ends of a molecule in the micrograph was about 5 nm. The results of TEM length estimates for a similarly sized population of n = 35 molecules was x = 247 nm and σ = 28 nm, with a maximum of 305 nm and a minimum of 180 nm. This length estimate is also lower than expected, but agrees very well with independent length measurements made in the lab of Dr. Art Veis at Northwestern (personal communication). These measurements were made on a solution of type I collagen prepared identically to ours (our collagen was provided by Dr. Veis). The collagen solution was spread on mica and rotary shadowed. The result of Dr. Veis' study of n = 310 molecules was x = 251.2 and σ = 47.5, with a range of 161 – 480 nm. In all likelihood, the extreme length of 480 nm represents a dimer of two molecules (2 x 240 = 480 nm). Thus independent measurements of similar samples by TEM are in close agreement. Interestingly, the early (and ac-

cepted) TEM study of collagen lengths by Hall and Doty (1958) support our findings. They found a "number average" of 245 nm and significant variability. Interestingly, this work is often cited to support a molecular "weight average" length of 282 nm.

Compared to TEM length measurements, our SFM measurements of 1/15 and 1/17 are about 10 – 12 % low. This is not too surprising, considering uncertainties in our scan tube calibration, from which we can clearly expect deviations of about 10 %. This is particularly a problem for these two experiments; they were not conducted close to a successful calibration run, and *thus* required interpolation of the calibration parameters. Also, these early experiments were completed before we realized the importance of controlling for the period of the scan. These effects hopefully resulted in largely systematic errors, which can be expected to offset the mean with some fixed error, but leave the shape of the distribution intact. This assumes that these uncontrolled parameters, particularly the scan period, remained constant over the course of each experiment.

Close examination of the histogram of Figure III-32 supports the presence of systematic errors. The distribution of lengths is actually composed of two separate distributions for 1/15 and 1/17. Both have similar shapes (and standard deviations), but are offset relative to each other by 17 nm. A systematic error, or some unknown variable in sample preparation, could account for this. Such systematic errors do not effect the shape of the sample distribution, as reflected in measures of variability.

While our SFM and TEM measurements of collagen monomer length are thus in some reasonable agreement, both are shorter than the range of values

derived by other physical methods. Our measurements are for single collagen molecules in solution as adsorbed to a charged substrate, which may be different than for the native, semi-crystalline state. Differences in the charge structure along the molecule, as a result of acidic pH, could also effect the intra-molecular electrostatic forces and possibly the length (and conformation). Both TEM and SFM measurements would also underestimate molecular length if the telopeptide regions of the molecule are invisible to both techniques.

Perhaps as interesting as the issue of average molecular length is the variability in length. Variation in molecular length, as seen in the standard deviations in our measurement, seems to be an unusual finding. The variability in our SFM measurements is substantially less than the variability observed in our TEM lengths (about half). This still leaves significant variability which may reflect real differences in molecular length. SFM thus allows for a more precise measurement of collagen length than TEM. This isn't surprising given the improvements in image quality, definition of the molecule, and the limitations of grain size in TEM micrographs.

The issues of collagen length and variability could be more accurately defined in an experiment which addresses the limitations of the data from 1/15 and 1/17. Foremost is the small sample size, limited by the extensive collagen coverage which makes finding both ends of a molecule difficult. Additionally, it is advantageous to conduct an experiment that is close in time to a calibration run. It is particularly important to control the calibration parameters in order to minimize systematic errors, and to understand how random errors will enter into the final result. These errors determine the accuracy and precision of the measurement, as reflected in the length and

variability of the imaged collagen molecules.

1/15 and 1/17 Features

The MacAcquire program can be used to measure the relative position of features of interest, such as bumps and kinks, as well as molecular lengths. These measurements do have an additional problem in that we are not presently able to distinguish between the C- and N-terminal ends of single collagen molecules in an image. As a result, measurements are made relative to the nearest molecular end. Therefore, we do not know where two bumps on two different molecules are relative to one another, as they may be on the same or opposite ends of the molecule. Nevertheless, we do know where a feature is located relative to the closest end of a molecule. This will potentially superimpose two different distributions, one for each "half" of the molecule. This is not a large concern if we are simply interested in ascertaining if there is any non-random structure in the location of features.

Most of the collagen molecules exhibit substantial curvature, and a few appear to be noticeably kinked. I will define "kink" as a change in the orientation of the molecular axis greater than 45 ° occurring over a length of about one apparent molecular width. Molecular curvature and kinks are interesting given the common belief that collagen molecules are rigid rods. Flexibility and kinks may correspond to the predicted flexible regions discussed by Nestler et al. (1983) and Hofmann et al. (1984). A histogram of kinks (1/15 and 1/17) fitting my definition is shown in Figure III-33a. The histogram is unremarkable, with the possible exception of 3 observations at 40 nm. This distribution is clearly limited by insufficient observations, and could certainly be due to chance alone.

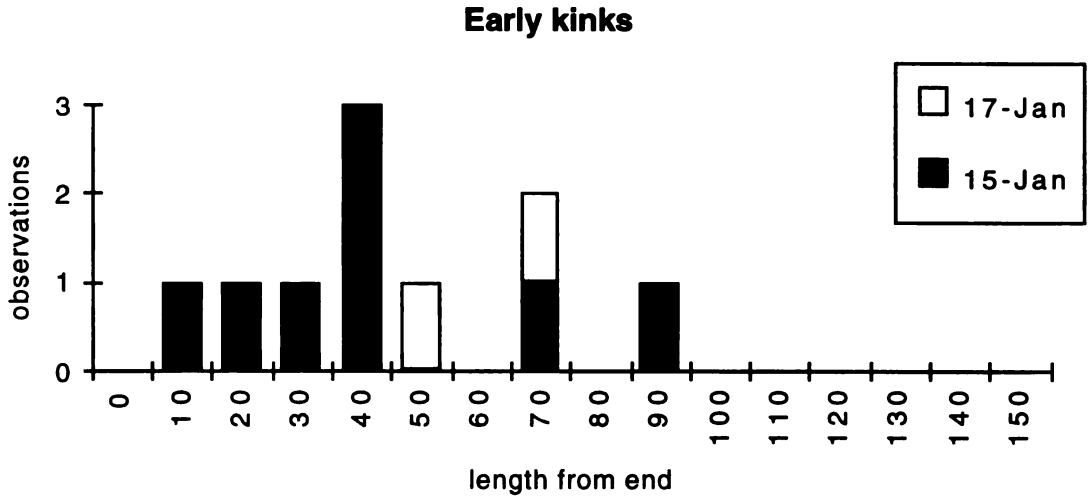

Figure III-33a Histogram of collagen kink position measurements as measured from nearest end of molecule.

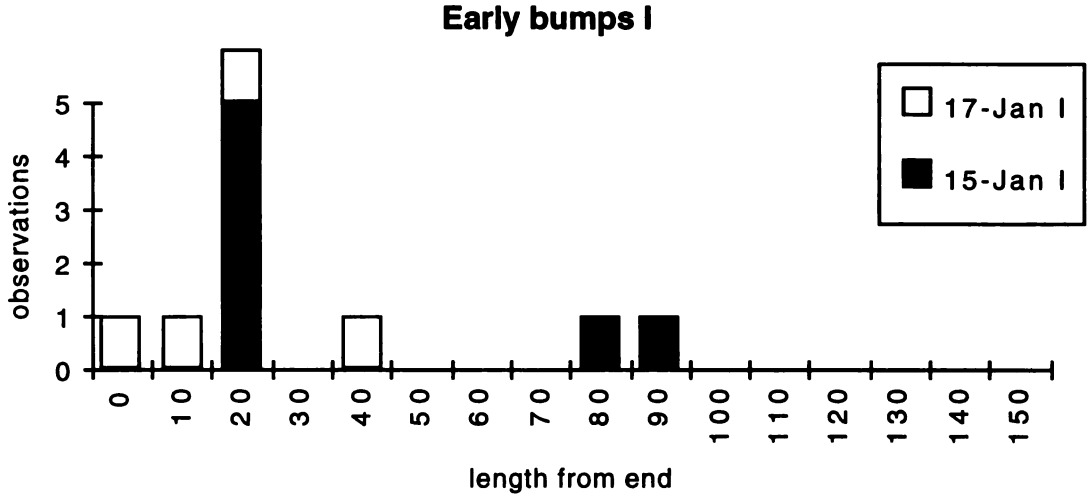

Figure III-33b Histogram of collagen bump position measurements as measured from nearest end of molecule.

A histogram of the position of strongly imaging bumps (bumps I), however, shows that they are unlikely to be randomly distributed (Figure III-33b). 6 out of 11 bumps are located between 20 and 30 nm from a molecular end. This implies that something about this area of the molecule makes it more likely to display bumps. If indeed the bumps are impurities decorating

the molecule, this specific adsorption may represent a biochemically reactive region of the protein.

The most interesting feature in Figure III-28a is the intermolecular tee, which appears to involve interaction between two collagen molecules. The association may be spurious, or it may represent the initial formation of larger collagen structures such as fibrils. Fibril formation at the molecular level is at present an incompletely understood process. Determination of a tee distribution is severely limited by the low number of quantifiable observations. Four tees lay between 80 and 108 nm from an end, with a mean of 95 nm and σ = 12 nm. This may represent a non-random distribution. Although these early data are intriguing, they are limited by few observations.

It has proven difficult to obtain large numbers of observations, partly a result of conducting these experiments at 143 K. This was compounded for the 1/15 and 1/17 experiments by the large number of adsorbed molecules, making unambiguous measurements difficult. Ideally, what would be most helpful is a single experiment with the proper collagen coverage utilizing a good tip. Obtaining a large sample population in a single experiment would be particularly valuable in controlling most of the known (and unknown) experimental variables. We obtained data in one experiment that met these criteria.

8/18 Experiment

Figure III-34 shows four fast mode scans of collagen obtained at 143 K on 8/18/92. This preparation had a reasonable number of evenly distributed molecules (image A). We obtained over sixty images from a number of different areas of the same 3 ng/μl collagen sample. Image resolution, while not outstanding, was quite good, allowing for reasonably accurate length and feature measurements. The RMS background roughness for these images is typically about 0.11 nm, which is higher than our earlier cold data, but still only half the value at room temperature. This roughness is evident in the background of the unprocessed 8/18 images.

The collagen molecules appear quite similar to our earlier LT data, with an apparent height of 0.6 to 1.0 nm. The apparent widths of about 9 to 10 nm are indicative of a good tip, and imaging forces were generally below 1 nN. Images B and C (Figure III-34) are interesting in that they show the same area, despite being obtained almost 3 hours apart with an interim cooling of the SFM. Cooling required first walking the sample back, followed by a new coarse approach. These images thus indicate the stability and reproducibility of our LT-SFM. Image C is slightly degraded with some sticking of the tip. Image D is a scan of the lower left portion of C, revealing an unusual tee.

The main advantage of the images of 8/18 is that they were well controlled compared to earlier data. The 8/18 data were obtained within 60 days, and 5 experiments, of our most thorough low temperature calibration run, and variables such as scan period were additionally recorded with the MacAcquire data parameters. We also made preliminary measurements of

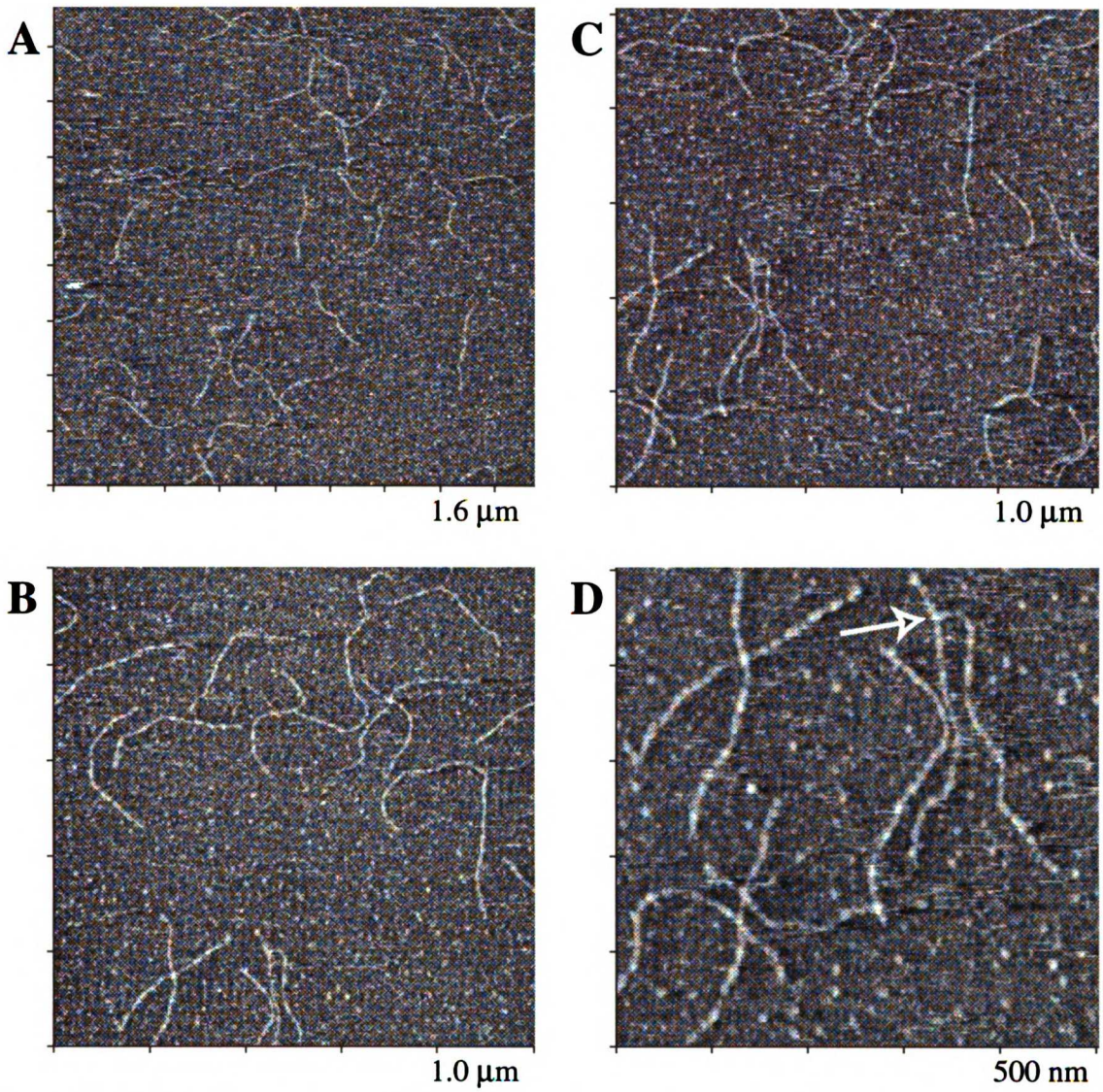

Figure III-34 Collagen data of 8/18. All are fast mode and low force images. Image A is a full size scan.

scan tube creep and lateral drift as a function of time. Their effects were minimized by allowing the scanner to equilibrate for about one minute after changing offsets. These factors will maximize both the accuracy and precision of 8/18 length estimates.

The other advantage of the 8/18 experiment was that many individual molecules were imaged in a single experiment. Almost all of the images were fast scans, acquired under identical conditions of scan period and scan

size. A total of 171 measurable molecules were imaged. Occasionally one molecule appeared in several different, but overlapping, images. This provided an internal check on the measurement process. The data was further analyzed by two skilled and one unskilled operator, allowing for some determination of operator induced errors, valuable when we consider issues of error and variability in the data.

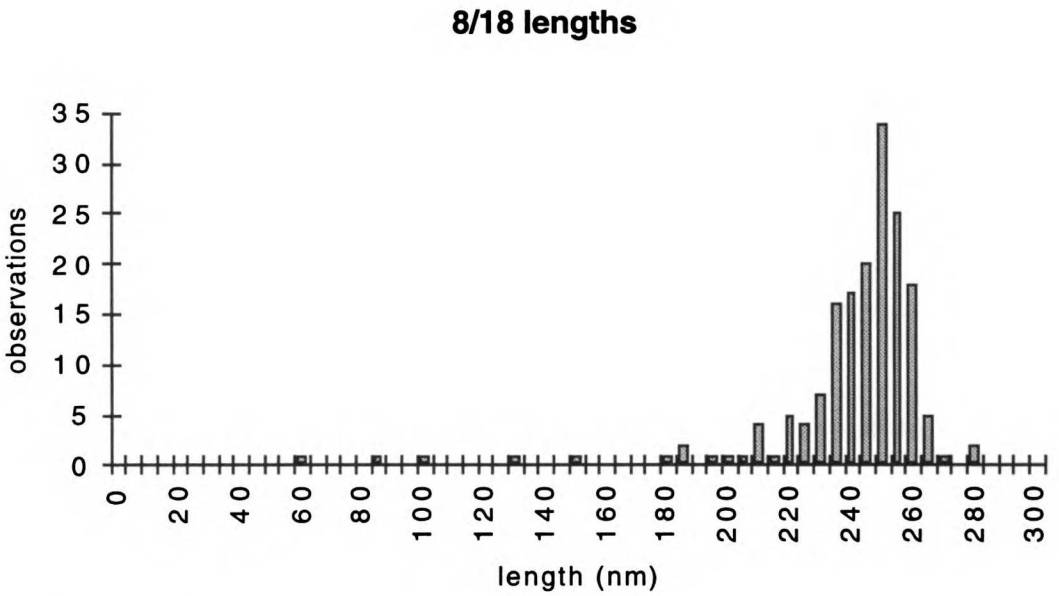

Figure III-35a Total lengths as measured for 8/18 data.

Collagen molecule length estimates were made on these data using the MacAcquire program. The resulting histogram (Figure III-35a) includes all length estimates except for one 538 nm dimer. There are 5 observations equal to or less than 150 nm that most likely represent fragments of collagen molecules, or possibly a molecule that has folded back on itself. This distribution also includes some "questionable" measurements, where I had some difficulty in determining the beginning or end of the molecule. If we somewhat arbitrarily restrict the data to a range of 150 nm to 300 nm to eliminate

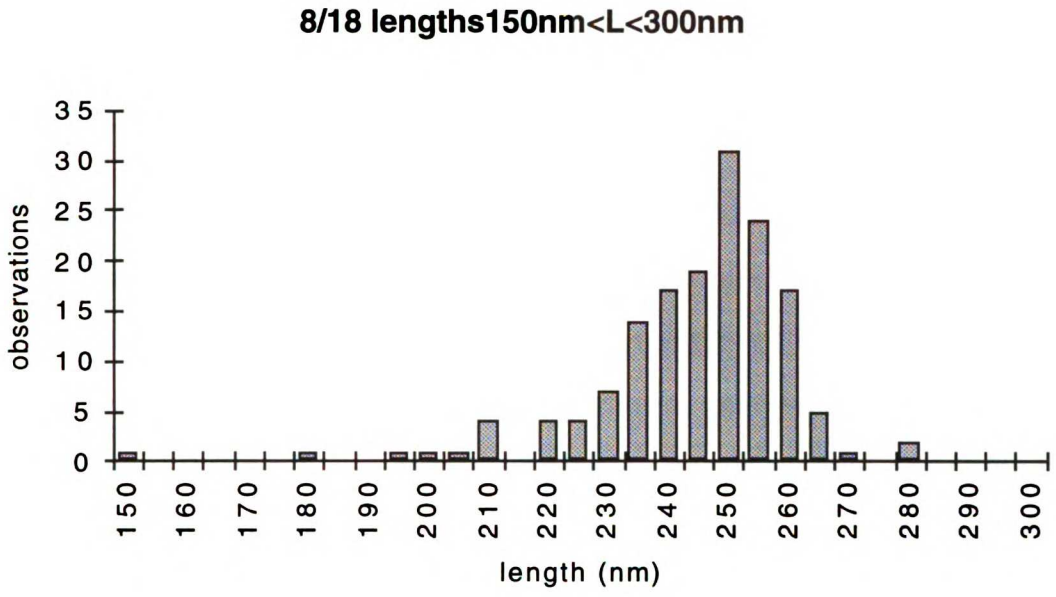

Figure III-35b Total lengths as measured for 8/18 data restricted to between 150 nm and 300 nm, and minus questionable measurements.

the "outliars," and remove the questionable measurements (often the same), we have the distribution depicted in the histogram of Figure III-35b. This histogram is only slightly different from III-35a, in that the variability has decreased, and has the advantage that it can now be directly compared to the length histogram for the early data (1/15 & 1/17) length measurements (Figure III-32). The resulting 8/18 length distribution is $x = 247$ nm, $\sigma = 16.8$ and $n = 153$ molecules. This mean is 26 nm, or about 10 %, larger than our early data mean, and is likely due to a systematic error between the two data sets. Given the calibration uncertainties of the early measurements, and the difference in means between 1/15 and 1/17, I believe that there is a systematic error in the early data. Note that the variabilities (or σ) are virtually identical for both the early and the 8/18 data. Moreover, there is good agreement between the 8/18 SFM length measurements and our TEM results. The means are identical: 247 nm. The variability of the TEM data, however, is

substantially larger (TEM σ = 28 nm vs SFM σ = 17 nm). This raises the issue of how much of the observed variability is due to a lack of experimental precision (to be minimized and avoided), and how much may be due to "real" variation in molecular length.

Some of the variability is certainly due to differences and uncertainties introduced by the operator using the curve length and calibration routines in the MacAcquire program. Repeated measurements of the same molecule, across several images, and by several operators, gave an indication of the magnitude of these effects. Repeated measurements yielded estimates that were within about 1 % of each other, with two exceptions. An untrained operator consistently had lengths about 2 % higher than the "trained" users, most likely due to a tendency to pick points at the extreme ends of the molecules. Estimates of the same molecule in different images varied by as much as 4 %, consistent with tube non-linearities and creep. Differences between the two trained users was slight, with only 1.7 nm (0.7 %) separating the two means, and with essentially identical variability.

Another strength of the 8/18 data is the relatively large sample size, which reveals more subtle patterns in the distribution of molecular features. The correlation of such patterns with the primary sequence of the collagen molecule helps make a case for the use of SFM to probe structure, and possibly function, directly at the molecular level. The earlier distributions for kinks, bumps and tees, although intriguing in that they appeared non-random, were limited to a few observations.

The distribution of kinks observed in the 8/18 data (n = 44) is shown in Figure III-36a. The distribution is interesting in that it appears to have 4

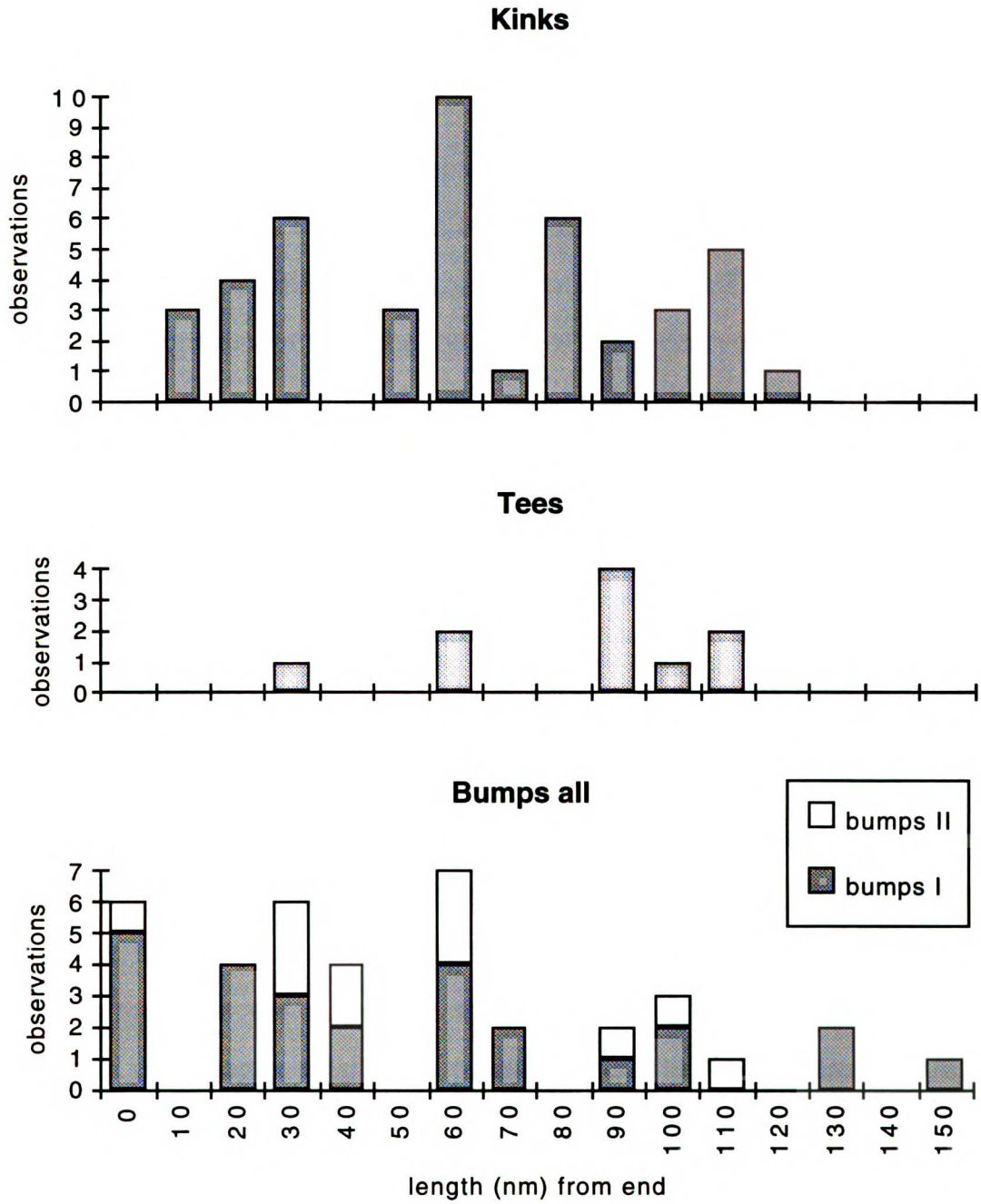

Figure III-36 a, b, c Histograms of 8/18 kink, tee, and bump data.

separate "peaks," possibly corresponding to preferential kinking at specific locations along the molecule. The early kink data (Figure III-33a) had a similar distribution, although offset by about 10 nm, and was limited to only

10 observations. It is unlikely that the 8/18 data are purely random; 10 observations lie within 60 nm to 70 nm.

There is a similar distribution pattern for intermolecular tees histogram III-36b. Tees occur at both 30 nm and 60 nm, corresponding exactly to the two largest bins for kinks. The largest concentration of tees is from 90 – 100 nm, in good agreement with the location of tees observed in the early data. This site does not correspond directly to a peak in the kink histogram, although there is a peak at 80 nm. It does appear that there may be some relationship between flexible and reactive regions of the molecule, as there is some consistency in the distributions of kinks and tees. The similarity between the two makes the possibility that either distribution is entirely random is rather unlikely. This correlation could be firmly established in the future with larger sample sizes.

Perhaps the most surprising finding is the non-random distribution of bumps along the molecule. The bumps are most likely not an intrinsic property of the molecule, and are probably some form of sample impurities adhering to the molecule. However, there are similar bumps in the background of most of our images, raising the possibility that the bumps are randomly superimposed on the molecules. Histogram III-36c demonstrates that is an unlikely possibility.

Histogram III-36c is actually composed of two separate distributions, representing "strongly" and "weakly" imaging bumps (bumps I & bumps II), and we will consider them together. Histogram III-36c is immediately striking in that the largest number of observations (7) is centered on the 60 – 70 nm bin, as was true for kinks. The second largest bump distribution at 30

nm, is similarly related to the kink histogram. The bump distribution is quite different, however, in that it has a high concentration at 0 – 10 nm, and several occurrences at 130 and 150 nm, in contrast to the histograms for kinks and tees. The early bump distribution had a maximum at 20 – 30 nm, consistent with our current observations. These bumps appear to be clearly related to the structure inherent in the molecule, and SFM may thus be revealing some unique features.

Net Charge and Bumps

I have attempted to correlate the distribution of bumps with the known properties of the collagen molecule. Collagen is an unusual molecule compared to globular proteins, with an extended linear conformation. As the molecule has no real interior space, the amino acid side chains all project outward, exposing any reactive regions. The exterior surface of the molecule thus has an axial pattern of both charged and hydrophobic regions, which are critical for physiological processes and biochemical interactions.

The complete distribution of charged side chains along the molecule is shown in Appendix I, part of which appears in Figure III-37. This appendix shows the distribution of charged amino acids for type I collagen as presented by Chapman and Hulmes (1982). The α-1 and α-2 chains are side by side, with charged residues indicated. The charges are then mapped above and below the molecular axis, resulting in the charge distribution shown. By convention, the residues are numbered from the junction of the N-telopeptide and the central helical region of the molecule. The helical region itself is 1014 residues long resulting in a complicated charge distribution.

A particularly elegant way of simplifying and condensing this charge

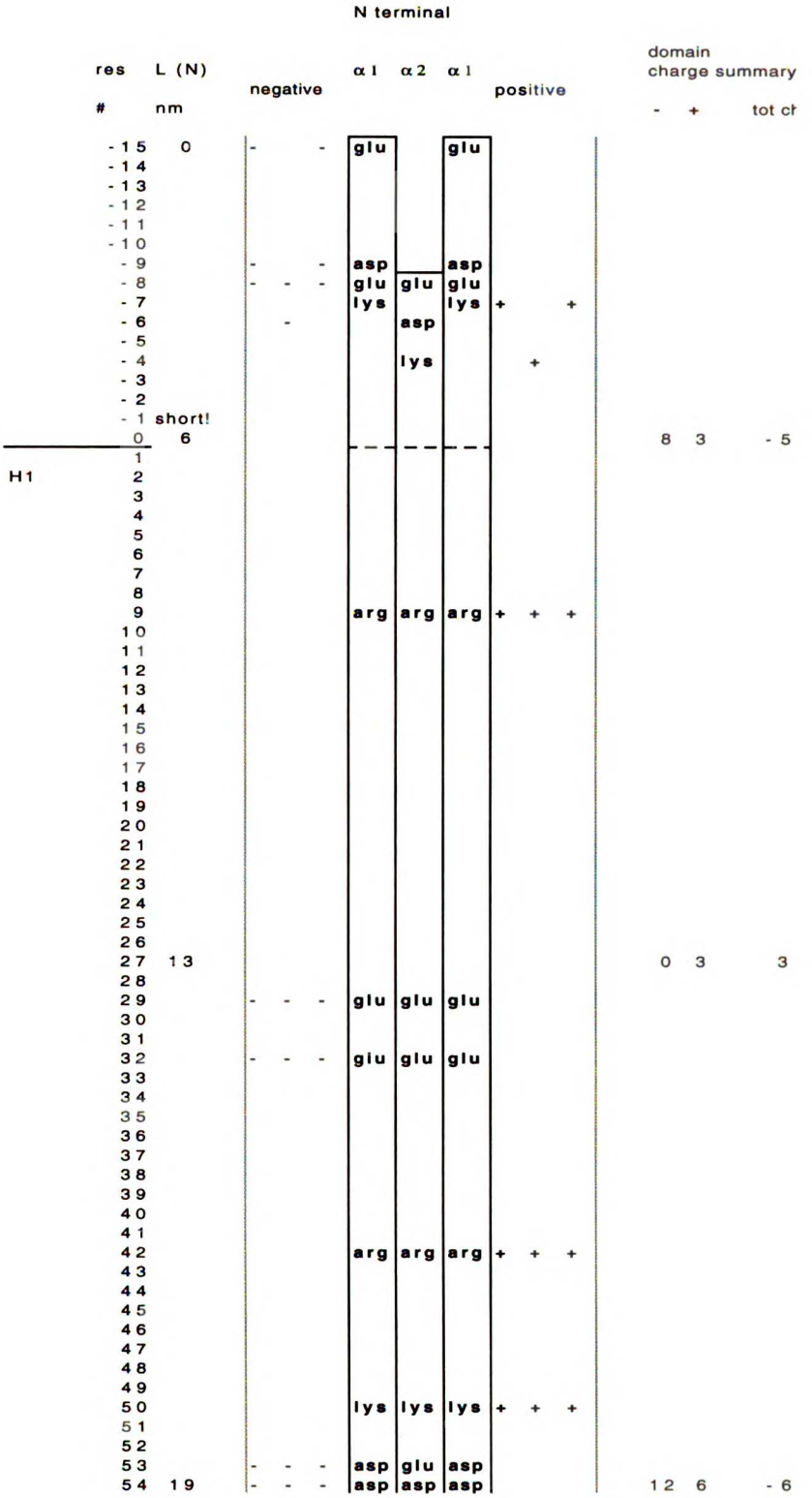

Figure III-37 N-terminal telopeptide and first two molecular domains (after Veis & George, 1994) showing charge distribution and net charge per domain. See Appendix I for complete plot.

distribution is presented by Veis and George (1994), and may be helpful in correlating the pattern of bumps. They point out that the net charge per molecular domain (vs charge per residue of III-37) is crucial in considering long-range electrostatic intermolecular interactions. They determined that regions of nine triplets (27 residues) "constitute the appropriate length charge-interaction domain," based on the compatibility with the "size of a kinetic unit in a negatively charged glycosaminoglycan chain." Glycosaminoglycans are polysaccharide chains which interact with the collagen molecule as part of the extracellular matrix. The net charge of this collagen molecular domains are shown in the left column of Figure III-37.

Following Veis and George, I calculated the net charge for these 9 triplet molecular domains along the collagen molecule. The complete distribution is shown in Appendix I. These data are summarized in a plot of total charge of each molecular domain along the collagen molecule (Figure III-38). For

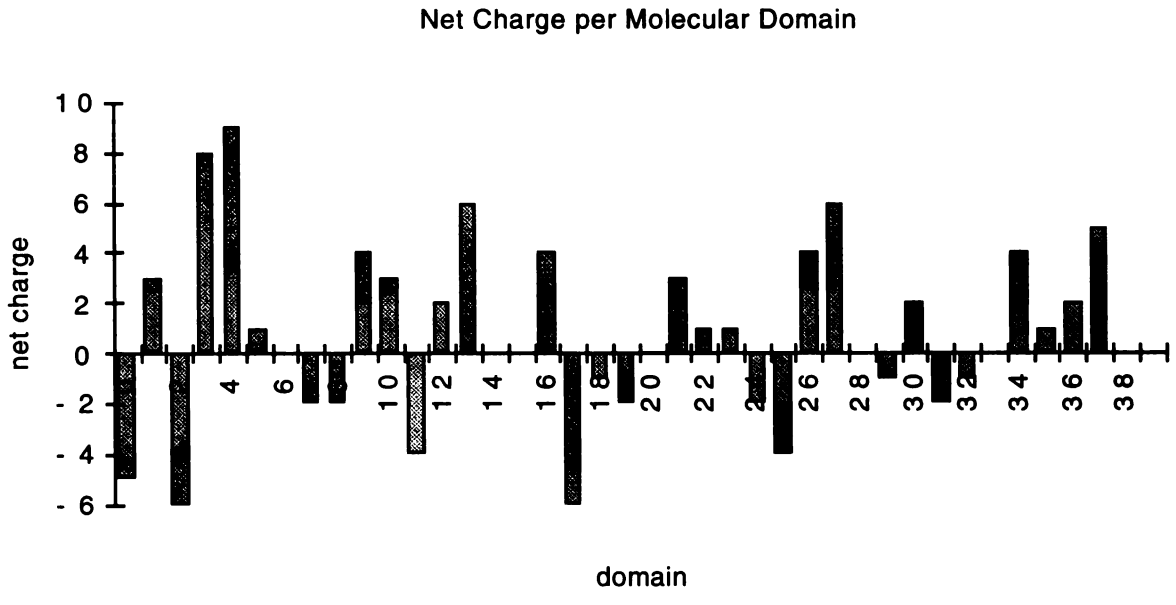

Figure III-38 Net charge per molecular domain composed of 9 triplets (27 residues) along the molecular axis. After Veis and George, 1994.

simplicity, both the N and C terminal telopeptides are considered as single domains.

Figure III-38 is interesting in that it is reminiscent of our histogram of bumps, and we will attempt to correlate the two. Bumps are characterized as a distance from the closest end of the molecule, since we cannot distinguish by SFM the N-terminal end from the C-terminal end. The molecular distribution is thus "folded over," or superimposed, into a distribution from the end to the middle of the molecular. As a result, we have a single distribution over one half of the molecular length.

Similarly, we can fold-over our charge distribution of Figure III-38 to generate a corresponding pattern reflected about the molecular midpoint. The resulting histogram of net charge per molecular domain is shown in Figure III-39a. The corresponding histogram of bumps is shown in 39b of the same figure. Histogram 39b is simply the same data as shown previously (Figure III-36c), but re-plotted into length bins which correspond to the molecular domains. This allows us to directly compare the distributions of net charge and bumps.

Figure III-39a and 39b reveal a clear association between charged molecular domains and bumps as observed by SFM. The bumps appear to be correlated with the positively charged domains, particularly if we for the moment ignore the bumps in the first (telopeptide) domain. There are similarities in the distributions centered at about the 26 nm and 64 nm domains. Bumps at 83 nm and 102 nm, however, do not correlate as well with the positive charge distribution, but do appear to match distributions offset by about one molecular domain. In fact, the pattern of all of the bumps seems

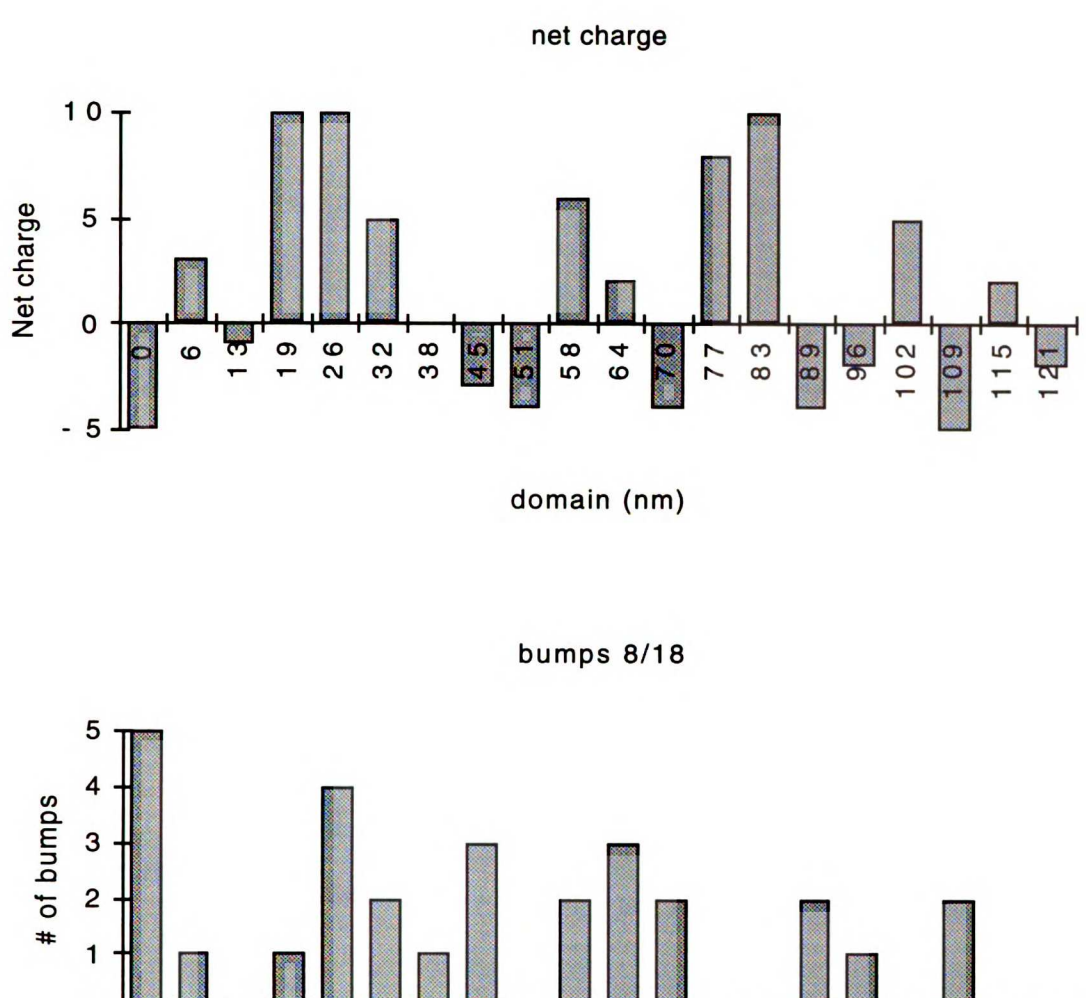

Figure III-39 a & b Top: Net charge distribution as measured from closest end of molecule and normalized to a molecular length of 250 nm. Bottom: Distribution of bumps observed for 8/18 data.

to be "shifted" slightly higher than the corresponding charge distributions. Figure III-40 is the histogram that results from shifting the bump distribution down one bin, which appears to more closely match the charge distribution.

We can examine the corresponding distributions more formally by calculating a "cross correlation function" between the total net charge and the

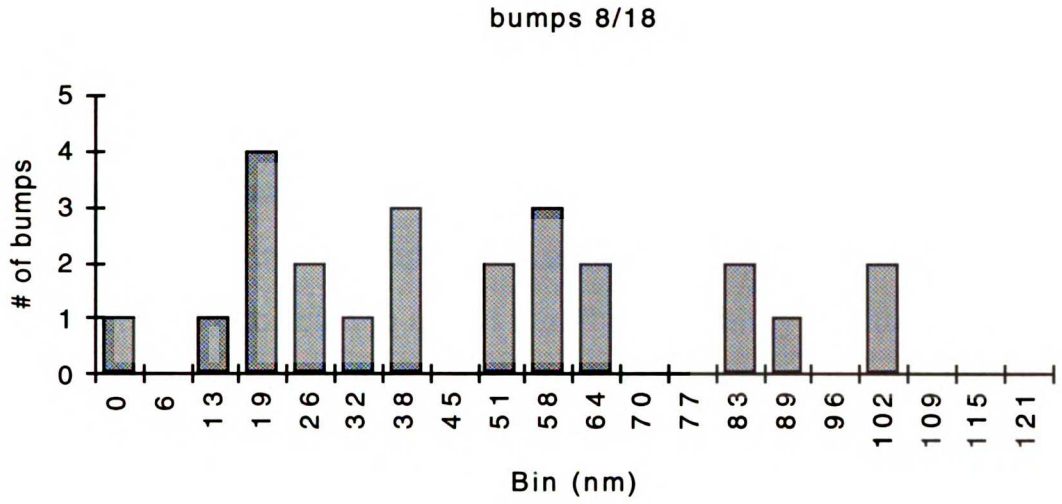

Figure III-40 Bump distribution of Figure III-39 shifted down one bin, resulting in a higher correlation coefficient with the net charge distribution.

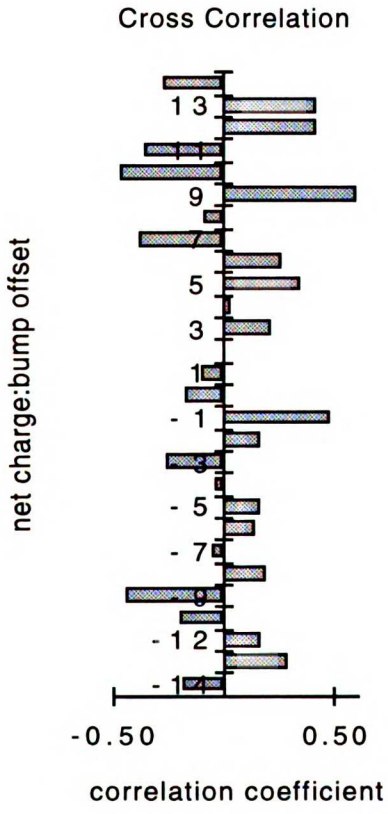

Figure III-41 Cross-correlation function demonstrates how the correlation coefficient varies for different associations of the distributions of bumps and net charge as discussed.

observed pattern of bumps. This is accomplished by calculating the correlation coefficient (Glantz, 1981) for each possible alignment of the molecular domains relative to the bumps. For example, the correlation coefficient (r) for the two distributions as shown in Figure III-39 is -0.18. We then shift the distributions relative to each other by one molecular domain and calculate the resulting r. A shift of -1 (as in Figure III-40) results in r = 0.48, confirming our observation that the distributions are slightly displaced relative to each

other. A plot of the complete cross correlation function is shown in Figure III-41.

The cross correlation function demonstrates that indeed there is a reasonable correlation between bumps and charged molecular domains. A value of r = 0.48 for the -1 correlation means that the probability that the relationship between these two distributions is due to random chance alone is less than 10 % (Taylor, 1982 pg. 183). Interestingly, the cross correlation function of Figure III-41 also indicates relatively strong correlations at both +9 and -9. In fact, the highest correlation observed (r = 0.60) is for +9, and note that the correlation at -9 is strongly negative. Again, both of these correlations have a less than 10 % chance of being random, even factoring in the reduced "population" of overlapping domains at these extended shifts. The correlations at +9 and -9 are particularly remarkable in that they correspond in both distance and polarity to a molecular axial stagger of about 58 nm, which is the same as the "1-D" stagger (normalized to a length of 250 nm) in the molecular arrangement of collagen molecules in natural fibrils!

It is remarkable that something as innocuous as the bumps observed in our SFM images of collagen, most likely due to some form of impurity, can correlate with anything known about the structure of the molecule. This might be reasonable, however, given the reactive nature of the collagen molecule.

The molecule can be thought of as a long, thin cylindrical structure, really a series of relatively long and stable triple helical regions (H1, H3, H5 and H7 in Appendix I) joined together with shorter, potentially less stable and possibly semi-flexible regions characterized by fewer proline and hy-

droxy-proline residues. This central helical region of the molecule, along with the N-terminal and C-terminal telopeptides, comprise the major functional domains of the molecule, or the basic molecular plan as described by Veis and George (1994). Superimposed on this are the charge distributions associated with the molecular domains as discussed earlier.

The result is a model of the collagen molecule with an asymmetric distribution of charged groups along the molecule. Additionally, the molecule has a distinct distribution of hydrophobic regions along the molecular axis, which can be plotted in an analogous manner (Hofmann *et al.*, 1978), and both are critical in the formation and stability of molecules and larger collagenous structures. Long range intermolecular interactions, however, are most likely dominated by electrostatic forces due to the charged molecular domains. The charged domains will also have some circumferential asymmetry in addition to this axial distribution, and both are important in molecular packing (Trus & Piez, 1976).

These charged molecular domains will of course determine much of the biochemical characteristics of the collagen molecule. They may have an affect on simple physical structural characteristics, such as length, as well. Electrostatic interactions of neighboring charged molecular domains will exert significant axial forces along the molecule, acting locally to shorten or lengthen the molecule as the helix is distorted. This may be exacerbated by regions of the molecule which are less stable, such as Bhatnagar's P-15 (Scaria *et al.*, 1991), that are near significant charge distributions. We (and most workers) have assumed that the length per residue is constant, which in reality may not be true, and may be an important factor in length variability.

Given this model of the triple helix, the bumps we observe by SFM are apt to be impurities preferentially adsorbed to reactive charged molecular domains. The correlation of bumps and net charge are good evidence of this. It is unlikely, give the current resolution limits of our SFM, that we are seeing perturbed regions of the molecule (such as P-15) directly. It is likely, however, that negative charge distributions on impurities will result in "decoration" of the collagen molecule, and in bumps observable by SFM. We do not know the identity of these bumps, but they are likely due to either impurities in our collagen preparation, or to contaminates introduced during sample preparation. Non-collagenous protein components of the extracellular matrix are typically anionic. Despite the purity of our initial collagen solution, it undoubtedly contained a small fraction of miscellaneous biological compounds. Given the extreme sensitivity of the SFM technique, some of these could certainly have been visible. As most biological macromolecules are slightly negatively charged, such impurities can be expected to react with positively charged collagen domains. Sample preparation can be expected to be significant, and variable, source of contamination as well.

The correlation between charged molecular domains and bumps is not exact however, and only significant at about the 5 – 10 % level. The correlation at -1 may not be too surprising, given the uncertainties and variabilities in the molecular structure. These could easily shift the relative distributions of bumps and molecular domains by one domain, which is only 27 residues out of over 1,000 (per single α chain). Our SFM calibration error could certainly account for this shift as well. It is also quite possible that the concept of molecular domains is not quite adequate over the entire molecule. This is almost certainly true in the telopeptide regions, which I have consid-

ered an additional "molecular domain," as defined by net charge distribution. This certainly does not apply to the C-terminal telopeptide (Appendix I). The last 22 residues of the collagen molecule, composed solely of the 2 α1 chains, has a net charge of +6, while the molecular domain total charge distribution of the entire telopeptide is 0. The strong positive charge asymmetry within this first molecular domain, composed of the telopeptides, may explain the large number of bumps at the very end of the molecule.

That the contamination features correlate at any level with the known charge distribution and structure of the collagen molecular is both surprising and unexpected. The somewhat limited correlation coefficient and the relatively few number of observations does mean that we do need to consider the possibility that correlation of these two patterns is only due to random effects. This is unlikely, given that we get a good correlation in spite of the limitations discussed, and that the correlation has a clear biochemical basis. The argument for randomness seems particularly remote in consideration of the correlations at +9 and -9, which fit well with models for the assembly of collagen molecules into fibrils.

Monte Carlo I

The length distributions of collagen (Figure III-35), as determined by low temperature SFM, is worth further consideration. The length estimates, as typified by the 8/18 experiment, are unusual in that they are shorter than expected, and are quite variable. The difficulties in interpreting how the mean and standard deviation of this sample might compare to the true population are formidable, given the uncertainties associated with the calibration

parameters, and the limited data sets available.

Establishing the extent and source of the uncertainties in the data may help evaluate the quality of the data, and its representation of real population parameters. To the extent that the parameters of absolute length and length variability can be shown to be real, and not purely the result of experimental uncertainty, we may be able to infer some biochemical or physical attributes of single collagen molecules. The ability of SFM to measure single molecules makes this a relatively unique approach. At the very least, we may be able to examine the accuracy and precision of direct SFM molecular measurement compared to other techniques, such as TEM.

We can anticipate the fundamental types of uncertainties associated with our measurements, which I will refer to as systematic and random (Taylor, 1982). Systematic errors are those which involve a repeated and consistent divergence, or error, of the sample statistics from the population parameters. For example, this error represents the bias in the estimate of the true (and usually unknown) population mean. Additionally, such an estimate will have a random uncertainty, which can be thought of as the lack of precision in the reported samples of the sample statistic. Unlike a systematic uncertainty, such a random error can be revealed by repeated measurements. This produces a distribution of estimates of a sample statistic, characterized by the standard deviation. It is important to note that the two experimental errors are independent, and in some sense reflect both the accuracy and precision of a given sample statistic. It is possible to have a precise (low variability) estimate with a large bias (or systematic) error (Moore, 1979).

Our data are characterized by significant calibration and experimental

errors which are both systematic and random in nature. Systematic errors are a particular problem, since they are not apparent from repeated measurements of sample statistics, and must be deduced by the experimenter (Taylor, 1982). Such errors can be anticipated and minimized by the experimenter, but are difficult to quantify. These errors are, however, by definition, consistent, and thus will introduce a consistent bias in our population parameter estimate. Given the limited experience and data sets available for the cryogenic SFM, it is very difficult to characterize the magnitude of the systematic uncertainty in our data. Such bias is clearly present, and would explain the differences in the sample means of our early (1/17 & 1/15) and 8/18 data. It should be noted, however, that the mean of our most tightly controlled data (8/18) is virtually identical with our TEM data.

Difficulty in estimating the systematic errors in our measurements does not preclude the characterization of the random experimental errors. Evaluating random errors may allow us to determine how much of the observed variability in the length data is due to real variability in the length of the collagen molecule. Random errors, as reflected in the standard deviation, or the variability, of the sample statistic, can be determined directly by repeated measurements of different samples of the same population. Unfortunately, we are limited to only a few data sets. Only one (8/18) is carefully controlled for the uncertainties in the calibration parameters associated with scan size and period. Furthermore, given the present constraints of time and the rather low ratio of experimental success to failure (not to mention experimental dismemberment), taking additional data is not an option in the immediate future. Clearly, some other method of evaluating the random uncertainties in the experimental parameters is needed.

One approach is to assume that we know enough about the experimental process that it can be successfully modeled. We can, in principle, construct a model that would mathematically incorporate all of the various experimental parameters. Furthermore, we have estimates of the uncertainties in these parameters, most notably the calibration parameters.

We could attempt rigorously to calculate the total experimental variability from these uncertainties in a deterministic fashion. This approach, however, can be expected to be difficult. The model would include uncertainties associated with a large number of parameters, including the calibration coefficients, long and short-term history of the scan tube, and immediate experimental parameters. Additionally, post experimental uncertainties such as operator errors during data analysis and measurement uncertainties associated with pixelization of the computer data must be considered. These factors will all contribute in some measure to the final variability.

Perhaps the most difficult aspect of such a deterministic approach is the difficulty in combining all of these various uncertainties mathematically. We could simply add the uncertainties, but this would overestimate the total uncertainty. If the original uncertainties are both independent and random, then the uncertainties add in quadrature (Taylor, 1982). From the calibration data, it is reasonable to assume that our uncertainties are indeed random, but they are certainly not all independent. The problem now additionally involves attempting to understand how all of our uncertainties are related in order to compute an accurate uncertainty.

Another approach is much more promising. Using the model for our experimental system, we can simulate the experimental process. As our

experimental parameters are random, we can incorporate each parameter into the model as a normal distribution of values, the characteristics of which (mean and standard deviation) have been determined or can be estimated. The uncertainty of each coefficient can be included as a random number from a distribution with the same mean and standard deviation. We can generate a large number of such random numbers, and run the model a large number of times. The final uncertainty can be inferred from the distribution of a large number of these simulated length "experiments" directly, avoiding the difficulties associated with a deterministic approach.

Such a random simulation has the advantage in that several of the required transforms were previously constructed for the calibration routines. We need to add a sequence for random generation of test molecules, and for final data analysis. Additionally, this approach allows for direct sensitivity analysis. We can observe changes in the output lengths in response to random changes in a single experimental parameter, without having to determine the dependence of that parameter.

This mathematical approach, relying on the randomization of the experimental coefficients, is commonly referred to as the Monte Carlo. Monte Carlo is a term for a class of mathematical techniques based on random numbers, much like games of chance, whose behavior and outcome can be used to study real phenomena. Kalos (1986) describes a Monte Carlo Method as one that involves deliberate use of random numbers in a calculation that has the structure of a stochastic process, a "sequence of states whose evolution is determined by random events." The reliance on random numbers make the Monte Carlo particularly well suited to computer analysis. In the case of many dimensional problems, the Monte Carlo can be

"computationally effective," compared to deterministic methods.

The Monte Carlo technique that is most immediately applicable to our SFM analysis is of a probabilistic (versus deterministic) nature. It is probabilistic in that it is directly concerned with the behavior and outcome of random processes, such as random uncertainties. Hammersley (1964) describes the simplest probabilistic approach as one in which we observe a series of random numbers, chosen in such a way that they directly simulate the random processes of the original problem. We then infer the desired solution from the behavior of these random numbers. In essence, this procedure amounts to a random sample from the population. It is important to emphasize the inferential nature of Monte Carlo analysis, which is like more conventional statistical techniques.

Monte Carlo II

It is quite remarkable that the Monte Carlo method, with its dependence on randomization, can infer useful results. It can, however, be used to test hypothesis and determine confidence limits for parameters, within certain limits. B.F. Manly has written an excellent book on Monte Carlo methods in biology (1991), and presents a particularly elegant description of this inference process, paraphrased here.

For example, simple "randomization testing," using only the original data set, can be used to test hypothesis and determine confidence intervals. Such testing "involves determining the significance level of a test statistic calculated for an observed set of data by comparing the statistic with the distribution of values that is obtained by randomly reordering the data values in

some sense." One can actually enumerate all possible data orders (thus the appeal of computers), or take a large random sample from the distribution. Confidence limits for that parameter are given by the range of values for which randomization testing yields a significant result.

Similarly, Monte Carlo methods can construct confidence intervals, and involves comparing an observed test statistic with values obtained by sampling a distribution. In the Monte Carlo, the sampled distribution does not result from a simple reordering of the observed data values, but rather from a distribution generated by some particular model for how the observed data arose. "Confidence intervals can be based directly on the variation in parameter estimates observed in data generated from the model."

As with most statistical analysis, randomization and Monte Carlo methodologies are based on faith and the null hypothesis. The null hypothesis is, of course, that logical argument in which statisticians disprove the opposite hypothesis (i.e., that there is no effect) in order to determine significance. This approach appears to me to be a bit like a double negative, and may be an attempt to avoid the stigma associated with being part of "that group of people whose aim in life is to be wrong 5 % of the time" (Kempthorne & Doerfler, 1969). The null hypotheses of randomness is useful in the present case in determining whether or not a certain pattern appearing in the data is purely a chance effect of observations in a random order. Randomization techniques are a way of determining if the null hypothesis is "reasonable in this type of situation." As with conventional statistics if this does not seem to be the case, the null hypothesis is somewhat discredited, resulting in some measure of significance. The significance level is the percent of observational values that are as extreme as the value in the randomization distribu-

tion, and can be interpreted much as conventional tests of significance.

Compared with standard statistical methods, randomization and Monte Carlo tests have several advantages. Their model structure make it relatively easy to take into account the peculiarities of a given problem, and incorporate non-standard test statistics. Additionally, they are valid even without random samples, a somewhat surprising result.

This leads to the one major disadvantage of randomization testing, which is that it is not necessarily possible to generalize conclusions from such a test to the population of interest. The test only tells us that a particular pattern in that data is unlikely to have arisen by chance, and is completely specific to the data at hand. The concept of a population from which other samples could be taken is not needed: the very reason why random sampling is not required. Generalization of results is then dependent on the assumption that the sample and data obtained are effectively the same as a random sample.

Similarly, randomization testing may not be applicable to testing hypothesis concerning absolute values of population parameters. This is true unless it is reasonable to assume that the observations in a sample are a random sample from a distribution that is symmetric about the population mean. This is like the issue of sample bias and systematic error discussed earlier, and is difficult to detect experimentally. As a result, making such assumptions becomes something of a "judgment call" for the experimenter. These constraints are not severe, if we restrict ourselves to the issue of length variability, and do not attempt to resolve the issue of absolute molecular length using Monte Carlo Methods.

In essence, I used the Monte Carlo technique to assess the significance of

the observed total variability in molecular length. This was accomplished by generating other variability samples for comparison, using random numbers in a model of our experimental process. Random number generators, with a defined distribution, were incorporated into the model, and used to represent various experimental parameters. The random numbers simulated the uncertainty in these parameters. This allowed me to model how the total variability incorporated all of the parameter variability directly, and how the total variability at the output changed with random parameter variations. This was quite similar to Marly's (1991, pg. xiii) use of Monte Carlo methods "to calculate confidence limits for population parameters. Essentially the idea is to use computer-generated data to determine the amount of variation to be expected in sample statistics." The use of a computer, while not an absolute requirement, is important. A large number of such random test statistics is required to avoid inferences being too strongly dependent on the properties of a small sample.

Model I

The ability to use a Monte Carlo method is dependent on model development which accurately simulates the experimental process, and incorporates all parameters and coefficients. For simplicity, I have restricted analysis to the 8/18 data. A simple schematic of the model is shown as Figure III-42, and is presented in its entirety in Appendix II. The model begins with a simulation of individual molecules on a flat surface in real (physical) space. The "molecules" are randomly distributed across the "image," and are composed of four articulated segments. They thus look like the 8/18 sample preparation they are supposed to emulate. This approach is not unlike the

"random walk" polymer simulation of Hammersley and Handscomb (1964 pg. 127), or the modeling of flexible collagen sites by Hofman et al. (1984). I then transformed these molecules from real space into "image space," where I could actually image and analyze the molecules with the SFM. This transformation is a function of the calibration parameters, and their uncertainties, as well as some of the peculiarities of the MacAcquire program.

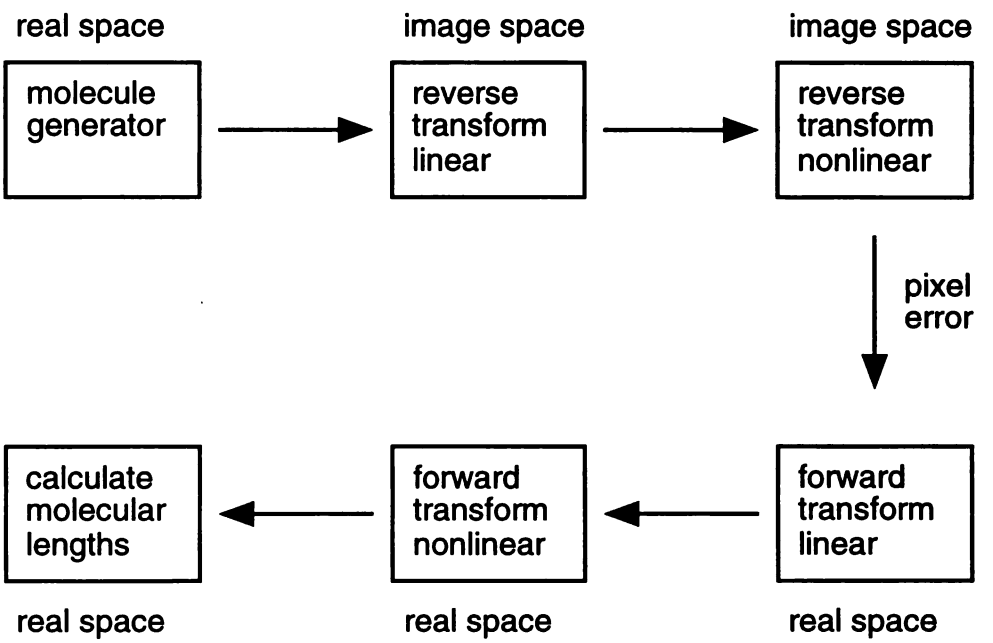

Figure III-42 Schematic diagram of Monte Carlo modeling process.

In image space, the model simulates the length-measuring process conducted by the operator, with uncertainties due to pixelization errors. These "as measured" molecules are then transformed from image space back into real space, which is what the MacAcquire program does in using the calibration coefficients to calculate actual molecular lengths. This set of model parameters is more complicated than the real to image transformation, as it encompasses additional uncertainties associated with "inter-operator" errors.

Such errors reflect the different calibration coefficients obtained by different operators analyzing the same calibration data. The original calibration parameters reflect the variation resulting from one operator analyzing the same data several times. The distributions of all of these uncertainties, based on repeated measurements, can each be incorporated as a mean coefficient value with a standard deviation. The coefficients and their uncertainties can then be modeled using a random number generator (RNG) which simulates the same distribution. Additional sources of variability can be incorporated by adding their contribution (if they are independent) to the total variability for that coefficient, again using a RNG.

Using these forward transform coefficients into real space, we can then calculate the end points and thus the apparent length of each molecular segment, and finally the total molecular length. Each "image" consists of 10 molecules, and is plotted to visualize the simulation. We remove those molecules which venture "outside" of our image boundary, chosen to correspond with the size of our 8/18 data images. The remaining molecular lengths can then be tabulated, and a total variability characterized for our simulated "experiment." Since all the original molecules were generated with the same initial length, this total uncertainty results only from the variability of our experimental parameters, and can be compared to the observed variability in the 8/18 data. This comparison will allow us to make some inference as to how much of the observed variability is due to actual variability in the length of the collage molecule.

The details and the results of the Monte Carlo simulation are included as Appendix II. Each simulation resulted in length variability estimates for a sample size comparable to the 8/18 data, and a total of 500 simulations were

conducted. The total variability of these simulations was found be about 9.5 nm. The variability observed in the 8/18 data was 16.8 nm, or almost double that from the Monte Carlo, thus about half of the observed variability is due to actual variation in molecular lengths. Again, no attempt was made to assess the accuracy of the mean of the length measurements, given the difficulties with systematic errors. However, the mean of the Monte Carlo simulation was equal to the input length, making the simulation an unbiased estimator, in itself a surprising result.

The Monte Carlo simulation allows us to additionally do some basic "sensitivity testing," in which we observe the change in the simulation variability in response to an arbitrary change in a modeled parameter. This is valuable, given the difficulties in establishing the calibration parameters, and allows us to test how sensitive our results are to uncertainties in a single coefficient. In particular, the linear "yy" coefficient is subject to significant experimental uncertainty, as it is in the slow scan direction; and is the most sensitive to the immediate scan tube history, our most difficult parameter to control. If we arbitrarily double the uncertainty (standard deviation) in the yy parameter and re-run the simulation, we find that the total molecular variability increases to 13.2 nm. This is still significantly less variable than the observed experimental results. In fact, we must double the uncertainties of all of the variables in the Monte Carlo simulation to get a final result that matches the observed variability. The model indicates that about half of the experimental variability is due to an actual variation in the length of collagen monomers.

The existence of real experimental variation in the molecular lengths of the collagen molecule is an interesting result, since it is common to think of

length as an intrinsic and fixed property of the molecule. This variation is further supported by the observed length variability in our TEM length measurements. The lower variability of the SFM measurements indicate that the SFM data has higher precision, not unexpected given the limitations of grain size in TEM replicas. The observed variability could be an intrinsic property of collagen molecules, or could arise from a number of factors.

All of our observations were made on molecules deposited onto a surface from a solution. This is fundamentally a much different environment than being confined to a fibril in the native state, and exposes a variety of reactive regions and molecular domains to the solvent environment. At the very least, the charge distribution can be expected to be directly related to the pH. At reasonably acidic pH (≈3.5 for 0.05 N acetic acid), the negative charges of glutamic acid ($pK_R = 4.25$) and aspartic acid ($pK_R = 3.86$) will be significantly neutralized, resulting in different charge-charge interactions along the molecular axis, and an expected impact on overall length. Local perturbation, intramolecular and intermolecular interaction (including other molecular species), hydrophobic effects, and the dynamics of precipitation and adsorption onto the substrate surface may all be important. These may all be compounded as a consequence of solvent drying on the surface during sample preparation, which will produce local environmental extremes of pH and ionic strength. Additionally, surface tension effects and drying artifacts are a concern, in a manner analogous to TEM investigations, and can complicate the interpretation of SFM images of single collagen molecules. SFM does, however, have the advantage of imaging and manipulation directly at the molecular level, with relatively high precision.

Collagen Network

One low temperature collagen experiment had a decidedly different and rather intriguing appearance from the experiments discussed. These data are important given the current uncertainties of the exact nature of fibril formation from individual collagen monomers. The molecules in this experiment appear to be associated into some form of a continuous structure resembling a network (Figure III-43). Closer examination of images A through C reveals that few, if any, molecular ends are visible, and that the molecules

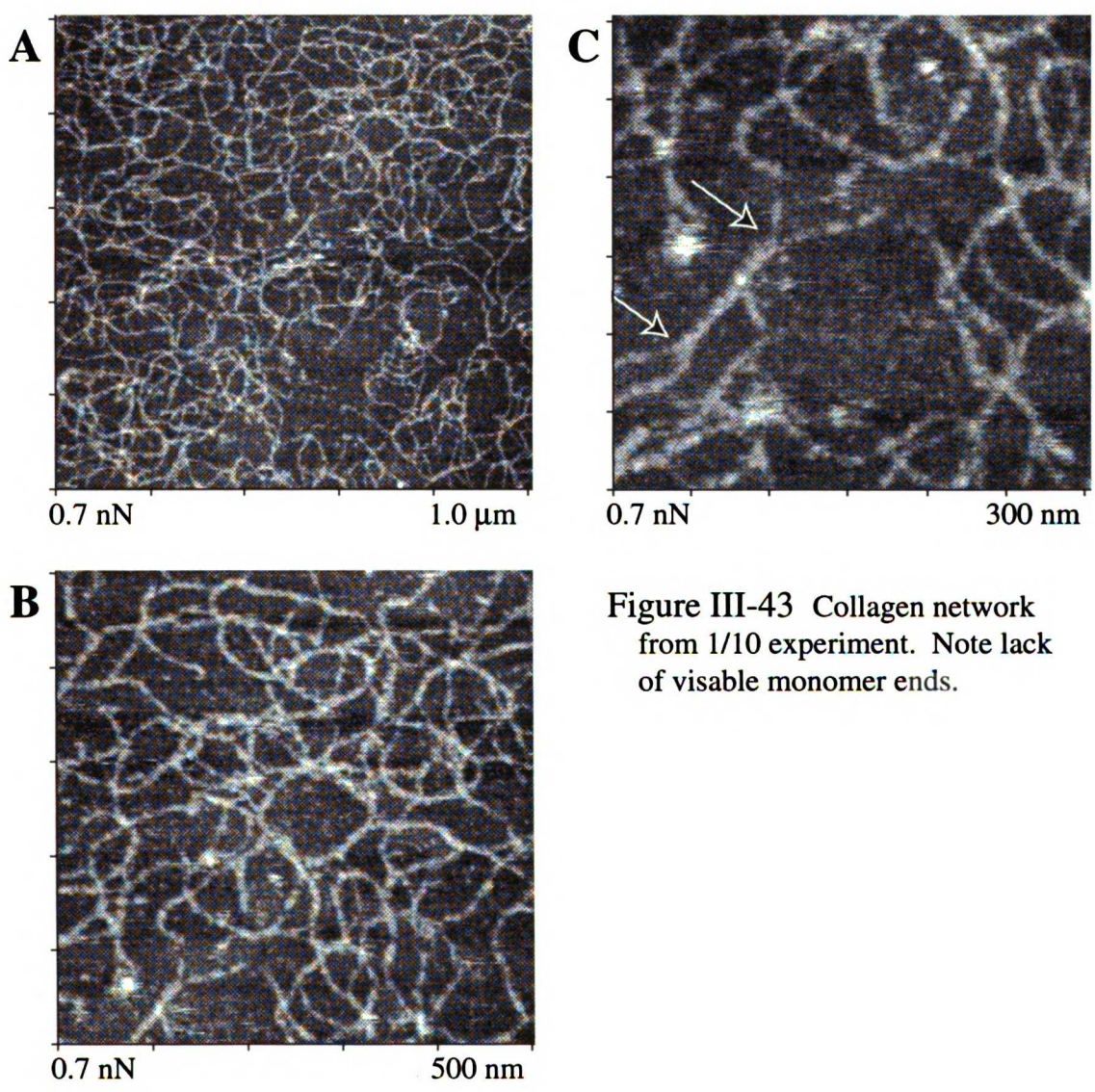

Figure III-43 Collagen network from 1/10 experiment. Note lack of visable monomer ends.

seem to have been organized in several ways. The predominant pattern appears to be similar to our previously observed tees, although at typically oblique angles. The molecules branch out in a series of "Y" shaped interactions. Unfortunately, the lack of molecular ends precludes determining the regions of such interactions. Several of the more extended structures are also consistent with an end to end association.

The intermolecular associations clearly have a lateral component as well. It appears that the two molecules of a Y structure tend to run together laterally before diverging, as shown in the 300 nm scan of image III-43 C. Two molecules are somehow associated laterally for about 75 nm (between arrows) before diverging at each end. This region has a characteristic pattern (for this experiment) of periodic imaging contrast that is suggestive of a twining of the two molecules. Rather than a twisting together of the molecules, this may be some change in imaging due to a reinforcing of some lateral molecular property, such as hydrophobicity.

The distinct diverging Y pattern could be indicative of the first steps of the association of collagen molecules into fibrils. These patterns have the appearance of structures that are being organized into extended linear networks. It is interesting to note how similar in appearance our images are compared to TEM micrographs of filamentous aggregates of collagen. Figure III-44 is a micrograph taken from a study of collagen fibril formation by Karl Piez (Piez, 1982). These aggregates of type I collagen were initiated from a 0.1 mg/ml (100 ng/μl) solution at pH 7.4 by an increase in temperature. The resulting aggregates are quite similar in appearance to our aggregates, although they are larger in size. SFM image III-43 A is at virtually the same magnification as Figure III-44, and indicates that Piez's aggregates are

associations of larger numbers of molecules.

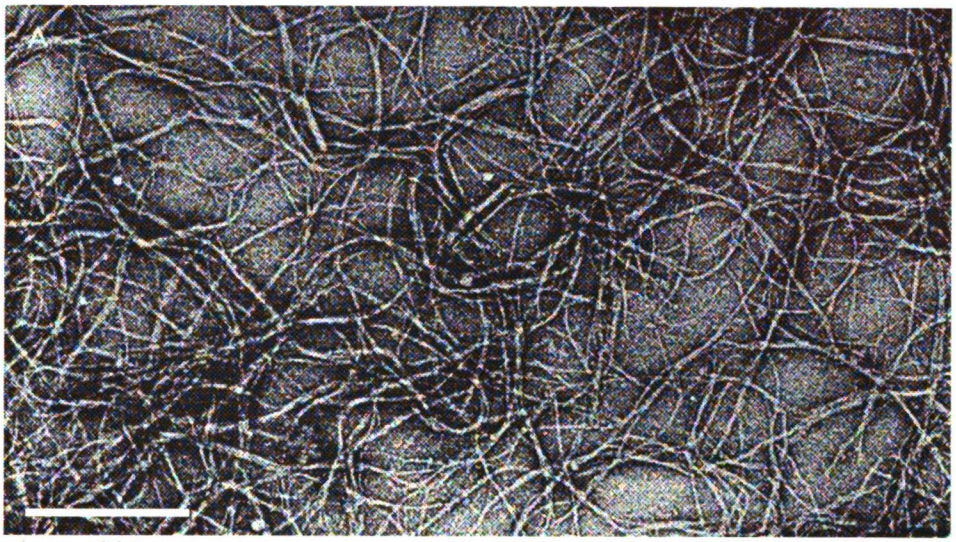

bar = 300 nm

Figure III-44 TEM shadowed collagen replica from Peiz (1982).

Our networked images could easily be the result of some slight change in an experimental variable, most likely associated with sample preparation. Fibril formation results from the interplay of collagen concentration, pH, ionic strength and temperature (Veis & George, 1994). A change in one of these factors during sample preparation could have resulted in aggregation. Our collagen samples were prepared in 0.05 N acetic acid, about the minimum concentration required to keep collagen in solution. While this minimizes additional deposition and impurities on the sample surface, it facilitates collagen aggregation, and such variables can be expected to be exacerbated during the N_2 drying step of sample preparation. Thus sample preparation variables are important, and may explain some of the more subtle differences among our collagen experiments. Whatever its origin, the intramolecular interactions shown in Figure III-43 raise the possibility of using SFM techniques to examine the unresolved nature of the packing of mol-

ecules into fibrils

Collagen fibrillogenesis is an area of very active study, with several unresolved fundamental aspects (Veis & Payne, 1988; Veis & George, 1994). Several possibilities exist for a multistep process of fibril formation that are more complicated than a "simple nucleation and growth process." Characterization of specific intermediate aggregates would be helpful in resolving these uncertainties, and are in an ideal size range for SFM study. SFM could be used to tease apart single fibrils with increasing force, or to observe the first stages of fibril formation at the molecular level.

We have conducted a preliminary series of fibrillogenesis experiments, based on thermal induction of fibrils from a neutral salt collagen solution at physiological pH (a system originally developed by Gross & Kirk, 1958). Fibril formation is an entropy driven self-assembly process (Helseth & Veis, 1981) with a characteristic sigmoidal growth pattern. Following George and Veis (1991), we set up and thermally initiated fibril formation, and removed samples of the collagen solution at time intervals encompassing the lag and initial growth phases. These samples were then immediately prepared for both TEM and SFM. However, the SFM samples were not successfully imaged due to technical difficulties. TEM images do indicate that samples could be obtained reflecting various initial stages of the assembly of molecules into fibrils, and that this approach should be pursued at a future date.

Collagen Force Series

An intrinsic advantage of SPM techniques, including SFM, is the ability to manipulate single molecules. In general, tip/sample force interactions are

minimized. However, one can use SFM to apply high forces to the sample in order to probe physical properties directly. The easiest and most direct approach is to increase imaging force, either by offsetting the feedback or the Z position of the sample. By increasing the deflection of the cantilever, one increases the contact force in proportion to the cantilever spring constant. Our cantilevers typically have a force/deflection constant of about 0.6 N/m or 0.6 nN/nm (a more appropriate size scale). Successive images can be taken at increasing force while monitoring changes in the image.

An example of such a force series is shown in Figure III-45. This is a sequence of 8 images taken of the same area of a collagen sample at room temperature in isopentane. The images are all about 1.0 μm^2 unless otherwise noted, and are all centered at the same point. Image A (III-45a) is a normal scan at a typical force of about 0.5 nN. Molecules are visible although somewhat masked by surface contamination, a problem common to essentially all of our room temperature images. Scan B through D were taken at increasing forces of 4 nN, 16 nN and 31 nN, with some interesting results. The molecules in D, the highest force image, are still visible, appear to be basically unchanged, and are still in their respective positions. The background image quality is improved, probably due to the tip "sweeping" away surface contamination. Also note in image D the horizontal streaks in the X scan direction. As imaging forces are increased, increased tip/sample interactions cause the tip to stick in the scan direction, which deflects the laser beam due to torsional bending. Such beam deflections appear as changes in height with a two quadrant photodetector. SFMs have been used to study stick-slip behavior and frictional effects, using 4 quadrant photodiode detectors (Radmacher *et al.*, 1992; Warmach *et al.*, 1994).

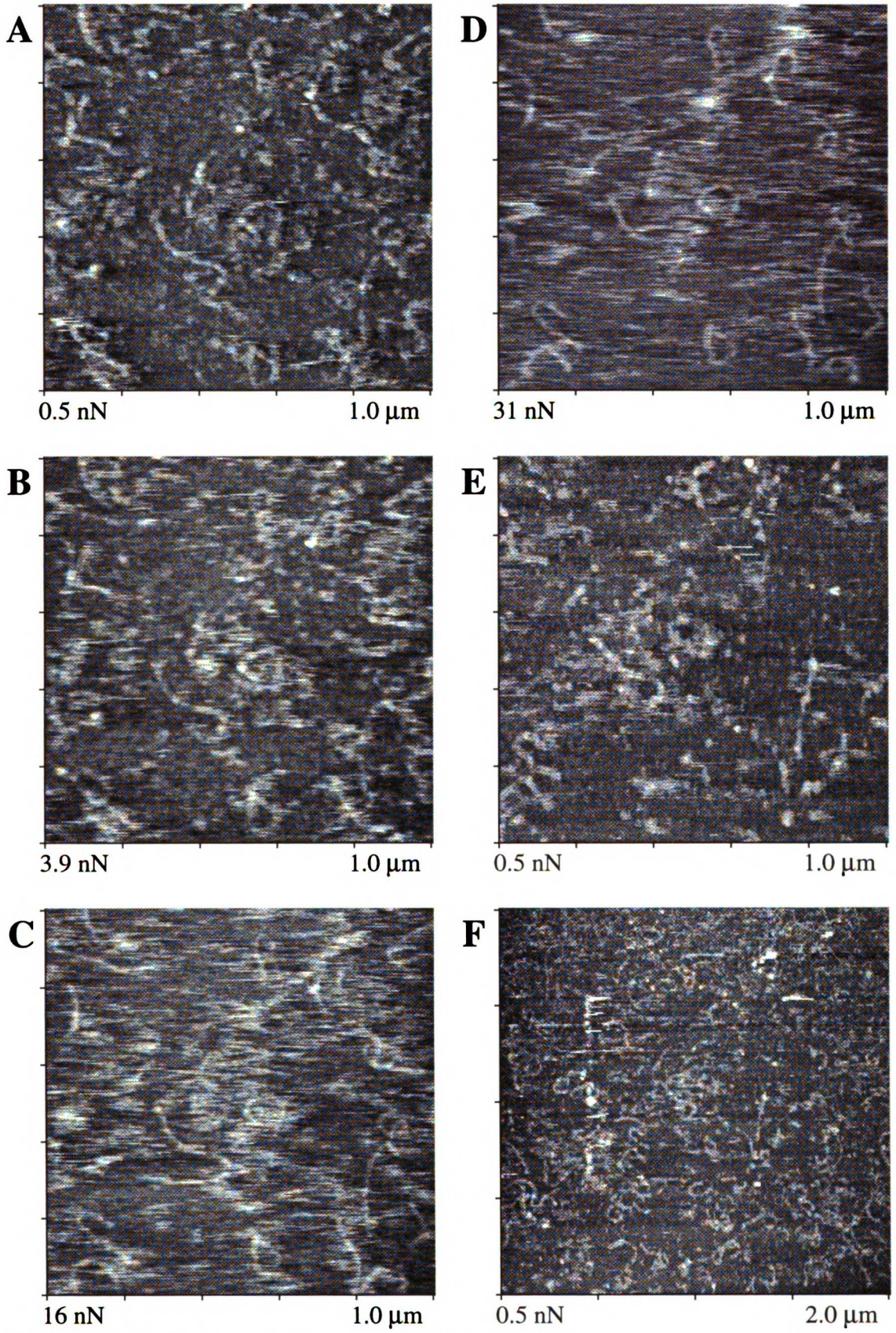

Figure III-45a Collagen force series at room temperature.

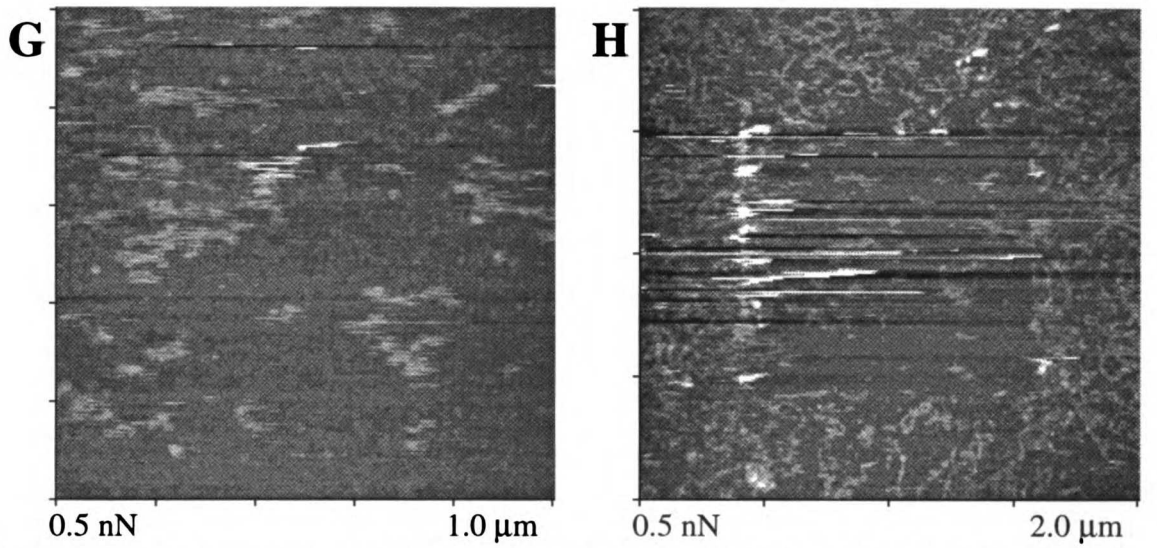

Figure III-45b Scan images taken after force series of III-45a, and after 125 nN scan.

The results of the force series is seen in images E and F (Figure III-45b), both taken at the original imaging force of 0.5 nN. Image E (1 µm) shows that most of the molecules are still on the surface, although some appear to be altered, either by partial removal or rearrangement. Image F was taken at the same force as E, but was a 2 µm scan. The 1 µm high force imaging area shows a noticeable edge on the left side due to the accumulation of swept debris. The sample surface is still mostly unchanged.

Following image F, a subsequent 1.0 nm scan was made at a force larger than 125 nN. At that force, the laser beam was deflected out of range of the detector, producing no image. Image G, however, was a 0.5 nN scan made immediately afterwards, showing a severely altered sample surface with no visible molecules. This is confirmed by image H, a 2.0 nm overall scan of the area. The 1.0 nm area at the center is devoid of any real surface features. At the left edge is a pronounced accumulation of material, deposited by the scanning tip. The tip itself may have lost some of its previous resolution. Surface features outside of the 1 nm area have also lost some of their con-

trast due to gray scale compression from the large relative height of the debris. This force series demonstrates the ability of the SFM to modify and test the sample surface in a controlled manner. This suggests the possibility of direct investigation of surface effects, such as molecular binding, as a function of molecular domains.

The possibility of using a force series to examine more subtle effects is demonstrated in Figure III-46. This is a series of room temperature collagen images like those of Figure III-45. Experimental conditions are similar, but the image scan size is 500 nm, the contamination less, and thus the collagen molecules are more discernible. Image A, taken at a force of 0.5 nN, shows several individual molecules in the center. Note the changes to the two molecules indicated with arrows. B through D are images of increasing force, and correspond closely to the previous force series of Figure III-45. As the force is increased, the surface and image begins to be altered as seen previously . However, in this series, higher magnification and better resolution allows us to observe progressive modification of individual collagen monomers.

These changes are apparent in two molecules (arrows in Figure III-46a). Image B, at 3.9 nN of force, shows no appreciable change in the appearance of either the "bow tie" shaped molecule or the "circular" molecule. The image quality is degraded due to the higher imaging force. Increasing imaging force (image C), and interactions between the sample and imaging tip, have completely obscured the molecules. A subsequent image (III-46b G), taken immediately after C, at a lower force of about 1.0 nN, shows alterations in the shapes of these two molecules. The "bow tie" has lost significant portions of its ends, and the circular molecule is beginning to "bulge" at

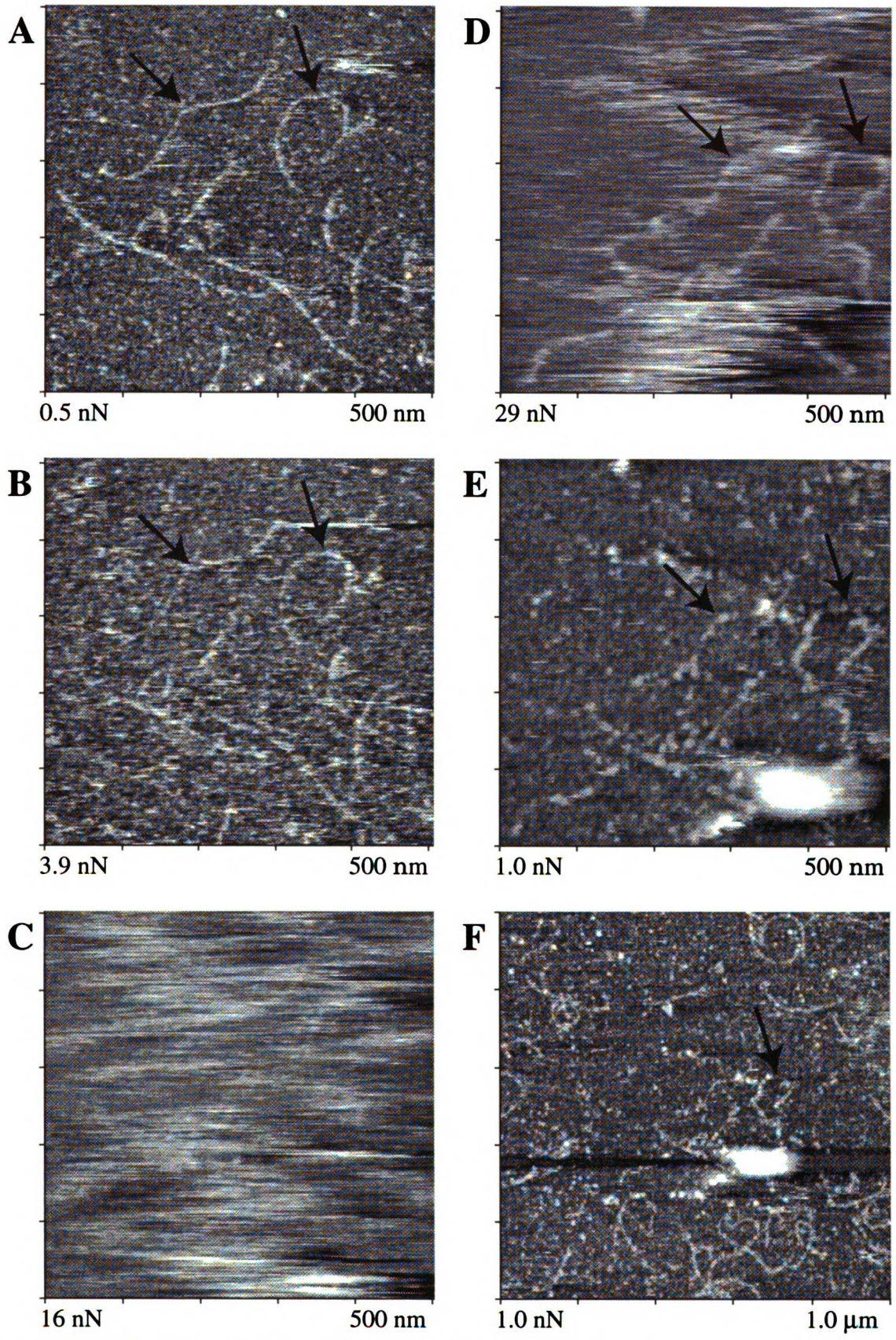

Figure III-46a Second collagen force series at room temperature.

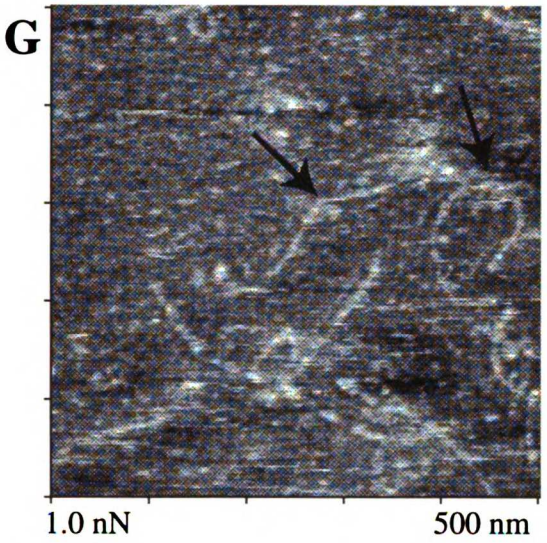

Figure III-46b Interim low force scan image taken between C (16 nN) & D (29 nN).

the upper right corner. In addition, the overall position of the molecules appears to have changed, due to the effects of lateral drift of the scanning tip relative to the sample. These effects of higher scanning forces have become more pronounced in images D, E and F. Image D, taken at a force of 29 nN, shows pronounced deformation and displacement of the molecules on the surface. Images E and F, both subsequently taken at low force, show that these changes are permanent, and that there has probably been selective removal of parts of the collagen molecule from the sample surface. Scan F is a 1 μm overview of the 500 nm high force scan area. By varying the imaging force, we are able to damage and selectively remove portions of molecules in a somewhat controlled and reproducible manner.

A final collagen force series at 143 K is shown in Figure III-47. These images are unusual in that the molecules are very distinct, with very low surface contamination; at least partly due to the low temperature of the experiment. Sample quality, in terms of clarity and cleanliness, allowed us to examine force/surface modification at a smaller size scale and at higher resolution. Image A is a 200 nm normal imaging force scan of several col-

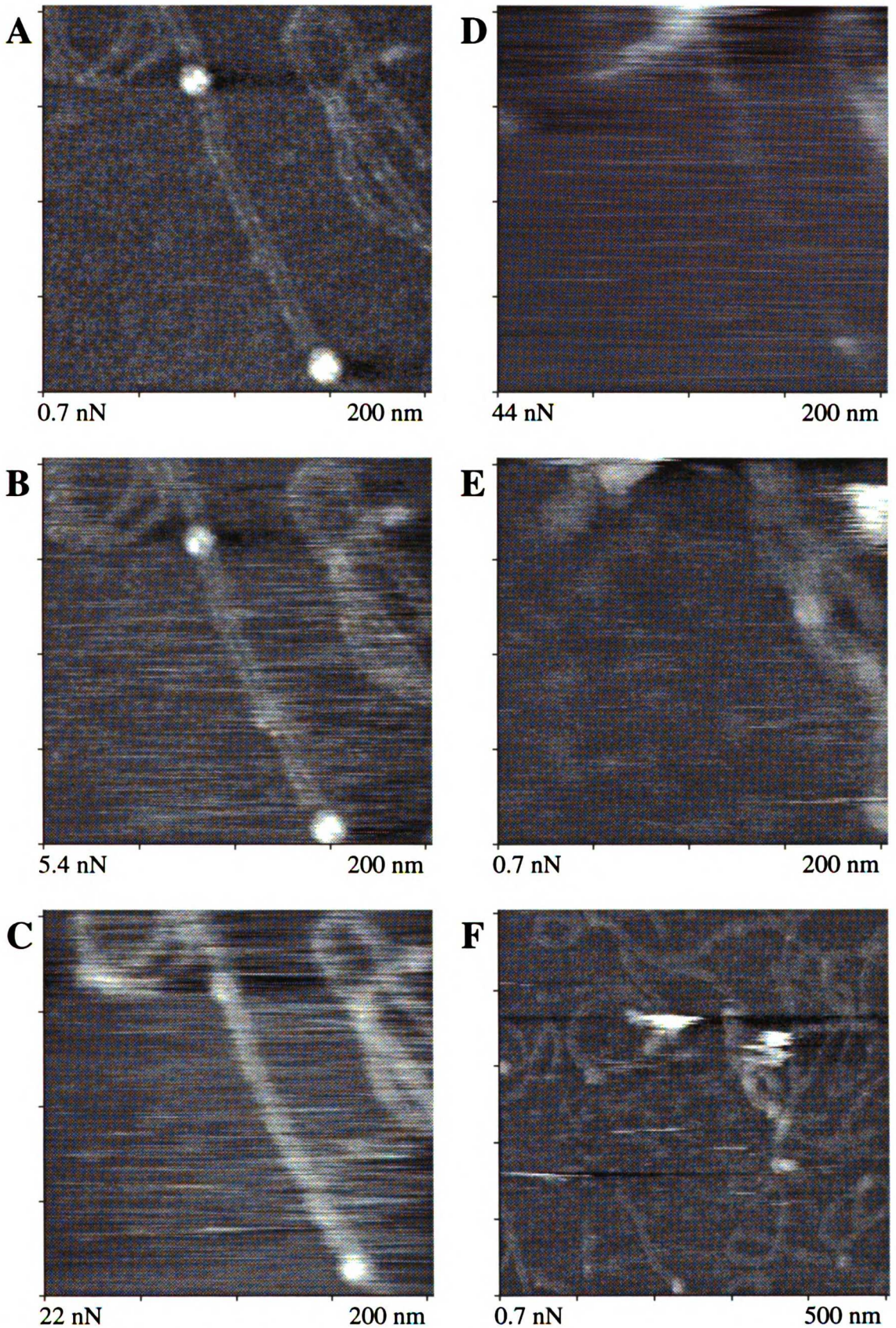

Figure III-47a Collagen force series at 143 K.

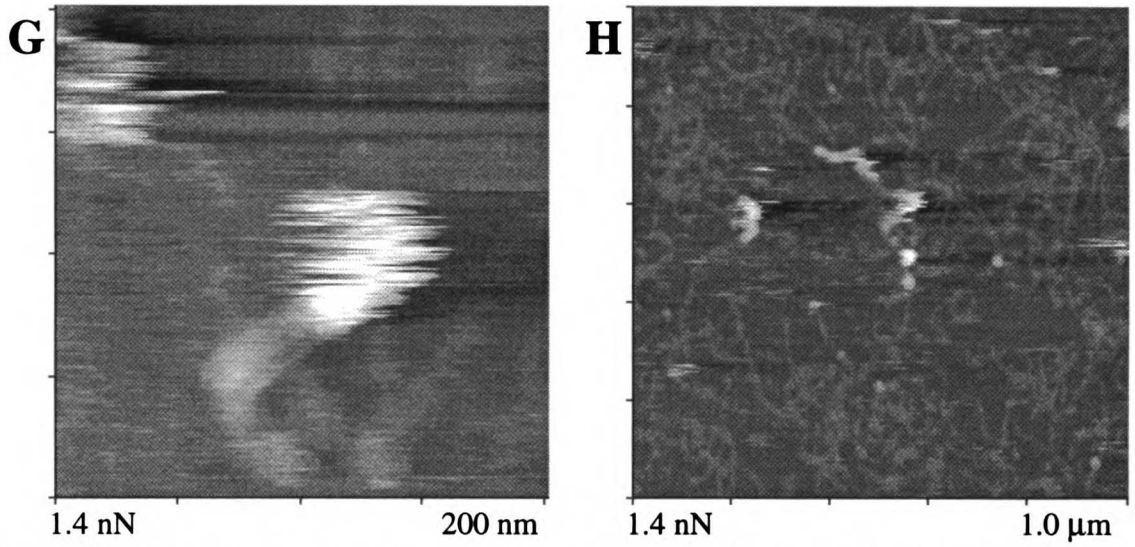

Figure III-47b Scan images taken after force series of Figure III-47a, and after 170 nN scan.

lagen molecules (shown earlier in Figure III-30). The diagonal structure is about 2/3 of a single molecule. This molecule has several pronounced bumps as previously discussed, and appears "double" as the result of a double tip. Despite the double tip, the molecular resolution is particularly good. Images III-47 B through D again are at increasing forces, up to a maximum of 44 nN. A return to an imaging force of less than 1 nN (image E) shows that the molecules have been dislocated to the right side of the image. This series is interesting in that the diagonal molecule is seen to remain basically intact, until its removal during the high force scan of image D. Compared to (and unlike) the room temperature force series data, we see no evidence of preferential removal or dislocation of the molecule up until this point. The 500 nm overview scan (Image F) shows that much of the sample has been pushed to the right side of the image, but not completely removed. Following a very high force scan at 170 nN, images III-47b G and H were taken at 200 nm and 1.0 µm respectively. Image G is close-up scan of the damaged molecules dislocated to the right in the previous images.

The structure at the center has been clearly displaced to the right by the scanning tip, and may have been cut from the upper left of the image. The 1.0 μm scan shows that the area imaged at high force has now been swept clean.

Machining

One of the attractions of SPM is the ability to modify the imaged sample directly. With SFM, by controlling the tip/sample force, it is possible to modify and interact with a single native molecule and immediately examine the results. The force series is an example of varying the imaging force to modify a molecule. Next we shall consider modifying both large and small scale biological samples with a controlled application of force.

We examined the feasibility of physically modifying portions of purple membrane. Lipid membranes are an interesting candidate due to their characteristic bilayer structure with embedded proteins. There is a large body of classical freeze-fracture work on membranes, showing that the bilayer splits during fracture. Low temperature might be helpful in SFM studies of membranes by minimizing lipid mobility.

Figure III-48 A shows purple membrane imaged at 143 K in n-pentane. A smaller scan image on the surface of the membrane at about 100 nN removed of the central portion of the membrane patch (image B). Interestingly, this fractured area is higher than the polylysine background, as depicted in the single line scan of plot C. This line scan proceeds from the background, through the fractured area, and onto the membrane surface. The difference in height between background and fractured area is about 0.6

nm (determined by a plane fit height difference routine). While clearly not high enough to represent half of the bilayer, this observation raises the possibility of splitting membranes directly and examining them with the SFM, without metal shadowing.

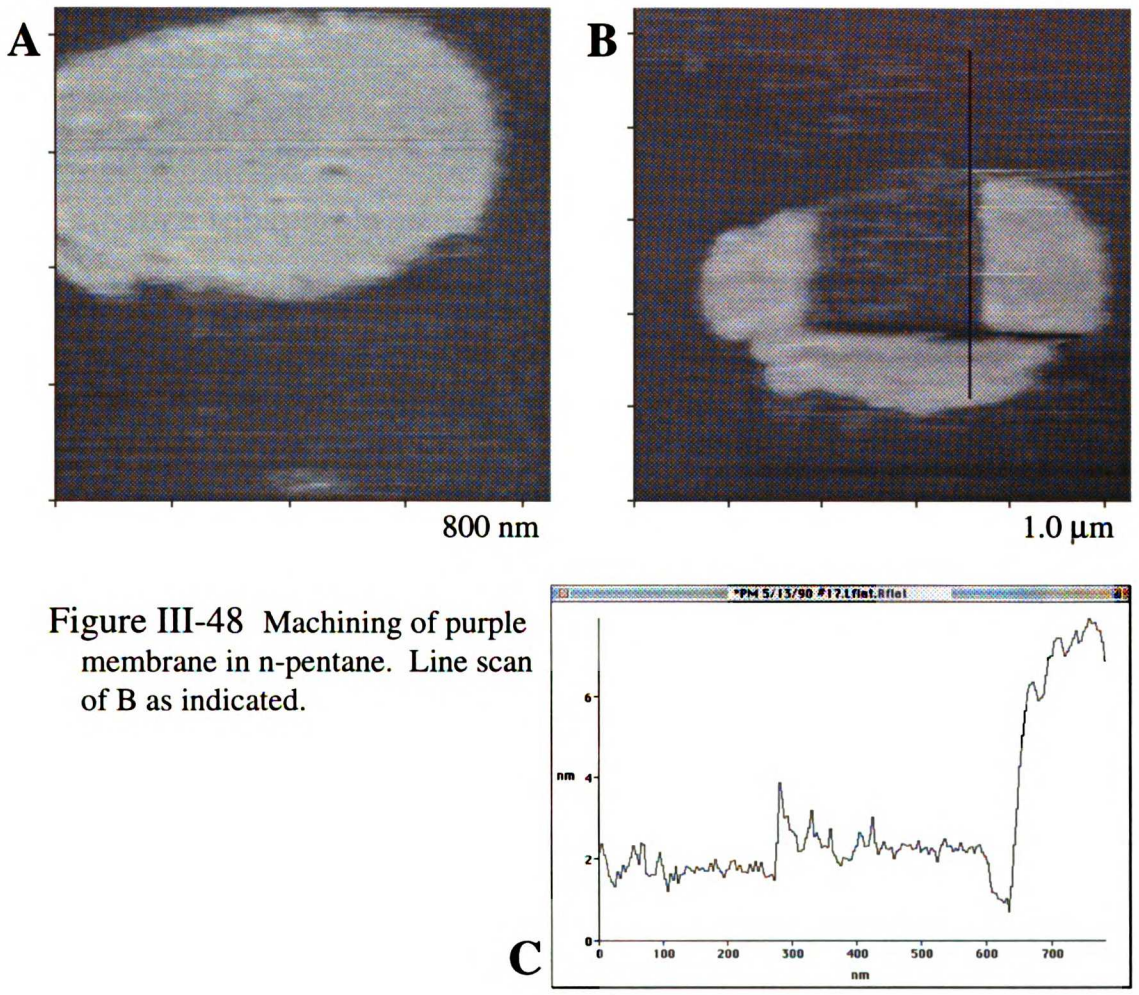

Figure III-48 Machining of purple membrane in n-pentane. Line scan of B as indicated.

We are unable to say with any certainty what the nature of this fractured area is. The tip was poor, and we could distinguish no differences in texture between the background and the fractured area. The residual height could be a layer of trapped contamination, or might be the remnants of some portion of the bound membrane. The RMS roughness of the area, about 0.3 nm, is

comparable to the intact membrane surface, and higher than the smoother (RMS = 0.2 nm) background. This indicates that the area may be representative of the original membrane surface. This might be due to the original surface being somehow imprinted in the underlying layer of stuff, or it is possible that some fraction of the lipid bi-layer has been left behind (i.e. the membrane split).

The 0.6 nm difference in height is about a quarter of the expected value of 2.3 nm for a split purple membrane. This could be at least partially accounted for by the layer of surface contamination surrounding a split membrane. Another possibility is that the membrane has split with removal of the protein component, resulting in large voids in which the remaining lipids would rearrange, lowering the apparent height of this layer. A split bi-layer would expose hydrophobic lipid tails to the hydrophobic pentane environment, possibly allowing for some rearrangement, while the hydrophilic head groups remain bound to the surface. Clearly SFM freeze-fracture is an interesting area for future study.

Our SFM is capable of more subtle and controlled removal or machining of large structures, as shown in Figure III-49. These are images of a large surface structure found during a low temperature attempt to image DNA. The DNA sample was provided by Dr. Lyubchenko, and we do not know the identity of this object. However, our ability to locally fracture and selectively remove this object at 143 K makes these data unique. Dimensionally, the structure is about 4.5 nm high, which is quite similar to purple membrane, but machined at a much lower force than that used for PM.

This object was originally imaged in fast mode. The feedback signal was

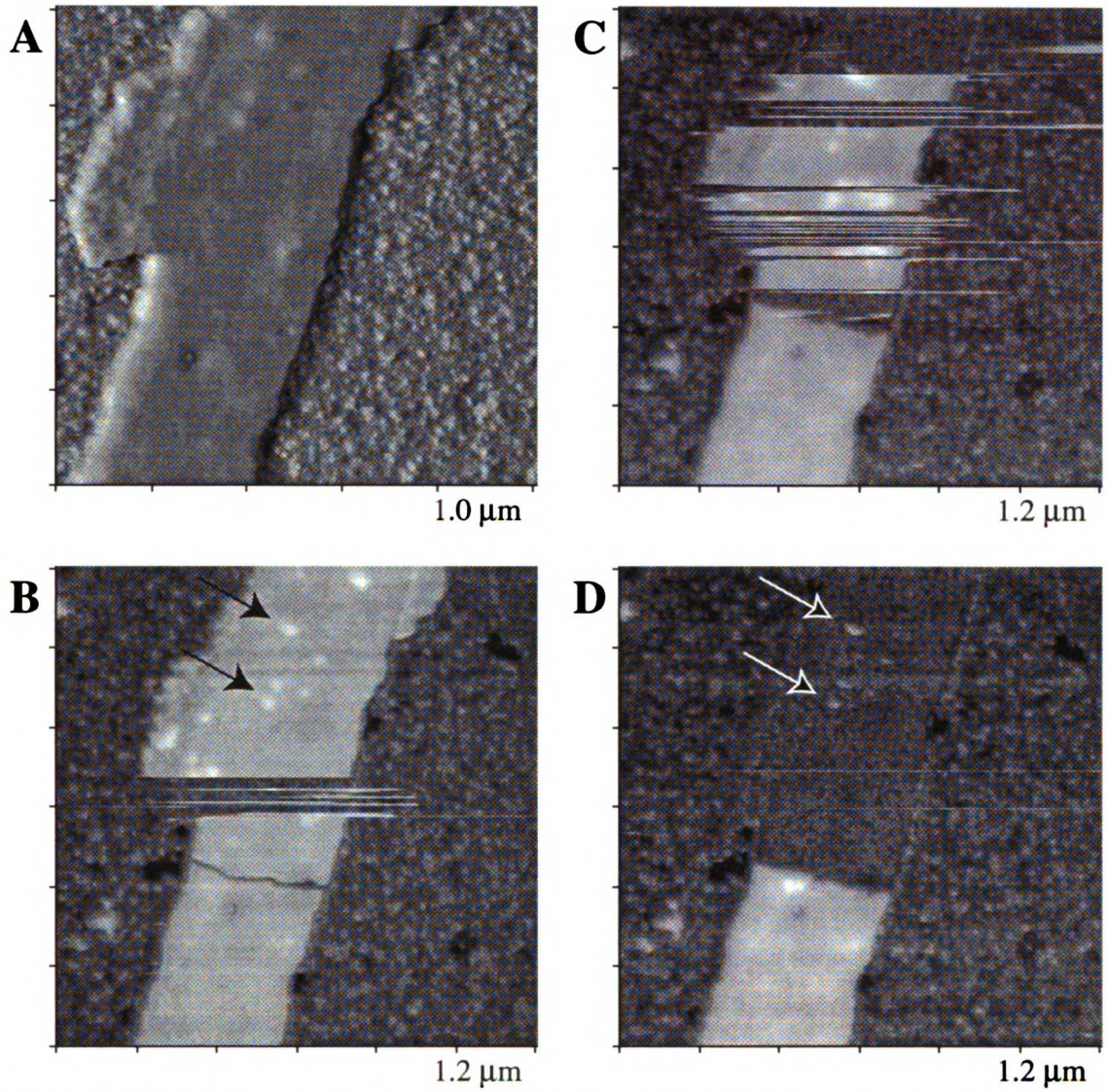

Figure III-49a Mystery object on DNA sample machined at 143 K by repeated scans at 5 nN. Arrows indicate sub-object imaging. Note fracture of object in image B. Images B – C taken in hold mode, image A in fast mode, resulting in different appearance.

set to maintain a constant imaging force over the face of the image (image III-49 A). Subsequent images (B – D) were taken in hold mode, with no feedback signal at all. The force, initially set at about 0.5 nN, would "drift" higher as the image was scanned, probably due to thermal effects or a tilt in Y. As a result, the scanning force varies across the image in the Y direction, from 0.5 nN at the bottom of the image to about 5 nN at the top. As the

object was scanned in image B, it was subjected to increasing force in the Y direction, which resulted in selective removal, or machining, in the X scan direction. About a dozen X scans in the middle of the images removed a portion of the object. Below this area is what appears to be an induced fracture, as if the object was brittle or fragile (at 143 K). Repeated scans as shown in C and D, with the same increasing force profile, resulted in the complete removal of the object from the break upward.

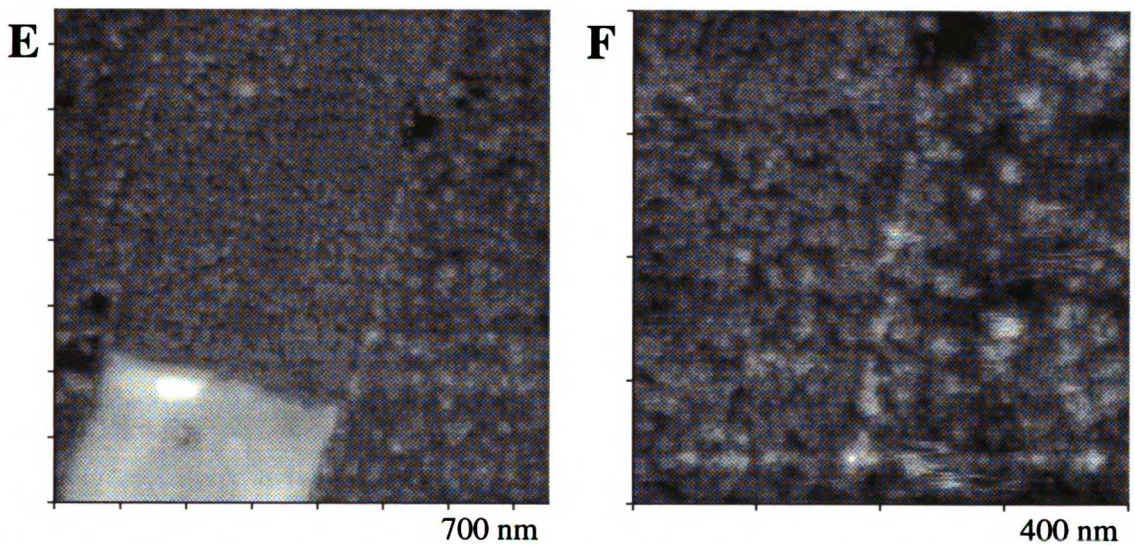

Figure III-49b High magnification images of surfaces from previous figure showing difference in surface roughness.

The area from which the object has been removed in image III-49 D shows some interesting features. The area has a clearly different texture from the surrounding background, and appears to be smoother. Bumps of an unknown nature, and apparently present underneath the object in image A and B, remain in the area (arrows). A close up of the area is shown in image E (III-49b), along with an image (F) of the transition from that area to the background. The area clearly has a smoother, and maybe more organized, structure than the background, with no apparent difference in height.

Clearly, the presence and removal of the object has altered the underlying surface, if no more than to decrease the background RMS roughness from 0.65 nm to 0.45 nm. The object itself had a surface roughness of 0.20 nm. For comparison, our cold collagen images typically have a background roughness of about 0.10 nm. Despite the uncertainty of the nature of this object, these images give some indication of the potential of SFM to modify and investigate a large scale object in a controlled manner.

Our most exacting example of molecular machining is the controlled dissection of a single collagen molecule. I selected a single molecule at the conclusion of the 8/18 low temperature collagen experiment. A normal fast mode image of this molecule, imaged at a force of about 1.2 nN, is depicted in Figure III-50. The SFM scanning tip was then repositioned to a constant Y position of about 150 nm, where the tip force was increased briefly to about 60 nN as the tip scanned back and forth in X. These high force X scans at a single Y position effectively cut the molecule (image B). Image B is a normal force scan (and essentially a repeat of image A) showing the cut in the lower portion of the molecule (arrow). The molecule has been severed, leaving two new ends that appear as bumps with a "sticky" quality, where the tip seems to momentarily adhere to the sample. This may represent damaged molecular subunits which are now de-stabilized, and possibly pulled back and free-floating. The disruption of both intermolecular and surface ionic bonds may produce significant realignment and interaction of the molecule. The stickiness of the new cut may reflect this reactivity. It is remarkable that the collagen molecule, with its significant positive charge, is so tightly bound to the mica surface, and that the localized cut does not result in more widespread disruption.

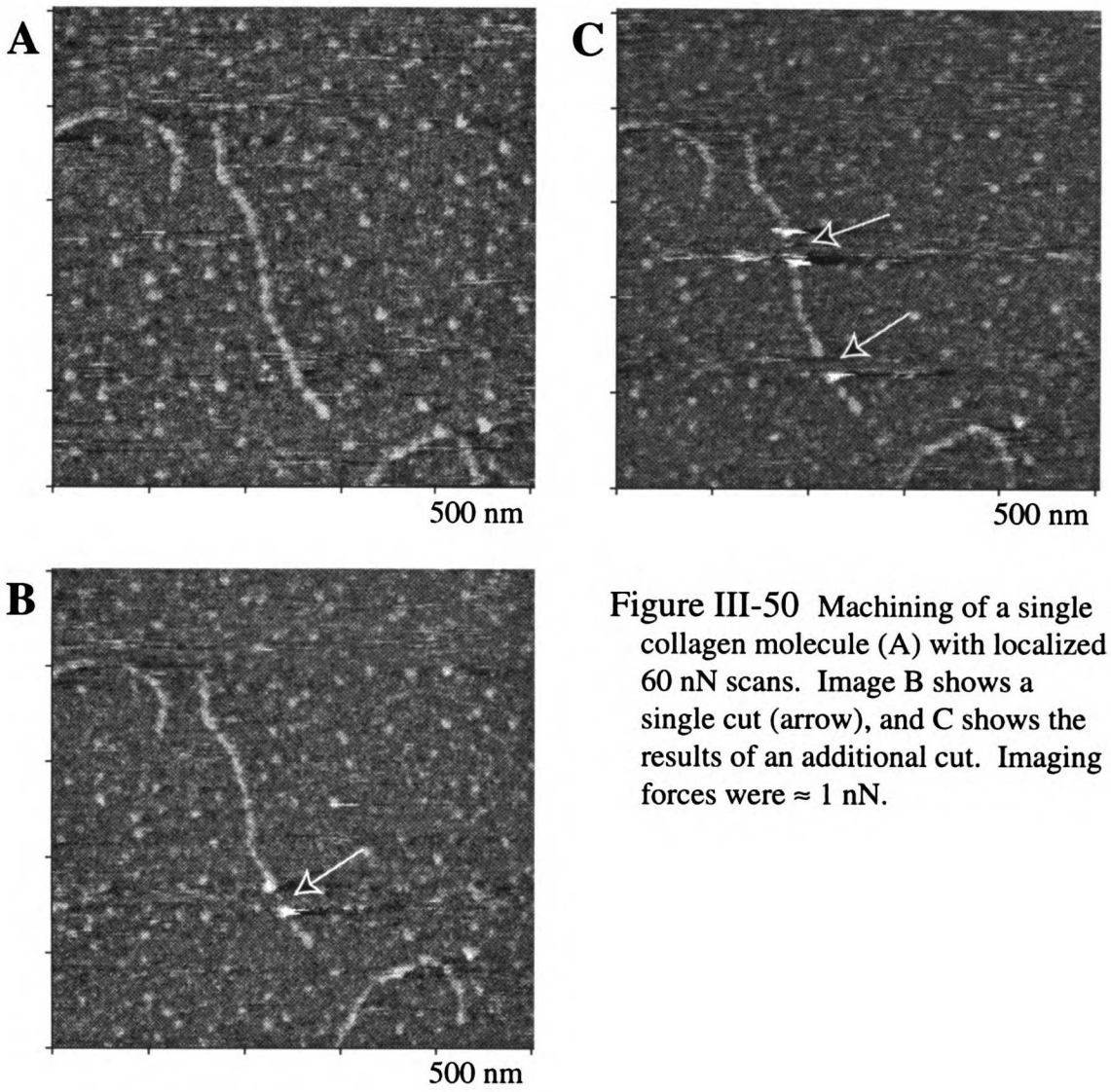

Figure III-50 Machining of a single collagen molecule (A) with localized 60 nN scans. Image B shows a single cut (arrow), and C shows the results of an additional cut. Imaging forces were ≈ 1 nN.

A second cut was made in the same collagen molecule, as shown in image C. The new cut, again indicated with an arrow, has a similar sticky appearance. The original cut has become less sticky, possibly indicating a reduction in the reactive nature of or binding to the free ends. This demonstrates the controlled nature in which a molecule can be locally altered. We were able to control the point of force application to a few tens of nm, and the resulting break is about 10 to 15 nm wide. A cut of 12.5 nm corresponds to a tip radius of about 140 nm, assuming that the entire cut was produced by the cutting action of the tip, and that the molecular ends do not pull back or

float free. However, considering the high local contact pressures and tip/ sample interactions these assumptions are unrealistic. Molecular "squishing" may be a more accurate description than true cutting.

Controlled cutting gives us a direct way to physically probe a single collagen molecule. Such investigations could be used to investigate intermolecular forces, or differences in surface binding forces of relatively small molecular domains. Similarly, intramolecular forces between collagen molecules, or single molecules and antibody complexes, could be examined. At the very least, SFM gives us the potential to examine changes in the physical properties of single molecules, such as elasticity, without constraint to bulk materials.

Elasticity

We have endeavored to extend such force investigations to the issue of biomolecular elasticity, in the hope of understanding how the elasticity changes with temperature. Force modulation allows measurement of surface elasticity with the SFM (Maivald *et al.*, 1991); and SFM has been used to measure the microelastic properties of biological samples (Tao *et al.*, 1992), although generally of large scale structures such as bone. The hypothesis that low temperature would stiffen biological samples, and reduce thermal fluctuations, was central to the design of our LT-SFM. To test this hypothesis we examined differences in ferritin elasticity between room temperature and 143 K. The LT-SFM is uniquely suited to this task.

Ferritin was chosen as a test sample because it is a well characterized protein that is large and symmetrical. In principle, the elasticity of a single

ferritin molecule could be approximated by measuring the change in height as a function of increasing force. We attempted to generate a continuous force curve for a single ferritin molecule, but found it difficult to keep the SFM tip "parked" on top of the molecule. However, ferritin molecules could be effectively compressed in steps by repeated imaging at increasing force. We found that they would regain their original height when the force was subsequently reduced to its original value. Measuring height change as a function of increasing imaging force, both at room temperature and at 143 K, can give us some insight as to how protein stiffness changes with temperature.

Figure III-51 is a side by side comparison of a ferritin force series at room temperature and at 143 K. The first images (A) are the low force initial scans at about 0.15 nN. Both series of images are of the same sample, using the same tip, and taken under the same scanning conditions. Only the temperature has been varied. Room temperature scans were obtained first, followed by microscope cooling with liquid N_2, and scanning at 143 K. The forces reported for each scan are the "average" force for the background, as the actual force varied slightly across the face of the image since the scans were taken in hold mode.

The second images (B) in the series, at an increased force of about 0.5 nN, show few obvious differences from the initial scans. Individual ferritin molecules are only slightly changed. However, molecular height appears lower in images C, as the increased force (about 1.0 nN) further compresses the molecules.

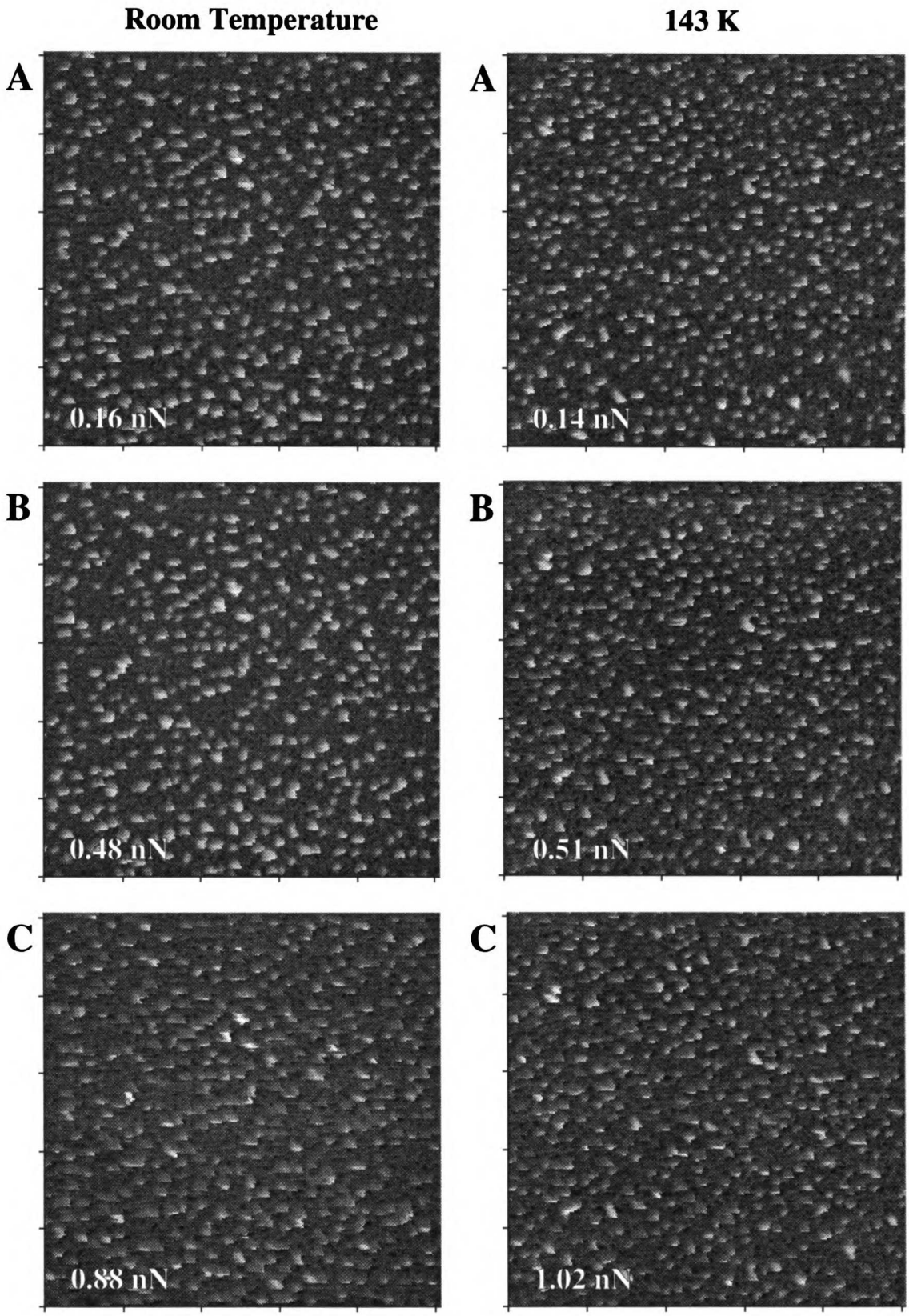

Figure III-51a Ferritin elasticity force series as indicated. Continued on next page.

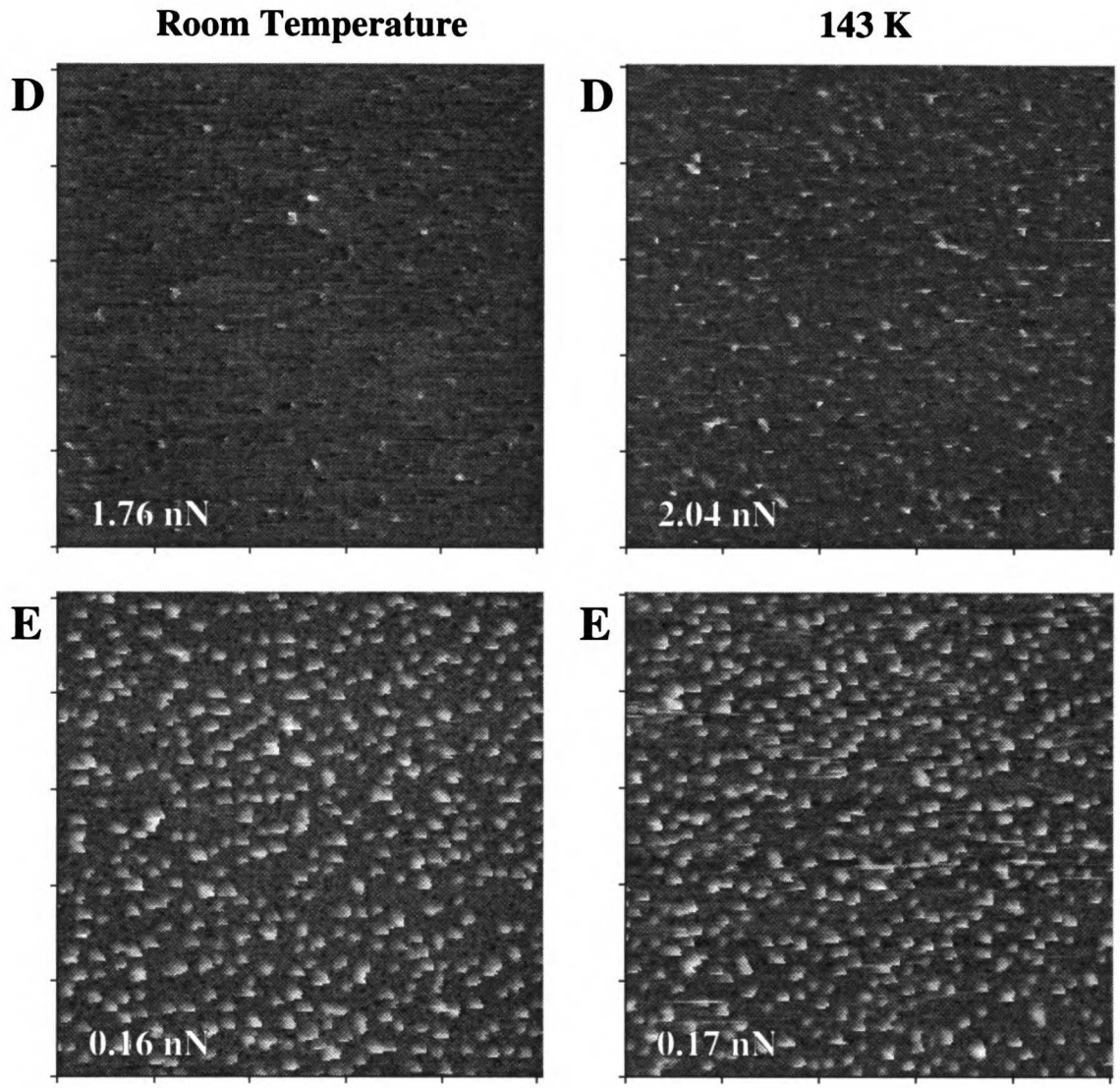

Figure III-51b Ferritin elasticity force series as indicated. Notice how molecules have virtually disappeared in images D (high force), but reappear at low force. All scans for this and the following figure are 1.0 μm.

When the force is again doubled, to about 2 nN, the molecules appear substantially compressed. Images D (Figure III-51b) show the same basic arrangement of molecules as the previous image, except that the majority of them have been compressed virtually into the background. The low temperature scan does appear to have slightly higher imaging heights, and was actually obtained at 10 % higher force. This may indicate that the ferritin

molecules are correspondingly stiffer at lower temperature.

Perhaps the most surprising images are shown in III-51b E. These are follow-up scans, made at a scan force of less than 0.2 nN. The individual molecules appear to have "bounced back" from the high force scans of images D, with no apparent damage. Comparison of these final images with the initial (A) scans shows that the molecules are in their original relative positions, and that they have returned to about their original relative height. The only visible change is some tip sticking in the final cold image, probably indicative of some tip contamination during the 2.0 nN scan.

For comparison, I have included an additional force series from the same experiment. These scans (Figure III-52) were made at room temperature immediately before the scans shown in Figure III-51 (warm), but were made in slow (feedback) mode, thus allowing for a continuous imaging force throughout the scan. This has the advantage of subjecting the molecules to the same uniform force, unlike hold mode in which the imaging force increases with sample height. The ferritin molecules in this series of scans exhibit about the same force characteristics as seen for the hold mode series of Figure III-51.

In principle one could measure the change in apparent height of each ferritin molecule at increasing force as a function of temperature. Practically, it is quite difficult to measure this change for a single molecule. There are several sources of experimental error in height determinations (note tip sticking in Figure III-51b, image E). Accurate measurement is hampered by the "glitchy" nature of the images, in which the tip appears momentarily to stick at the top of a molecule, distorting its apparent height. A large sample

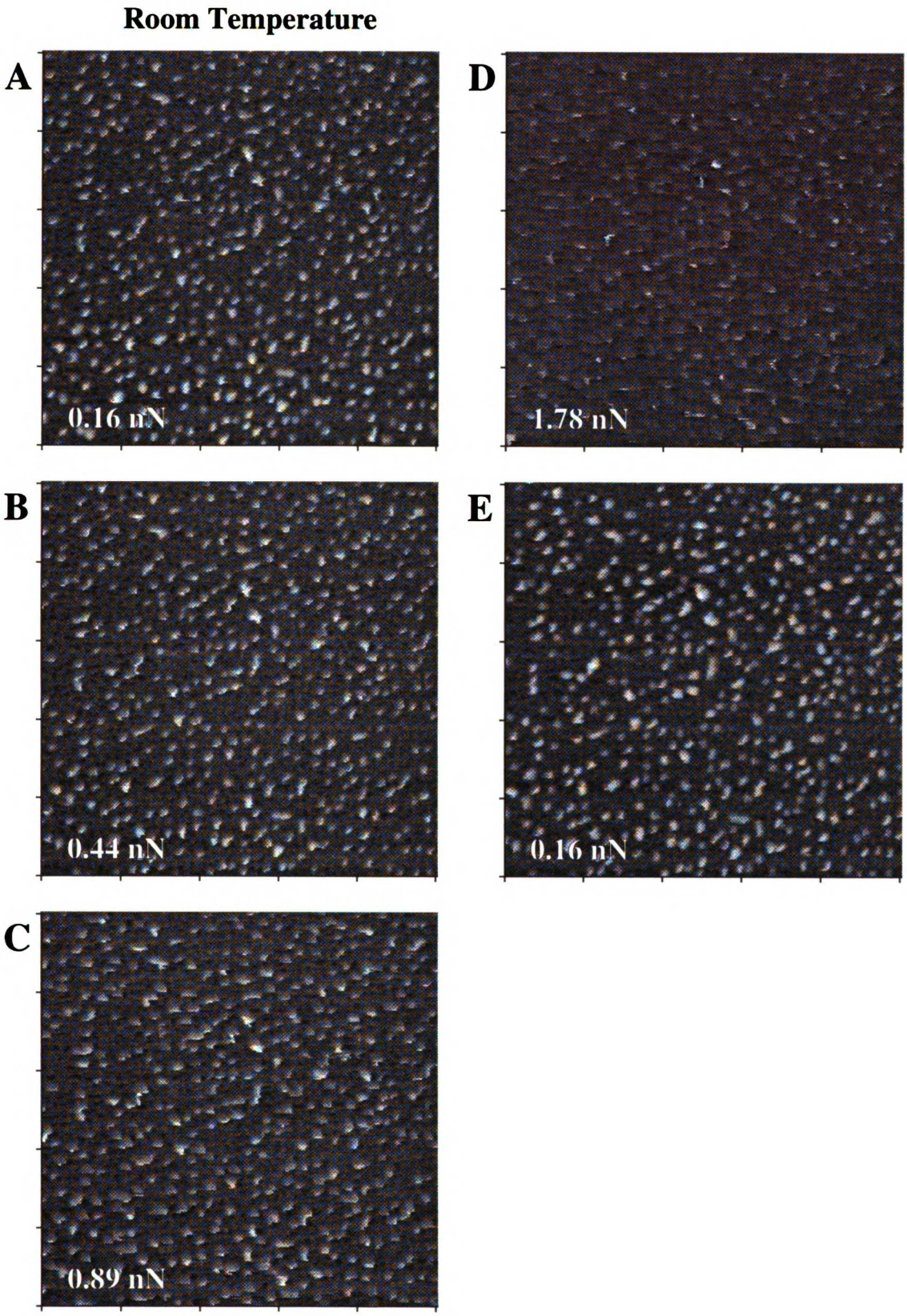

Figure III-52 Room temperature ferritin elasticity force series, but in slow mode.

of molecules could be measured, resulting in a distribution of heights, but randomly picking molecules in the image is difficult. Moreover, it is difficult to find individual molecules where height can be determined independently from neighboring molecules by the MacAcquire "feature height" routine.

We can, however, use the RMS surface roughness routine in a preliminary attempt to quantify the change in height with force (in the spirit of the quick and dirty). As the molecules are compressed, the overall "roughness" of the entire surface can be expected to in some way to be reduced. This method has the advantage in that it includes the apparent height change for all of the molecules in the image, and is an easy measurement to make. It has the disadvantage in that it is not obvious how the change in overall roughness correlates to the change in molecular height, and that measurements will incorporate changes in the background as well. Furthermore, the routine uses the edge of the image to establish its surface reference plane, and that edge will include several molecules. In addition, height anomalies, such as sticking, will be incorporated into the roughness estimate.

Despite these difficulties, the RMS roughness may yield insight into the relative elasticity of ferritin at room temperature and 143 K. The roughness can be expected to at least reflect the change in apparent height of the molecules, and we have the advantage that all images are of the same individual sample, with very similar distributions of molecules across the image. I have quite simply measured the RMS roughness for each complete image in the preceding figures with the MacAcquire program. The results were then normalized to the initial low force images, setting them at a RMS value of 100 %. The change in RMS due to increasing force is reported as a percent-

age change relative to this low force value.

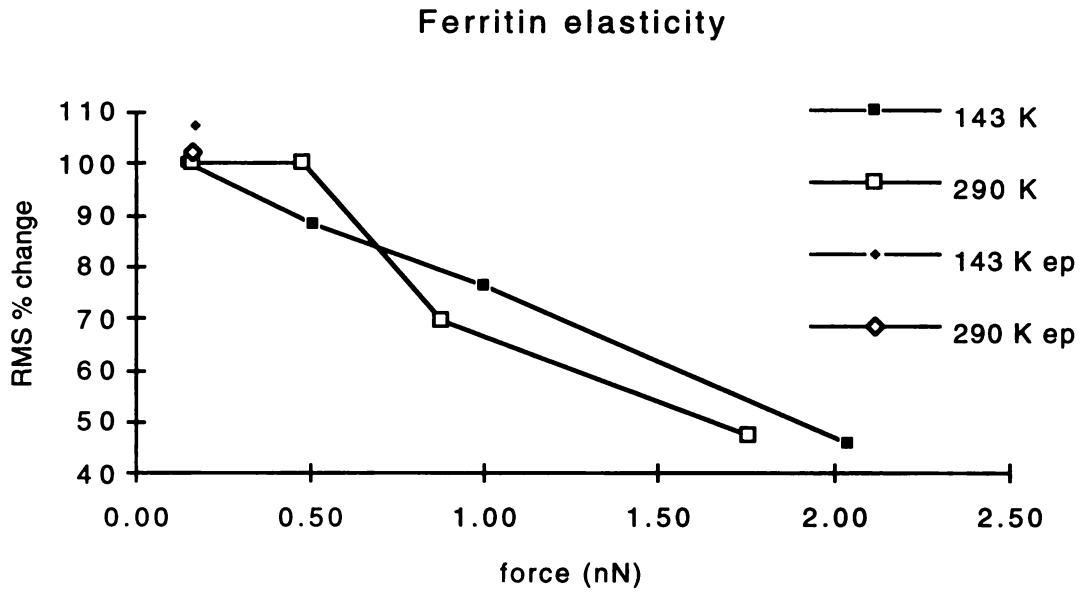

Figure III-53 Ferritin elasticity as indicated by a change in surface roughness at room temperature and 143 K. Ep stands for end-point, and represents the surface roughness for the final low force scan in each series.

The results of this limited analysis are shown in Figure III-53. This graph is a plot of the RMS % change in the images of Figure III-51 versus imaging force. For example, the 143 K data decreases quite linearly (in itself rather surprising), to about 50 % at an imaging force of 2.0 nN. The room temperature curve has a sigmoidal appearance, which might say something interesting about the warm elasticity. Unfortunately, there is a reasonable probability that the second point (at 0.5 nN) was actually obtained at a force of 0.2 nN, due to a force change during the image scan. As a result, this second warm data point might actually be located about on top of the first point, giving a linear plot similar to the cold data.

This possibility is reinforced by a similar plot of RMS % change for the room temperate data acquired in slow scan mode (Figure III-54). As discussed in the calibration section, it is difficult to compare scans obtained

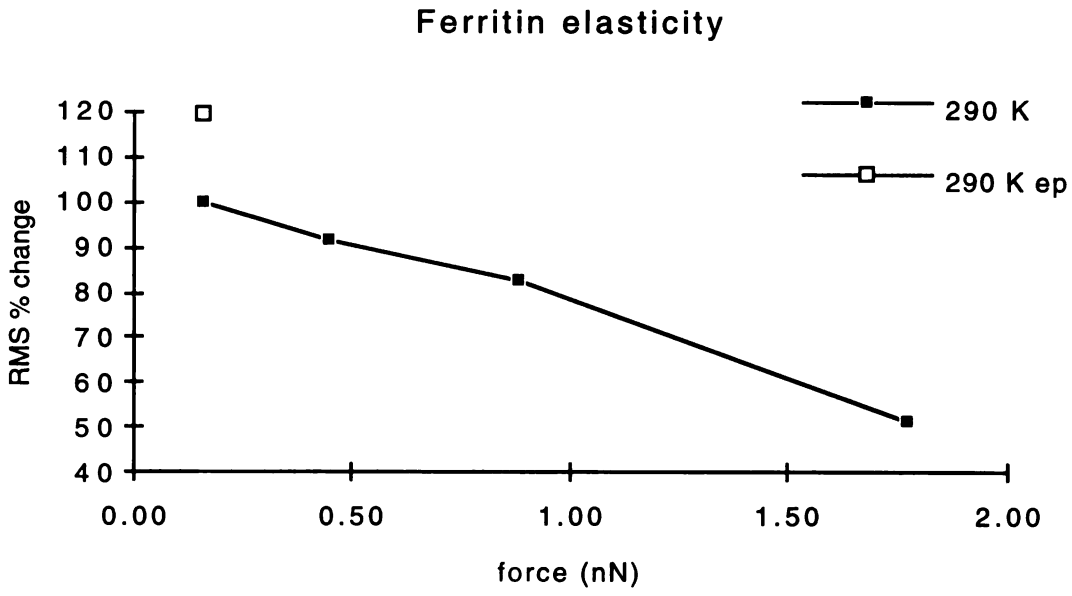

Figure III-54 Room temperature force series and change in surface roughness acquired in slow (feed-back) mode.

under different scan conditions. However, the basic shape of this curve is very similar to the 143 K curve of Figure III-53, calling into question the sigmoidal shape of the warm force curve.

In any event, it appears that cold samples are slightly less elastic than warm. At higher forces, warm ferritin molecules are more compressed, at least as related by the RMS measurement. The difference in these curves, however, is not large, and the uncertainties in our measurements are relatively high, making this a questionable result, although it is in the right direction.

This uncertainty is exacerbated by the glitchyness of the ferritin images. As the ferritin molecules are individually scanned, the tip occasionally appears to stick in some way on top of the molecule. This could be due to some tip/sample interaction, the presence of contamination, or transient force increase when on top of the molecule (hold mode). The result is that

many of the molecules have a glitch superimposed on their apparent height, which results in a significant error in any height estimate for that molecule. One can hope that this glitching is at least constant from image to image, making the error somewhat systematic. That is unlikely, however, due to the dependence of glitchyness on imaging force. Such an increase in glitchyness may explain why the final low force scan seems to return to a slightly higher apparent height after the force series. The presence of glitch artifacts in these images makes it all the more surprising that the RMS force curves appear to be so linear.

The various errors and uncertainties just discussed, and the rather limited data set, makes it difficult to put much faith in the slight decrease in elasticity at 143 K. This is a particularly interesting question in light of the original rationale for designing the low temperature SFM. These data suggest that the effect of temperature on elasticity is in the expected direction. Measurements of individual molecules from these images also indicate an increased stiffening of ferritin molecules at low temperature, and of about the same magnitude as indicated by Figure III-53. Determining if these differences are significant, however, can only be established with more experimental data.

The unique aspect of this experiment is that it demonstrates the potential of the SFM to measure an intrinsic physical property of a biomaterial at the molecular level. SFM has been used to measure surface elasticities (Maivald *et al.*, 1991), and the microelastic properties of biological surfaces including cartilage (Weisenhorn *et al.*, 1992) and bone (Tao *et al.*, 1992), but at relatively large size scales and at room temperature. Unlike these and most other measurements on bulk materials, we are able to probe the nature

of the physical characteristic of a single molecule, and how that characteristic varies with a changed environment.

While the precision of this initial elasticity experiment was obviously somewhat limited, it does lead to the surprising finding that there is not a large change in elasticity with temperature. It was, of course, our hope that the cryogenic temperatures of our SFM would result in a significant stiffening of the biological sample, thereby improving both resolution and stability. Intuitively, it is easy to expect that frozen things get much harder. Indeed, much of the design and the thinking about this SFM was inspired by freeze-fracture techniques in more classical microscopic work. In freeze-fracture, freezing (and thus solidifying) the sample allows one to cleave and investigate normally soft or fluid samples with molecular precision.

Freeze-fracture, and possibly our intuition, depends on the freezing of water for the transition to the solid state. The very notion of freezing is in fact somehow rooted in the concept of water freezing from liquid into solid. And in most biological materials, the high water content in some sense results in the freezing of the entire sample, as in freeze-fracture. But the actual freezing of such a sample is mostly confined to the water matrix, as these data indicate. The increase in the stiffness of the actual protein molecule, even with tightly-bound water, in the absence of a water environment, appears to be small over the 150 °C temperature range of our LT-SFM.

Freeze-Fracture

Freeze-fracture has been an inordinately successful microscopic technique at the cellular level. Freeze fracture techniques, developed initially for

TEM, are routinely used as morphological and cytochemical methodologies, and thus can be used as a physical fractionation and separation technique (Fisher, 1989b). This is particularly useful as applied to the study of lipid bilayers, which can in turn be split, allowing for the examination of both internal and external surfaces. In this way, integral transmembrane proteins can be studied, as well as protein associations on both the cellular and extracellular sides of a membrane.

The possibility of incorporating freeze-fracture technique with SPM in general and STM in particular has been reviewed (Fisher, 1989a), and was an integral part of the design of this low temperature SFM. SFM at 143 K would have an advantage in that it could in theory examine freeze-fractured surfaces directly, without resorting to metal replicas. SFM would thus be a particularly attractive enhancement to current freeze-fracture technologies, especially in light of its ability to interact with and probe the frozen sample surface. Although we developed a SFM freeze-fracture technique, we have not yet obtained any biological images. I feel that this lack of success was mostly due to time constraints, and that we have in fact resolved most of the technical difficulties. Given the potential of the technique and our near success, I will outline our efforts here.

The advantage of our machine is the ability to examine rapidly frozen (and fractured) biological structures. The freezing process is a particularly attractive alternative to more conventional chemical cellular fixation techniques (Hayat, 1989). Chemical fixatives are limited by diffusion rates into the sample, and generally reflect the response of the cell to the fixative, and not the living state. This is of particular concern considering that many cellular processes occur on a millisecond time scale. Artifacts are also a

concern with chemical fixation, including chemical alteration of the sample, drying and dehydration effects, and denaturation.

Alternatively, the biological sample can be fixed rapidly in something close to its native state by very rapid freezing. Cryofixation effectively preserves the distribution and function of most components of a biological system, such as a cell or membrane, with a "near-instantaneous arrest" of cellular metabolism. Ideally, the result is cellular and membrane morphologies in their native conformations. One of the advantages of cryofixation is that structural artifacts, associated mostly with the formation of ice crystals, are relatively easily interpretable.

The principle concern of cryofixation is to employ very high rates of cooling to minimize the formation and size of ice crystals, and concomitant sample damage. With proper cooling techniques, one can achieve a near vitreous state in which the microcrystalline structure is limited to less than 10 nm. The difficulties in achieving this vitreous state, and the requisite high cooling rates, are the limited thermal conductivity of water and ice, and the mass of the sample. Large samples can be additionally prepared with cryoprotectants to minimize damage. We have chosen to freeze our samples of RBC membrane directly in a bath maintained at liquid nitrogen temperatures, as outlined in Fisher (1982b), substituting pentane for freon-22.

Our final SFM freeze-fracture protocol is described in the materials and methods section. Some of the highlights and difficulties of this methodology were in transferring and cleaving the sample in the SFM, while continuously maintaining cryo temperatures. We had to resolve several additional technical problems as well, such as charge separation during sample cleav-

ing. The largest remaining difficulty is most likely the large thermal mass associated with the initial freezing of the sample. Due to the required cleaving step in freeze-fracture, the sample was prepared on a glass surface glued directly to a magnetic sample carrier. This resulted in a large thermal mass, and a relatively slow rate of cooling. This can be expected to result in formation of relatively large, and potentially disruptive, ice crystals.

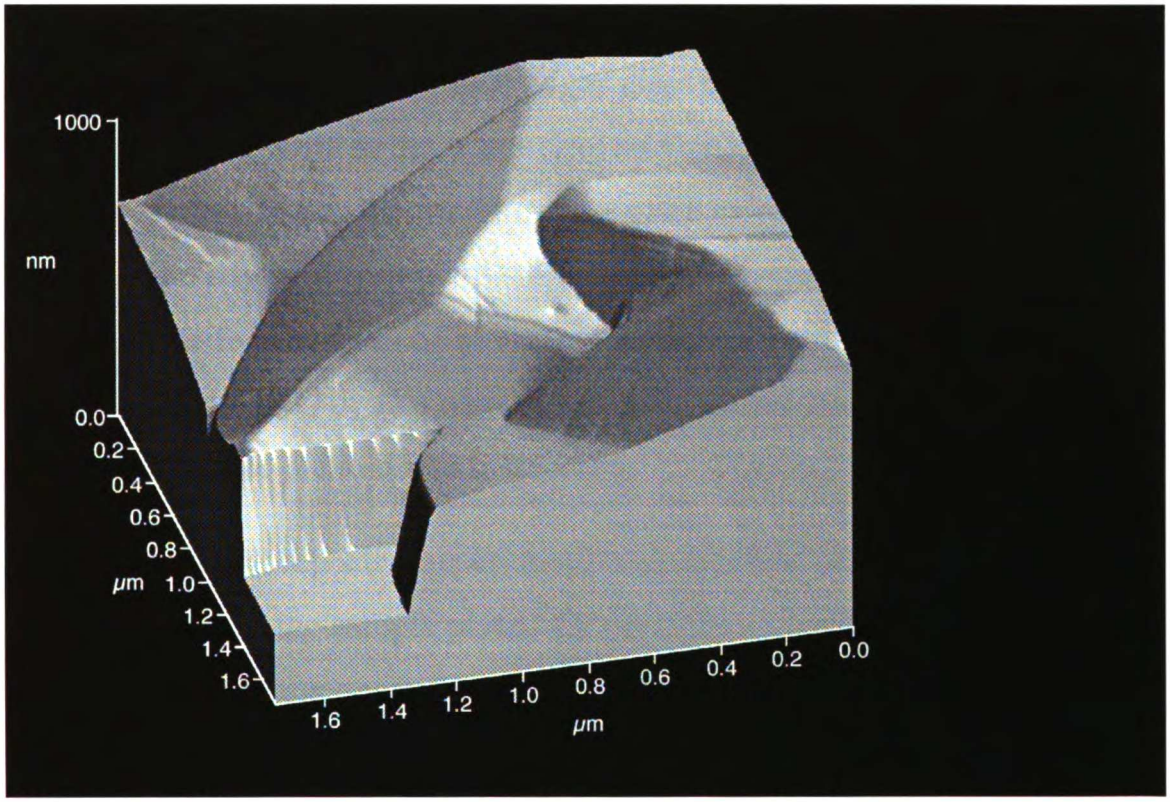

Figure III-55 Image of ice aquired at 143 K during attempts at freeze-fracture.

While we were not able to obtain any images of the RBC membrane, we were successful in scanning a cleaved ice surface at 143 K. Figure III-55 is one such full size scan, showing distinct crystal surfaces. These ice crystals are larger than desirable for freeze-fracture, due to the relatively slow cooling rate during sample preparation. Additionally, our LT-SFM operates at

143 K, above the 130 K vitrification temperature of water (Yannas, 1968). Although we were unable to image sample membranes, this SFM image of ice is in itself unique and has been subject to interest in the SFM community, and raises the possibility of direct physical studies at nearly molecular size scales.

I believe that we did not see a freeze-fractured RBC membrane surface due to the small surface area of our sample, as dictated by the sample carrier. Freeze-fracture controls, on much larger glass coverslips, indicated that the cleaving process starts in the water (ice) section of the sample, and jumps to the membrane plane as the fracture propagates towards the center of the sample. The edges of the controls thus typically appear to be plane fractures in the ice itself. The small SFM sample surface size ensured that the entire sample is "confined" by this edge effect, and that the fracture never established itself in the plane of the membrane.

It is likely that repeated experiments may result in one sample that does initially cleave in the sample plane. Or possibly a sample preparation technique, involving larger sample areas, could be developed that would insure stable membrane cleaving. Unfortunately, time did not permit us to pursue any of these options. However, the possibilities of combining SFM with freeze-fracture, makes this approach worth pursuing in future studies.

Finally

With this work, we have demonstrated the ability to image, modify, and study a wide range of biological materials with a unique LT-SFM. We applied this LT-SFM to samples as varied as large membrane structures, RNA, globular proteins, and collagen with excellent results. Our low temperature

images of biological molecules are the first reported. Our Type I collagen studies produced the first SFM images of single collagen monomers, both at low and room temperatures. These appear to be the first collagen molecules imaged by any SPM technique.

The high quality of our monomeric collagen micrographs at 143 K enabled us to image individual features and associations not readily visible with TEM, or accessible to methods based on averaged structures for a large number of molecules (x-ray diffraction). Some features could be correlated with collagen models based on other structural studies.

The most unusual aspect of this work was the use of cryogenic temperatures with the expectation of improving SFM resolution. Imaging at 143 K has resulted in significant improvements compared to room temperature. The reproducibility and stability of our low temperature images is unsurpassed. This improvement may partially reflect imaging in a nonpolar environment. Quantitatively, our LT-SFM images do not show a large and consistent resolution improvement over our room temperature work, although our highest resolution images were all obtained at 143 K. This is largely due to the resolution limits imposed by the imaging tip itself. The quality of LT-SFM images are significantly improved over comparable room temperature work.

Part of this qualitative improvement is due to the reduction in thermal background noise observed in these data. Room temperature collagen images generally have an average RMS background roughness of 0.20 nm, compared to an average value of 0.10 nm for cold data. This reduction is about what we expected from the equipartition theorem, and is superimposed

on the finite roughness of impurities adsorbed to the mica. The reduced thermal background "noise" effectively enhances the topographic "signal" of the LT-SFM images.

We do not consistently observe an increase in molecular resolution that might be attributable to the decrease in thermal vibrational modes at 143 K. Unfortunately, SFM studies are currently limited by the structure of the imaging tip. The variability in our data from tip to tip (and with a single tip), and the increase in apparent collagen monomer widths, demonstrate the importance of tip shape on image quality and resolution. Images are always convolutions of "non-ideal" tip shape with sample topology, elasticity, and deflection. As these effects are largely non-linear, "convolution" is something of a misnomer (Schwarz *et al.*, 1993). SFMs are fundamentally limited by the tip shape (Steadman, 1988), and tip design is an area of active research. Interestingly, tips are "sharp" at two levels of structure. The overall shape of the tip, sharp at tens of nm, determines the basic resolution of the tip. However, atomic scale structures at the very end of the tip allow for local atomic level imaging. As a result, tips are often capable of imaging either at the atomic level, or at the level of the overall tip shape, with a resolution "hole" in between. The result is little or no lateral topographic information on a size scale from a few atoms to tens of nm.

This size scale is of particular interest in biological studies, as it encompasses the structure of protein amino acids and DNA base pairs. Furthermore, this is the scale at which we can expect significant resolution improvement due to reduced thermal vibrational modes. The ability to consistently detect sub-structures of about 1 nm depends on the future development of sharper, well characterized SFM tips. At that time, the importance of reduc-

ing thermal molecular motions will make LT-SFM very attractive.

Although tip resolution currently hinders quantifying the overall image quality advantages of LT-SFM, these studies do show the utility of low temperature imaging. In addition to improving image quality, LT-SFM intrinsically allows for studies that require low temperature, as shown by the ferritin elasticity data. Direct freeze-fracture studies on biological samples will be another application.

It should be noted that the use of pentane as an imaging environment in the LT-SFM was likely a factor in the stability of biological samples, allowing for the imaging of collagen at room temperature. Pentane, a nonpolar hydrocarbon, can be expected to significantly impact the adsorption of biological compounds on the substrate. Hydrophobic effects, critical to protein folding, do enhance adsorption and stability. A hydrophobic environment is in some ways more representative of a "native" environment for collagen molecules than an aqueous solution. Propanol has been recently used to stabilize DNA samples (based on insolubility) for SFM imaging (Hansma *et al.*, 1992).

Stabilized biological samples open up new possibilities for direct studies with SFM in addition to imaging. Samples can be physically probed at the molecular, and to some extent atomic, level. Biochemical studies are currently in progress in which enzymatically active tips can be used to examine molecular interactions. Observations of enzymatic activity, antibody binding, or any area in which molecular scale forces are of interest will benefit from improvements in SFM technology. Conductive SFM tips can in principle allow for examination of electrical phenomena at the molecular level,

an original premise of this project.

SFM is a part of SPM, a new class of technologies with tremendous potential in a wide variety of disciplines, opening the door on the nanometer world. It is a technique in its infancy, akin to the early days of TEM, and is evolving from a developmental, and descriptive phase into an active area of novel interdisciplinary experimentation. In the future, SPM will allow for the direct manipulation of matter at a scale where the distinctions between physics, biology, and chemistry are no longer adequate.

Bibliography

1. Albrecht, T. R., H. A. Mizes, J. Nogami, Sang-il Park, and C. F. Quate. 1 February 1988. [Observation of tilt boundaries in graphite by scanning tunneling microscopy and associated multiple tip effects]. *Appl. Phys. Lett. (USA)* vol.52 (no.5): 362-4.

2. Barrett, R. C., and C. F. Quate. June 1991. Optical scan- correction system applied to atomic force microscopy. *Rev. Sci. Instrum. (USA)* vol.62 (no.6): 1393-9.

3. Baselt DR, Revel JP, and Baldeschwieler JD. December 1993. Subfibrillar structure of type I collagen observed by atomic force microscopy. *Biophys J* 65 (6): 2644-55.

4. Baselt, D. R., J. P. Revel, and J. D. Baldeschwieler. December 1993. Subfibrillar structure of type I collagen observed by atomic force microscopy. *Biophys. J. (USA)* vol.65 (no.6): 2644-55.

5. Buckley, J. E., J. L. Wragg, H. W. White, A. Bruckdorfer, and D. L. Worcester. March 1991. Large-scale periodic features associated with surface boundaries in scanning tunneling microscope images of graphite. *J. Vac. Sci. Technol. B, Microelectron. Process. Phenom. (USA)* vol.9 (no.2, pt.2): 1079-82.

6. Butt, H. J., K. H. Downing, and P. K. Hansma. December 1990. Imaging the membrane protein bacteriorhodopsin with the atomic force microscope. *Biophys. J. (USA)* vol.58 (no.6): 1473-80.

7. Chapman, J. A., and D. J. S. Hulmes. 1984. Electron microscopy of the collagen fibril. *Ultrastructure of the Connective Tissue Matrix*. A. Ruggeri, and P. M. Motta, Boston: Martinus Nijhoff Publishers.

8. Clemmer, C. R., and T. P. Beebe. 8 February 1991. Graphite: a mimic for DNA and other biomolecules in scanning tunneling microscope studies. *Science (USA)* vol.251 (no.4994): 640-2.

9. Drake, B., C. B. Prater, A. L. Weisenhorn, S. A. C. Gould, T. R. Albrecht, C. F. Quate, D. S. Cannell, H. G. Hansma, and P. K. Hansma. 24 March 1989. Imaging crystals, polymers, and processes in water with the atomic force microscope. *Science (USA)* vol.243 (no.4898): 1586-9.

10. Fisher, K. A. 1989b. Membrane- splitting analyses of membrane- spanning proteins. *Freeze-Fracture Studies of Membranes*. S. W. Hui,Boca Raton, Florida: CRC Press.

11. —. 1989a. Monolayer freeze-fracture and scanning tunneling microscopy. *Journal of Electron Microscopy Technique* 13: 355-371.

12. —. 1982a. Preparation of planar membrane monolayers for spectroscopy and electron microscopy. *Methods in Enzymology* 88: 230-235.

13. —. 1982b. Spectroscopic assays for measuring quantities of erythrocyte membrane "halves". *J. Cell Biol.* 92: 44-52.

14. Fisher, K. A., and W. Stoeckenius. 1977. Freeze-fractured purple membrane particles: protein content. *Science* 197: 72-74.

15. Fisher, K. A., K. C. Yanagimoto, and W. Stoeckenius. 1978. Oriented adsorbtion of purple membrane to cationic surfaces. *J. Cell Biology* 77: 611-621.

16. Fisher, K. A., K. C. Yanagimoto, S. L. Whitfield, R. E. Thomson, M. G. L. Gustafsson, and J. Clarke. 1990. Scanning tunneling microscopy of planar biomembranes. *Ultrmicroscopy* 33: 117-126.

17. George, A., and A. Veis. 1991. FTIRS in H2O demonstrates that collagen monomers undergo a conformational transition prior to thermal self-assembly in vitro. *Biochemistry* 30: 2372-2377.

18. Glantz, S. A. 1981. *Primer of Biostatistics.*, New York: McGraw- Hill.

19. Griffith, J. E., D. A. Grigg, M. J. Vasile, P. E. Russell, and E. A. Fitzgerald. 1991. Characterization of scanning probe microscope tips for linewidth measurement. *J. Vac. Sci. Technol. B* 9 (6): 3586-3589.

20. Gross, J., and D. Kirk. 1958. The heat precipitation of collagen from neutral salt solutions: some rate-regulating factors. *J. Biol. Chem.* 233 (2): 355-360.

21. Hall, C. E., and P. Doty. 1958. A comparison between the demensions of some macromolecules determined by electron microscopy and by physical chemical methods. *J. American Chemical Society* 80 (6): 1269-1274.

22. Hammersley, J. M. and D. C. Handscomb. 1964. *Monte Carlo Methods.*, London: Chapman & Hall.

23. Hansma, HG, Vesenka J, Siegerist C, Kelderman G, Morrett H, Sinsheimer RL, Elings V, Bustamante C, and Hansma PK. 22 May 1992. Reproducible imaging and dissection of plasmid DNA under liquid with the atomic force microscope. *Science* 256 (5060): 1180-4.

24. Hansma, H. G., J. Vesenka, C. Siegerist, G. Kelderman, H. Morrett, R. L. Sinsheimer, V. Elings, C. Bustamante, and P. K. Hansma. 22 May 1992. Reproducible imaging and dissection of plasmid DNA under liquid with the atomic force microscope. *Science (USA)* vol.256 (no.5060): 1180-4.

25. Hayat, M. A. 1989. *Principles and Techniques of Electron Microscopy: Bilogical Applications*, 3rd ed., Boca Raton, Florida: CRC Press.

26. Helseth, D. L., and A. Veis. 1981. Collagen self-assembly in vitro. *J. Biological Chemistry* 256 (14): 7118-7128.

27. Henderson E, Lyubchenko YL, Jacobs BL, and Lindsay SM. July 1992. Atomic force microscopy of conventional and unconventional nucleic acid structures Atomic force microscopy of reovirus dsRNA: a routine technique for length measurements. *J Microsc Nucleic Acids Res* 167 (Pt 1) 20 (15): 77-84 3983-6.

28. Hofman, H., V. Tilman, and K. Kuhn. 1984. Localization of flexable sites in thread-like molecules from electron micrographs. *J. Mol. Biol.* 172: 325-343.

29. Hofmann, H., P. P. Fietzek, and K. Kuhn. 1978. The role of polar and hydrophobic interactions for the molecular packing of Type I collagen: a three-dimensional evaluation of the amino acid sequence. *J. Mol. Biol.* 125: 137-165.

30. Howland, R. S. 1994. *How to Buy a Scanning Probe Microscope*. Sunnyvale, California: Park Scientific Instruments.

31. Kalos, M. H. and P. A. Whitlock. 1986. *Monte Carlo Methods*., New York: John Wiley & Sons.

32. Kempthorne, O., and T. E. Doerfler. 1969. The behaviour of some significance tests under experimental randomization. *Biometrika* 56: 231-248.

33. Kordylewski L, Saner D, and Lal R. March 1994. Atomic force microscopy of freeze-fracture replicas of rat atrial tissue. *J Microsc* 173 (Pt 3): 173-81.

34. Kuwabara, M., D. R. Clarke, and D. A. Smith. 11 June 1990. Anomalous superperiodicity in scanning tunneling microscope images of graphite. *Appl. Phys. Lett. (USA)* vol.56 (no.24): 2396-8.

35. Lyubchenko YL, Jacobs BL, and Lindsay SM. 11 August 1992. Atomic force microscopy of reovirus dsRNA: a routine technique for length measurements. *Nucleic Acids Res* 20 (15): 3983-6.

36. Maivald, P., H. J. Butt, S. A. C. Gould, C. B. Prater, B. Drake, J. A. Gurley, V. B. Elings, and P. K. Hansma. 1991. Using force modulation to image surface elasticities with the atomic force microscope. *Nanotechnology*. vol.2 (no.2):103-106.

37. Mamin, H. J., E. Ganz, D. W. Abraham, R. E. Thomson, and J. Clarke. 15 December 1986. [Contamination-mediated deformation of graphite by the scanning tunneling microscope]. *Phys. Rev. B, Condens. Matter (USA)* vol.34 (no.12): 9015-18.

38. Manly, B. F. J. 1990. *Randomization and Monte Carlo Methods in Biology*., London: Chapman and Hall.

39. Moore, D. S. 1979. *Statistics: Concepts and Controversies*. San Francisco, California: W. H. Freeman and Company.

40. Nestler, F. H. M., S. Hvidt, J. D. Ferry, and A. Veis. 1983. Flexibility of

collagen determined from dilute solution viscoelastic measurements. *Biopolymers* 22: 1747-1758.

41. Radmacher, M., R. W. Tillmann, M. Fritz, and H. E. Gaub. 25 September 1992. From molecules to cells: imaging soft samples with the atomic force microscope. *Science (USA)* vol.257 (no.5078): 1900-5.

42. Rong, Z. Y., and P. Kuiper. 15 December 1993. Electronic effects in scanning tunneling microscopy: Móire pattern on a graphite surface. *Phys. Rev. B, Condens. Matter (USA)* vol.48 (no.23): 17427-31.

43. Salmeron, M., T. Beebe, J. Odriozola, T. Wilson, D. F. Ogletree, and W. Siekhaus. January 1990. Imaging of biomolecules with the scanning tunneling microscope: problems and prospects. *J. Vac. Sci. Technol. A, Vac. Surf. Films (USA)* vol.8 (no.1): 635-41.

44. Scaria, P. V., K. R. Sorensen, and R. S. Bhatnagar. 1990. *Am. Peptide Symp.* 11: 605-607.

45. Schwarz, U. D., H. Haefke, P. Reimann, and H. J. Guntherodt. March 1994. Tip artefacts in scanning force microscopy. *J. Microsc. (UK)* vol.173, pt.3: 183-97.

46. Smith, D. P. E., and J. E. Frommer. 1993. Ordered organic mololayers. *STM and SFM in Biology.* O. Marti, and M. Amrein, San Diego, California: Academic Press.

47. Tao, N. J., S. M. Lindsay, and S. Lees. 1992. Measuring microelastic properties of biological material. *Biophys. J.* vol.63: 1165-1169.

48. Taylor, J. R. 1982. *An Introduction to Error Analysis.* Mill Valley, California: University Science Books.

49. Tiedje, T., J. Varon, H. Deckman, and J. Stokes. March 1988. [Tip contamination effects in ambient pressure scanning tunneling microscopy imaging of graphite]. *J. Vac. Sci. Technol. A, Vac. Surf. Films (USA)* vol.6 (no.2): 372-5.

50. Todd, J. D., and J. B. Pethica. 11 December 1989. A shear model for STM imaging of layered materials. *J. Phys., Condens. Matter. (UK)* vol.1 (no.49): 9823-31.

51. Trus, B. L., and K. A. Piez. 1976. Molecular packing of collagen: three-dimensional analysis of electrostatic interactions. *J. Mol. Biol.* 108: 705-732.

52. Veis, A., and A. George. 1994. Fundamentals of interstitial collagen self-assembly. *Extracellular Matrix Assembly and Structure.* P. D. Yurchenco, D. E. Birk, and R. P. Mecham, San Deigo, California: Academic Press.

53. Veis, A., and K. Payne. 1988. Collagen Fibrillogenesis. *Collagen.* M. E.

Nimni, 113-137. Boca Raton, Florida: CRC Press.

54. Warmack, R. J., X. Y. Zheng, T. Thundat, and D. P. Allison. February 1994. Friction effects in the deflection of atomic force microscope cantilevers. *Rev. Sci. Instrum. (USA)* vol.65 (no.2): 394-9.

55. Weisenhorn, A. L., M. Khorsandi, S. Kasas, V. Gotzos, and H. J. Butt. 1993. Deformation and height anomaly of soft surfaces studied with an AFM. *Nanotechnology*. vol.4 (no.2): 106-113.

56. Woodhead-Galloway, J. 1982. Structure of the collagen fibril: an interpretation. *Collagen in Health and Disease*. J. B. Weiss, and M. I. V. Jayson, London: Churchill Livingstone.

57. Worcester DL, Miller RG, and Bryant PJ. December 1988. Atomic force microscopy of purple membranes. *J Microsc* 152 (Pt 3): 817-21.

58. Worcester, D. L., H. S. Kim, R. G. Miller, and P. J. Bryant. January 1990. Imaging bacteriorhodopsin lattices in purple membranes with atomic force microscopy. *J. Vac. Sci. Technol. A, Vac. Surf. Films (USA)* vol.8 (no.1): 403-5.

59. Xhie, J., K. Sattler, M. Ge, and N. Venkateswaran. 15 June 1993. Giant and supergiant lattices on graphite. *Phys. Rev. B, Condens. Matter (USA)* vol.47 (no.23): 15835-41.

60. Yannas, I. 1968. Vitrification temperature of water. *Science* 160: 298.

Appendix I

amino acid sequence of calf skin type I collagen

After J. A. Chapman et al 1981
in Weiss 1982

include histidine as + (pK=6.5)

Charge summary: after Veis 1994
9-triplets (27 residues)
net charge per molecular domain

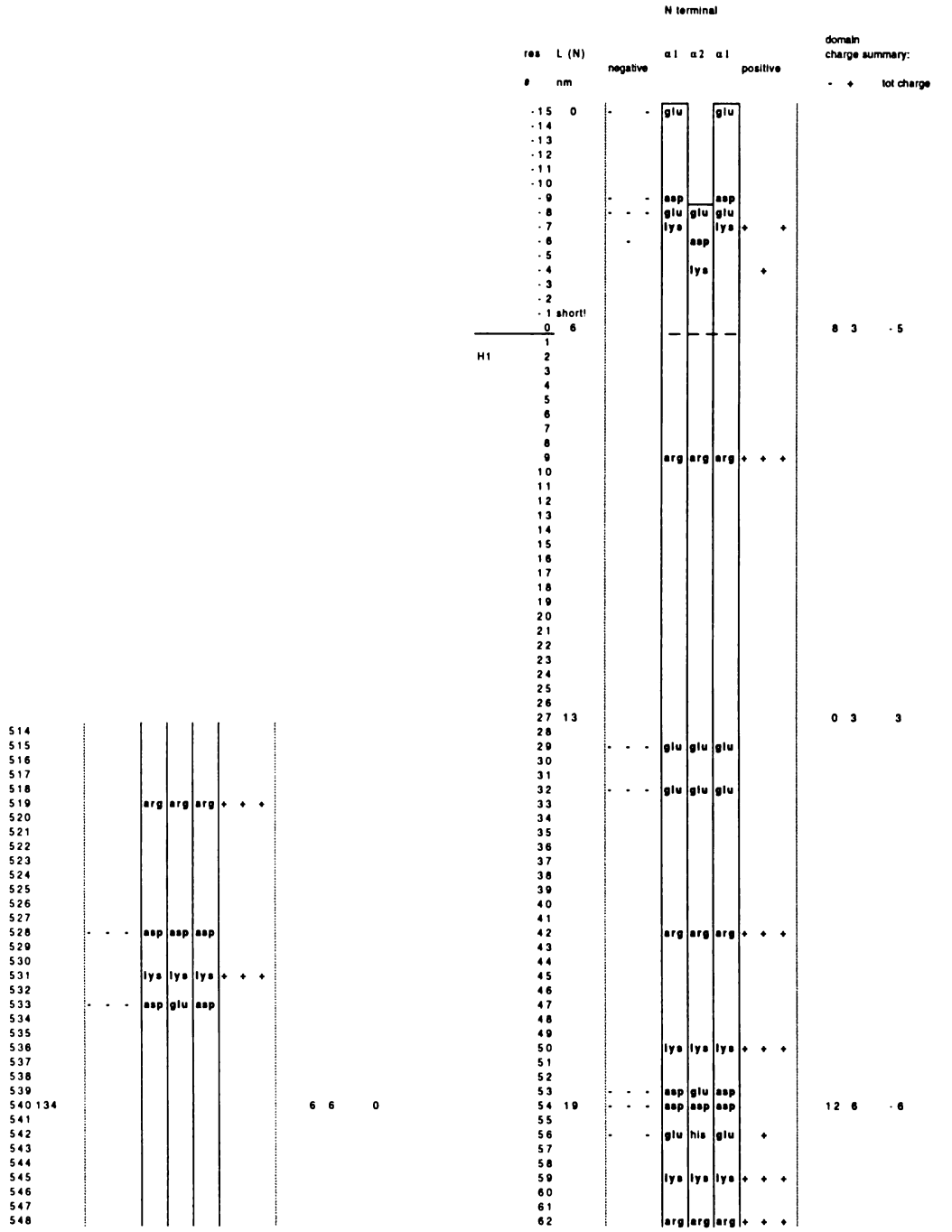

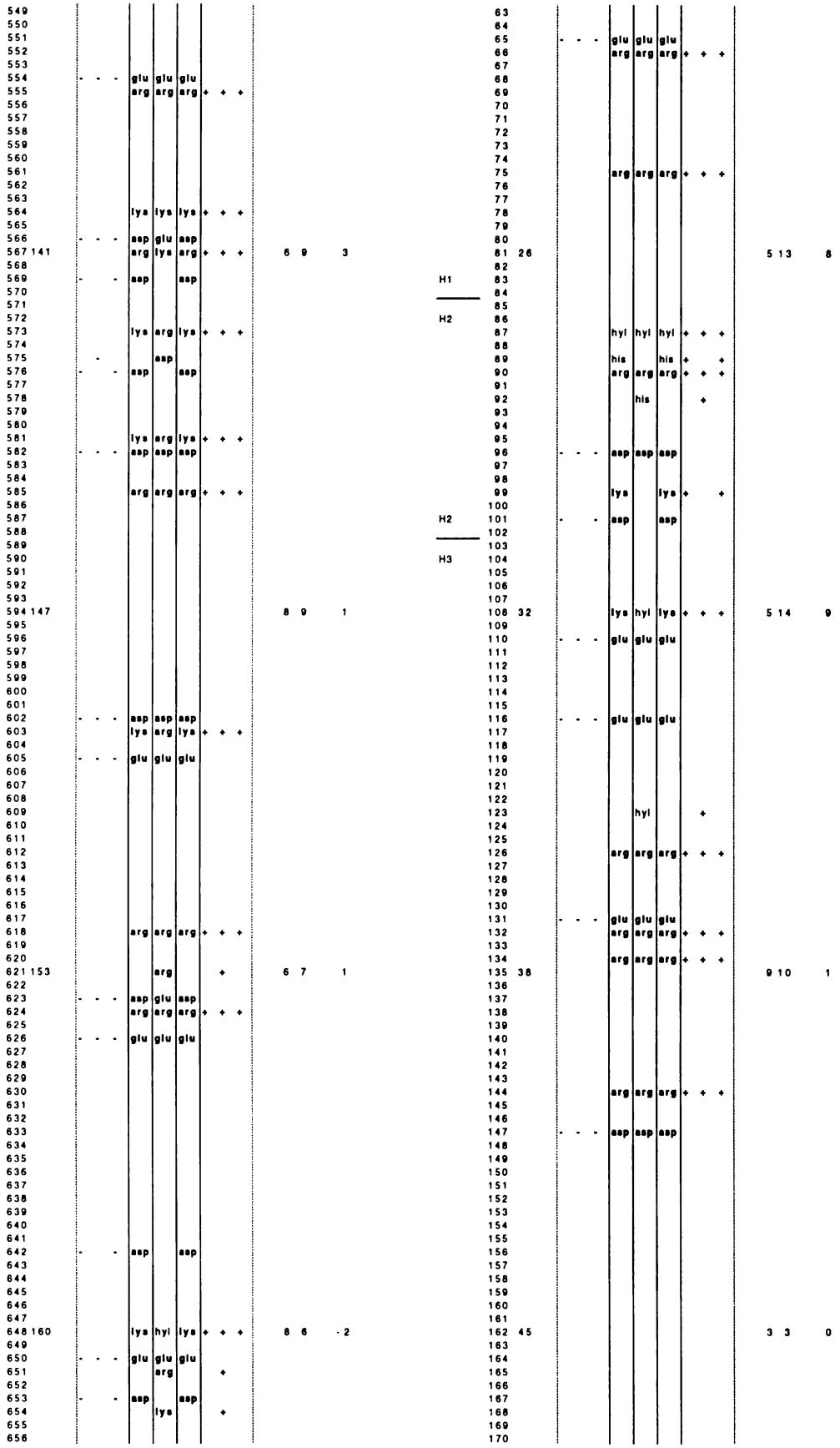

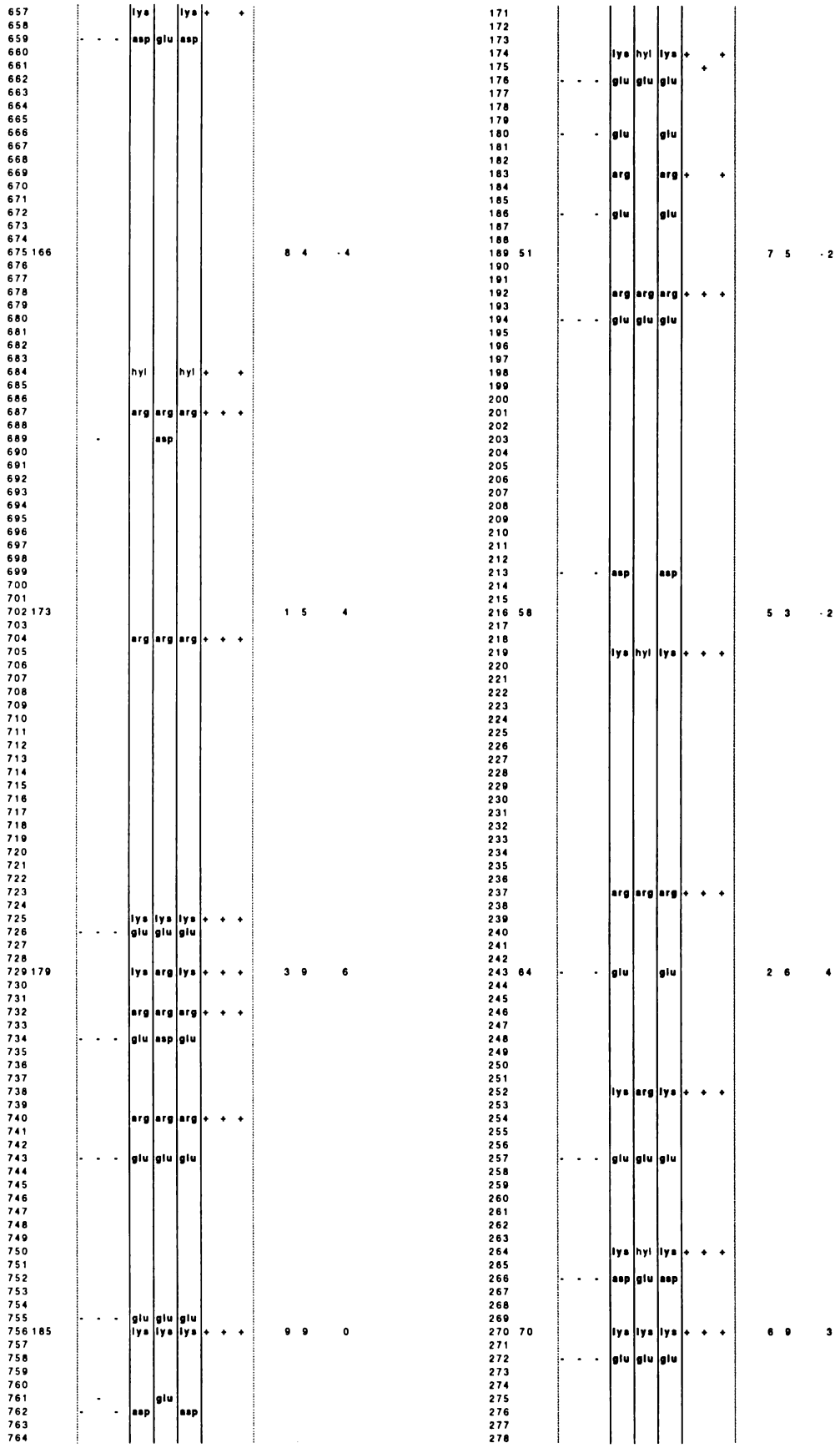

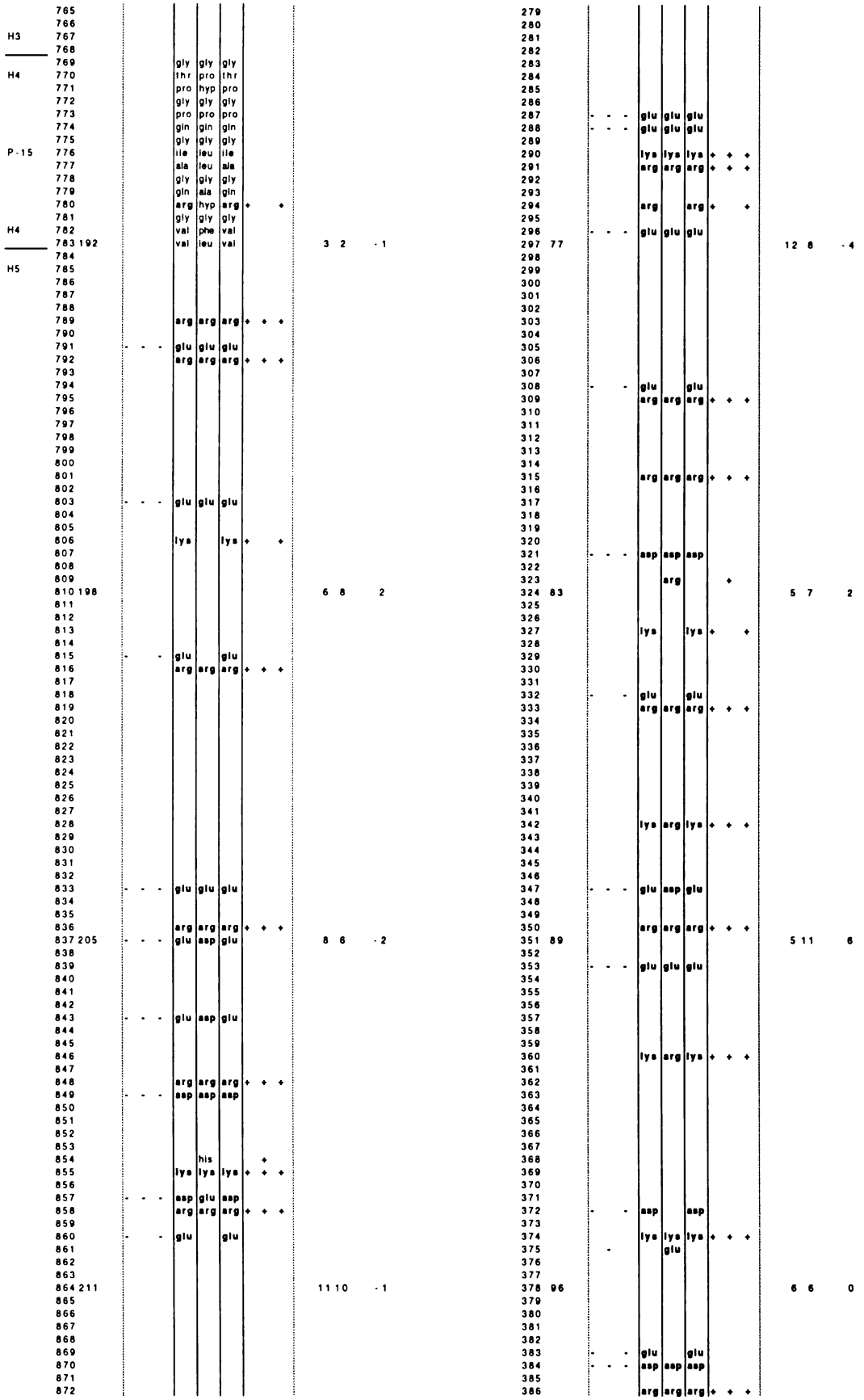

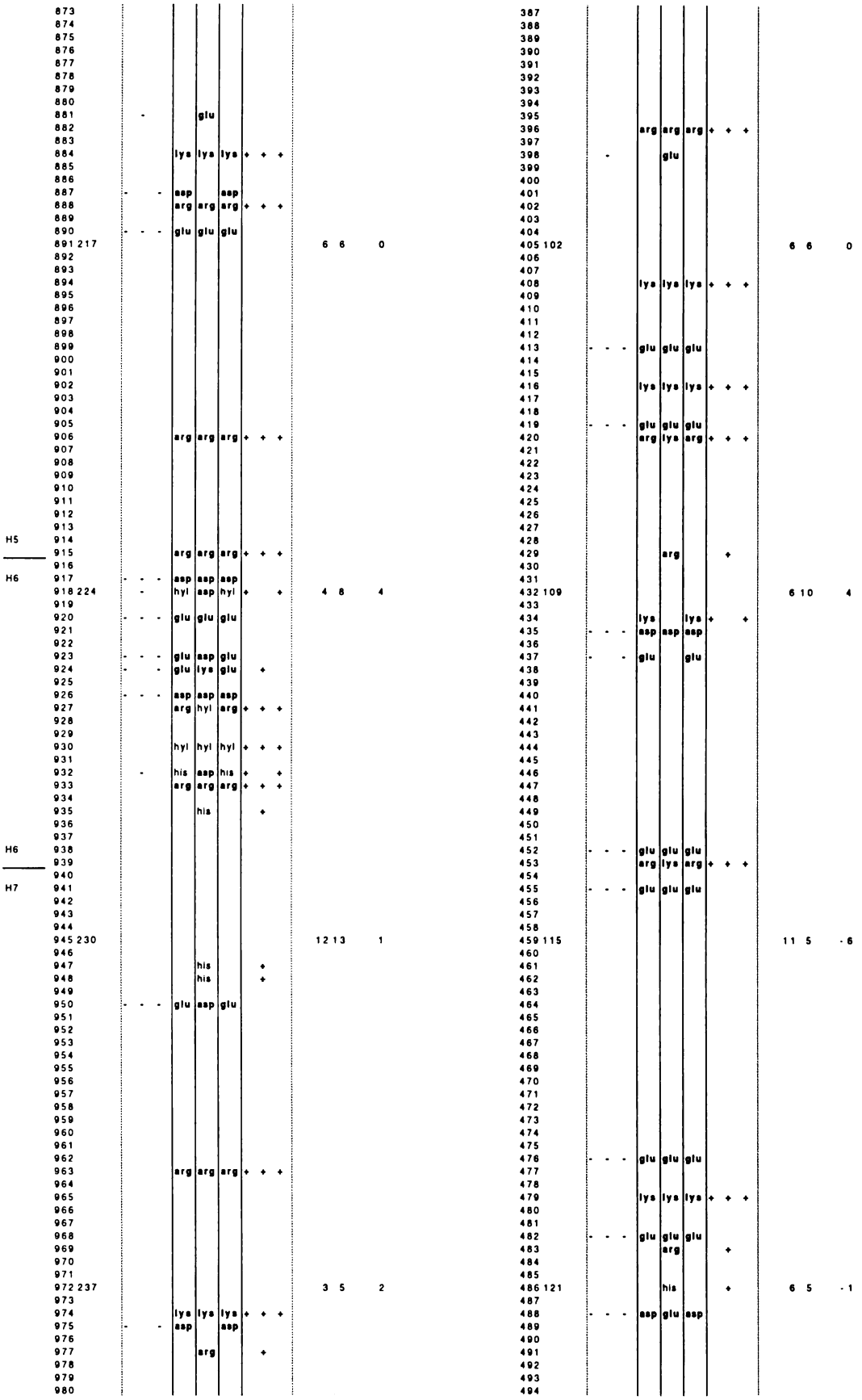

	873													
	874													
	875													
	876													
	877													
	878													
	879													
	880													
	881			-			glu							
	882													
	883													
	884					lys	lys	lys	+	+	+			
	885													
	886													
	887		-		-	asp		asp						
	888					arg	arg	arg	+	+	+			
	889													
	890		-	-	-	glu	glu	glu						
	891	217										6	6	0
	892													
	893													
	894													
	895													
	896													
	897													
	898													
	899													
	900													
	901													
	902													
	903													
	904													
	905													
	906					arg	arg	arg	+	+	+			
	907													
	908													
	909													
	910													
	911													
	912													
	913													
H5	914													
	915					arg	arg	arg	+	+	+			
	916													
H6	917		-	-	-	asp	asp	asp						
	918	224		-		hyl	asp	hyl	+		+	4	8	4
	919													
	920		-	-	-	glu	glu	glu						
	921													
	922													
	923		-	-	-	glu	asp	glu						
	924		-		-	glu	lys	glu		+				
	925													
	926		-	-	-	asp	asp	asp						
	927					arg	hyl	arg	+	+	+			
	928													
	929													
	930					hyl	hyl	hyl	+	+	+			
	931													
	932			-		his	asp	his	+		+			
	933					arg	arg	arg	+	+	+			
	934													
	935						his			+				
	936													
	937													
H6	938													
	939													
	940													
H7	941													
	942													
	943													
	944													
	945	230										12	13	1
	946													
	947						his			+				
	948						his			+				
	949													
	950		-	-	-	glu	asp	glu						
	951													
	952													
	953													
	954													
	955													
	956													
	957													
	958													
	959													
	960													
	961													
	962													
	963					arg	arg	arg	+	+	+			
	964													
	965													
	966													
	967													
	968													
	969													
	970													
	971													
	972	237										3	5	2
	973													
	974					lys	lys	lys	+	+	+			
	975		-		-	asp		asp						
	976													
	977						arg			+				
	978													
	979													
	980													

387													
388													
389													
390													
391													
392													
393													
394													
395													
396					arg	arg	arg	+	+	+			
397													
398			-			glu							
399													
400													
401													
402													
403													
404													
405	102										6	6	0
406													
407													
408					lys	lys	lys	+	+	+			
409													
410													
411													
412													
413		-	-	-	glu	glu	glu						
414													
415													
416					lys	lys	lys	+	+	+			
417													
418													
419		-	-	-	glu	glu	glu						
420					arg	lys	arg	+	+	+			
421													
422													
423													
424													
425													
426													
427													
428													
429						arg			+				
430													
431													
432	109										6	10	4
433													
434					lys		lys	+		+			
435		-	-	-	asp	asp	asp						
436													
437		-		-	glu		glu						
438													
439													
440													
441													
442													
443													
444													
445													
446													
447													
448													
449													
450													
451													
452		-	-	-	glu	glu	glu						
453					arg	lys	arg	+	+	+			
454													
455		-	-	-	glu	glu	glu						
456													
457													
458													
459	115										11	5	-6
460													
461													
462													
463													
464													
465													
466													
467													
468													
469													
470													
471													
472													
473													
474													
475													
476		-	-	-	glu	glu	glu						
477													
478													
479					lys	lys	lys	+	+	+			
480													
481													
482		-	-	-	glu	glu	glu						
483						arg			+				
484													
485													
486	121					his			+		6	5	-1
487													
488		-	-	-	asp	glu	asp						
489													
490													
491													
492													
493													
494													

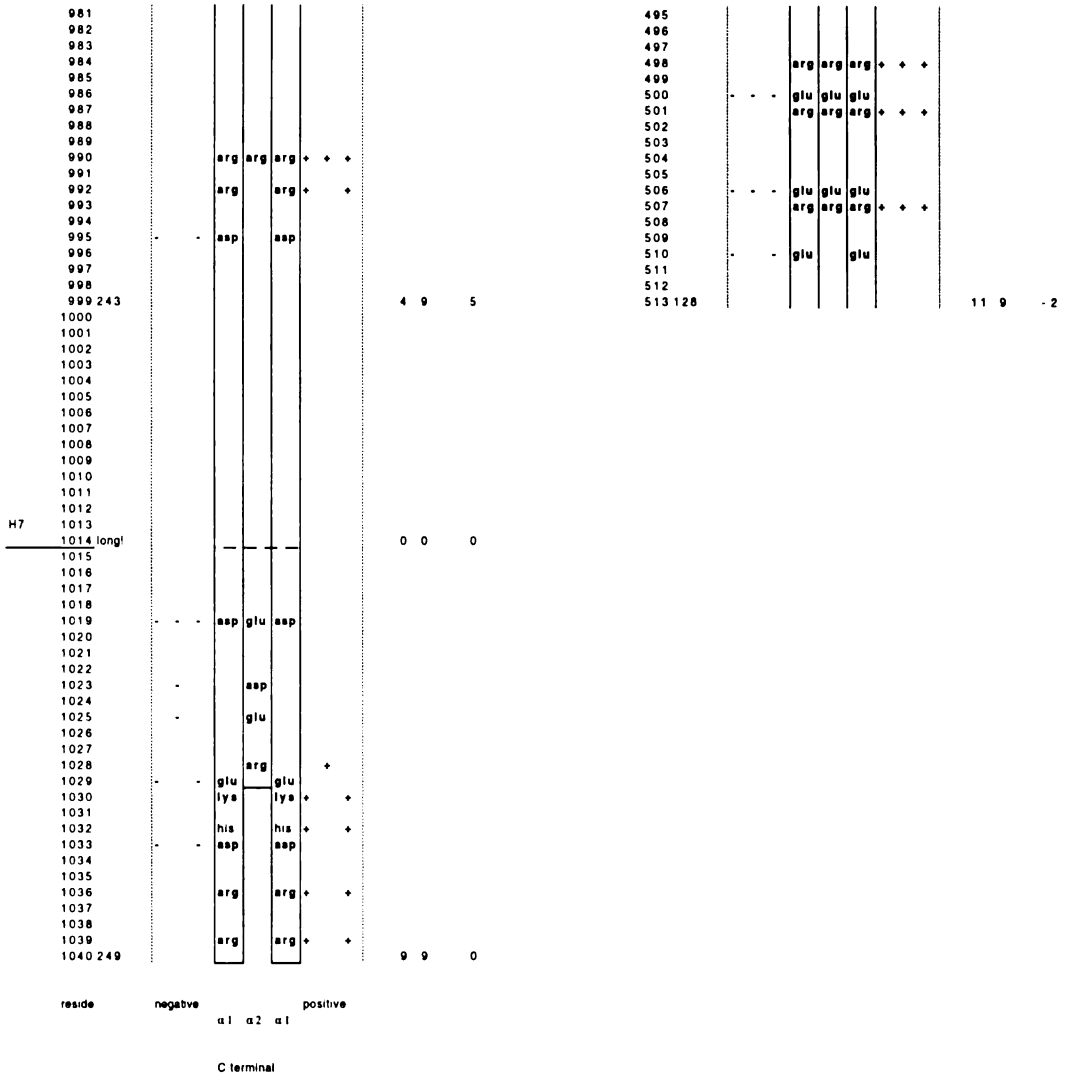
H7
longl
reside
negative
positive
α1 α2 α1
C terminal

Appendix II

Line Segment Generator:

Real space

segment Length:
angstroms !
L= 625

exp 1 — single run

exp 2 — multiple runs

exp 3 — post to trans 4 results

exp 4 — yy param sensitivity test

Parameters enter:
not linked!

calibration

	xx (Ax)	yy (By)	yx (Ay)	xxx (Axx)yyy (Byy)		
rel cal 1 um .217 s:	70.49	71.52	0.0237	0.0837	0.1003	mean
	0.88	2.07	0.0244	0.0239	0.0152	std dev
cal 8 v .217 s:	74.83	78.57	0.0071	0.1400	0.1464	linefit
	1.36	2.79	0.0263	0.0416	0.0451	95 % conf
	0.68	1.40	0.0132	0.0208	0.0226	st dev (95%/2)
	0.18	0.37	0.0035	0.0056	0.0060	std error intercept
	0.15	0.32	0.0030	0.0047	0.0051	std error slope @.217
rel cal interop	0.11	0.14	0.0467	0.0123	0.0060	
8v cal interop	0.36	0.36	0.0053	0.0134	0.0151	

full scan voltage
=4.644*25(XY HV gain)

ramp v	XY HV gain scan v	
4.644	25	116.1

BIG clear

BIG global

formulas:

initial clear

Y2=Y1+L*SIN(A1) Y3=Y2+L*SIN(A2) Y4=Y3+L*SIN(A3) Y5=Y4+L*SIN(A4)

initial global

X2=X1+L*COS(A1) X3=X2+L*COS(A2) X4=X3+L*COS(A3) X5=X4+L*COS(A4)

numbers above buttons are RNG parameters

RNG buttons:

uniform 4000 to -4000	uniform 0 to 360	0	0	0	RNG mean
		45	45	45	RNG st dev
initial X,Y	initial angle	delta ang 1	delta ang 2	delta ang 3	not linked!

Y1	X1	A1	Y2	X2	dA	new A2	Y3	X3	dA	new A3	Y4	X4	dA	new A4	Y5	X5
-1578	-1137	169	-1458	-1750	-11	158	-1228	-2331	-37	121	-695	-2657	13	134	-247	-3093
-2441	-3850	233	-2939	-4227	56	289	-3529	-4023	-38	251	-4120	-4228	13	264	-4741	-4297
-3623	-1377	137	-3199	-1837	-6	131	-2730	-2250	23	154	-2457	-2812	-16	138	-2038	-3275
-226	2412	77	383	2552	43	121	921	2234	-12	109	1513	2033	-27	82	2131	2125
3053	363	330	2736	902	64	394	3085	1421	-82	312	2619	1838	12	324	2254	2345
2202	2371	121	2736	2047	19	141	3133	1565	-31	109	3723	1357	-36	73	4320	1541
3300	-3975	102	3911	-4106	-18	84	4533	-4040	-28	56	5051	-3691	-5	51	5539	-3301
621	-3751	24	873	-3179	46	69	1458	-2958	-2	67	2034	-2717	1	68	2615	-2485
733	3413	261	116	3310	19	279	-501	3409	2	281	-1115	3528	46	327	-1456	4051
-3937	2954	170	-3830	2338	61	231	-4314	1942	101	332	-4605	2496	47	380	-4396	3085
-298	-1621	156	-42	-2192	-35	121	496	-2511	-26	95	1119	-2561	-6	89	1743	-2548
2275	2063	256	1670	1908	8	264	1048	1840	-17	247	472	1598	19	267	-152	1561
-751	72	206	-1024	-491	58	264	-1645	-556	-83	181	-1659	-1181	-13	169	-1536	-1794
-2829	1111	182	-2856	487	1	184	-2896	-137	38	222	-3313	-603	-18	204	-3565	-1175
1090	336	343	902	932	34	377	1084	1530	-73	304	568	1883	11	316	133	2331
-2655	2036	118	-2103	1743	-5	113	-1528	1499	-33	80	-912	1607	-68	12	-783	2218
2439	1790	328	2105	2318	-16	312	1641	2737	-39	273	1016	2767	8	280	402	2880
1058	-2223	317	632	-1765	13	330	322	-1223	-63	267	-302	-1253	-18	249	-888	-1472
1228	3027	337	988	3604	102	440	1603	3714	4	444	2224	3783	42	486	2730	3416
-3654	3865	151	-3355	3316	-24	127	-2856	2939	-39	89	-2232	2954	-69	20	-2021	3543
-1124	55	239	-1659	-268	-94	145	-1297	-778	31	176	-1250	-1401	-30	146	-898	-1918
-3665	-910	161	-3459	-1500	8	169	-3341	-2114	24	193	-3484	-2723	-74	119	-2940	-3030
1968	3576	258	1358	3441	-30	228	897	3019	-4	224	463	2569	-57	167	604	1960
-1299	-2997	92	-675	-3022	4	96	-54	-3093	-14	83	567	-3016	-9	74	1168	-2847
-1523	279	137	-1100	-181	-3	134	-651	-616	-25	109	-61	-823	19	129	427	-1212
-30	-562	146	323	-1078	-81	64	886	-805	3	68	1464	-567	-23	45	1902	-122
282	3688	296	-282	3957	-14	281	-895	4080	42	323	-1272	4578	-32	291	-1856	4800
3666	-3301	313	3207	-2876	1	314	2758	-2441	-8	306	2253	-2073	45	351	2158	-1456
451	-3809	304	-67	-3459	61	365	-15	-2836	9	373	129	-2228	-78	295	-435	-1961

Reverse Transform coefficints:
Linear terms
Real to image space

Angstroms to image units

Linear clear

Linear global

	70.49				71.52			
	0.88	0.18	0.15		2.07	0.37	0.32	
	rel cal xx r>i	δv cal σ b	δv cal σ m	Linear Total xx	rel cal yy r>i	δv cal σ b	δv cal σ m	Linear Total yy
	69.71	0.38	0.14	70.23	69.49	-0.56	0.18	69.12
	72.09	-0.20	-0.13	71.76	69.12	-0.42	0.48	69.19
	70.74	0.09	-0.36	70.47	69.57	0.45	0.14	70.16
	69.84	0.11	-0.27	69.68	70.30	0.25	0.11	70.66
	70.43	0.10	-0.30	70.24	72.90	-0.12	-0.24	72.54
	70.90	0.07	-0.06	70.91	72.31	0.07	-0.80	71.58
	69.95	-0.43	0.18	69.70	66.63	-0.47	0.61	66.76
	69.36	0.06	0.04	69.46	68.72	0.35	-0.37	68.69
	69.70	0.00	-0.34	69.36	69.79	0.13	-0.25	69.67
	71.37	0.00	-0.09	71.27	71.54	0.71	0.19	72.44
	71.68	0.21	0.16	72.04	69.84	0.07	-0.03	69.88
	68.89	0.06	-0.10	68.85	68.80	0.24	0.39	69.42
	70.43	-0.01	0.08	70.50	72.65	0.35	0.19	73.20
	70.76	-0.23	-0.06	70.47	69.87	0.08	0.19	70.14
	71.30	0.03	0.04	71.36	70.29	-0.04	-0.02	70.22
	70.11	0.11	-0.01	70.21	72.51	0.91	0.23	73.65
	70.96	0.20	-0.07	71.09	70.14	0.47	0.02	70.64
	71.40	0.09	-0.04	71.44	69.28	0.27	0.29	69.84
	69.85	-0.14	0.20	69.92	71.20	0.19	-0.46	70.92
	68.95	-0.06	-0.10	68.79	69.95	-0.47	0.47	69.95
	71.16	-0.08	0.14	71.21	66.65	-0.09	-0.20	66.36
	70.52	0.22	-0.10	70.65	68.82	-0.42	0.50	68.90
	71.10	-0.06	-0.22	70.82	71.33	0.20	-0.01	71.52
	71.13	-0.08	-0.20	70.85	71.88	-0.30	0.06	71.64
	70.77	0.33	0.13	71.23	65.24	0.19	-0.20	65.23
	69.69	-0.34	-0.07	69.28	72.21	-0.28	0.05	71.98
	70.98	-0.33	-0.11	70.54	72.19	-0.58	0.27	71.88
	69.83	0.17	-0.12	69.89	71.71	-0.34	0.17	71.53
	71.19	-0.09	-0.14	70.96	74.93	0.20	-0.31	74.82
	70.36	0.00	-0.04	70.33	71.27	0.30	-0.11	71.45
	70.44	0.45	-0.03	70.86	72.22	0.01	-0.31	71.92
	70.73	0.15	-0.08	70.80	69.63	0.11	0.32	70.07
	70.49	-0.17	0.04	70.36	69.84	-0.67	-0.83	68.33

xx	yy	Y1	X1	Y2	X2	Y3	X3	Y4	X4	Y5	X5	Overrange test: *=-0.5<Xi,Yi<0.5
70.23	69.12	-0.20	-0.14	-0.18	-0.21	-0.15	-0.29	-0.09	-0.33	-0.03	-0.38	good
70.23	69.12	-0.30	-0.47	-0.37	-0.52	-0.44	-0.49	-0.51	-0.52	-0.59	-0.53	overrange
70.23	69.12	-0.45	-0.17	-0.40	-0.23	-0.34	-0.28	-0.31	-0.34	-0.25	-0.40	good
70.23	69.12	-0.03	0.30	0.05	0.31	0.11	0.27	0.19	0.25	0.27	0.26	good
70.23	69.12	0.38	0.04	0.34	0.11	0.38	0.17	0.33	0.23	0.28	0.29	good
70.23	69.12	0.27	0.29	0.34	0.25	0.39	0.19	0.46	0.17	0.54	0.19	overrange
70.23	69.12	0.41	-0.49	0.49	-0.50	0.56	-0.50	0.63	-0.45	0.69	-0.40	overrange
70.23	69.12	0.08	-0.46	0.11	-0.39	0.18	-0.36	0.25	-0.33	0.33	-0.30	good
71.76	69.19	0.09	0.41	0.01	0.40	-0.06	0.41	-0.14	0.42	-0.18	0.49	good
71.76	69.19	-0.49	0.35	-0.48	0.28	-0.54	0.23	-0.57	0.30	-0.55	0.37	overrange
71.76	69.19	-0.04	-0.19	-0.01	-0.26	0.06	-0.30	0.14	-0.31	0.22	-0.31	good
71.76	69.19	0.28	0.25	0.21	0.23	0.13	0.22	0.06	0.19	-0.02	0.19	good
71.76	69.19	-0.09	0.01	-0.13	-0.06	-0.20	-0.07	-0.21	-0.14	-0.19	-0.22	good
71.76	69.19	-0.35	0.13	-0.36	0.06	-0.36	-0.02	-0.41	-0.07	-0.44	-0.14	good
71.76	69.19	0.14	0.04	0.11	0.11	0.13	0.18	0.07	0.23	0.02	0.28	good
71.76	69.19	-0.33	0.24	-0.26	0.21	-0.19	0.18	-0.11	0.19	-0.10	0.27	good
70.47	70.16	0.30	0.22	0.26	0.28	0.20	0.33	0.12	0.34	0.05	0.35	good
70.47	70.16	0.13	-0.27	0.08	-0.22	0.04	-0.15	-0.04	-0.15	-0.11	-0.18	good
70.47	70.16	0.15	0.37	0.12	0.44	0.20	0.45	0.27	0.46	0.34	0.42	good
70.47	70.16	-0.45	0.47	-0.41	0.41	-0.35	0.36	-0.27	0.36	-0.25	0.43	good
70.47	70.16	-0.14	0.01	-0.20	-0.03	-0.16	-0.10	-0.15	-0.17	-0.11	-0.23	good
70.47	70.16	-0.45	-0.11	-0.42	-0.18	-0.41	-0.26	-0.43	-0.33	-0.36	-0.37	good
70.47	70.16	0.24	0.44	0.17	0.42	0.11	0.37	0.06	0.31	0.07	0.24	good
70.47	70.16	-0.16	-0.37	-0.08	-0.37	-0.01	-0.38	0.07	-0.37	0.14	-0.35	good
69.68	70.66	-0.19	0.03	-0.13	-0.02	-0.08	-0.08	-0.01	-0.10	0.05	-0.15	good
69.68	70.66	0.00	-0.07	0.04	-0.13	0.11	-0.10	0.18	-0.07	0.23	-0.02	good
69.68	70.66	0.03	0.46	-0.03	0.49	-0.11	0.50	-0.16	0.57	-0.23	0.59	overrange
69.68	70.66	0.45	-0.41	0.39	-0.36	0.34	-0.30	0.27	-0.26	0.26	-0.18	good
69.68	70.66	0.06	-0.47	-0.01	-0.43	0.00	-0.35	0.02	-0.28	-0.05	-0.24	good

Reverse transform coefficents:
Non-Linear terms
Real to image space

coeff clear

coeff global

0.1003			
0.0152	0.0060	0.0051	
rel cal yyy	δv cal σ b	δv cal σ m	Reverse Total yyy
0.1011	0.0009	0.0017	0.1037
0.0967	-0.0043	-0.0011	0.0913
0.1051	0.0026	0.0058	0.1135
0.0846	0.0094	-0.0029	0.0911
0.1094	-0.0044	-0.0030	0.1020
0.0741	-0.0042	-0.0045	0.0655
0.1372	0.0132	-0.0038	0.1466
0.1059	0.0058	-0.0022	0.1095
0.0889	0.0025	0.0137	0.1052
0.1121	0.0010	-0.0054	0.1077
0.1274	0.0079	-0.0016	0.1337
0.1041	0.0019	-0.0137	0.0923
0.1189	-0.0025	-0.0034	0.1129
0.0931	0.0043	0.0038	0.1012
0.0896	-0.0112	-0.0027	0.0758
0.1158	0.0034	-0.0044	0.1148
0.1142	0.0085	0.0024	0.1250
0.0949	0.0035	0.0012	0.0996
0.0958	-0.0046	0.0001	0.0914
0.0998	-0.0033	-0.0001	0.0965
0.0813	0.0051	0.0008	0.0872
0.1120	0.0084	-0.0064	0.1141
0.0694	-0.0031	0.0032	0.0696
0.1092	0.0023	0.0069	0.1184
0.0892	0.0004	-0.0038	0.0858
0.1130	0.0004	0.0006	0.1140
0.0919	-0.0053	0.0037	0.0903
0.0979	0.0009	-0.0001	0.0986
0.0617	-0.0054	0.0025	0.0588
0.0869	0.0095	0.0072	0.1037
0.1102	0.0036	-0.0025	0.1113
0.0886	0.0054	-0.0080	0.0859
0.1005	0.0058	0.0034	0.1096

0.0837			
0.0239	0.0056	0.0047	
rel cal xxx	δv cal σ b	δv cal σ m	Reverse Total xxx
0.0985	0.0098	-0.0070	0.1013
0.0924	0.0040	0.0047	0.1011
0.0681	0.0059	-0.0067	0.0673
0.0687	-0.0109	-0.0054	0.0524
0.0972	-0.0063	0.0001	0.0910
0.1190	-0.0040	0.0046	0.1197
0.0856	0.0003	-0.0017	0.0842
0.0728	0.0057	0.0021	0.0805
0.0829	0.0047	0.0043	0.0919
0.1231	-0.0020	-0.0075	0.1136
0.0871	0.0013	-0.0034	0.0851
0.0919	-0.0004	0.0082	0.0998
0.0903	0.0056	-0.0028	0.0931
0.0884	-0.0101	-0.0038	0.0745
0.0446	-0.0003	0.0003	0.0446
0.0876	0.0005	-0.0020	0.0861
0.0773	0.0073	-0.0010	0.0836
0.0127	-0.0077	0.0006	0.0056
0.0869	0.0011	-0.0015	0.0864
0.1168	-0.0061	-0.0013	0.1094
0.0515	-0.0030	0.0018	0.0503
0.0705	-0.0013	-0.0026	0.0666
0.1028	-0.0070	-0.0005	0.0953
0.0921	-0.0054	-0.0017	0.0850
0.1145	-0.0040	0.0052	0.1156
0.0727	-0.0012	0.0008	0.0723
0.0708	-0.0085	0.0051	0.0674
0.1032	-0.0082	0.0016	0.0966
0.0982	-0.0049	0.0028	0.0960
0.0840	-0.0046	-0.0099	0.0696
0.0664	0.0033	-0.0018	0.0679
0.1313	0.0023	0.0047	0.1382
0.0479	0.0077	-0.0001	0.0554

0.0237			
0.0244	0.0035	0.003	
rel cal yx	δv cal σ b	δv cal σ m	Reverse Total yx
0.0084	-0.0032	-0.0002	0.0050
0.0155	0.0044	-0.0022	0.0177
0.0051	0.0034	0.0014	0.0099
0.0179	0.0015	0.0024	0.0218
0.0052	-0.0021	0.0000	0.0031
-0.0146	-0.0020	0.0046	-0.0120
0.0269	-0.0010	0.0018	0.0277
0.0272	0.0034	0.0026	0.0332
0.0232	-0.0008	-0.0031	0.0192
0.0334	0.0020	0.0080	0.0434
-0.0029	0.0050	-0.0001	0.0020
0.0258	-0.0029	-0.0036	0.0192
0.0066	0.0029	0.0029	0.0124
0.0249	0.0017	0.0031	0.0298
0.0313	0.0020	0.0027	0.0360
0.0321	-0.0016	-0.0029	0.0275
0.0087	0.0051	-0.0066	0.0072
0.0321	-0.0032	-0.0022	0.0266
0.0354	-0.0028	-0.0012	0.0314
0.0223	-0.0044	-0.0038	0.0142
0.0235	-0.0008	-0.0021	0.0206
0.0379	-0.0021	0.0021	0.0379
0.0324	-0.0039	0.0016	0.0301
-0.0057	0.0004	-0.0080	-0.0133
-0.0372	-0.0011	0.0003	-0.0381
0.0377	-0.0034	-0.0019	0.0324
0.0198	0.0000	0.0026	0.0224
0.0437	-0.0062	0.0037	0.0413
0.0424	-0.0022	0.0010	0.0412
-0.0059	0.0009	-0.0049	-0.0099
0.0056	-0.0027	0.0057	0.0086
0.0293	0.0027	0.0010	0.0330
0.0034	0.0032	-0.0015	0.0050

yyy
0.10
0.10
0.10
0.10
0.10
0.10
0.10
0.10
0.09
0.09
0.09
0.09
0.09
0.09
0.09
0.09
0.11
0.11
0.11
0.11
0.11
0.11
0.11
0.11
0.09
0.09
0.09
0.09
0.09

xxx
0.10
0.10
0.10
0.10
0.10
0.10
0.10
0.10
0.10
0.10
0.10
0.10
0.10
0.10
0.10
0.10
0.07
0.07
0.07
0.07
0.07
0.07
0.07
0.07
0.05
0.05
0.05
0.05
0.05

yx
0.01
0.01
0.01
0.01
0.01
0.01
0.01
0.01
0.02
0.02
0.02
0.02
0.02
0.02
0.02
0.02
0.01
0.01
0.01
0.01
0.01
0.01
0.01
0.01
0.02
0.02
0.02
0.02
0.02

Reverse transform:

Real to Image space

Operator pixel error at ends:

Image space

Pixel size (image units)

0.00391

Discreate RNG:

value	probability
1	0.33
0	0.34
-1	0.33

reverse transforms:

y=(-1+sqrt(1-4*Byy*Yr))/2*Byy

x=(-1+sqrt(1-4*Axx(Ay*y-Xr)))/2*Axx

new pixelated ends

new y5=y5 + (RNG)*(pixel size)*COS(ATAN(y5-y4)/(x5-x4))*SIGN(x5-x4)

new x5=x5 + (RNG)*(pixel size)*SIN(ATAN(y5-y4)/(x5-x4))*SIGN(x5-x4)

new y1=y1 + (RNG)*(pixel size)*SIN(ATAN(y2-y1)/(x2-x1))*SIGN(x2-x1)

new x1=x1 + (RNG)*(pixel size)*COS(ATAN(y2-y1)/(x2-x1))*SIGN(x2-x1)

pixel clear | pixel err 1 | pixel err 5

pixel global

y1	x1	y2	x2	y3	x3	y4	x4	y5	x5			new y1	new x1	new y5	new x5
-0.20	-0.14	-0.19	-0.22	-0.16	-0.29	-0.09	-0.34	-0.03	-0.40		-1	-1	-0.20	-0.14	-0.03	-0.39
-0.31	-0.50	-0.38	-0.55	-0.46	-0.52	-0.54	-0.55	-0.63	-0.56		0	-1	-0.31	-0.50	-0.63	-0.55
-0.47	-0.17	-0.42	-0.23	-0.35	-0.28	-0.32	-0.36	-0.26	-0.42		0	0	-0.47	-0.17	-0.26	-0.42
-0.03	0.29	0.05	0.30	0.11	0.27	0.19	0.24	0.26	0.25		0	0	-0.03	0.29	0.26	0.25
0.37	0.04	0.33	0.11	0.37	0.17	0.32	0.22	0.27	0.28		0	0	0.37	0.04	0.27	0.28
0.27	0.28	0.33	0.24	0.38	0.19	0.44	0.16	0.51	0.18		1	0	0.26	0.28	0.51	0.18
0.40	-0.52	0.46	-0.53	0.54	-0.53	0.59	-0.48	0.65	-0.43		0	1	0.40	-0.52	0.65	-0.42
0.08	-0.48	0.11	-0.41	0.18	-0.38	0.25	-0.35	0.32	-0.32		1	1	0.08	-0.49	0.32	-0.31
0.09	0.39	0.01	0.38	-0.06	0.39	-0.14	0.41	-0.18	0.47		0	0	0.09	0.39	-0.18	0.47
-0.51	0.35	-0.50	0.28	-0.57	0.24	-0.61	0.30	-0.58	0.37		0	1	-0.51	0.35	-0.58	0.37
-0.04	-0.20	-0.01	-0.27	0.06	-0.31	0.14	-0.32	0.21	-0.32		0	0	-0.04	-0.20	0.21	-0.32
0.28	0.24	0.20	0.22	0.13	0.21	0.06	0.19	-0.02	0.18		1	1	0.28	0.24	-0.02	0.18
-0.09	0.01	-0.13	-0.06	-0.21	-0.06	-0.21	-0.14	-0.19	-0.22		0	-1	-0.09	0.01	-0.20	-0.21
-0.36	0.14	-0.37	0.06	-0.37	-0.01	-0.43	-0.07	-0.46	-0.13		0	0	-0.36	0.14	-0.46	-0.13
0.13	0.04	0.11	0.11	0.13	0.18	0.07	0.22	0.02	0.27		-1	0	0.13	0.04	0.02	0.27
-0.34	0.24	-0.27	0.21	-0.19	0.18	-0.11	0.19	-0.10	0.26		0	0	-0.34	0.24	-0.10	0.26
0.29	0.21	0.25	0.28	0.20	0.33	0.12	0.33	0.05	0.34		-1	1	0.29	0.22	0.05	0.34
0.13	-0.28	0.08	-0.22	0.04	-0.15	-0.04	-0.15	-0.11	-0.18		1	0	0.13	-0.28	-0.11	-0.18
0.15	0.36	0.12	0.43	0.19	0.44	0.27	0.45	0.32	0.40		1	1	0.15	0.36	0.33	0.40
-0.47	0.46	-0.43	0.40	-0.37	0.35	-0.28	0.36	-0.26	0.42		1	0	-0.48	0.47	-0.26	0.42
-0.14	0.01	-0.21	-0.03	-0.16	-0.09	-0.16	-0.17	-0.11	-0.24		1	1	-0.14	0.01	-0.11	-0.24
-0.48	-0.11	-0.45	-0.18	-0.43	-0.26	-0.45	-0.34	-0.38	-0.38		0	0	-0.48	-0.11	-0.38	-0.38
0.24	0.42	0.16	0.41	0.11	0.36	0.06	0.31	0.07	0.24		-1	0	0.23	0.42	0.07	0.24
-0.16	-0.37	-0.08	-0.38	-0.01	-0.39	0.07	-0.38	0.14	-0.36		1	-1	-0.17	-0.37	0.14	-0.36
-0.19	0.04	-0.14	-0.02	-0.08	-0.07	-0.01	-0.10	0.05	-0.15		0	1	-0.19	0.04	0.05	-0.15
0.00	-0.07	0.04	-0.14	0.11	-0.10	0.18	-0.07	0.23	-0.02		-1	-1	0.00	-0.07	0.22	-0.02
0.03	0.44	-0.03	0.48	-0.11	0.49	-0.16	0.55	-0.23	0.58		0	-1	0.03	0.44	-0.23	0.58
0.43	-0.43	0.38	-0.37	0.33	-0.31	0.27	-0.27	0.26	-0.19		-1	1	0.43	-0.42	0.26	-0.18
0.05	-0.48	-0.01	-0.44	0.00	-0.36	0.02	-0.28	-0.05	-0.24		0	-1	0.05	-0.48	-0.05	-0.25

Forward Transform coefficints:
Non-Linear terms
Image to Real space

0.1003
0.0152 0.0026 0.006 0.0151

rel cal yyy	θv cal	rel cal inop σ	θv cal inop σ	Free	Free	Forward Total yyy
0.0894	0.0253	0.0122	-0.0160			0.1109
0.1091	0.0172	-0.0186	0.0083			0.1159
0.1029	0.0083	0.0002	-0.0380			0.0733
0.1196	0.0205	0.0024	-0.0086			0.1340
0.1273	0.0092	0.0060	-0.0214			0.1212
0.0983	0.0243	-0.0099	0.0189			0.1316
0.1045	0.0128	0.0055	-0.0253			0.0976
0.1071	0.0118	0.0003	-0.0058			0.1134
0.0794	0.0165	-0.0067	0.0199			0.1090
0.1006	0.0178	-0.0033	0.0070			0.1221
0.1239	-0.0102	0.0044	-0.0031			0.1151
0.0913	-0.0363	-0.0057	-0.0072			0.0422
0.0875	0.0081	0.0032	0.0088			0.1076
0.0763	0.0016	-0.0008	-0.0161			0.0612
0.1112	0.0136	-0.0177	-0.0377			0.0694
0.0991	0.0354	0.0058	-0.0063			0.1340
0.0968	-0.0031	-0.0042	0.0075			0.0971
0.0826	-0.0115	-0.0103	-0.0051			0.0557
0.0827	0.0010	-0.0017	-0.0045			0.0776
0.1029	-0.0044	-0.0047	-0.0062			0.0877
0.1185	-0.0071	-0.0028	-0.0241			0.0846
0.0863	0.0374	-0.0020	0.0095			0.1311
0.1083	-0.0090	-0.0041	0.0257			0.1209
0.0773	-0.0152	0.0043	0.0110			0.0774
0.1048	0.0104	-0.0081	0.0042			0.1113
0.0778	0.0230	-0.0109	-0.0044			0.0855
0.0907	-0.0426	-0.0032	-0.0203			0.0246
0.0681	-0.0148	0.0018	0.0167			0.0718
0.0879	-0.0104	-0.0025	-0.0101			0.0649
0.0976	-0.0110	-0.0069	0.0387			0.1184
0.1077	-0.0298	0.0014	-0.0340			0.0453
0.1231	-0.0293	-0.0028	-0.0234			0.0677
0.1051	-0.0136	0.0022	0.0042			0.0979

0.0837
0.0239 0.0208 0.0123 0.0134

rel cal xxx	θv cal	rel cal inop σ	θv cal inop σ	Free	Free	Forward Total xxx
0.0513	0.0052	-0.0016	-0.0152			0.0396
0.0962	0.0105	0.0029	-0.0031			0.1065
0.1138	0.0020	0.0067	0.0046			0.1271
0.1244	-0.0578	0.0037	-0.0030			0.0672
0.1243	-0.0390	-0.0159	-0.0201			0.0494
0.0897	-0.0033	-0.0013	-0.0041			0.0811
0.0830	0.0059	0.0077	0.0241			0.1207
0.0593	0.0049	-0.0051	0.0010			0.0601
0.0525	-0.0002	-0.0020	-0.0058			0.0444
0.0742	0.0013	-0.0069	0.0026			0.0712
0.0659	0.0052	0.0034	0.0041			0.0787
0.1027	-0.0178	0.0267	0.0079			0.1195
0.1008	0.0085	0.0113	0.0146			0.1352
0.1047	-0.0120	0.0165	0.0184			0.1276
0.1114	-0.0172	-0.0030	-0.0019			0.0894
0.1043	-0.0056	0.0156	-0.0154			0.0989
0.0767	-0.0182	0.0141	-0.0011			0.0715
0.0688	-0.0372	0.0000	-0.0059			0.0257
0.1027	0.0025	0.0023	-0.0097			0.0978
0.1249	-0.0113	0.0355	0.0084			0.1575
0.0727	-0.0132	-0.0023	-0.0053			0.0520
0.0808	0.0045	0.0141	-0.0231			0.0763
0.0813	0.0253	-0.0060	-0.0122			0.0884
0.0777	0.0024	0.0109	-0.0037			0.0873
0.0706	0.0101	-0.0063	-0.0090			0.0653
0.1022	-0.0129	-0.0064	0.0029			0.0857
0.0907	-0.0026	0.0178	-0.0121			0.0938
0.0317	-0.0041	0.0013	0.0060			0.0350
0.0608	-0.0006	-0.0059	0.0230			0.0773
0.0966	-0.0098	-0.0197	-0.0397			0.0274
0.0643	0.0375	-0.0097	-0.0043			0.0878
0.0967	0.0110	-0.0100	0.0024			0.1000
0.1067	0.0110	-0.0115	0.0084			0.1146

yyy
0.11
0.11
0.11
0.11
0.11
0.11
0.11
0.11
0.12
0.12
0.12
0.12
0.12
0.12
0.12
0.12
0.07
0.07
0.07
0.07
0.07
0.07
0.07
0.07
0.13
0.13
0.13
0.13
0.13

xxx
0.04
0.04
0.04
0.04
0.04
0.04
0.04
0.04
0.11
0.11
0.11
0.11
0.11
0.11
0.11
0.11
0.13
0.13
0.13
0.13
0.13
0.13
0.13
0.13
0.07
0.07
0.07
0.07
0.07

Forward Transform:

Image to Real space

0.0237
0.0244 0.0132 0.0467 0.0053

rel cal yx	θv cal	rel cal inop σ	θv cal inop σ	Free	Free	Forward Total yx
0.0163	0.0141	-0.0241	-0.0039			0.0024
0.0048	-0.0137	0.0090	0.0040			0.0042
0.0053	-0.0262	0.0268	0.0023			0.0083
0.0705	-0.0096	0.0697	-0.0059			0.1246
0.0473	-0.0006	-0.0047	-0.0027			0.0393
0.0325	-0.0285	-0.0563	0.0030			-0.0494
0.0160	-0.0113	-0.0529	0.0005			-0.0476
0.0538	-0.0048	0.0025	0.0002			0.0516
0.0333	-0.0172	0.0380	-0.0051			0.0489
0.0461	-0.0025	-0.0834	-0.0046			-0.0443
0.0151	-0.0078	-0.0121	0.0014			-0.0034
0.0197	0.0104	-0.0351	0.0115			0.0065
0.0227	0.0092	-0.0013	0.0055			0.0361
0.0481	-0.0293	0.0079	-0.0004			0.0262
0.0586	-0.0124	0.0676	-0.0011			0.1128
0.0184	0.0011	-0.0404	0.0011			-0.0197
0.0201	0.0304	0.0412	-0.0005			0.0912
-0.0077	-0.0090	0.0038	-0.0120			-0.0250
0.0050	-0.0260	0.0269	-0.0020			0.0039
0.0250	0.0113	-0.0684	0.0028			-0.0292
-0.0086	-0.0067	0.0413	-0.0006			0.0253
0.0287	-0.0079	0.0237	0.0038			0.0482
0.0350	-0.0047	0.0707	0.0042			0.1051
0.0305	-0.0007	0.0259	-0.0009			0.0548
0.0322	0.0078	-0.0605	0.0029			-0.0176
0.0651	-0.0040	0.0418	-0.0014			0.1014
0.0361	-0.0070	-0.0517	-0.0049			-0.0275
0.0323	0.0076	0.0664	0.0041			0.1103
0.0280	0.0023	0.0092	-0.0004			0.0392
0.0261	-0.0010	0.0385	0.0011			0.0648
0.0402	-0.0002	-0.0577	-0.0052			-0.0228
0.0537	0.0075	0.0395	0.0004			0.1012
0.0240	-0.0072	-0.0649	0.0056			-0.0424

forward transform

'Yr=By'y+Byy'(y)^2

'Xr=Ax'x+Axx'(x)^2+Ay'y

using new 'pixel ends'

yx	Y1	X1	Y2	X2	Y3	X3	Y4	X4	Y5	X5
0.00	-0.20	-0.14	-0.18	-0.22	-0.15	-0.29	-0.09	-0.33	-0.03	-0.39
0.00	-0.30	-0.49	-0.37	-0.54	-0.44	-0.51	-0.51	-0.54	-0.58	-0.54
0.00	-0.45	-0.17	-0.40	-0.23	-0.34	-0.28	-0.31	-0.35	-0.25	-0.41
0.00	-0.03	0.29	0.05	0.31	0.11	0.27	0.19	0.25	0.27	0.26
0.00	0.38	0.04	0.34	0.11	0.39	0.17	0.33	0.22	0.28	0.28
0.00	0.27	0.29	0.34	0.25	0.39	0.19	0.47	0.16	0.54	0.19
0.00	0.41	-0.51	0.49	-0.52	0.57	-0.51	0.63	-0.47	0.70	-0.42
0.00	0.08	-0.48	0.11	-0.40	0.18	-0.37	0.25	-0.34	0.33	-0.31
0.00	0.09	0.41	0.01	0.40	-0.06	0.41	-0.14	0.43	-0.18	0.49
0.00	-0.48	0.36	-0.47	0.29	-0.53	0.24	-0.56	0.31	-0.54	0.38
0.00	-0.04	-0.19	-0.01	-0.26	0.06	-0.30	0.14	-0.31	0.22	-0.31
0.00	0.29	0.25	0.21	0.23	0.13	0.22	0.06	0.19	-0.02	0.19
0.00	-0.09	0.01	-0.13	-0.06	-0.20	-0.06	-0.21	-0.14	-0.19	-0.21
0.00	-0.35	0.14	-0.35	0.06	-0.36	-0.01	-0.41	-0.07	-0.44	-0.13
0.00	0.13	0.04	0.11	0.11	0.14	0.18	0.07	0.23	0.02	0.28
0.00	-0.33	0.25	-0.26	0.21	-0.19	0.18	-0.11	0.19	-0.10	0.27
0.01	0.29	0.22	0.26	0.29	0.20	0.34	0.12	0.34	0.05	0.36
0.01	0.13	-0.27	0.08	-0.21	0.04	-0.15	-0.04	-0.15	-0.11	-0.18
0.01	0.15	0.37	0.12	0.45	0.20	0.47	0.27	0.47	0.33	0.42
0.01	-0.46	0.49	-0.42	0.42	-0.36	0.37	-0.28	0.37	-0.25	0.44
0.01	-0.14	0.01	-0.21	-0.03	-0.16	-0.09	-0.15	-0.17	-0.11	-0.23
0.01	-0.46	-0.11	-0.43	-0.18	-0.42	-0.25	-0.44	-0.33	-0.37	-0.36
0.01	0.24	0.45	0.17	0.43	0.11	0.38	0.06	0.32	0.07	0.24
0.01	-0.16	-0.36	-0.08	-0.36	-0.01	-0.37	0.07	-0.36	0.14	-0.34
0.12	-0.18	0.02	-0.13	-0.04	-0.08	-0.08	-0.01	-0.10	0.06	-0.15
0.12	0.00	-0.07	0.04	-0.13	0.11	-0.09	0.18	-0.05	0.23	0.01
0.12	0.03	0.46	-0.03	0.49	-0.11	0.50	-0.15	0.55	-0.22	0.57
0.12	0.45	-0.36	0.40	-0.31	0.34	-0.27	0.28	-0.23	0.27	-0.15
0.12	0.06	-0.46	-0.01	-0.43	0.00	-0.35	0.02	-0.27	-0.05	-0.25

Length segments:

Image units

LS1:		LS2:		LS3:		LS4:	
Y2-Y1	X2-X1	Y3-Y2	X3-X2	Y4-Y3	X4-X3	Y5-Y4	X5-X4
0.01	-0.07	0.03	-0.07	0.07	-0.04	0.05	-0.05
-0.06	-0.05	-0.07	0.03	-0.07	-0.03	-0.07	-0.01
0.05	-0.06	0.06	-0.05	0.03	-0.07	0.05	-0.06
0.08	0.02	0.07	-0.04	0.07	-0.02	0.08	0.01
-0.04	0.07	0.04	0.06	-0.06	0.05	-0.05	0.06
0.07	-0.04	0.05	-0.06	0.07	-0.03	0.07	0.02
0.08	-0.02	0.08	0.01	0.07	0.05	0.06	0.05
0.03	0.08	0.07	0.03	0.07	0.03	0.08	0.03
-0.08	-0.01	-0.08	0.01	-0.08	0.02	-0.04	0.06
0.01	-0.07	-0.06	-0.05	-0.04	0.07	0.03	0.07
0.03	-0.07	0.07	-0.04	0.08	-0.01	0.08	0.00
-0.08	-0.02	-0.08	-0.01	-0.07	-0.03	-0.08	0.00
-0.03	-0.07	-0.08	-0.01	0.00	-0.07	0.01	-0.07
0.00	-0.07	0.00	-0.07	-0.05	-0.06	-0.03	-0.07
-0.02	0.07	0.02	0.07	-0.06	0.04	-0.05	0.05
0.07	-0.04	0.07	-0.03	0.08	0.01	0.02	0.07
-0.04	0.06	-0.06	0.05	-0.08	0.00	-0.08	0.02
-0.05	0.06	-0.04	0.06	-0.08	0.00	-0.07	-0.03
-0.03	0.08	0.07	0.01	0.07	0.01	0.06	-0.05
0.04	-0.07	0.06	-0.05	0.08	0.00	0.03	0.08
-0.07	-0.04	0.05	-0.06	0.01	-0.07	0.05	-0.06
0.03	-0.07	0.02	-0.07	-0.02	-0.07	0.07	-0.04
-0.07	-0.02	-0.06	-0.05	-0.05	-0.06	0.02	-0.08
0.08	0.00	0.08	-0.01	0.08	0.01	0.07	0.02
0.05	-0.05	0.05	-0.05	0.07	-0.02	0.06	-0.04
0.04	-0.06	0.07	0.04	0.07	0.04	0.05	0.06
-0.07	0.03	-0.07	0.01	-0.05	0.06	-0.07	0.02
-0.05	0.04	-0.06	0.05	-0.06	0.04	-0.01	0.08
-0.06	0.04	0.01	0.08	0.02	0.08	-0.07	0.02

Length segments:

Volts

full scan voltage from initial parameters

LS1:		LS2:		LS3:		LS4:	
Y2-Y1	X2-X1	Y3-Y2	X3-X2	Y4-Y3	X4-X3	Y5-Y4	X5-X4
1.63	-8.50	3.33	-8.56	7.70	-4.86	6.16	-6.22
-7.17	-5.74	-8.49	3.15	-8.48	-3.10	-8.51	-0.99
6.09	-6.73	6.75	-6.10	3.92	-8.36	6.04	-6.96
8.81	1.90	7.80	-4.39	8.58	-2.80	8.97	1.24
-4.61	7.61	5.07	7.25	-6.77	5.82	-5.30	7.03
8.17	-4.73	5.78	-6.71	8.58	-2.91	8.70	2.54
8.89	-2.02	9.05	0.99	7.56	5.29	7.49	6.19
3.82	9.03	8.48	3.29	8.37	3.58	8.87	3.60
-8.93	-1.31	-8.91	1.50	-8.82	1.78	-4.89	7.40
1.49	-8.63	-6.79	-5.42	-4.07	7.79	3.08	8.64
3.69	-7.98	7.78	-4.54	9.05	-0.82	9.11	0.06
-9.32	-2.17	-9.05	-0.83	-8.37	-3.27	-9.48	-0.42
-3.91	-7.78	-8.91	-0.78	-0.20	-8.70	1.68	-8.12
-0.38	-8.71	-0.57	-8.69	-5.90	-6.40	-3.54	-7.91
-2.59	7.92	2.65	8.31	-7.49	5.03	-6.31	6.35
7.85	-4.21	8.22	-3.52	8.83	1.38	1.86	8.52
-4.42	7.31	-6.50	6.16	-8.79	0.45	-9.15	1.77
-6.32	6.62	-4.40	7.53	-8.90	-0.41	-8.39	-3.03
-3.57	9.01	8.66	1.62	8.70	1.01	7.43	-5.77
4.66	-8.60	7.36	-5.60	9.16	0.21	3.07	8.71
-8.12	-4.79	5.23	-7.19	0.68	-8.70	5.32	-7.51
3.05	-8.23	1.75	-8.48	-2.11	-8.31	8.04	-4.18
-8.11	-1.88	-6.50	-6.24	-6.14	-6.62	1.99	-8.92
9.43	-0.37	8.88	-0.97	8.82	1.03	8.06	2.16
5.90	-5.97	6.29	-5.57	8.31	-2.10	7.28	-5.10
4.75	-6.52	8.01	4.70	8.28	4.23	5.98	6.63
-7.98	3.09	-8.62	0.89	-5.27	6.70	-7.73	2.24
-6.36	5.12	-6.53	5.56	-7.32	4.54	-1.44	9.10
-7.35	4.19	0.73	8.90	2.05	8.85	-7.58	2.83

Length segments:
Linear terms
Angstroms

linear clear

linear global

70.49					
0.88	0.68	0.11	0.36		
rel cal xx i>r	8v cal 95%/2	rel cal inop σ	8v cal inop σ	Free	Total xx
70.86	-1.02	-0.24	0.06		69.66
71.50	-1.15	-0.06	0.08		70.36
71.07	0.65	-0.06	0.68		72.35
70.14	-0.88	0.14	0.39		69.78
69.25	0.28	0.01	0.73		70.27
70.23	0.35	-0.18	-0.06		70.35
71.41	0.10	0.00	-0.25		71.26
69.31	0.01	0.15	-0.24		69.22
71.32	-0.47	-0.05	0.24		71.05
69.37	0.09	-0.14	-0.28		69.03
69.21	0.36	0.07	0.27		69.91
70.66	-0.36	-0.09	-0.17		70.03
70.65	0.09	0.16	-0.44		70.46
70.00	-0.23	-0.05	0.26		69.98
70.43	-0.15	0.13	-0.21		70.20
71.50	0.07	0.13	0.12		71.81
71.94	0.47	-0.01	-0.10		72.30
71.67	0.38	-0.06	0.03		72.01
71.35	0.31	0.03	0.72		72.41
70.48	-1.05	-0.03	0.39		69.78
68.75	0.60	0.02	0.40		69.77
71.14	-0.16	-0.04	-0.18		70.76
70.07	-0.91	-0.05	0.26		69.38
71.27	-1.15	0.09	0.24		70.45
70.23	0.44	0.06	-0.49		70.24
70.01	1.00	0.07	0.04		71.11
68.83	-0.47	-0.01	0.70		69.05
70.16	-0.58	0.13	-0.72		68.99
72.81	-0.05	0.05	0.01		72.82
70.02	-0.64	-0.02	-0.34		69.03
70.60	0.35	-0.11	-0.01		70.82
71.88	-0.03	-0.18	-0.12		71.55
70.74	0.03	-0.11	-0.05		70.60

71.52					
2.07	1.4	0.14	0.36		
rel cal yy i>r	8v cal 95%/2	rel cal inop σ	8v cal inop σ	Free	Total yy
71.88	-0.53	-0.06	-0.01		71.28
68.72	1.59	-0.10	-0.16		70.04
72.07	2.43	-0.05	-0.80		73.66
73.68	0.45	-0.02	-0.07		74.04
70.95	-1.98	0.08	-0.64		68.42
70.78	0.50	0.08	0.14		71.50
72.79	1.92	-0.20	-0.26		74.25
68.58	-1.30	-0.03	0.28		67.53
73.92	-2.05	-0.12	0.29		72.03
68.99	-0.45	-0.13	-0.29		68.13
73.06	-0.25	0.03	-0.14		72.70
72.99	1.18	-0.01	-0.05		74.12
71.74	1.72	0.01	0.66		74.13
67.80	-0.45	-0.26	0.10		67.19
69.76	0.27	0.11	0.19		70.33
71.66	-0.27	-0.05	-0.08		71.26
73.85	0.49	0.06	-0.44		73.96
71.02	2.49	-0.24	-0.71		72.56
72.04	-1.44	-0.08	0.09		70.61
73.02	-0.07	0.29	0.63		73.88
70.54	-0.54	-0.03	0.22		70.20
74.01	-0.86	-0.10	0.12		73.17
70.58	1.25	0.16	-0.06		71.93
67.30	-0.49	0.10	0.21		67.12
71.97	-1.58	0.00	-0.01		70.38
70.34	-0.84	-0.01	-0.62		68.86
71.63	2.27	-0.07	0.20		74.04
72.70	2.08	0.07	-0.23		74.62
71.91	-0.56	-0.15	1.01		72.22
68.81	-0.39	-0.01	0.01		68.43
74.06	0.73	0.05	0.09		74.94
69.80	-1.66	-0.01	-0.06		68.06
70.42	0.77	0.06	0.03		71.28

		LS1:		LS2:		LS3:		LS4:	
xx cal	yy cal	Y2-Y1	X2-X1	Y3-Y2	X3-X2	Y4-Y3	X4-X3	Y5-Y4	X5-X4
69.66	71.28	116	-592	237	-596	549	-338	439	-433
69.66	71.28	-511	-400	-605	220	-604	-216	-607	-69
69.66	71.28	434	-469	461	-425	280	-582	431	-485
69.66	71.28	628	133	556	-306	612	-195	640	87
69.66	71.28	-328	530	361	505	-482	405	-378	490
69.66	71.28	583	-330	412	-467	611	-203	620	177
69.66	71.28	634	-141	645	69	539	368	534	431
69.66	71.28	272	629	604	229	596	249	633	251
70.36	70.04	-626	-92	-624	106	-618	125	-343	521
70.36	70.04	105	-607	-476	-381	-285	548	216	608
70.36	70.04	259	-561	545	-319	634	-58	638	5
70.36	70.04	-653	-152	-634	-58	-586	-230	-664	-30
70.36	70.04	-274	-548	-624	-55	-14	-612	117	-572
70.36	70.04	-26	-613	-40	-611	-413	-450	-248	-557
70.36	70.04	-181	557	185	585	-524	354	-442	447
70.36	70.04	550	-296	576	-248	618	97	130	599
72.35	73.66	-325	529	-479	445	-647	33	-674	128
72.35	73.66	-465	479	-324	545	-655	-30	-618	-220
72.35	73.66	-263	652	638	118	641	73	547	-418
72.35	73.66	343	-623	542	-405	674	15	226	630
72.35	73.66	-598	-347	385	-520	50	-630	392	-543
72.35	73.66	225	-596	129	-613	-156	-601	592	-302
72.35	73.66	-597	-136	-479	-451	-452	-479	147	-645
72.35	73.66	695	-27	654	-70	650	74	594	156
69.78	74.04	437	-417	466	-388	616	-146	539	-356
69.78	74.04	352	-455	593	328	613	295	443	463
69.78	74.04	-591	216	-638	62	-391	467	-572	156
69.78	74.04	-471	357	-484	388	-542	317	-106	635
69.78	74.04	-544	293	54	621	151	618	-562	198

Total Length:

Final lengths:

	all lengths	good lengths
		macro counter # 0
mean	2519	mean 2520
st dev	90	st dev 86
count	264	count 179
max	2871	max 2755
min	2263	min 2263

LS1:	LS2:	LS3:	LS4:	Total length	range test	
604	642	645	617	2507	good	2507
649	644	642	611	2545	overrange	
639	642	646	648	2575	good	2575
642	634	642	645	2564	good	2564
624	621	630	618	2493	good	2493
669	623	644	645	2581	overrange	
649	649	653	686	2637	overrange	
686	646	646	681	2659	good	2659
632	633	631	623	2519	good	2519
616	610	618	645	2489	overrange	
618	631	636	638	2523	good	2523
670	637	629	664	2601	good	2601
612	626	612	583	2434	good	2434
613	612	611	610	2446	good	2446
586	613	633	628	2460	good	2460
625	627	626	613	2490	good	2490
621	654	648	686	2609	good	2609
668	634	656	656	2614	good	2614
703	649	645	688	2685	good	2685
711	676	675	670	2731	good	2731
692	647	632	670	2640	good	2640
637	627	621	665	2549	good	2549
612	658	659	662	2590	good	2590
695	658	654	614	2621	good	2621
604	607	633	646	2489	good	2489
575	678	680	640	2574	good	2574
629	641	609	593	2472	overrange	
591	620	628	644	2483	good	2483
618	624	636	595	2473	good	2473

Molecule plots:

plot sans legend:

Image #	molecule #	
	X1	Y1
	X2	Y2
	X3	Y3
	X4	Y4
	X5	Y5

	# 1		# 2		# 3		# 4		# 5		# 6		# 7		# 8	
Image #1	-0.14	-0.20	-0.49	-0.30	-0.17	-0.45	0.29	-0.03	0.04	0.38	0.29	0.27	-0.51	0.41	-0.48	0.08
	-0.22	-0.18	-0.54	-0.37	-0.23	-0.40	0.31	0.05	0.11	0.34	0.25	0.34	-0.52	0.49	-0.40	0.11
	-0.29	-0.15	-0.51	-0.44	-0.28	-0.34	0.27	0.11	0.17	0.39	0.19	0.39	-0.51	0.57	-0.37	0.18
	-0.33	-0.09	-0.54	-0.51	-0.35	-0.31	0.25	0.19	0.22	0.33	0.16	0.47	-0.47	0.63	-0.34	0.25
	-0.39	-0.03	-0.54	-0.58	-0.41	-0.25	0.26	0.27	0.28	0.28	0.19	0.54	-0.42	0.70	-0.31	0.33

	# 1		# 2		# 3		# 4		# 5		# 6		# 7		# 8	
Image #2	0.41	0.09	0.36	-0.48	-0.19	-0.04	0.25	0.29	0.01	-0.09	0.14	-0.35	0.04	0.13	0.25	-0.33
	0.40	0.01	0.29	-0.47	-0.26	-0.01	0.23	0.21	-0.06	-0.13	0.06	-0.35	0.11	0.11	0.21	-0.26
	0.41	-0.06	0.24	-0.53	-0.30	0.06	0.22	0.13	-0.06	-0.20	-0.01	-0.36	0.18	0.14	0.18	-0.19
	0.43	-0.14	0.31	-0.56	-0.31	0.14	0.19	0.06	-0.14	-0.21	-0.07	-0.41	0.23	0.07	0.19	-0.11
	0.49	-0.18	0.38	-0.54	-0.31	0.22	0.19	-0.02	-0.21	-0.19	-0.13	-0.44	0.28	0.02	0.27	-0.10

	# 1		# 2		# 3		# 4		# 5		# 6		# 7		# 8	
Image #3	0.22	0.29	-0.27	0.13	0.37	0.15	0.49	-0.46	0.01	-0.14	-0.11	-0.46	0.45	0.24	-0.36	-0.16
	0.29	0.26	-0.21	0.08	0.45	0.12	0.42	-0.42	-0.03	-0.21	-0.18	-0.43	0.43	0.17	-0.36	-0.08
	0.34	0.20	-0.15	0.04	0.47	0.20	0.37	-0.36	-0.09	-0.16	-0.25	-0.42	0.38	0.11	-0.37	-0.01
	0.34	0.12	-0.15	-0.04	0.47	0.27	0.37	-0.28	-0.17	-0.15	-0.33	-0.44	0.32	0.06	-0.36	0.07
	0.36	0.05	-0.18	-0.11	0.42	0.33	0.44	-0.25	-0.23	-0.11	-0.36	-0.37	0.24	0.07	-0.34	0.14

	# 1		# 2		# 3		# 4		# 5		# 6		# 7		# 8	
Image #4	0.02	-0.18	-0.07	0.00	0.46	0.03	-0.36	0.45	-0.46	0.06	0.38	0.06	-0.35	-0.41	0.12	0.06
	-0.04	-0.13	-0.13	0.04	0.49	-0.03	-0.31	0.40	-0.43	-0.01	0.38	-0.01	-0.41	-0.37	0.07	0.00
	-0.08	-0.08	-0.09	0.11	0.50	-0.11	-0.27	0.34	-0.35	0.00	0.39	-0.09	-0.44	-0.31	0.05	-0.08
	-0.10	-0.01	-0.05	0.18	0.55	-0.15	-0.23	0.28	-0.27	0.02	0.43	-0.15	-0.41	-0.24	0.08	-0.14
	-0.15	0.06	0.01	0.23	0.57	-0.22	-0.15	0.27	-0.25	-0.05	0.38	-0.21	-0.39	-0.16	0.13	-0.20

	# 1		# 2		# 3		# 4		# 5		# 6		# 7		# 8	
Image #5	-0.35	0.03	0.14	0.38	-0.42	0.41	0.04	0.47	0.07	-0.30	0.00	-0.12	-0.22	-0.45	0.13	-0.37
	-0.38	0.09	0.22	0.39	-0.44	0.34	0.00	0.40	0.05	-0.22	0.01	-0.20	-0.18	-0.50	0.11	-0.30
	-0.46	0.11	0.29	0.39	-0.52	0.33	0.04	0.34	0.01	-0.16	0.07	-0.24	-0.16	-0.57	0.04	-0.27
	-0.52	0.15	0.35	0.44	-0.59	0.35	0.07	0.27	-0.04	-0.11	0.14	-0.21	-0.08	-0.58	-0.01	-0.22
	-0.49	0.22	0.38	0.51	-0.63	0.28	0.12	0.23	-0.12	-0.12	0.16	-0.14	-0.01	-0.55	-0.06	-0.17

	# 1		# 2		# 3		# 4		# 5		# 6		# 7		# 8	
Image #6	0.02	0.35	0.35	-0.12	-0.32	-0.20	-0.42	-0.02	-0.43	0.05	-0.22	-0.06	-0.20	0.02	-0.38	0.04
	0.06	0.41	0.30	-0.05	-0.29	-0.14	-0.44	0.05	-0.48	0.11	-0.15	-0.09	-0.22	0.10	-0.40	-0.03
	0.10	0.48	0.29	0.02	-0.24	-0.09	-0.48	0.12	-0.56	0.14	-0.08	-0.13	-0.27	0.16	-0.44	-0.10
	0.09	0.56	0.22	0.04	-0.22	-0.02	-0.54	0.17	-0.61	0.20	-0.02	-0.18	-0.27	0.23	-0.46	-0.17
	0.07	0.63	0.14	0.03	-0.15	0.01	-0.61	0.20	-0.63	0.28	-0.04	-0.26	-0.33	0.29	-0.45	-0.24

	# 1		# 2		# 3		# 4		# 5		# 6		# 7		# 8	
Image #7	0.10	-0.20	-0.17	0.42	-0.11	-0.13	0.06	0.48	0.46	-0.05	0.47	-0.16	0.13	0.42	-0.32	-0.15
	0.07	-0.28	-0.24	0.40	-0.15	-0.19	0.14	0.44	0.42	0.02	0.46	-0.25	0.07	0.46	-0.39	-0.12
	0.06	-0.36	-0.27	0.33	-0.20	-0.24	0.19	0.38	0.42	0.10	0.45	-0.33	0.01	0.52	-0.45	-0.08
	0.10	-0.44	-0.28	0.25	-0.21	-0.32	0.26	0.39	0.47	0.16	0.39	-0.37	-0.06	0.49	-0.50	-0.01
	0.11	-0.52	-0.29	0.17	-0.28	-0.36	0.31	0.32	0.42	0.22	0.34	-0.44	-0.12	0.45	-0.56	-0.04

Image 1

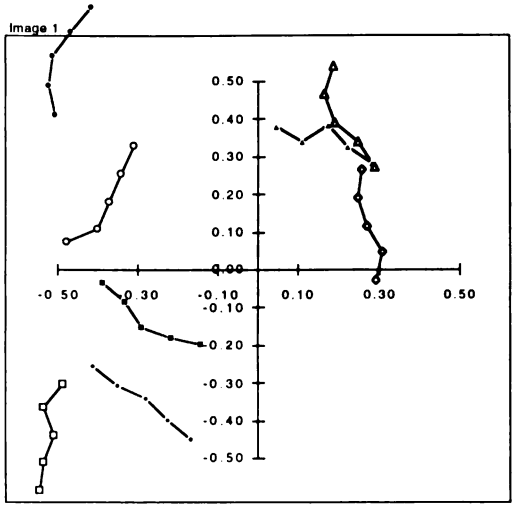

Image 2

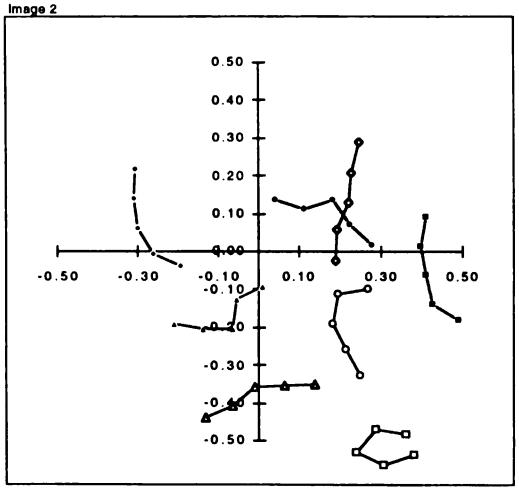

Image 3

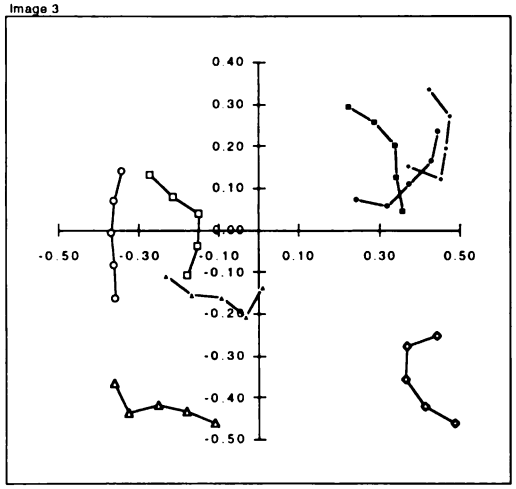

Image 4

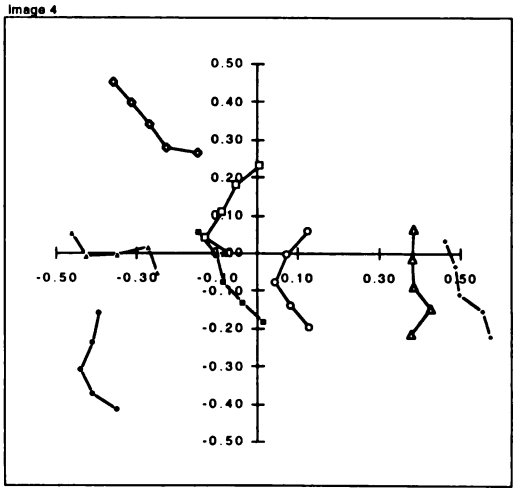

Image 5

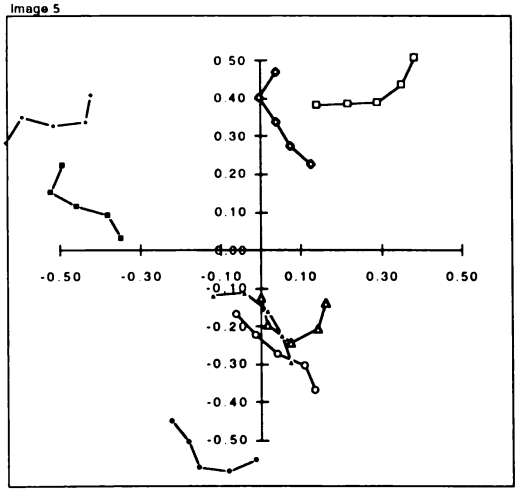

Image 6

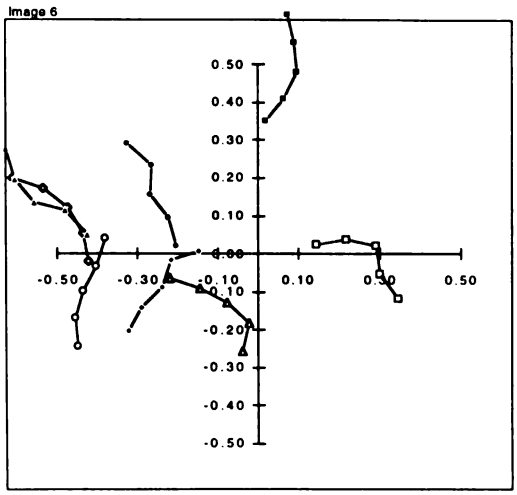

			Experiment #								
			9	8	7	6	5	4	3	2	1
	mean	st dev									
mean	2504	13	2520	2520	2503	2489	2489	2495	2495	2504	2521
st dev	89	8	86	86	94	100	100	82	80	92	85
count	9		179	179	179	188	188	169	200	185	179
max	2794		2755	2755	2760	2794	2794	2774	2703	2757	2752
min	2249		2263	2263	2283	2249	2249	2327	2307	2297	2285
		Expenment results:	2507	2507		2431	2431		2430	2480	2511
								2494	2611		
			2575	2575		2449	2449	2510			2594
			2564	2564	2403	2406	2406	2584	2544	2545	2552
			2493	2493	2462	2361	2361	2524	2465	2497	2479
					2417	2444	2444	2414	2674	2469	
					2492	2445	2445		2509		
			2659	2659	2539			2448	2581	2570	2643
			2519	2519		2496	2496		2553	2453	2521
					2585	2606	2606		2599	2443	
			2523	2523	2586	2530	2530	2462			2518
			2601	2601					2472	2483	2591
			2434	2434	2578	2525	2525	2405	2497	2447	2438
			2446	2446		2538	2538		2559	2445	2451
			2460	2460		2480	2480		2526	2416	2458
			2490	2490		2397	2397	2518		2461	2502
			2609	2609	2378	2563	2563		2429	2603	2605
			2614	2614	2417	2536	2536			2603	2614
			2685	2685		2540	2540	2484	2574	2591	2680
			2731	2731	2445	2481	2481	2347	2440	2599	2739
			2640	2640	2357	2499	2499	2346	2569	2526	2642
			2549	2549				2526		2546	2554
			2590	2590					2522		2588
			2621	2621		2520	2520		2482	2683	2622
			2489	2489	2456	2334	2334	2351		2471	2493
			2574	2574		2329	2329	2422	2506	2757	2567
					2488	2409	2409	2452	2457	2675	
			2483	2483	2382	2410	2410	2440	2454	2663	2469
			2473	2473	2356	2476	2476			2663	2473

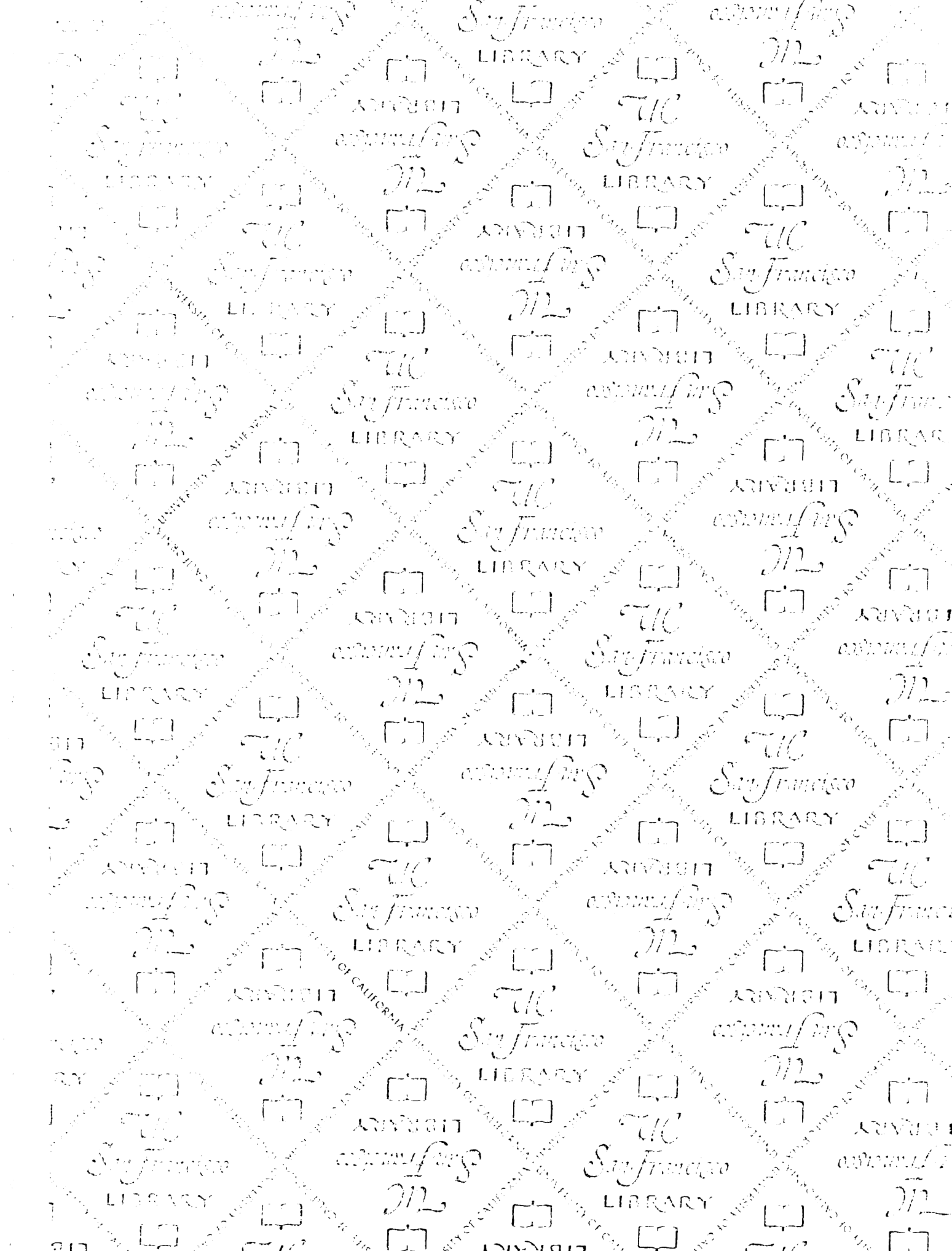
The San Francisco Public Library
Property of the San Francisco Public Library

For reference

Not to be taken from the room.